GDAŃSK UNIVERSITY OF TECHNOLOGY

The author of the doctoral dissertation: Aiswarya Manohar
Scientific discipline: Materials Engineering

DOCTORAL DISSERTATION

Title of doctoral dissertation: Engineering Laser-Induced Graphene for Multifunctional Electrochemical Interfaces

Title of doctoral dissertation (in Polish): Inżynieria laserowo indukowanego grafenu do tworzenia wielofunkcyjnych interfejsów elektrochemicznych

Supervisor *signature*
Prof. dr. hab. inz Jacek Ryl
Auxiliary supervisor *signature*
Dr Mohsen Khodadadi Yazdi, PhD

Gdańsk, 2026

POLITECHNIKA GDAŃSKA

STATEMENT

The author of the doctoral dissertation: Aiswarya Manohar

I, the undersigned, declare that I am aware that in accordance with the provisions of Art. 27 (1) and (2) of the Act of 4th February 1994 on Copyright and Related Rights (Journal of Laws of 2021, item 1062), the university may use my doctoral dissertation entitled:
Engineering Laser-Induced Graphene for Multifunctional Electrochemical Interfaces
for scientific or didactic purposes.[1]

Gdańsk,..... .....

signature of the PhD student

Aware of criminal liability for violations of the Act of 4th February 1994 on Copyright and Related Rights and disciplinary actions set out in the Law on Higher Education and Science(Journal of Laws 2021, item 478), as well as civil liability, I declare, that the submitted doctoral dissertation is my own work.

I declare, that the submitted doctoral dissertation is my own work performed under and in cooperation with the supervision of Prof. dr. hab. inz Jacek Ryl, the auxiliary supervision of Dr Mohsen Khodadadi Yazdi, PhD.

This submitted doctoral dissertation has never before been the basis of an official procedure associated with the awarding of a PhD degree.

All the information contained in the above thesis which is derived from written and electronic sources is documented in a list of relevant literature in accordance with Art. 34 of the Copyright and Related Rights Act.

I confirm that this doctoral dissertation is identical to the attached electronic version.

Gdańsk,..... .....

signature of the PhD student

I, the undersigned, agree to include an electronic version of the above doctoral dissertation in the open, institutional, digital repository of Gdańsk University of Technology.

Gdańsk,..... .....

signature of the PhD student

[1] Art 27. 1. Educational institutions and entities referred to in art. 7 sec. 1 points 1, 2 and 4–8 of the Act of 20 July 2018 – Law on Higher Education and Science, may use the disseminated works in the original and in translation for the purposes of illustrating the content provided for didactic purposes or in order to conduct research activities, and to reproduce for this purpose disseminated minor works or fragments of larger works.

2. If the works are made available to the public in such a way that everyone can have access to them at the place and time selected by them, as referred to in para. 1, is allowed only for a limited group of people learning, teaching or conducting research, identified by the entities listed in paragraph 1.

GDAŃSK UNIVERSITY OF TECHNOLOGY

DESCRIPTION OF DOCTORAL DISSERTATION

The Author of the doctoral dissertation: Aiswarya Manohar

Title of doctoral dissertation: Engineering Laser-Induced Graphene for Multifunctional Electrochemical Interfaces

Title of doctoral dissertation in Polish: Inżynieria laserowo indukowanego grafenu do tworzenia wielofunkcyjnych interfejsów elektrochemicznych

Language of doctoral dissertation: English

Supervisor: Prof. dr. hab. inz Jacek Ryl

Auxiliary supervisor*: Dr Mohsen Khodadadi Yazdi

Date of doctoral defense :

Keywords of doctoral dissertation in Polish: Słowa kluczowe: Grafen indukowany laserowo, inżynieria powierzchni, platformy elektrochemiczne, interfejsy hydrożelowe, elektroanaliza

Keywords of doctoral dissertation in English: Laser-Induced Graphene (LIG), Surface Engineering, Electrochemical platforms, Hydrogel Interfaces, Electroanalysis

Summary of doctoral dissertation in Polish: Indokowany laserowo grafen (LIG) jest obiecującym materiałem elektrodowym ze względu na szybki, skalowalny i ekonomiczny proces jego wytwarzania, który pozwala na dostosowanie jego właściwości końcowych. Na parametry użytkowe materiału istotny wpływ mają warunki wytwarzania, dobór prekursora oraz modyfikacje powierzchni. W niniejszej pracy opracowano metodologię wytwarzania LIG, inżynierii powierzchni, ilościowej analizy elektrochemicznej oraz projektowania materiałów w oparciu o dobór prekursora. Parametry procesu laserowego poddano systematycznej optymalizacji i powiązano z właściwościami fizykochemicznymi, elektrycznymi oraz elektrochemicznymi materiału LIG. Następnie zoptymalizowany LIG poddano modyfikacjom z wykorzystaniem ekologicznych membran hydrożelowych, nanozymów Ir-Pt, wielofunkcyjnego kopolimeru o właściwościach antyadhezyjnych i antybakteryjnych oraz biofunkcjonalizacji oksydazą glukozową, co pozwoliło na precyzyjne kształtowanie transportu międzyfazowego, aktywności katalitycznej i funkcjonalności biochemicznej. Kompleksowa analiza i charakterystyka pozwoliły na ustalenie ilościowych zależności między strukturą, właściwościami a parametrami użytkowymi materiału. Opracowane platformy zweryfikowano z użyciem modelowych analitów. Dalsze badania wykazały potencjał wytwarzania LIG z prekursorów celulozowych i fluoropolimerowych oraz zastosowania metody transferu LIG wspomaganej polimerem PEGDA. Opracowane procedury inżynierii powierzchni mogą znaleźć zastosowanie w elastycznych i noszonych urządzeniach elektrochemicznych, platformach mikroprzepływowych, interfejsach bioelektronicznych, układach elektrokatalitycznych oraz innych technologiach elektrochemicznych.

Summary of doctoral dissertation in English: Laser-induced graphene (LIG) is a promising material due to its rapid, scalable, cost-effective and customizable fabrication. Its performance is strongly influenced by fabrication parameters, precursor selection and surface modifications. This dissertation establishes methodology for the LIG fabrication, surface engineering, quantitative electrochemical analysis and precursor-dependent materials design. Laser parameters were systematically optimized and correlated with the physicochemical, electrical and electrochemical properties of LIG. The optimized LIG was subsequently engineered using sustainable hydrogel membranes, Ir-Pt nanozymes, antifouling and antibacterial multifunctional copolymer and glucose oxidase biofunctionalization to tailor interfacial transport, catalytic activity and biological functionality. A comprehensive analysis and characterization established quantitative structure-property-performance relationships. The developed platforms were validated using model analytes. The extended future investigations showed the possibility to fabricate cellulose-derived LIG, fluoropolymer-derived LIG and PEGDA-assisted LIG transfer. The established surface engineering protocols have the potential to be extended to flexible and wearable electrochemical devices, microfluidic platforms, bioelectronic interfaces, electrocatalytic systems and other electrochemical technologies.

Acknowledgement

The completion of this dissertation marks the end of an inspiring and transformative journey. I would like to express my sincere gratitude to everyone who has contributed, directly or indirectly, to this work.

First and foremost, I would like to express my deepest gratitude to my supervisor, ***Prof. dr hab. inż. Jacek Ryl****, for his invaluable guidance, continuous encouragement, scientific insight, constructive criticism and unwavering support throughout my doctoral studies. I am sincerely grateful for the trust he placed in me and for the many opportunities he provided to broaden my scientific knowledge and research experience. His mentorship has been instrumental in shaping this dissertation and in my development as an independent researcher. I would also like to express my sincere appreciation to* ***Dr. Mohsen Khodadadi Yazdi*** *(Associate Professor, Gdańsk University of Technology) for his guidance, support and willingness to share his expertise. His valuable discussions, thoughtful suggestions and continuous encouragement have significantly contributed to the successful completion of this work.*

I am deeply grateful to all members of the ***Division of Electrochemistry and Surface Physical Chemistry****,* ***Institute of Nanotechnology and Materials Engineering****,* ***Faculty of Applied Physics and Mathematics****,* ***Gdańsk University of Technology****, for providing an inspiring, collaborative and supportive research environment. The exchange of ideas, technical assistance and numerous scientific discussions have greatly enriched my doctoral experience.*

I would like to express my sincere appreciation to ***Ms. Angelika Łepek*** *(PhD student, Division of Electrochemistry and Surface Physical Chemistry, Gdańsk University of Technology) and* ***Dr. Tomasz Swebocki*** *(Associate Professor, Gdańsk University of Technology) for their valuable discussions, technical support and encouragement throughout my research. Their willingness to share knowledge and experience has been greatly appreciated.*

I would also like to extend my heartfelt thanks to my office mates ***Ms. Martyna Czudec*** *(PhD student, Faculty of Applied Physics and Mathematics, Gdańsk University of Technology) and* ***Mr. Michał Dominów*** *(PhD student, Faculty of Applied Physics and Mathematics, Gdańsk University of Technology) for creating such a positive, friendly and supportive working atmosphere. The countless conversations, mutual encouragement and even our friendly "race board" competitions made every day in the laboratory enjoyable and memorable. Those moments of healthy competition and shared motivation brought both balance and positivity to my doctoral journey.*

I would also like to express my sincere appreciation to ***Ms. Beata Toma****, MSc, Eng., Senior Specialist, Faculty of Technical Physics and Applied Mathematics, Gdańsk University of Technology and* ***Ms. Lucyna Namysł****, MA, Senior Specialist, Office of the Institute of Nanotechnology and Materials Science, Faculty of Technical Physics and Applied Mathematics, Gdańsk University of Technology, for their invaluable administrative support, kindness and assistance throughout my doctoral studies. Their professionalism and willingness to help greatly facilitated many aspects of my academic journey.*

To my friends and fellow PhD students, thank you for your friendship, encouragement and the many conversations and shared experiences that made this journey both enjoyable and unforgettable.

I would also like to thank all laboratory technicians and administrative staff for their assistance and for ensuring an excellent research environment throughout my studies. I would also like to express my sincere appreciation to my students, whose curiosity, enthusiasm and eagerness to learn made teaching an enjoyable and rewarding experience. Interacting with them not only enriched my doctoral journey but also contributed significantly to my growth as a researcher, mentor and educator.

My deepest gratitude reserved for my family. To my parents, thank you for your unconditional love, unwavering faith in me and the countless sacrifices you have made throughout my life. Your encouragement has always given me the strength to pursue my goals, even during the most difficult moments. To my family members, thank you for your constant support, patience and understanding throughout this journey.

Finally, I would like to express my sincere gratitude to everyone who has contributed to this work, whether directly or indirectly, even if their names are not mentioned here. Every word of encouragement, every act of kindness and every shared moment has been an important part of this journey.

This dissertation represents not only several years of scientific research but also a period of continuous learning, personal growth, perseverance and resilience. I am sincerely grateful to everyone who has accompanied and supported me throughout this remarkable journey.

Funding

I gratefully acknowledge the financial support provided by the National Science Centre (NCN), Poland, under the OPUS LAP project (Grant Number: 2023/51/I/ST7/01948). I also gratefully acknowledge the financial support provided by the Excellence Initiative - Research University (IDUB) programme at Gdańsk University of Technology through the Polonium Scholarship (192483;01.11.2022-30.09.2023) and the Francium Scholarships (15/1/2023/IDUB/III.2b/Fr, 50/1/2024/IDUB/III.2b/Fr, 14/Francium/2025-2026 for second, third, fourth year of doctoral studies respectively). These scholarships supported my doctoral studies, research activities, participation in scientific conferences and international scientific collaboration.

STRESZCZENIE

Grafen indukowany laserowo (LIG) powstaje w jednym kroku, bez używania maskowania i bezpośrednio w warunkach otoczenia, poprzez wypalanie wzoru w polimerze. Ta prostota wytwarzania, w połączeniu z rozwiniętą porowatością i dobrym przewodnictwem, uczyniła go atrakcyjnym materiałem elektrodowym. Jednocześnie jednak właściwości elektrochemiczne LIG silnie zależą od parametrów wiązki lasera i rodzaju prekursora, podczas gdy dotychczasowe prace koncentrowały się głównie na optymalizacji pod kątem określonych, pojedynczych zastosowań. Brakuje natomiast opisu powiązań między warunkami obróbki laserowej, strukturą materiału, modyfikacją powierzchni i odpowiedzią elektrochemiczną, co pozwoliłoby projektować takie elektrody w sposób przewidywalny.

Celem rozprawy było ustalenie wybranych z tych zależności oraz sprawdzenie, czy właściwości elektroanalityczne LIG można kształtować poprzez kolejne, kontrolowane modyfikacje interfejsu elektrodowego.

W pierwszym etapie zbadano wpływ mocy, prędkości skanowania, odstępu ścieżek i położenia ogniska wiązki na morfologię, uporządkowanie struktury grafitowej, chemię powierzchni, zwilżalność, przewodnictwo i odpowiedź elektrochemiczną LIG wytwarzanego z folii poliimidu o dwóch różnych grubościach. Wskazano warunki dające najkorzystniejszą odpowiedź elektrochemiczną i wykazano, że nawet jednoprocentowa zmiana mocy wiązki mierzalnie wpływa zarówno na strukturę, jak i kinetykę przeniesienia elektronu.

W drugim etapie, na zoptymalizowanym podłożu, wykonano trzy modyfikacje. Membrany hydrożelowe z chitozanu, alginianu i agaru posłużyły do zbadania wpływu warstwy hydrożelowej na dyfuzję i transport międzyfazowy. Następnie metodą elektroosadzania wprowadzono bimetaliczne nanostruktury irydowo-platynowe, uzyskując wzrost powierzchni elektroaktywnej, spadek oporu przeniesienia ładunku oraz wyraźną poprawę aktywności elektrokatalitycznej w procesie utleniania nadtlenku wodoru. Na tak przygotowanej powierzchni wytworzono metodą elektropolimeryzacji kopolimer APTAC/SBMA, łączący ugrupowania kationowe i zwitterjonowe, w którym unieruchomiono oksydazę glukozową.

Otrzymana platforma Ir-Pt-CoP-GOx@LIG umożliwiła oznaczanie glukozy w zakresie liniowym 0,5-7,5mM, z czułością 15,4 μA/mM/cm^2 i granicą wykrywalności 6,55 μM, przewyższając układ odniesienia z enzymem unieruchomionym w chitozanie. Elektroda zachowywała mierzalną odpowiedź na glukozę w sztucznym pocie przy pH 5,4 i 6,0, przy obniżonej czułości względem buforu oraz utrzymywała część odpowiedzi analitycznej przez cztery godziny ekspozycji na BSA, przy czym straty sygnału malały wraz ze zmniejszaniem nadpotencjału elektrody. Materiał polimerowy wykazywał aktywność przeciwbakteryjną wobec *Escherichia coli* i *Staphylococcus aureus* opornego na metycylinę w badaniu półilościowym.

W ostatniej części pokazano badania rozwojowe, wciąż realizowane. Wśród nich sprawdzono możliwość przeniesienia opracowanej technologii wytwarzania LIG na inne podłoża. Dla celulozy zaproponowano opracowanie dwustopniowej strategii naświetlania pozwalającej uzyskać ciągłe struktury przewodzące, których właściwości strukturalne potwierdzono spektroskopią Ramana. Dla politetrafluoroetylenu jako podłoża wyznaczono wstępne okno przetwarzania, znacznie węższe niż dla poliimidu i celulozy. Zbadano też przeniesienie LIG na elastyczne podłoże PEGDA, uzyskując zachowanie morfologii warstwy przy

jednoczesnym braku stabilnego przewodnictwa. Wyniki tej części mają charakter rozpoznawczy i nie obejmują badań elektrochemicznych.

Rozprawa pokazuje, że kolejne modyfikacje powierzchni LIG pełnią odrębne funkcje: poprawiają transport, aktywność katalityczną, unieruchamiają enzym i działają przeciwbakteryjnie, wszystko to bez utraty aktywności elektrochemicznej powierzchni. Opisane zależności między obróbką laserową a odpowiedzią elektrochemiczną stanowią punkt wyjścia do projektowania elektrod LIG w innych układach analitycznych.

Słowa kluczowe: Grafen indukowany laserowo, inżynieria powierzchni, platformy elektrochemiczne, interfejsy hydrożelowe, elektroanaliza

ABSTRACT

Laser-induced graphene (LIG) is produced in a single step, without masking and directly under ambient conditions, by burning a pattern into a polymer. This simplicity of fabrication, combined with a well-developed porosity and good conductivity, has made it an attractive electrode material. At the same time, the electrochemical properties of LIG depend strongly on the laser beam parameters and on the type of precursor, whereas previous work has concentrated mainly on optimization for specific, individual applications. However, a description of the links between laser processing conditions, material structure, surface modification and electrochemical response that would allow such electrodes to be designed in a predictable way is still missing.

The aim of this dissertation was to establish selected relationships of this kind and to determine whether the electroanalytical properties of LIG can be shaped through successive, controlled modifications of the electrode interface.

In the first stage, the influence of laser power, scanning speed, hatch spacing and focal position on the morphology, ordering of the graphitic structure, surface chemistry, wettability, conductivity and electrochemical response of LIG produced from polyimide (PI) foil of two different thicknesses was examined. Conditions giving the most favourable electrochemical response were identified and it was shown that even a one per cent change in beam power measurably affects both the structure and the kinetics of electron transfer.

In the second stage, three modifications were carried out on the optimized substrate. Hydrogel membranes of chitosan, alginate and agar were used to examine the influence of a hydrogel layer on diffusion and interfacial transport. Bimetallic iridium-platinum nanostructures were then introduced by electrodeposition, giving an increase in electroactive surface area, a decrease in charge transfer resistance and a clear improvement in electrocatalytic activity in the oxidation of hydrogen peroxide. On the surface prepared in this way, an APTAC/SBMA copolymer combining cationic and zwitterionic moieties was formed by electropolymerization, and glucose oxidase was immobilized within it.

The resulting Ir-Pt-CoP-GOx@LIG platform allowed glucose to be determined over a linear range of 0.5-7.5mM, with a sensitivity of 15.4 μA/mM/cm^2 and a detection limit of 6.55μM, outperforming the reference system with the enzyme immobilized in chitosan. The electrode retained a measurable glucose response in artificial sweat at pH 5.4 and 6.0, with lower sensitivity than in buffer and preserved part of its analytical response over four hours of exposure to BSA, the loss of signal decreasing as the electrode overpotential was reduced. The polymer material showed antibacterial activity against *Escherichia coli* and methicillin-resistant *Staphylococcus aureus* in a semi-quantitative assay.

The final part presents development work that is still in progress. It includes an assessment of whether the fabrication route developed for LIG can be transferred to other substrates. For cellulose, a two-step irradiation strategy was proposed that yields continuous conductive structures, whose structural properties were confirmed by Raman spectroscopy. For polytetrafluoroethylene as a substrate, a preliminary processing window was determined, considerably narrower than for polyimide and cellulose. The transfer of LIG onto a

flexible PEGDA support was also examined, preserving the morphology of the layer but without stable conductivity. The results of this part are exploratory and do not include electrochemical measurements.

The dissertation shows that successive modifications of the LIG surface perform distinct functions-improving transport, providing catalytic activity, immobilizing the enzyme and acting against bacteria, without loss of electrochemical activity of the surface. The relationships described between laser processing and electrochemical response provide a starting point for the design of LIG electrodes in other analytical systems.

Keywords: Laser-Induced Graphene (LIG), Surface Engineering, Electrochemical platforms, Hydrogel Interfaces, Electroanalysis

TABLE OF CONTENTS

CHAPTER 1 - INTRODUCTION 17
CHAPTER 2 - REVIEW OF LITERATURE 18
2.1 Electrochemical interfaces 18
2.2 Carbon-based electrode materials for electrochemical interfaces 19
2.2.1 Traditional carbon platforms: workhorses with inherent limitations 20
2.2.2 The nanocarbon revolution: enhanced performance with new complexities 20
2.2.3 Pursuing practicality: drive towards scalable and patternable alternatives 22
2.3 Laser-induced graphene (LIG) 22
2.3.1 Discovery and evolution of laser-induced graphene 23
2.3.2 Fundamentals of laser-material interaction 25
2.3.3 Influence of laser parameters on LIG morphology and conductivity 27
2.3.4 Structure-property relationships and fabrication-dependent variability 30
2.3.5 Morphological and surface characteristics of LIG 31
2.4 Correlation of electrochemical characteristics of LIG with structure -property relationship 38
2.5 Surface engineering strategies 38
2.6 Hydrogel-based surface modification strategies 39
2.7 Nanomaterials surface engineering and noble metal nanoparticles 42
2.8 Antifouling and antibacterial interfaces 43
2.9 Multifunctional coatings 45
2.10 Surface modification techniques 46
2.10.1 Physical immobilization techniques 46
2.10.2 Electrochemical modification techniques 46
2.10.3 Chemical immobilization strategies 48
2.11 Stability and reproducibility concerns 50
2.12 LIG-based electrochemical interfaces: reported applications and limitations 51
2.13 Research gaps identified in the literature 51
CHAPTER 3 - OBJECTIVES AND SCOPE 54
3.1 Central research questions and hypothesis 54
CHAPTER 4 - MATERIALS AND METHODS 56
4.1 Materials 56
4.1.1 Carbon precursor substrates and processing materials. 56
4.1.2 Hydrogel and polymer materials 56
4.1.3 Monomers and polymerization reagents 56
4.1.4 Electrodeposition precursors 56

4.1.5 Electrochemical reagents 57
4.1.6 Other reagents 57
4.2 Experimental instrumentation 57
4.2.1 Laser fabrication system 57
4.2.2 Physicochemical characterization 57
4.2.3 Electrochemical instrumentation 58
4.2.4 Optical characterization 58
4.3 Methods - fabrication and translational strategies 58
4.3.1 Fabrication of polyimide-derived LIG 59
4.3.2 Fabrication of cellulose-derived LIG 60
4.3.3 Preliminary fabrication of PTFE-derived laser-induced carbon structures 60
4.3.4 PEGDA-assisted transfer of LIG (LIGT) 61
4.3.4.1 Preparation of PEGDA formulations and transfer procedure 61
4.3.4.2 Preliminary characterization 61
4.3.4.3 Proposed experimental design for future optimization 62
4.4 Research methodology - surface engineering protocols 62
4.4.1 Development of hydrogel membrane (HM) coated LIG electrodes 62
4.4.2 Electrodeposition of nanomaterials - Ir and Pt decorated LIGs 63
4.4.3 Electropolymerization of APTAC and SBMA 64
4.4.4 GOx immobilization 64
4.4.5 Physicochemical characterization 65
4.4.6 Electrochemical evaluation and electroanalytical validation 65
4.4.6.1 Interference and operational stability 66
4.4.6.2 Practical applicability under physiologically relevant conditions - Artificial sweat test 67
4.4.7 Evaluation of antifouling and antibacterial functionalities 67
4.4.8 Data processing and electrochemical calculations 67
4.4.8.1 Chronoamperometric modelling 68
4.4.8.2 Determination of EASA 69
4.4.8.3 Heterogeneous electron transfer rate constant (k^0) 70
4.4.8.4 Charge transfer resistance (R_{ct}) 70
4.4.8.5 Electroanalytical performance calculations 70
CHAPTER 5 - RESULTS AND DISCUSSION 71
5.1 Fundamentals of LIG formation and performance evolution 71
5.1.1 The influence of lasing parameters and effect of thickness of Kapton foil 71
5.1.2 Morphological characteristics of LIG 73
5.1.3 Structural and surface characterization of LIG 75

5.1.4 Wettability and surface properties 78
5.1.5 Electrical conductivity of LIG 80
5.1.6 Electrochemical characterization of LIG 83
5.1.7 Electroactive surface area (EASA) 85
5.1.8 Electron transfer kinetics 87
5.1.9 Charge transfer resistance and electrochemical impedance analysis 88
5.1.10 Preliminary assessment of influence of laser focus position (Z-offset) on LIG fabrication 89
5.2 Hydrogel-LIG interface engineering 92
5.2.1 Morphological characteristics of hydrogel-coated LIGs 93
5.2.2 Surface chemistry of hydrogel-coated LIG 94
5.2.3 Wettability and hydrophilicity 95
5.2.4 Electrochemical behaviour of hydrogel-modified LIG electrodes 97
5.2.5 Heterogeneous electron transfer kinetics 99
5.2.6 Electrochemical impedance spectroscopy analysis 100
5.2.7 Effect of chitosan crosslinking density on electrochemical performances 101
5.2.8 Transition from hydrogel interphase engineering to metallic functionalization 103
5.3 Nanozyme-based bimetallic surface engineering 103
5.3.1 Electrodeposition of Iridium and Platinum nanostructures 104
5.3.2 Morphological characterization of Ir-Pt NPs 105
5.3.3 Structural and surface chemical characterization of Ir-Pt interfaces 108
5.3.4 Electrochemical behaviour of bimetallic functionalized LIG 109
5.3.4.1 Integrated correlation between theoretical metal loading, electroactive surface area and electron-transfer kinetics 113
5.3.5 Electrochemical impedance spectroscopy and interfacial charge transfer 114
5.3.6 Electrocatalytic activity towards hydrogen peroxide oxidation 115
5.3.7 Analytical performance and long term stability 116
5.4 Multifunctional copolymer based surface engineering of Ir-Pt decorated LIG 117
5.4.1 Electropolymerization of functional copolymers - APTAC and SBMA 118
5.4.1.1 Electropolymerization strategy 118
5.4.1.2 Polymer growth and redox peaks 118
5.4.1.3 Proposed electropolymerization mechanisms of APTAC and SBMA 120
5.4.2 Morphological characterization of polymer-modified electrodes 122
5.4.3 Surface chemical characterization of copolymer modified Ir-Pt decorated LIGs 124
5.4.4 Proof-of-concept validation: electroanalytical performance of the multifunctional copolymer for glucose sensing 126

5.4.4.1 Electroanalytical glucose sensing 126
5.4.4.2 Selectivity of the glucose sensing platform 128
5.4.4.3 Operational stability 129
5.4.4.4 Validation in artificial sweat 130
5.4.5 Electrochemical response under protein-containing conditions 132
5.4.6 Antibacterial assays of multifunctional copolymer interface 133
5.4.6.1 Antibacterial assessment of individual polymers 134
5.4.6.2 Semi-quantitative antibacterial assessment of the multifunctional copolymer 135
CHAPTER 6 - FUTURE PERSPECTIVES AND ONGOING RESEARCH 138
Extension of the LIG engineering to alternative precursors and translation towards next-generation LIG platforms 138
6.1 Influence of substrate chemistry: PI versus cellulose-derived LIG 138
6.1.1 Preliminary assessments and development of the laser processing strategy 139
6.1.2 Influence of laser parameters - cellulose-derived LIGs/ Paper-LIGs 140
6.1.3 Structural evolution and graphitic ordering of cellulose-derived LIG 144
6.1.4 Electrical percolation and conductive network formation 146
6.1.5 Future characterization and scientific outlook 148
6.2 Exploration of fluoropolymer precursors: towards laser modified fluoropolymer-derived carbon architectures 148
6.2.1 Preliminary establishment of the laser processing window 149
6.2.2 Preliminary physicochemical characterization 151
6.3 Exploratory PEGDA-assisted transfer of LIG (LIGT) onto flexible hydrogel substrates 153
6.3.1 Evaluation of feasibility of PEGDA-assisted LIG transfer 153
6.3.2 Preliminary structural and electrical assessment of transferred LIG 154
Exploratory studies and future perspectives. 157
CONCLUSIONS 159
REFERENCES 161
List of Figures 173
List of Tables 176

LIST OF IMPORTANT SYMBOLS

Symbol	Description
α	Charge transfer coefficient
A	Electrode area
C	Concentration of electroactive species
D	Diffusion coefficient
E	Applied electrode potential
E°	Standard electrode potential
EASA	Electrochemically active surface area
E_{pa}	Anodic peak potential
E_{pc}	Cathodic peak potential
F	Faraday constant (96,485 C/mol)
I	Electric current
I_{pa}	Anodic peak current
I_{pc}	Cathodic peak current
k°	Standard heterogeneous electron transfer rate constant
n	Number of electrons transferred
Q	Electric charge
R	Universal gas constant
R^2	Coefficient of determination
R_{ct}	Charge transfer resistance
R_s	Sheet resistance
T	Absolute temperature
t	Time
ν	Scan rate
σ	Electrical conductivity
Z	Impedance
Z'	Real impedance
Z''	Imaginary impedance

LIST OF ABBREVIATIONS

Abbreviation	Full term
APTAC	(3-Acrylamidopropyl)trimethylammonium chloride
BDD	Boron-doped diamond
BSA	Bovine serum albumin
CA	Chronoamperometry
CE	Counter electrode
CPE	Carbon paste electrode
CP	Chronopotentiometry
CV	Cyclic voltammetry
CVD	Chemical vapor deposition
DI	Deionized water
DLW	Direct laser writing
EASA	Electrochemically active surface area
EDX	Energy dispersive X-ray spectroscopy
EIS	Electrochemical impedance spectroscopy
FTIR	Fourier-transform infrared spectroscopy
GCE	Glassy carbon electrode
GelMA	Gelatin methacryloyl
GO	Graphene oxide
GOx	Glucose oxidase
H_2O_2	Hydrogen peroxide
HM	Hydrogel membrane
HRTEM	High-resolution transmission electron microscopy
LIG	Laser-induced graphene
LOD	Limit of detection
NP	Nanoparticle
PBS	Phosphate buffered saline
PDMS	Polydimethylsiloxane
PEG	Poly(ethylene glycol)
PEGDA	Poly(ethylene glycol) diacrylate
PI	Polyimide
PPy	Polypyrrole
PTFE	Polytetrafluoroethylene
PANI	Polyaniline
rGO	Reduced graphene oxide

SEM	Scanning electron microscopy
SPCE	Screen-printed carbon electrode
SBMA	Sulfobetaine methacrylate
TEM	Transmission electron microscopy
TPO	Diphenyl(2,4,6-trimethylbenzoyl)phosphine oxide (photoinitiator)
UV-Vis	Ultraviolet-visible spectroscopy
WE	Working electrode
XPS	X-ray photoelectron spectroscopy

CHAPTER 1 - INTRODUCTION

The growing demand for advanced analytical technologies in healthcare, environmental monitoring, food safety, sustainable manufacturing and energy applications has accelerated the development of functional materials capable of meeting increasingly demanding performance requirements[1]. At the same time, the continued evolution of portable, flexible and miniaturized devices, including wearable electronics, point-of-care diagnostic systems and bioelectronic technologies, has increased the need for material platforms that combine high performance with scalable manufacturing, mechanical flexibility and long-term operational stability[2]. As a result, the development of advanced materials for electrochemical technologies has become an important research area in contemporary materials engineering[3].

Among the available analytical technologies, electrochemical systems have attracted considerable attention because of their high sensitivity, rapid response, low power consumption, portability and compatibility with miniaturized devices[4]. The performance of these systems is largely determined by the characteristics of the electrode-electrolyte interface, where electron transfer, mass transport and electrochemical reactions occur[1]. As a result, the design of electrode materials capable of providing favourable structural, physicochemical and electrical properties remains central to improving the performance and reliability of advanced electrochemical systems[1].

Laser-induced graphene (LIG) has emerged as a promising electrode material because it combines direct laser fabrication with a porous conductive architecture that is readily integrated into patterned electrochemical devices[5]. The simplicity of its fabrication process, together with compatibility with a broad range of precursor materials, has stimulated extensive research into its application in electrochemical sensing, energy storage, catalysis and flexible electronics[6]. At the same time, the properties of LIG can be modified through fabrication and post-processing strategies, providing opportunities to investigate how these factors influence electrochemical performance[7,8].

Despite the rapid growth of this field, many studies have focused on individual fabrication methods, material modifications, or specific applications. A broader understanding of how fabrication, material characteristics and surface modification collectively influence the physicochemical and electrochemical properties of LIG remains incomplete. Addressing these relationships is important for advancing the development of LIG as an electrochemical material and for guiding future design strategies.

Against this background, this dissertation investigates LIG from a materials engineering perspective. The work examines how fabrication and surface modification influence the structural, physicochemical and electrochemical characteristics of LIG through a series of experimental studies. The thesis aims to advance the understanding of LIG as an electrochemical material through investigations spanning fabrication, characterization and surface modification. The following chapter reviews the current state of knowledge on electrochemical interfaces, LIG and surface modification strategies, providing the scientific foundation for identifying the research gaps addressed in this dissertation.

CHAPTER 2 - REVIEW OF LITERATURE

2.1 Electrochemical interfaces

Electrochemical systems operate through interactions occurring at the electrode-electrolyte interface, where electrical energy is converted into chemical energy or vice versa through oxidation and reduction reactions[2]. The characteristics of this interface govern the efficiency, sensitivity and stability of electrochemical processes[9]. Electron transfer, ion transport, adsorption and electrochemical reactions all occur at the electrode surface, making the physicochemical properties of electrode materials fundamental determinants of electrochemical performance[1].

The analytical and functional performance of electrochemical systems depends strongly on several material-related factors[10]. Electrical conductivity governs the efficient transport of electrons between the electrode and the external circuit, thereby influencing charge transfer efficiency and signal generation[1]. The electrochemically active surface area (EASA) determines the number of accessible reaction sites available for electrochemical processes and is therefore closely associated with current response and analytical sensitivity[1,2]. Electrode porosity and hierarchical surface morphology facilitate electrolyte penetration and mass transport, improving accessibility to electroactive sites while promoting efficient diffusion of reactants and products[1,2]. In addition, surface wettability influences the interaction between the electrode and the electrolyte, affecting electrolyte spreading, interfacial contact and molecular transport[1,2]. Surface chemistry, including the presence of defects and functional groups, further governs adsorption behaviour, catalytic activity, biomolecule immobilization and heterogeneous electron-transfer kinetics, all of which contribute to the overall electrochemical response[1,2,10].

These parameters are not independent but closely interconnected. For example, modifications that increase surface roughness or porosity generally increase the EASA, while changes in surface chemistry simultaneously influence wettability, adsorption behaviour and charge transfer characteristics[1,10]. Thus, electrochemical performance is determined not by a single material property but by the combined influence of the structural, physicochemical and interfacial characteristics of the electrode material[1,2,10].

Historically, electrochemical systems relied predominantly on conventional electrode materials such as platinum, gold, mercury, graphite and glassy carbon because of their favourable electrical conductivity, chemical stability and reproducible electrochemical behaviour[11]. Although these materials remain important in electrochemical research, their relatively limited opportunities for structural modification and surface functionalization have encouraged the development of advanced electrode materials capable of providing enhanced electrochemical performance[12,13]. More than functioning solely as electrically conductive substrates, modern electrode materials are increasingly designed to provide controllable surface morphology, accessible active sites, favourable surface chemistry and improved interfacial characteristics suited to specific electrochemical applications[12,14].

Although conventional metallic electrodes remain widely used, their limited opportunities for structural modification and surface functionalization have motivated the development of advanced electrode materials with improved electrochemical characteristics[12]. Thus, the increasing research has focused on designing electrode materials with tailored structural and surface properties to enhance charge transfer, mass transport and interfacial interactions[15]. Modern electrochemical platforms require interfaces capable of simultaneously

promoting rapid electron transfer, facilitating efficient mass transport, minimizing nonspecific adsorption, supporting biomolecular immobilization and maintaining long-term operational stability under complex operating conditions[16]. As a result, the electrode surface has evolved from a passive current collector into an active functional interface whose structural, chemical and biological characteristics collectively determine electrochemical performance[17,18].

This transition has fundamentally altered the philosophy of electrode design[11]. In preference to selecting materials solely on the basis of their intrinsic electrical conductivity or chemical inertness, contemporary electrochemical research increasingly focuses on engineering interfaces through deliberate control of surface morphology, hierarchical architecture, porosity, surface chemistry, defect density, catalytic functionality and biological compatibility[11,19]. Such engineering strategies enable precise regulation of electron-transfer kinetics, EASA, interfacial wettability, catalytic activity, diffusion pathways and biomolecular interactions, thereby allowing electrochemical systems to be optimized for specific analytical and technological applications[20].

As a result, electrochemical interface engineering has emerged as a multidisciplinary research field integrating principles of electrochemistry, materials science, nanotechnology, surface chemistry, polymer science and bioengineering[19]. Among the wide variety of materials investigated under this engineering philosophy, carbon-based materials have demonstrated an unparalleled combination of electrical conductivity, structural diversity, chemical stability, mechanical flexibility and surface tunability. Their unique ability to accommodate controlled structural and chemical modifications has positioned carbon materials at the forefront of electrochemical interface engineering and has driven the development of increasingly sophisticated electrode architectures for next-generation electrochemical platforms. The following section therefore examines the evolution of carbon-based electrode materials and discusses why they have become the dominant platform for modern electrochemical interface design.

2.2 Carbon-based electrode materials for electrochemical interfaces

Carbon-based materials have become the most extensively investigated class of electrode materials because they combine favourable electrical conductivity, chemical stability, broad electrochemical potential windows and tunable surface chemistry[21]. These characteristics have enabled their widespread use in electrochemical sensing, energy storage, electrocatalysis and bioelectronic interfaces. This class of materials offers a uniquely advantageous combination: a broad electrochemical potential window that minimizes solvent electrolysis, excellent chemical and electrochemical stability across a wide pH range and a rich, tunable surface chemistry that facilitates the covalent and non-covalent immobilization of biorecognition elements[19,22]. The summary of different types of carbon nanostructures for electrochemical platforms and active biofunctionalized surface for electrode design is shown in Figure 1.

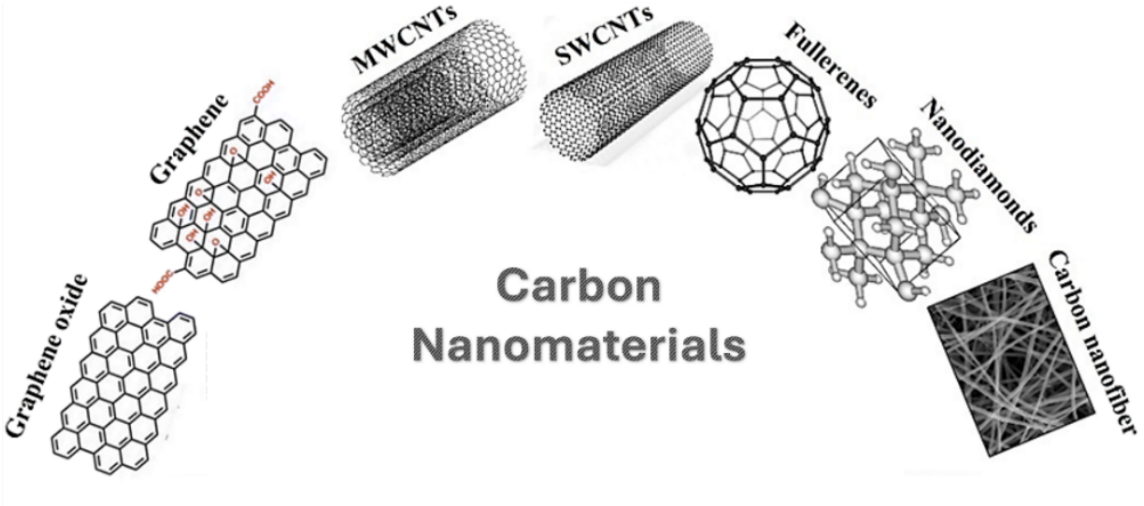


Figure 1: Different types of carbon nanostructures for electrochemical platforms (Adapted from[23]).

These intrinsic properties have cemented carbon as the workhorse material for platforms ranging from sophisticated laboratory analyzers to mass-produced disposable diagnostic strips[21,24].

2.2.1 Traditional carbon platforms: workhorses with inherent limitations

The electrochemical technology landscape was built upon traditional carbon allotropes such as glassy carbon electrodes (GCE), carbon paste electrodes (CPE) and screen-printed carbon electrodes (SPCEs) and later advanced with materials like boron-doped diamond (BDD) electrodes[25,26,27]. Glassy carbon, a dense, sp^2-bonded form with a smooth, impermeable surface, provides a hard, polishable substrate with low background noise, making it a standard for fundamental studies and high-precision voltammetry[28,29]. CPEs, composed of graphite or carbon powder suspended in a hydrophobic binder, offer the advantage of easy surface renewal and modification via bulk mixing of modifiers[30,31]. Most impactful for commercialization, SPCEs enable low-cost, mass-produced, disposable electrochemical interface strips through thick-film fabrication, a cornerstone of point-of-care diagnostics[14,32]. The BDD electrodes have been widely investigated as model systems for elucidating how surface structure, termination and effective electroactive area influence electrochemical activity[33,34,35]. BDD has this considerable interest owing to its wide potential window, low background current and chemical stability[36,37]. These materials offer robustness and ease of fabrication[14]. But their conventional sp^2-based electrodes exhibits low surface area and limited surface functionalization options can restrict sensitivity and integration with biomolecules[38]. However, these conventional forms share significant constraints. Their effective EASA is relatively low and geometrically defined, limiting current density and thus sensitivity[21,24].

2.2.2 The nanocarbon revolution: enhanced performance with new complexities

The rapid development of nanotechnology introduced a new generation of carbon nanomaterials possessing significantly enhanced surface area, electrical conductivity and tunable physicochemical properties and research intensely focused on nanostructured carbon materials, primarily carbon nanotubes (CNTs) and graphene[39,40,41]. Single-walled and multi-walled CNTs integrate exceptional electrical conductivity with a high aspect ratio, creating a nanoscale network that dramatically increases the electrode's effective surface area and facilitates electron transfer kinetics for a range of biomolecules and redox mediators[42]. Graphene, a

single atomic layer of sp²-hybridized carbon and its derivative reduced graphene oxide (rGO), offer a two-dimensional landscape of high surface area, exceptional conductivity, abundant defect sites that can act as catalytic hotspots and thereby numerous applications[43,44] . The evolution of carbon electrodes platforms is shown in Figure 2.

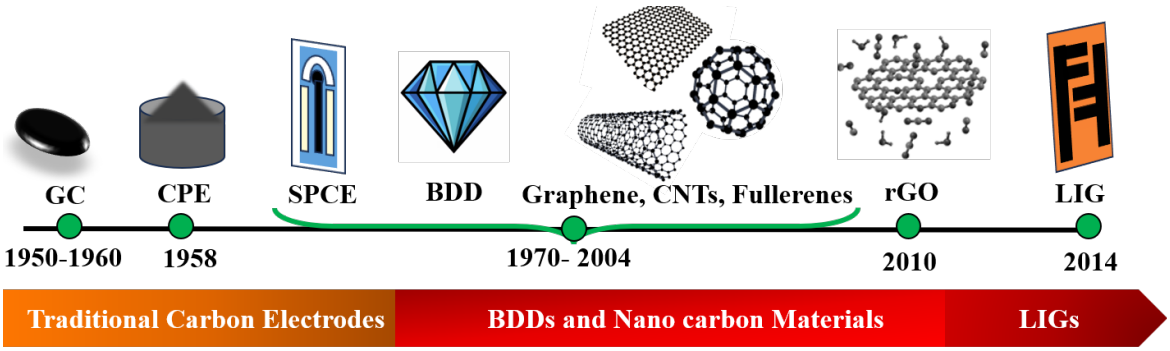


Figure 2: Evolution of carbon platforms.

The integration of these nanomaterials has led to documented enhancements in sensor sensitivity, lower overpotentials for analyte detection and improved detection limits[43,45]. This performance leap introduces formidable fabrication challenges[46]. CNTs suffer from strong van der Waals forces, leading to aggregation in solution, which results in inconsistent film formation and poor reproducibility between electrodes and also large-scale processing limited their widespread industrial implementation[42,47].

Table 1. Comparison of different carbon electrode materials with respect to their electrochemical advantages and key limitations

Material	Advantages	Major limitations
Glassy carbon	Stable, reproducible	Low EASA
Carbon paste	Easily modified	Poor mechanical stability
SPCE	Disposable, scalable	Limited surface area
CNT	Excellent conductivity	Aggregation
Graphene	High conductivity and EASA	Restacking, transfer
rGO	Functionalizable	Residual defects

Pristine graphene produced via chemical vapor deposition (CVD) requires complex transfer processes onto substrates, often introducing contaminants and cracks[48]. As a result, rGO, derived from the chemical reduction of graphene oxide, is processable from solution but contains residual oxygen groups and defects that can compromise electrical conductivity and long-term stability, while the chemical reduction steps themselves can be environmentally burdensome and difficult to control with high precision[49,50]. These processing complexities directly conflict with the essential industrial requirements of scalability, batch-to-batch reproducibility and cost-effectiveness[51]. These challenges have motivated the exploration of alternative

graphenic materials that combine high electrochemical performance with scalable and patternable[52]. Table 1 summarises the materials and its major limitations.

2.2.3 Pursuing practicality: drive towards scalable and patternable alternatives

The struggle between the superior electrochemical properties of nanostructured carbons and their problematic processing has boosted the exploration of next-generation, engineered graphene-like materials[53,43]. The ideal candidate would preserve the high conductivity and surface area of graphene while being amenable to direct, maskless and scalable patterning on flexible substrates under ambient conditions[54,55].

The processing limitations and conventionally synthesized graphene have stimulated interest in alternative graphenic materials that can be fabricated directly into conductive electrode architectures through simple and scalable manufacturing strategies. In this context, direct laser writing (DLW) has emerged as a versatile fabrication strategy for producing functional carbon-based materials[56,57]. DLW encompasses a class of laser-based techniques in which focused laser irradiation is used to locally modify the chemical structure, morphology, or conductivity of a precursor material in a programmable and maskless manner[58]. These approaches enable high spatial resolution, rapid prototyping and compatibility with diverse substrates, including flexible and polymeric systems, making them particularly attractive for the fabrication of electrochemical sensor architectures[59,60].

Recent advancements point to materials such as LIG and other forms of pyrolytic or porous carbons derived from controlled carbonization of precursors[5,59,61]. Unlike conventional graphene fabrication methods that rely on multi-step synthesis and transfer processes, LIG is produced directly on the target substrate in a single step under ambient conditions[5]. This process, typically performed under ambient atmospheric conditions, bypasses the need for catalysts, high-temperature furnaces, vacuum chambers, or complex transfer steps that plague other graphene production, thereby simplifying fabrication and improving scalability[54]. This DLW-based approaches, including LIG and related laser-pyrolyzed carbons, enable the direct writing of conductive, high-surface-area electrode patterns without the use of inks or masks, or post-transfer steps[62]. This capability facilitates rapid prototyping and the integration of complex electrode architectures within compact platforms[63].

In parallel, alternative strategies such as controlled pyrolysis of photoresists and polymeric films have also been explored to fabricate patterned carbon microstructures with tunable porosity and surface chemistry using standard microfabrication techniques[24,64]. These emerging fabrication schema represent a shift from material-centric optimization toward integrated considerations of manufacturability, design flexibility and system-level integration[13,65]. By bridging the gap between high-performance nanomaterials and scalable device fabrication, they provide a pathway toward the realization of robust and application-oriented electrochemical interfaces[7,66,67].

2.3 Laser-induced graphene (LIG)

The translation of electrochemical interfaces from laboratory-scale prototypes to real-world applications critically depends on the availability of rapid, scalable and cost-effective fabrication strategies[32,68,69]. In contrast to conventional electrode preparation methods, which often involve multi-step processing, cleanroom facilities, or complex material transfer procedures, modern biosensor development increasingly emphasizes

manufacturing approaches that enable high-throughput production, patterning flexibility and compatibility with diverse substrates, including flexible and disposable platforms[18,70,71]. Several fabrication techniques have been explored to address these requirements[72]. Screen-printing technology has been widely adopted for the mass production of disposable electrodes due to its simplicity, low cost and scalability, forming the basis of many commercial point-of-care diagnostic devices[73].

Inkjet printing and aerosol jet printing further extend this capability by enabling digital, mask-free deposition of functional inks with precise control over electrode geometry and material composition[74,75]. In parallel, photolithographic and microfabrication approaches offer high resolution and reproducibility but often require complex infrastructure and are less suited for rapid prototyping or large-area manufacturing[76].

Laser-based fabrication methods have emerged as a powerful class of rapid manufacturing techniques for electrochemical platforms[77]. These approaches enable direct writing of conductive patterns onto substrates without the need for masks, inks, or processing steps[77]. Laser processing offers advantages in terms of speed, spatial resolution and compatibility with a wide range of precursor materials, making it particularly attractive for the development of next-generation electrochemical platforms[5].

Despite these advances, a key challenge remains in identifying fabrication strategies that simultaneously provide high electrochemical performance, structural tunability and scalability[66,78]. Within this context, LIG has emerged as a promising material platform that integrates rapid manufacturing with favorable/tunable electrochemical properties, as discussed in the following section.

2.3.1 Discovery and evolution of laser-induced graphene

LIG was first discovered by James M. Tour and co-workers in 2014 at Rice University found that a commercial CO_2 laser could directly convert polyimide (PI) into conductive, porous graphene under ambient conditions[5,54,79,80]. This discovery is a simple one-step method, which bypasses traditional multi-step synthesis, revolutionized the field by enabling the direct patterning[54,61,62].

The laser irradiation on carbon-rich polymer precursors (commonly PI) in a mask-free, ambient processing step that rapidly converts the polymer into a porous, graphitic network[54] as shown in Figure 3. The process is rapid, patternable, compatible with flexible and low-cost substrates and readily scalable for patterned electrodes and interconnects, enabling cost-effective fabrication of electrodes[77,81,82]. These characteristics position LIG as a promising platform for applications requiring rapid prototyping and customizable electrode geometries[83]. Other than CO_2, UV and femtosecond pulsed lasers are used to achieve finer control over LIG's structure. It demonstrates how this method reduces the heat-affected zone, enabling smaller features (~10 μm), smoother edges and more controlled porosity[84,85]. This directly correlates precise structuring with improved properties for high-resolution flexible circuits and sensor platforms[8,66,86,87].

The laser-induced conversion process produces a three-dimensional, hierarchically porous morphology EASA and interconnected conductive pathways[66,86]. These features facilitate efficient electrolyte penetration, rapid electron transport and flexible electrode patterning, all of which are advantageous for sensitive and miniaturized electrochemical platforms and allows LIG to be integrated into wearable, flexible and embeddable electronics beyond the scope of 2D to functional 3D structures[87,88,89,90].

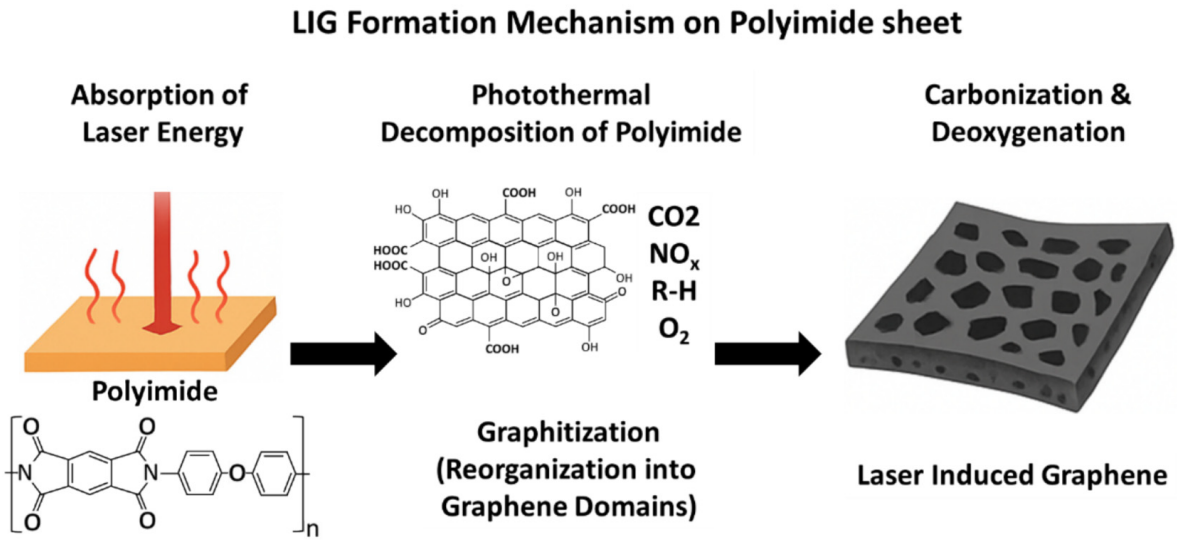


Figure 3: Representation of LIG formation on PI by laser irradiation (Adapted from[91]).

Numerous investigations have demonstrated that LIG can be fabricated not only from PI but also from a broad range of carbon-containing precursor materials, including wood, cellulose paper, textiles, lignin-rich biomass, natural leaves, food-derived materials and fluoropolymer-based substrates[80]. This remarkable precursor versatility has significantly expanded the application potential of laser processing while supporting the development of sustainable and environmentally friendly manufacturing approaches based on renewable resources and waste-derived materials[80,88].

In parallel with the diversification of precursor materials, considerable advances have been achieved in laser processing technologies[80,88]. Although the earliest investigations primarily employed continuous-wave CO_2 lasers operating at a wavelength of 10.6µm, subsequent studies have demonstrated successful graphitization using ultraviolet, visible, near-infrared, femtosecond, picosecond, nanosecond, diode and fiber laser systems[84,92]. Each laser source provides distinct laser-material interaction mechanisms, energy deposition characteristics and processing windows, enabling researchers to tailor graphitic structures across multiple length scales[93]. As a result, LIG has evolved from a single fabrication technique into a versatile manufacturing platform encompassing diverse laser technologies, precursor chemistries and structural architectures[8,94].

In addition to its simplicity, versatility and scalability, the ability to directly write electrode geometries enables facile customization of layouts/configurations for diverse analytical applications as shown in Figure 4 including sensing, energy storage and supercapacitors[79,90,95,96,97].

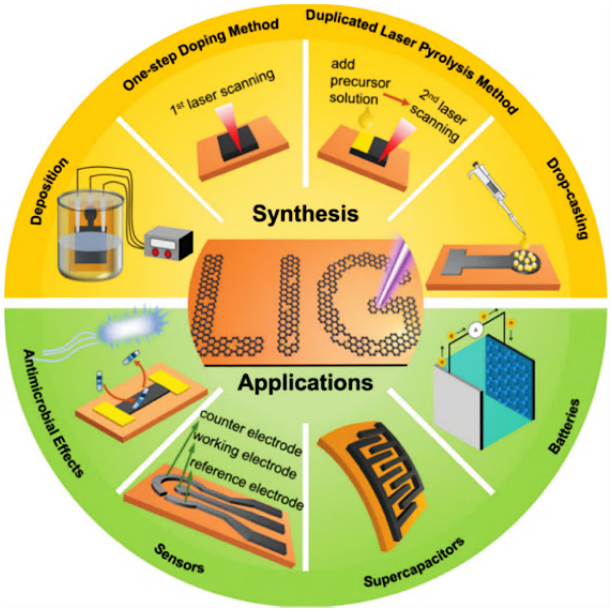


Figure 4: Synthesis and applications of LIG (Adapted from[98]).

2.3.2 Fundamentals of laser-material interaction

The successful formation of LIG is fundamentally governed by the interaction between laser radiation and the precursor material. LIG is generated by direct laser irradiation of carbon-rich precursors, most commonly PI, resulting in localized photothermal conversion of the polymer into a porous, graphitic carbon structure[5,99]. The LIG on different substrates and key characteristics shown in Figure 5.

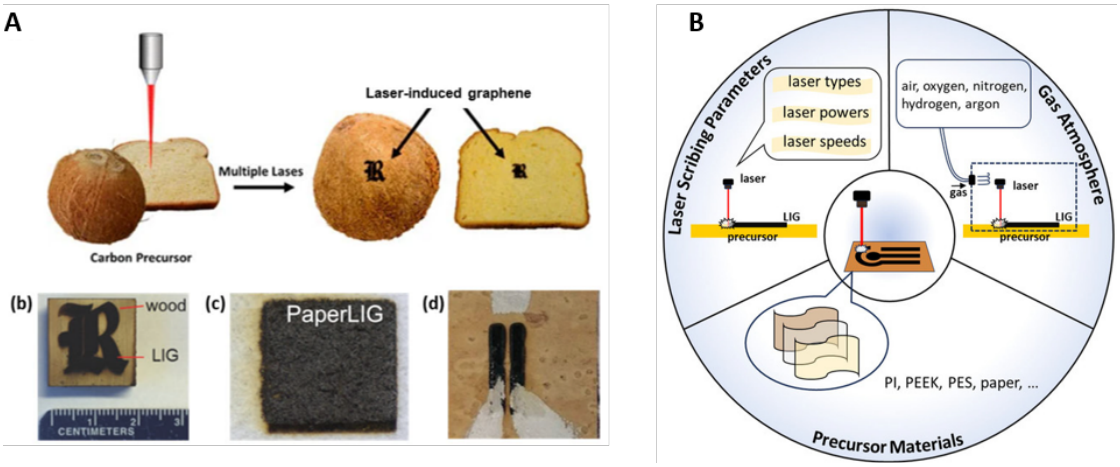


Figure 5: LIG formation on different precursors. (A) LIG was produced on coconut and bread (a), wood (b), paper (c) and cork (d). (B) Key factors affecting the characteristics (Adapted from[100]).

As a result, identical laser parameters may produce substantially different graphitic structures when applied to different precursor materials. PI, cellulose, lignin-rich biomass, fluoropolymers and other carbon-containing substrates therefore exhibit distinct processing windows that must be optimized individually to achieve controlled graphitization[62,101]. This process is typically performed under ambient conditions and does not require catalysts, vacuum systems, or post-processing steps, making it inherently compatible with scalable and maskless electrode fabrication[62,101]. During laser irradiation, the incident photon energy is efficiently absorbed and converted into heat within the focal region, producing highly localized temperatures that can

exceed ~2000-2500 °C[5,80]. This rapid thermal excitation induces polymer decomposition through bond scission and pyrolysis[5,102]. Non-carbon elements such as oxygen, nitrogen and hydrogen are released as volatile species (e.g., CO, CO_2, H_2O, HCN), while the remaining carbon atoms reorganize into sp^2-hybridized graphitic domains through nucleation and growth processes[5,54,103]. The rapid evolution of gaseous byproducts generates internal pressure, leading to the formation of a three-dimensional, foam-like porous architecture[62,66]. The photothermal conversion, gas evolution and graphitic restructuring is summarized in Figure 6.

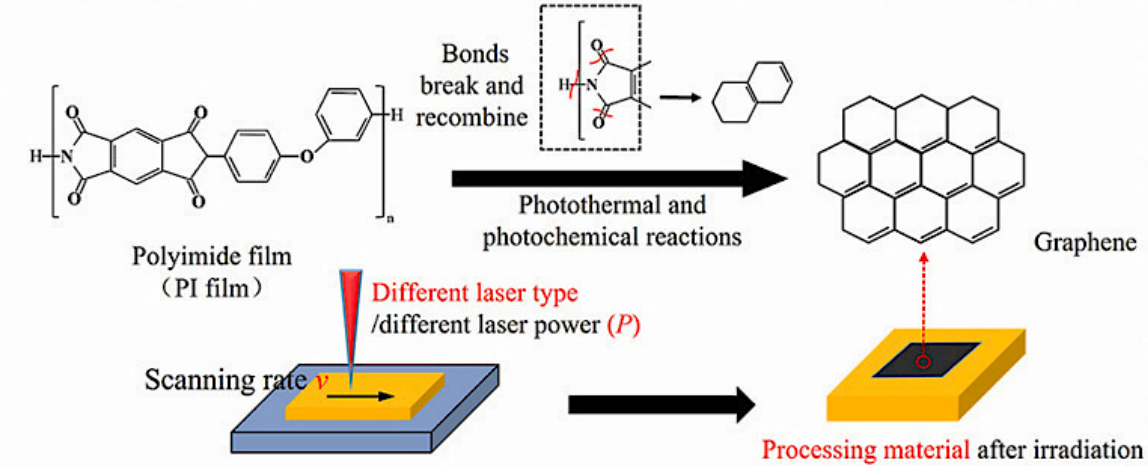


Figure 6: Illustration of photothermal conversion of a PI foil into a patterned LIG electrode via direct CO_2 laser irradiation (Adapted from[104]).

The hierarchical porous structure, while advantageous for increasing EASA and facilitating mass transport, introduces important trade-offs[83,105]. The highly porous and defect-rich morphology enhances analyte accessibility and catalytic activity but can reduce mechanical robustness and lead to structural fragility under mechanical or electrochemical stress[105,106]. Additionally, the tortuous pore network creates complex diffusion fields that may deviate from ideal planar diffusion behaviour, influencing electrochemical response kinetics[1,107]. From an electrical perspective, although LIG exhibits good conductivity, the presence of defects, grain boundaries and disordered domains results in lower conductivity compared to pristine graphene, highlighting a balance between electrochemical activity and charge transport efficiency[63,108,109].

Table 2. Principal laser processing parameters and their primary effects on LIG formation.

Parameter	Primary Influence	Secondary Influence
Power	Energy density	Ablation
Speed	Residence time	Heat accumulation
Hatch spacing	Track overlap	Uniformity
Focus	Beam diameter	Energy distribution
Passes	Heat accumulation	Graphitic thickness
Atmosphere	Oxidation	Surace chemistry

Table 2 summarised the principal laser processing parameters and their primary effects on LIG formation. The interaction between these variables determines the thermochemical conversion pathway and the final structure-property relationships of LIG.

The surrounding atmosphere plays a critical role in determining both energy transfer and final material properties[102,110]. Processing in inert environments (e.g., Ar, N_2) minimizes oxidation and promotes higher graphitic content and improved electrical conductivity[88,102,111]. In contrast, processing in air or reactive atmospheres (e.g., O_2, NH_3) introduces oxygen- and nitrogen-containing functional groups into the carbon lattice, enabling heteroatom doping and modification of surface chemistry and electrochemical activity[67,88,111,112,113]. However, such functionalization may also disrupt the conjugated sp^2 network, increasing electrical resistance[50,51]. This tunability of surface chemistry under ambient processing conditions represents a key advantage of LIG over conventional graphene fabrication techniques such as CVD, which require controlled environments and multi-step processing[54,79].

Even though the photothermal mechanism is widely accepted as the dominant pathway, the exact atomic-scale kinetics remain incompletely understood[79,114]. Due to the extreme temperatures and ultrafast timescales involved, in-situ characterization is challenging[105]. It has been proposed that photochemical effects may also contribute, where high photon flux enables direct bond cleavage prior to full thermal equilibration, effectively lowering activation barriers for decomposition[79,88]. From a materials engineering perspective, LIG formation should therefore be regarded as a coupled thermochemical process in which laser energy deposition, heat transfer, polymer decomposition, gas evolution, carbonization, graphitization and pore formation occur simultaneously rather than as independent phenomena.

2.3.3 Influence of laser parameters on LIG morphology and conductivity

The properties of LIG are strongly dependent on laser processing parameters, including laser power, scan speed, focal position, interval of spacing (hatch spacing), scribing mode (defocus, focus) and number of passes[79,101,105]. This tunability is a double-edged sword: it allows for customizing LIG for specific applications but also introduces complexity in achieving standardized, reproducible fabrication[105,115]. Table 3 shows the influence of lasing parameters on formation of LIG pattern. The primary parameters governing the conversion are laser power (P), scan speed (S), intervals of lasing, the number of lasing passes (N), spot size but more practically by the laser power and speed ratio (P/S), is the key governing parameter controlling the degree of carbonization and graphitization[54,80,105,115].

Numerous studies have demonstrated that increasing laser power or decreasing scan speed increases energy deposition, promoting greater graphitization and reduced sheet resistance (R_s), up to an optimal threshold beyond which structural damage or ablation may occur[5,99]. In addition to laser power, scanning speed and hatch spacing, the focal position (Z-offset) represents an important processing parameter that controls the distance between the laser focal plane and the substrate surface. At the machine's default position (Z = 0), the laser beam is focused directly on the substrate. Introducing positive or negative Z-offsets results in defocused irradiation, modifying the energy density delivered to the material and consequently influencing the graphitization process. Appropriate adjustment of the Z-offset can broaden the processing window, improve process stability and facilitate controlled photothermal conversion. For thicker precursor materials, progressive adjustment of the Z-offset during multi-pass processing can promote the formation of multilayer

3D graphene structures while reducing thermal damage to previously graphitized layers. A significant hurdle in the widespread adoption of LIG technology is the lack of standardization in reporting laser parameters and system characteristics[116]. Critical variables such as the exact laser spot size (which determines fluence), the substrate's thermal conductivity and thickness and the focal plane accuracy can affect the outcome[67,116].

Table 3. Influence of laser processing parameters on LIG formation and properties.

Parameter	Effect within optimal range	Effect when excessive / outside the range	References
Laser power (P)	**Increased P, higher graphitisation, lower R_s**	**Over-ablation, structural collapse, increased defect density**	**5,105,115**
Scan speed (S)	**Decreased S, higher energy input gives better conversion**	**Too low S cause burning / delamination**	
P/S ratio	**Increased P/S, more complete carbonisation, lower R_s**	**Very high P/S cause material ablation**	**5,105,112,115**
Number of passes (N)	**N = 2-3, enhanced conductivity, thicker LIG**	**N > 5 gives embrittlement, oxidation (in air)**	**88,99**
Z-offset (focal position	**Moderate positive or negative defocusing adjusts the laser spot size and energy density, improving process stability, broadening the processing window and, for thick precursors, facilitating multilayer or 3D LIG formation**	**Excessive defocusing reduces energy density below the graphitization threshold, resulting in incomplete carbonization, poor conductivity and discontinuous graphene formation.**	**117,110**
Defocusing	**Positive defocus, may introduce carbonisation than graphitization. Wider line width, more uniform but less graphitised**	**Large defocus may cause very low conductivity**	
Atmosphere	**Inert (Ar/N_2), higher graphitisation, fewer oxygen groups**	**Air/O_2 cause heteroatom doping (O, N) but lower conductivity**	**88,102,111**

Consequently, optimal parameters reported in one study are often not directly transferable to a different laser system or setup[105]. This variability underscores the need for the community to move beyond reporting basic power and speed toward standardized metrics like calculated fluence and comprehensive characterization of the resulting material's properties to enable meaningful cross-comparison and accelerate technological maturation[116].

A systematic increase in energy dose achieved by either increasing laser power or decreasing scan speed generally promotes more complete conversion of the polymer into graphitic carbon[5,80]. An excessive energy dose, often termed over-lasing, leads to ablation instead of conversion[115]. The excessive heat can burn through the material, vaporizing the carbon itself, resulting in a loss of structural integrity and increased defect density. This defines a critical processing window for achieving high-quality LIG[66,114].

Overall, laser processing parameters determine the entire sequence of physicochemical transformations leading to LIG formation. Their influence extends from the initial laser-material interaction to the final

structural architecture and ultimately governs electrical conductivity, surface chemistry, electrochemical activity, mechanical integrity and long-term device performance. Consequently, systematic optimization of laser processing parameters constitutes the fundamental basis for engineering LIG with application-specific properties.

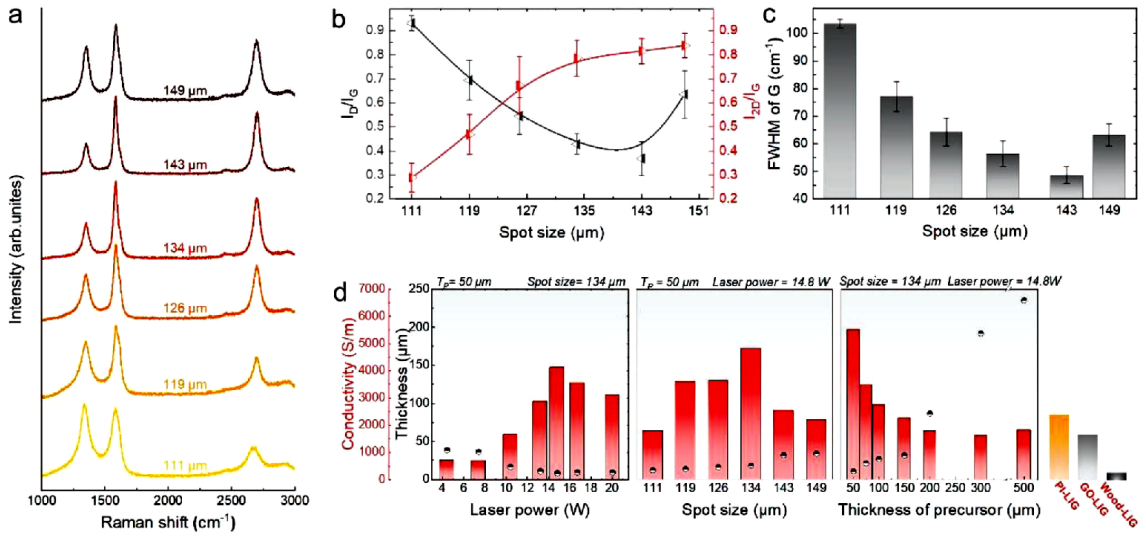


Figure 7: Characterization of LIG using different laser parameters: a) Raman spectra of LIG prepared under various laser spot sizes. The applied laser power was fixed at 14.8 W and the precursor thickness was fixed at 50µm. b) Statistical analysis of I_D/I_G and I_{2D}/I_G and c) FWHM of the G peak as a function of laser spot size. d) Correlations of conductivity and thicknesses of LIG with laser power, spot size and precursor thickness (Adapted from[118]).

Beyond simple power and speed, defocusing the laser beam has been reported to alter energy distribution across the substrate, resulting in modified pore size distributions and more uniform surface morphologies in some cases[62,117]. In addition to laser power and scan speed, the scanning strategy (raster vs. parallel line-by-line scanning) has shown to induce anisotropic microstructures, as the directional laser path can preferentially orient graphene flakes and edge planes[119]. Due to this, the choice of scanning direction has a direct impact on macroscopic properties such as wettability, electrical conduction and electromechanical sensitivity, highlighting the importance of its optimisation for targeted applications[119,120]. Proper alignment can reduce anisotropic properties, ensuring uniform sensitivity and predictable behaviour. Multiple lasing passes can further enhance graphitic content and electrical conductivity but may also introduce mechanical fragility if excessive thermal stress is accumulated[99,103].

Multiple lasing passes (N > 1) are a common strategy to enhance conductivity and graphitic content incrementally through the formation of an initial conductive layer[99,103]. The first pass initiates conversion and creates a partially conductive, absorptive layer[99,103]. Subsequent passes are then absorbed more efficiently by this layer, driving further graphitization[88]. Each pass also applies thermal stress and excessive passes can cause embrittlement, delamination from the substrate, or excessive oxidation if performed in air[99]. However, repeated irradiation introduces cumulative thermal stress, which can result in embrittlement, delamination and increased susceptibility to oxidation under ambient conditions[90]. These parameters collectively determine the energy delivered per unit area and its spatial-temporal distribution, thereby controlling the degree of carbonization, graphitization and structural evolution[79,92,105]. The effective energy dose is often approximated

by the ratio of laser power to scan speed (P/S), which governs local temperature rise and heat residence time[92,105,115].

Increasing laser power or decreasing scan speed enhances energy deposition, promoting graphitic domain formation and reducing R_s[54,105]. However, this relationship is valid only within an optimal processing window. Insufficient energy input results in incomplete carbonization and poor conductivity, whereas excessive energy input (over-lasing) leads to ablation, structural collapse and increased defect density, ultimately degrading electrical performance[92,99]. Therefore, LIG formation is governed by a balance between energy input, heat dissipation and material response[54].

Additional parameters such as focal position and pulse repetition rate influence the spatial and temporal distribution of energy[110,115]. Defocusing reduces peak energy density while increasing the interaction area, often yielding more uniform but less graphitized structures[117]. Similarly, higher repetition rates promote thermal accumulation, whereas lower repetition rates allow partial cooling between pulses, affecting defect density and structural ordering[92,114]. Variations in scanning strategy can further influence heat distribution and structural uniformity, although their quantitative impact on electrochemical performance remains underexplored[101].

Overall, LIG formation is governed by a complex, multi-parameter space in which processing conditions dictate energy conversion pathways, structural evolution and resulting electrochemical properties[66]. A systematic understanding of these relationships is essential for achieving reproducible, application-specific LIG-based electrodes, forming a central focus of this work.

2.3.4 Structure-property relationships and fabrication-dependent variability

LIG's electrochemical baseline is set by its microstructure (porosity, pore size distribution, macro- vs micro-porosity), graphitic domain size and defect density and surface functional groups (oxygen, nitrogen, etc.) introduced during photothermal conversion[5,8,80,114]. These features determine conductivity, EASA, wettability and nucleation sites for subsequent chemical/electrochemical functionalization[7,99]. The formation of LIG is governed by a photothermal conversion mechanism, in which localized laser irradiation induces rapid heating of the polymer precursor, leading to pyrolytic decomposition and carbonization[5,80].

Upon laser exposure, the temperature in the irradiated region can rise sharply (typically exceeding 2000 K in localized zones), resulting in the breaking of C–O, C–N and C=O bonds and the release of volatile species such as CO, CO_2 and small hydrocarbons[88,102,114]. This process leaves behind a carbon-rich residue that undergoes rearrangement into sp^2-bonded graphitic domains, forming a porous, conductive network[5]. Simultaneously, the rapid gas evolution contributes to the development of a three-dimensional, hierarchically porous morphology characteristic of LIG[8,66].

As a consequence of this formation mechanism, the electrochemical baseline properties of LIG are intrinsically linked to its microstructure, including porosity, pore size distribution, graphitic domain size and defect density, as well as the presence of surface functional groups such as oxygen- and nitrogen-containing species introduced during processing[54,62,114]. These structural and chemical features govern key properties such as electrical conductivity, EASA, wettability and the availability of nucleation sites for subsequent chemical or electrochemical functionalization[6,82].

Importantly, the photothermal nature of the conversion process makes LIG highly sensitive to fabrication parameters. Variations in laser power, scan speed, focal conditions, number of passes, intervals and substrate composition can significantly alter the extent of carbonization, degree of graphitization and resulting morphology[54,79,82]. LIG produced under different conditions can exhibit substantial variability in electrochemical performance, necessitating systematic control and reporting of laser processing parameters for reproducible sensor fabrication[5,121,122]. Several experimental studies and reviews emphasize the dominant role of laser parameter space on morphology and R_s[105]. This sensitivity highlights both the tunability of LIG and the importance of deliberate interface engineering strategies when designing reliable biosensing platforms[12].

The advantages arise directly from its formation mechanism and resulting hierarchical architecture In addition to conventional surface LIG, alternative configurations such as interfacial LIG (I-LIG), where lasing occurs between layered polymer substrates, have been reported[106]. This approach enables improved control over the formation of ultrathin, mechanically robust and conductive graphene structures with modified porosity and enhanced structural integrity[8,123].

The hierarchical porous morphology significantly enhances EASA and facilitates electrolyte penetration and mass transport, which are advantageous for electrochemical sensing applications[79,88]. However, these structural features introduce important trade-offs. The presence of defects, grain boundaries and disordered domains reduces electrical conductivity compared to pristine graphene, while the highly porous architecture can compromise mechanical integrity and introduce complex diffusion pathways that deviate from ideal planar behaviour[109]. Thus, LIG inherently represents a balance between electrochemical activity and electrical transport properties[83].

Although the photothermal mechanism is widely accepted as the dominant pathway for LIG formation, the precise atomic-scale kinetics remain incompletely understood[54,115]. Due to the extreme temperatures and rapid processing timescales, in-situ characterization is challenging[54]. It has been proposed that photochemical effects may also contribute, whereby high photon flux enables direct bond cleavage prior to full thermal equilibration, effectively lowering activation barriers for decomposition[79,124]. The relative contributions of photothermal and photochemical processes remain an active area of investigation[88].

2.3.5 Morphological and surface characteristics of LIG

The functional efficacy of LIG in electrochemical biosensing arises from its unique hierarchical structure and chemically active surface, which differ significantly from those of ideal graphene and rGO[51]. Unlike planar graphene systems, LIG exhibits a three-dimensional, porous architecture that integrates structural heterogeneity with high electrochemical accessibility[5,62,99].

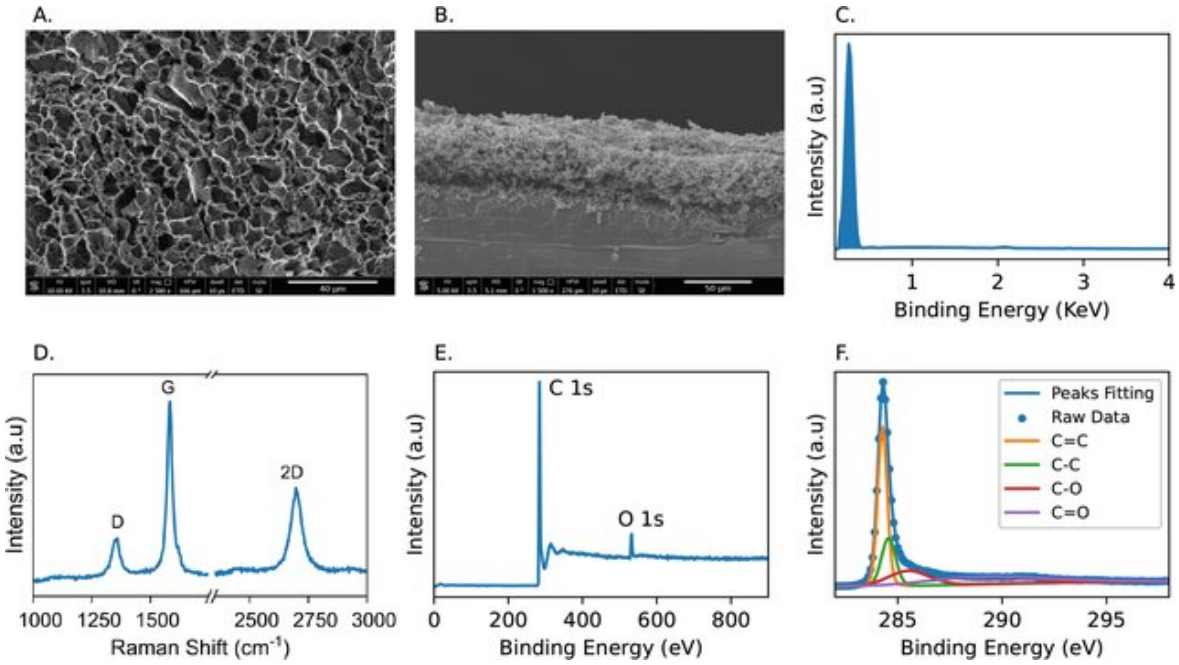


Figure 8: Morphological, structural and surface characteristics of LIG. (A) and cross-section (B) SEM images of the LIG structure. (C) EDX analysis results of LIG. (D) Raman spectrum of the LIG. (E) XPS survey of the LIG surface. (F) High-resolution XPS spectrum for C 1s peak (Adapted from[125]).

Morphological characterization using scanning electron microscopy (SEM) and transmission electron microscopy (TEM) consistently reveals that LIG consists of an interconnected network of graphitic flakes and fibers forming a foam-like structure[5]. LIG is not ideal graphene, it is a turbostratic, defect-rich, few-layer graphitic material produced by rapid photothermal conversion which is confirmed by TEM.

TEM investigations consistently demonstrate that LIG does not consist of perfectly crystalline graphene but rather comprises interconnected graphitic nanodomains embedded within partially amorphous carbon as shown in Figure 9. High-resolution transmission electron microscopy (HR-TEM) further confirms the presence of nanocrystalline graphitic domains interspersed with amorphous carbon regions, reflecting incomplete graphitization under rapid photothermal conditions[79,80,126].

The architecture is composed of few-layer graphene domains arranged in a highly defective and tortuous configuration[5,88]. Importantly, LIG exhibits a hierarchical pore distribution, spanning multiple length scales[103]. While micropores (<2 nm) and mesopores (2-50 nm) arise from carbonization and gas evolution processes, larger macropores extend into the micrometer range and can reach tens to hundreds of micrometers depending on laser parameters and precursor structure[54,127].

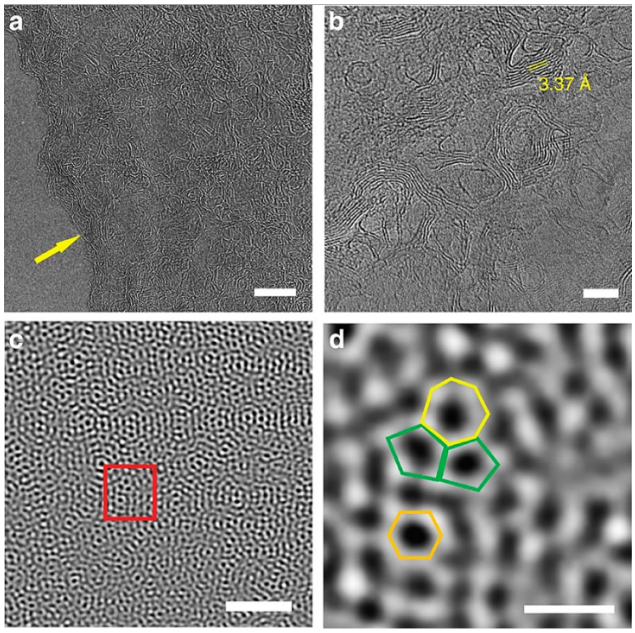


Figure 9: Representative TEM and HR-TEM images of LIG illustrating interconnected graphitic nanosheets, turbostratic stacking and lattice fringes characteristic of few-layer graphitic domains formed during rapid laser-induced carbonization (Adapted from[5]).

This multi-scale porosity plays distinct functional roles. Micropores and mesopores contribute primarily to increased surface area and enhanced electrochemical activity by providing abundant edge-plane sites and defect-rich regions[83,127]. The meso- and microscale processes occurs during irradiation, including photothermal decomposition, gas evolution, swelling, pore formation, jet fragmentation and the development of 3D porous graphene architecture is represented in Figure 10. The atomic and nanoscale transformation involving polymer bond cleavage, formation of volatile intermediates, carbonization and graphitization resulting in defect rich graphitic domains within the LIG structures.

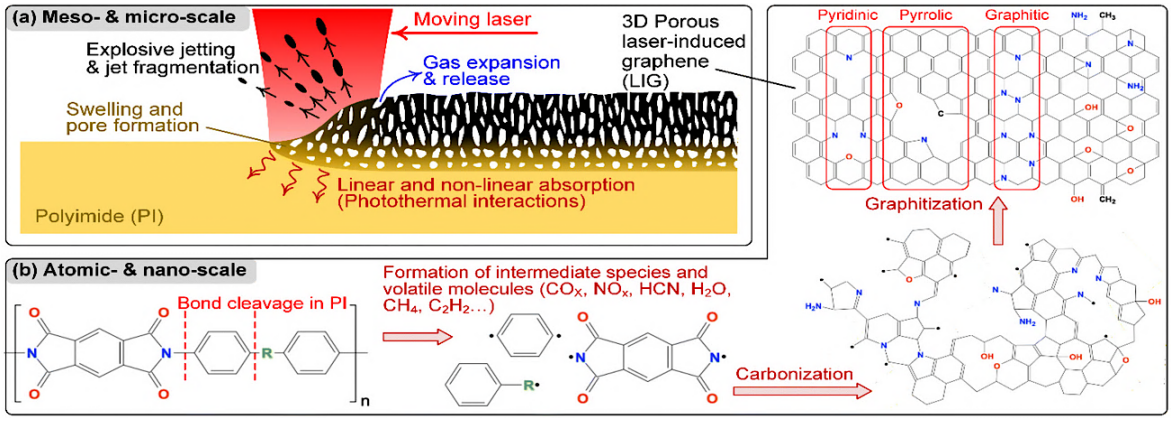


Figure 10: Representation of multiscale formation mechanism from PI. a) Meso- and microscale evolution of porous architecture by laser induced photothermal effects, gas expansion and pore generation. b) Atomic and nanoscale conversion through polymer bond cleavage, carbonization and graphitization resulting interconnected graphitic domains (Adapted from[128]).

However, their contribution to direct immobilization of large biomolecules (e.g., enzymes, proteins, cells) is limited due to steric constraints[12]. In contrast, macropores and interconnected micro-scale voids facilitate electrolyte penetration, convective and diffusive transport and provide accessible surfaces for effective immobilization of biorecognition elements[89,127]. Thus, the performance of LIG arises not simply from high surface area, but from the synergistic interplay between nano-scale reactivity and micro-scale accessibility[129,130]. The hierarchical structural organization of LIG illustrating the multiscale architecture from the macroscopic porous network to graphitic domains, structural defects and atomic-scale edge sites summarized in Table 4. The different structural features collectively determine charge transport, mass transport, catalytic activity and electrochemical performance. From an electrochemical perspective, this hierarchical architecture enhances EASA while simultaneously influencing mass transport behaviour[1,107]. The porous network enables shorter diffusion pathways and increased analyte flux compared to planar electrodes, although the tortuous geometry can also introduce non-ideal diffusion regimes that deviate from classical planar or semi-infinite diffusion models[1,130]. Additionally, the structural heterogeneity and presence of defects may introduce trade-offs, including reduced electrical conductivity relative to pristine graphene and potential variability in electrode performance[39].

Table 4. Multiscale architecture of LIG and its electrochemical function

Hierarchical Level	Electrochemical function
Macropores	**Electrolyte transport**
Mesopores	**Analyte diffusion**
Micropores	**Active surface area**
Graphitic domains	**Conductivity**
Edge planes	**Electron transfer**
Defects	**Catalytic activity**

Raman spectroscopy provides further insight into the structural characteristics of LIG, typically exhibiting prominent D (~1350 cm^{-1}) and G (~1580 cm^{-1}) bands and often a 2D band (~2700 cm^{-1}), with an intensity ratio I_D/I_G (often between 0.8 and 1.2) indicative of defect density and edge-plane abundance[5,131]. Unlike pristine graphene, where defects are generally undesirable, the high defect density in LIG is often beneficial for electrochemical applications, as these sites act as active centers for adsorption and redox reactions[46,53]. In fact, these defect sites and edge planes are electrochemically active[132]. They serve as catalytic hotspots, lowering the overpotential for many redox reactions and providing abundant anchoring points for covalent functionalization[133]. A pronounced D band reflects the presence of structural defects, edge sites and disordered sp^2 carbon domains. Unlike pristine graphene, where a low I_D/I_G ratio is indicative of high crystallinity, LIG commonly exhibits moderate to high I_D/I_G ratios due to its defect-rich and edge-dominated structure[131]. These defect sites are often associated with enhanced electrochemical activity, as they provide

active sites for adsorption and electron transfer processes[131]. HR-TEM further supports this structural picture, revealing graphitic domains interspersed with amorphous carbon regions and topological defects[134].

Collectively, morphological characterization techniques provide a comprehensive understanding of the hierarchical architecture of LIG across multiple length scales. More importantly, they establish direct relationships between laser processing conditions and structural development, thereby forming the basis for subsequent structural, chemical, electrical and electrochemical characterization. Morphological analysis therefore represents the first step toward understanding how processing-induced structural evolution governs the functional behaviour of LIG.

In addition to structural features, the surface chemistry of LIG plays a critical role in its functionality[102]. X-ray photoelectron spectroscopy (XPS) analyses reveal the presence of oxygen- and nitrogen-containing functional groups, depending on precursor composition and processing environment. These functional groups enhance hydrophilicity, modulate surface charge and provide anchoring sites for biomolecule immobilization or further chemical modification[88,112]. Thus, the combined effects of hierarchical porosity, defect-rich structure and tunable surface chemistry underpin the versatility of LIG[66,67]. XPS provides insight into the elemental composition and surface chemistry of LIG. Studies have consistently shown that LIG contains oxygen- and, in some cases, nitrogen-containing functional groups, depending on the precursor material and processing conditions[50,51,54]. These functional groups influence surface wettability, charge distribution and chemical reactivity and can serve as anchoring sites for subsequent surface modification or biomolecule immobilization[66,67]. The presence of heteroatoms such as oxygen and nitrogen introduces additional active sites and modifies the electronic structure of the carbon framework, which can influence electrochemical behaviour[50,51]. However, the exact composition and distribution of these functional groups are highly dependent on fabrication parameters[105]. This will be further discussed in relation to experimental observations in subsequent sections.

Complementary information regarding chemical bonding may also be obtained using Fourier-transform infrared spectroscopy (FTIR). FTIR provides qualitative identification of functional groups through characteristic vibrational absorption bands and is particularly valuable for evaluating precursor chemistry, polymeric coatings, hydrogel networks and biomolecular modifications applied to LIG[5,79]. Although graphitic carbon itself exhibits relatively weak infrared absorption owing to the absence of strong dipole-active vibrations, FTIR remains highly effective for monitoring chemical changes introduced during post-fabrication surface modification and for confirming successful immobilization of functional materials[62,79].

In summary, LIG is a product of its dynamic formation process, yielding a material whose structure is intrinsically tied to its function[79,135]. Its porous 3D architecture maximizes surface area and mass transport, its defective graphitic lattice provides electrochemical activity and its inherent surface chemistry offers a platform for biofunctionalization[62,83]. The ability to precisely engineer these characteristics through laser parameters positions LIG as a uniquely versatile and manufacturable electrode material, poised to address many of the scalability and integration challenges that have constrained the translation of nanocarbon-based electrochemical platforms from the laboratory to the marketplace[65,67,78].

The advantages arise directly from its formation mechanism and resulting hierarchical architecture and can be interpreted in terms of their impact on key performance parameters such as EASA, R_{ct}, mass transport and interfacial functionality[83]. A primary advantage of LIG is its inherently hierarchical porous structure, which

provides a high EASA and a large density of electrochemically accessible sites[96]. This structural feature enhances Faradaic current responses and supports increased loading of catalytic materials or biorecognition elements, thereby improving analytical sensitivity[62,136]. In parallel, the interconnected graphitic network facilitates efficient electron transport, contributing to relatively low R_{ct} compared to non-conductive or poorly structured carbon substrates[5,79]. In addition to electronic properties, the porous morphology of LIG promotes enhanced mass transport within the electrode structure[77]. The presence of open, interconnected pores enables efficient diffusion of analytes and reaction products, reducing diffusion limitations commonly observed in dense or planar electrodes[137]. This is particularly beneficial for enzymatic electrochemical biosensors, where substrate and product transport can significantly influence response time and signal stability[89,129,138].

The continuous modulation of LIG from hydrophilic to superhydrophobic (water contact angle of 160°) can be achieved by modulating the localized inert atmosphere used in LIG fabrication[100]. Atmospheric oxygen depletion effectively suppresses the generation of oxygen-containing surface functionalities on LIG, decreasing its surface energy and consequently reducing its hydrophilicity[100,139]. Figure 11 shows the influence of atmosphere determining the hydrophilic/hydrophobic nature of LIG. The hydrophilic/hydrophobic properties of the electrode surfaces play a critical role in the performance of electrochemical sensing interfaces. A hydrophilic surface facilitates the penetration of sample solutions into the electrode's internal structure, thereby enhancing the enrichment of target analytes and improving detection sensitivity[100].

Another key advantage lies in the intrinsic surface chemistry of LIG. The presence of oxygen- and nitrogen-containing functional groups introduced during photothermal conversion provides reactive sites for subsequent functionalization[114,116]. These surface functionalities facilitate the immobilization of biomolecules, polymers and nanomaterials through both covalent and non-covalent interactions, enabling versatile interface engineering without extensive pre-treatment steps[5,62,88].

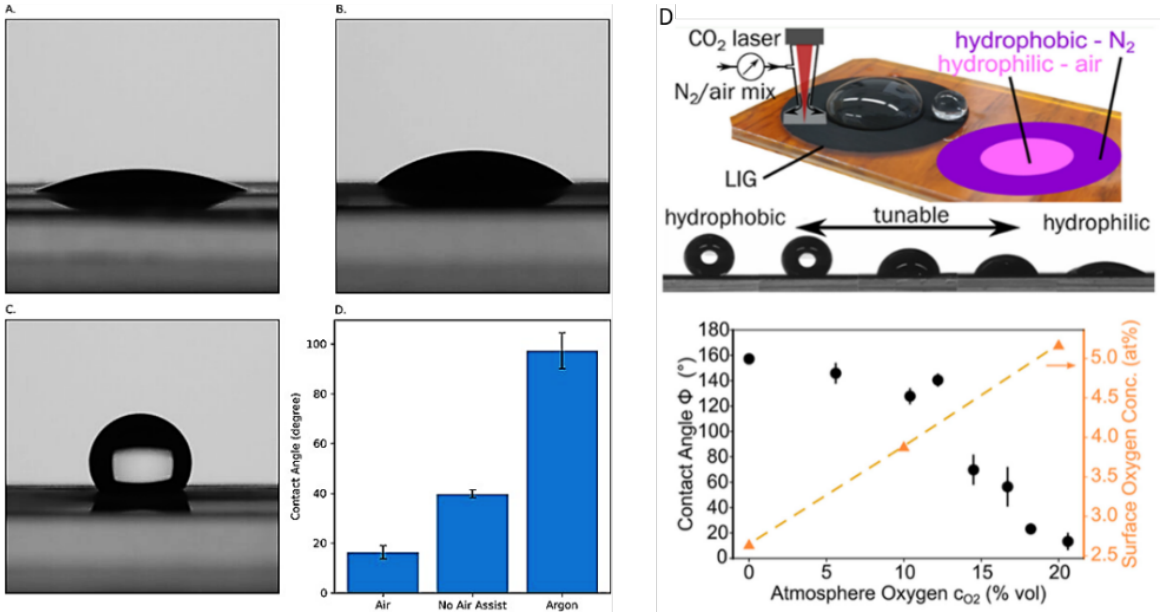


Figure 11: Influence of atmosphere and contact angle Enlarged view of contact angle test on LIGs engraved using (A) air assist with compressed air, (B) without air assist and (C) air assist with argon (Adapted from[125]) , D) Schematic of the contact angle of the LIG surface in different concentrations of oxygen (Adapted from[100]).

From a fabrication perspective, LIG enables direct, mask-free patterning of conductive electrodes in a single step under ambient conditions[91]. This approach eliminates the need for inks, binders, or transfer processes, allowing rapid prototyping and scalable production with high customizability[140]. The ability to precisely define electrode geometries and integrate different elements on flexible substrates further supports the development of wearable and point of care (POC) electroanalytical devices[89,141]. As discussed, these advantages are not independent but interrelated. The same structural and chemical features that enhance electrochemical performance also enable flexible surface modification strategies, including the integration of catalytic nanoparticles, conducting polymers and hydrogel-based or antifouling coatings[12,142]. Thus, multifunctionality positions LIG as a versatile platform for systematically tuning interfacial properties to meet application-specific requirements especially in electrochemical biosensing[66].

Electrical conductivity is strongly influenced by the processing conditions employed during laser fabrication. Laser power, scanning speed, hatch spacing, focal position, wavelength and precursor composition collectively determine the extent of graphitization and therefore govern the formation of continuous conductive pathways throughout the laser-patterned structure[54,88,94]. Insufficient graphitization generally produces isolated carbon domains separated by insulating amorphous regions, resulting in high electrical resistance[115]. Conversely, excessive laser energy may induce structural collapse, oxidation, or material ablation that likewise deteriorates electrical performance. Consequently, optimization of laser processing parameters seeks to establish a balance between graphitic ordering, structural integrity and hierarchical porosity. Table 5 summarises the characterization techniques commonly employed for LIG.

Table 5. Characterization techniques commonly employed for LIG

Technique	Property evaluated	Information obtained	Relevance to electrochemical performance
SEM	Morphology	Porosity, connectivity, laser tracks	Mass transport, accessible surface
TEM/HRTEM	Nanostructure	Graphitic layers, lattice fringes	Graphitization quality
AFM	Surface topology	Roughness, thickness	Surface interactions
Raman	Structural order	Defects, crystallinity	Electron transport
XPS	Surface chemistry	Functional groups, elemental composition	Surface modification, catalysis
FTIR	Chemical bonds	Functional groups	Polymer and biomolecule interactions
Four-point probe	Electrical properties	Sheet resistance, conductivity	Charge transport
Contact angle	Wettability	Hydrophobicity/hydrophilicity	Electrolyte wetting, hydrogel adhesion

Among the various electrical characterization techniques, the four-point probe method has become the most widely employed approach for evaluating the electrical properties of LIG because it minimizes the influence of contact resistance and provides reliable measurements of R_s[121]. Unlike two-point measurements, where

contact resistance contributes significantly to the measured value, the four-point probe separates current injection from voltage measurement, thereby enabling accurate determination of the intrinsic resistance of the graphitized structure[82,121]. This R_s is particularly suitable for thin conductive materials because it allows direct comparison between electrodes having different geometries and dimensions. Integration of these techniques provides a comprehensive understanding of how laser processing and subsequent surface engineering influence the chemical characteristics of LIG, thereby establishing the basis for rational design of multifunctional electrochemical interfaces.

2.4 Correlation of electrochemical characteristics of LIG with structure -property relationship

A comprehensive understanding of LIG requires integration of electrochemical characterization with structural, chemical and electrical analyses more than interpreting individual parameters independently[105,115]. Electrochemical descriptors such as response from cyclic voltammetry (CV), EASA, heterogeneous electron-transfer rate constant (k^0), charge transfer resistance and chronoamperometry (CA) or chronopotentiometry (CP) provides complementary information regarding the electrochemical properties and functional performance of LIG-based electrodes via studying electrode-electrolyte interface[1].

The electrochemical behaviour of LIG is therefore best understood through a processing-structure-property-performance[66,128,130]. Laser processing determines graphitization, pore architecture, defect density and surface chemistry; these structural features govern conductivity, wettability and accessible surface area, which subsequently influence electron-transfer kinetics, interfacial impedance, catalytic activity and sensing performance[54,66]. Establishing these correlations has become the central objective of contemporary LIG research and forms the basis for rational electrode design[130].

This integrated perspective also explains why no single electrochemical parameter is sufficient to evaluate LIG[115]. Instead, complementary electrochemical techniques must be interpreted together with morphological, structural, chemical and electrical characterization to obtain a comprehensive understanding of material behaviour[54,130]. Such a multidisciplinary approach enables systematic optimization of laser processing conditions and provides the scientific foundation for engineering multifunctional electrochemical interfaces tailored to specific sensing and bioelectronic applications[83].

2.5 Surface engineering strategies

LIG possesses a unique combination of high electrical conductivity, hierarchical porosity, mechanical flexibility and abundant electrochemically active edge-plane sites, making it an attractive material for electrochemical sensing applications[66]. These intrinsic characteristics alone are often insufficient to satisfy the increasingly demanding requirements of practical electrochemical platforms especially for sensors[66]. While unmodified “bare” LIG provides an efficient conductive network, it generally exhibits limited molecular selectivity, susceptibility to biofouling, insufficient catalytic activity for many electrochemical reactions and restricted capability for stable immobilization of biomolecules[121,139]. The prolonged operation in complex biological or environmental media may lead to signal drift, non-specific adsorption and gradual deterioration of electrochemical performance[143]. As a result of this, the practical implementation of LIG-

based electrochemical platforms increasingly relies on rational engineering of the electrode-electrolyte interface by preference to modification of the graphitic substrate itself[12,144].

Surface engineering provides an effective strategy to overcome these limitations by introducing application-specific functionalities while preserving the favourable electrical properties of the underlying graphitic network[15]. Instead of altering the bulk structure of LIG, surface modification focuses on tailoring the interfacial chemistry, morphology and biological functionality responsible for electron transfer, molecular recognition, catalytic activity, wettability and long-term operational stability[66,109]. Through appropriate interface engineering, LIG can be transformed from a passive conductive substrate into a multifunctional electrochemical platform capable of supporting highly sensitive, selective and robust analytical devices[145,146].

The hierarchical porous architecture of LIG is particularly advantageous for surface engineering because it provides a large electrochemically accessible surface area together with abundant defect sites and oxygen-containing functional groups that promote strong interactions with polymers, hydrogels, metallic nanostructures and biological recognition elements[147]. These structural characteristics facilitate the formation of stable multifunctional interfaces while maintaining efficient electrical communication between the modified surface and the underlying conductive graphene network[104]. As a result, the electrochemical performance of LIG can be systematically tailored according to the intended analytical application[147]. This evolution reflects a broader transition in electrochemical materials engineering from single-function electrodes toward multifunctional electrochemical interfaces capable of simultaneously satisfying multiple performance requirements[82,140].

The successful integration of functional materials (hydrogels, nanomaterials and multifunctional materials) depends not only on their intrinsic physicochemical properties but also on the method by which they are incorporated onto the LIG surface[12,148]. Accordingly, surface engineering strategies involve both the selection of appropriate functional materials and the development of suitable modification techniques capable of producing stable, electrically accessible and mechanically robust interfaces[148]. The following sections therefore discuss the principal classes of surface engineering materials employed for LIG, followed by the surface modification techniques used to construct multifunctional electrochemical interfaces.

2.6 Hydrogel-based surface modification strategies

Unmodified conductive surfaces often suffer from biofouling, denaturation of immobilized biomolecules and uncontrolled mass transport, leading to signal drift, reduced sensitivity and poor stability[149,150]. To engineer a more hospitable and functional interface, researchers have increasingly turned to hydrogel coatings[151,152]. Hydrogels are three-dimensional polymer networks capable of retaining large amounts of water, making them attractive for biosensing applications that require biocompatible and hydrated environments[153,154]. Hydrogels mimic key aspects of native extracellular matrices, offering a versatile platform to enhance biosensor functionality[155,156]. Their utility stems from a triad of core attributes: the provision of a biocompatible, hydrated microenvironment that helps preserve the conformation and activity of sensitive biological recognition elements like enzymes and antibodies; the ability to modulate mass transport of analytes and interferents through tunable mesh sizes and charged polymer backbones and the capacity to mitigate non-specific adsorption of proteins and other fouling agents, thereby enhancing selectivity and operational stability[151,157]. The selection and engineering of the hydrogel are thus as crucial as the choice of the underlying

electrode material, defining the local chemical and physical landscape in which the biochemical recognition event occurs[158,159]. Hydrogels can facilitate enzyme immobilization, modulate mass transport and reduce non-specific adsorption at electrode surfaces[160].

Hydrogels employed in electrochemical systems can be broadly classified as natural or synthetic according to the origin of their polymeric building blocks. Natural hydrogels, including chitosan, alginate, agarose, gelatin and cellulose derivatives, are widely investigated because of their biocompatibility, biodegradability and abundance of functional groups suitable for biomolecule immobilization[161]. However, their mechanical properties, swelling behaviour and structural reproducibility are often influenced by the natural variability of the source materials[152,162]. Synthetic hydrogels, including poly(ethylene glycol) (PEG)-based systems, polyacrylamide, poly(acrylic acid), zwitterionic polymers and methacrylate-derived networks, provide greater control over mechanical properties, crosslinking density, chemical composition and transport characteristics[151]. Their highly tunable structure enables precise regulation of diffusion, hydration and interfacial chemistry, making them particularly suitable for applications requiring reproducible electrochemical performance[151].

The natural and synthetic hydrogels are increasingly combined to exploit complementary advantages and hybrid hydrogel systems integrate the biological compatibility of natural polymers with the structural tunability of synthetic networks, thereby improving mechanical stability while preserving favourable biological interactions[157,162]. This strategy has become particularly attractive for advanced electrochemical interfaces where simultaneous optimization of conductivity, biocompatibility and long-term operational stability is required[161].

Hydrogels influence the electrochemical behaviour of LIG by regulating the transport of electrons, ions and electroactive molecules across the electrode-electrolyte interface[163]. Their hydrated three-dimensional networks facilitate electrolyte retention and molecular diffusion while maintaining intimate contact with the conductive LIG substrate[151,161]. Thus the charge transfer efficiency depends not only on the intrinsic conductivity of LIG but also on the structural characteristics of the hydrogel layer, including its thickness, porosity, swelling behaviour and crosslinking density[151].

An appropriately engineered hydrogel enhances interfacial performance by providing sufficient permeability for analyte transport without compromising electrical communication with the underlying electrode[153,162]. In reverse, excessive hydrogel thickness or dense polymer networks may increase diffusion resistance and reduce electrochemical accessibility, resulting in diminished analytical performance[163]. Optimizing the balance between transport properties and structural stability therefore remains a key consideration in hydrogel-based electrochemical interface design[151,162].

These observations highlight that hydrogels should not be regarded as passive coatings but as active interfacial materials that regulate mass transport and charge transfer[164]. Their integration with LIG enables simultaneous optimization of electrochemical performance, mechanical stability and biological functionality[164].

Among natural polymer hydrogels, chitosan (CS) has emerged as a preeminent material for biosensor interface engineering[165]. Derived from the deacetylation of chitin, a plentiful polysaccharide found in crustacean shells, CS offers a compelling combination of properties[166]. CS is a cationic polysaccharide and is widely used in different platforms due to its film-forming ability, biocompatibility and presence of amine

functional groups[167]. Its backbone features abundant primary amine groups, which confer a positive charge in neutral and acidic solutions and serve as versatile handles for chemical conjugation[168]. Thus, these groups enable covalent or electrostatic immobilization of enzymes and other biomolecules[168]. This cationic nature enables electrostatic adsorption of negatively charged biomolecules or substrates and facilitates covalent immobilization via well-established carbodiimide (e.g., EDC/NHS) chemistry, allowing for the stable anchoring of enzymes, antibodies, or DNA probes[169]. CS exhibits excellent film-forming ability, biocompatibility, biodegradability and inherent antibacterial properties, making it suitable for both in vitro and potential in vivo sensing applications[170,171]. In practice, CS is typically dissolved in a weak acidic solution (e.g., acetic acid) to protonate the amine groups, forming a viscous solution that can be drop-cast, spin-coated, or electrodeposited onto an electrode surface[172,173]. Upon drying or through crosslinking (glutaraldehyde or genipin), it forms a stable, adherent hydrogel film[174,175]. For enzymatic platform, encapsulating an enzyme like glucose oxidase within a CS matrix has been shown to enhance operational stability[165]. The hydrogel stabilizes the enzyme's tertiary structure, reduces leaching and can provide a protective barrier against harsh environmental conditions[176,177]. However, the integration of CS presents a fundamental trade-off between biochemical benefit and electrochemical performance[10,12]. As an inherently insulating biopolymer, a CS film introduces a barrier to electron transfer between the immobilized redox center and the underlying electrode[1,19]. Excessive film thickness can lead to high charge transfer resistance, sluggish response times due to hindered analyte diffusion and a decrease in sensitivity[178,179]. Consequently, research focuses heavily on optimization strategies: controlling film thickness at the micron or sub-micron scale, creating porous or nanostructured CS morphologies to enhance permeability and formulating CS composites with conductive nanomaterials like carbon nanotubes, graphene, or metal nanoparticles to create conductive hydrogel networks that bridge this critical performance gap[172]. Even though CS coatings have been reported to improve enzyme stability and sensor lifetime; however, excessive film thickness or poor conductivity can hinder electron transfer[168]. For applications requiring exceptionally gentle biomolecule entrapment or specific ionic microenvironments, neutral and anionic polysaccharide hydrogels like agarose and alginate provide valuable alternatives to CS[151,180].

Agarose (Agar) and sodium alginate (Alg) are neutral and anionic polysaccharides, respectively, commonly used for gentle immobilization of biomolecules[181,182]. Agarose, a linear polysaccharide derived from seaweed, forms thermally reversible physical gels[183,184]. A hot agarose solution containing biomolecules is applied to an electrode and, upon cooling, forms a rigid, porous network held together by helical bundles and hydrogen bonds[185,186]. The pore size is tunable based on the agarose concentration, allowing control over the diffusion of analytes of different sizes[187]. Its neutral charge minimizes non-specific ionic interactions, making it suitable for immobilizing a wide range of biomolecules without undesirable electrostatic effects[188].

Alg, a copolymer of guluronic and mannuronic acids, forms ionotropic gels through a mild ionic crosslinking process[180,189]. Exposure to divalent cations like calcium (Ca^{2+}) or barium (Ba^{2+}) causes the guluronate blocks to cooperatively bind the ions, forming the characteristic "egg-box" structure and instantaneously gelling the solution[190,191]. This allows for the simple, room-temperature encapsulation of even very delicate biological entities like whole cells or labile enzymes[192,193]. As an anionic polymer, alginate creates a locally charged microenvironment that can influence the partitioning and diffusion of charged analytes[193]. For instance, it can attract positively charged species or repel negatively charged interferents, adding an extra layer of

selectivity[164]. These hydrogels provide distinct ionic environments that can influence analyte diffusion and local pH near the electrode surface[160].

While both agarose and alginate offer excellent biocompatibility and gentle immobilization, their primary challenge in electrochemical sensing is their high electrical insulation[12,164]. Unlike CS, which can be made conductive through composite formation, pure agarose and alginate films severely insulate the electrode[176]. Therefore, their successful integration typically follows one of two strategies[164]. First, they can be used in very thin layers or patterned structures (e.g., microgels) that minimally impact electron tunneling while still providing a protective niche[180,185]. Second and more commonly, they are employed in layered or composite architectures[164]. In a layered design, the hydrogel acts as an outer, selective diffusion membrane atop a conventional conductive sensor surface or a thinner, more permeable CS layer[163]. In composite designs, alginate or agarose is blended with conductive materials prior to gelling[193]. For example, the incorporation of carbon nanotubes or graphene oxide into an alginate solution before Ca^{2+} crosslinking can yield a hybrid hydrogel that retains the benign immobilization properties of alginate while establishing percolation pathways for electron conduction[164,194]. The choice between agarose's physical gelation and alginate's ionic crosslinking often hinges on the sensitivity of the biological component to heat or the need for a specific charged matrix to tailor the local electrochemical environment[188].

Comparative studies indicate that while agarose and alginate offer mechanical stability and biocompatibility, their integration with conductive substrates requires careful control to avoid insulating effects[105,115]. Hydrogel modification represents a powerful strategy to engineer the critical bio-electronic interface[161,162]. CS, with its cationic functionality and ease of chemical modification, is a workhorse for stable biomolecule attachment but requires careful conductivity management[165]. Agarose and alginate offer benign, tunable entrapment but necessitate innovative layering or compositing to overcome their insulating nature[180]. The judicious selection and nano-engineering of these hydrogel systems are essential to unlock their full potential in creating robust, sensitive and selective electrochemical interfaces[151].

2.7 Nanomaterials surface engineering and noble metal nanoparticles

The pursuit of ever-lower detection limits and enhanced signal-to-noise ratios in electrochemical platforms has driven the integration of engineered nanomaterials, with noble metal nanoparticles occupying a central role[195,196,197]. These materials serve not merely as conductive scaffolds but as active catalytic components that fundamentally amplify the electrochemical signal generated[198,199]. This strategy of catalytic amplification is particularly pivotal in enzymatic biosensors where the final electroactive product, often H_2O_2, must be efficiently oxidized or reduced at the electrode surface[195,200]. Noble metals such as Pt, Pd, Au and Ir exhibit exceptional electrocatalytic activity toward H_2O_2 reactions[201]. Their high surface-to-volume ratio and unique electronic structures facilitate the cleavage of the O–O bond and the transfer of electrons at significantly reduced overpotentials compared to bulk carbon or metal electrodes[195,202]. By lowering the required operating potential, these nanoparticles minimize the driving force for the oxidation of common endogenous interferents (e.g., ascorbic acid, uric acid) present in biological samples, thereby enhancing selectivity alongside sensitivity[203]. This catalytic prowess extends beyond enzymatic byproducts to the direct electroanalysis of small molecules, the oxygen reduction reaction (ORR) in oxidase-based platforms and the facilitation of electron transfer in label-free affinity-based detection schemes, establishing metal nanoparticles

as versatile workhorses for signal enhancement[204]. Furthermore, bimetallic and alloy nanostructures create synergistic catalytic effects, while their integration with the porous LIG framework generates hierarchical interfaces capable of simultaneously enhancing electrical conductivity and catalytic amplification.

The catalytic efficacy of noble metal nanoparticles is not a monolithic property but varies significantly with composition, size, shape and surface chemistry[205,206,207]. Platinum nanoparticles (PtNPs) are arguably the most studied catalysts for H_2O_2 electrooxidation, a critical reaction in first-generation oxidase-based biosensors (e.g., glucose, cholesterol)[195]. Pt's high catalytic activity stems from its optimal surface adsorption energies for reactive intermediates. Specially, noble metal nanoparticles such as gold (Au), silver (Ag), platinum (Pt), palladium (Pd), corresponding bi- or tri-metallic alloys and core-shell nanoparticles have primarily engaged in the progress of electrochemical sensor and biosensor platforms for in vivo and in vitro biomedical analyses owing to their exceptional size and shape dependent physical, chemical and electrochemical properties[205,208]. However, a major drawback is the susceptibility of Pt to poisoning by chloride ions and adsorbed reaction byproducts, which can lead to signal fading[195]. Gold nanoparticles (AuNPs), while slightly less active than Pt for H_2O_2, offer superior biocompatibility, ease of functionalization via thiol chemistry and strong catalytic activity for the reduction of H_2O_2, making them ideal for cathodic detection schemes that further reduce interference from oxidizable species[200]. Iridium and its oxides are gaining attention for their outstanding chemical stability and high catalytic activity across a wide pH range, particularly in neural and chronic sensing applications where long-term interfacial stability is paramount[209]. The choice of material is thus application-specific: Pt for maximum sensitivity in controlled media, Au for robust biofunctionalization and Ir for demanding, fouling environments[206,210].

Beyond monometallic particles, advanced bimetallic and alloy nanoparticles (e.g: Pt-Pd, Au-Pt, Pt-Ir) are engineered to synergistically combine properties[211]. A core-shell structure with a Pt shell on a Pd core, for instance, can maximize the utilization of expensive Pt while tuning electronic properties for improved activity[212]. Furthermore, the integration of these metallic catalysts with high-surface-area carbon substrates creates hierarchical nanostructures[211]. In these composites, the carbon network provides electrical conductivity and a vast immobilization platform, while the dispersed nanoparticles act as dense catalytic hotspots[213]. This synergy can lead to multiplicative improvements in sensitivity, as the local concentration of the enzymatic product is efficiently converted to an electronic signal across the entire three-dimensional electrode architecture[211,213]. These materials exhibit high catalytic activity toward H_2O_2 oxidation and reduction, enabling lower operating potentials and improved sensitivity[201].

2.8 Antifouling and antibacterial interfaces

For practical applications, maintaining long-term interfacial stability is equally important as achieving high analytical sensitivity[214]. Exposure to complex biological or environmental samples frequently results in nonspecific adsorption of proteins, cells and microorganisms, leading to surface fouling, signal drift and deterioration of electrochemical performance[215]. The translation of electrochemical platforms from controlled laboratory settings into real-world applications in biological fluids, environmental waters, or industrial process streams introduces a formidable challenge: surface fouling[69,216]. Electrochemical platforms deployed in real biological or environmental media face two interrelated surface chemistry challenges: (1) non-specific adsorption and biofouling that degrade analytical performance and (2) microbial colonization that can both

alter signals and compromise device hygiene and lifetime[150,216]. This phenomenon involves the non-specific, irreversible adsorption of proteins, lipids, polysaccharides and entire cells onto the sensor interface, forming an occlusive biofilm[217]. This biofilm acts as a physical and chemical barrier, severely degrading performance by hindering analyte diffusion to the recognition layer, increasing impedance, promoting signal drift and ultimately leading to platform failure[179]. For implantable or chronically deployed platforms, microbial adhesion and subsequent biofilm formation present an additional, critical risk of infection and device rejection[218]. Therefore, the engineering of interfaces that can resist or mitigate fouling is not merely an enhancement but a fundamental requirement for reliable, long-term biosensor operation[218]. Modern strategies to address this challenge are bifurcated yet complementary: antifouling chemistries that passively resist the initial adsorption of biomolecules and antibacterial/antimicrobial coatings that actively inhibit the colonization and proliferation of microorganisms[219]. The integration of these functionalities into a stable, conformal coating that does not compromise the underlying sensor's electrochemical activity represents a significant frontier in interface engineering[220].

For platforms like biosensors operating in complex biological or environmental matrices, surface fouling by proteins, cells, or microorganisms can severely degrade performance[221,222]. Antifouling strategies include the use of hydrophilic and zwitterionic polymers that form hydration layers resistant to protein adsorption, as well as antibacterial coatings that inhibit microbial growth[221,223].

Zwitterionic materials such as sulfobetaine methacrylate (SBMA) have demonstrated excellent antifouling properties, while cationic polymers can provide antibacterial functionality[224,225]. Combining these approaches in multifunctional coatings has been proposed as a route toward long-term stable biosensor operation[220].

Passive antifouling approaches aim to create a thermodynamically and kinetically unfavorable surface for biomolecular adhesion[150]. The prevailing design principle is to engineer surfaces that promote the formation of a tightly bound hydration layer at the polymer-water interface[226]. Biomolecules must displace this energetically favorable water shell to adsorb, a process that is entropically and enthalpically costly[217]. The most established material for this purpose is poly(ethylene glycol) (PEG) and its derivatives[227]. PEG's antifouling efficacy is attributed to its high chain mobility, hydrophilicity and steric repulsion[223]. In aqueous environments, hydrated PEG chains undergo rapid conformational fluctuations, creating a dynamic, repulsive barrier that proteins cannot readily adhere to[228]. However, PEG coatings suffer from limitations, including oxidative degradation in biological media (particularly in the presence of transition metal ions or reactive oxygen species) and susceptibility to chain densification and loss of repellency over time[229,230].

These drawbacks have spurred the adoption of more robust zwitterionic polymers, such as poly(sulfobetaine methacrylate) (pSBMA), poly(carboxybetaine) and poly(phosphorylcholine)[231]. Zwitterionic materials contain both positive and negative charged groups within the same monomer unit, resulting in a net neutral charge but an extremely high dipole moment[232]. This leads to a stronger electrostatic interaction with water molecules via ionic solvation, forming an exceptionally dense and stable hydration layer that is highly resistant to protein adsorption[233]. Studies have shown that surfaces grafted with zwitterionic polymers can reduce non-specific protein adsorption from blood serum or plasma to levels near the theoretical detection limit, significantly outperforming PEGylated surfaces in long-term stability tests[231]. For electrochemical interfaces, these polymers are typically applied as ultrathin coatings via surface-initiated polymerization, dopamine-based co-deposition, or as a component of a hydrogel matrix[142]. A critical consideration is ensuring

the coating does not electrically insulate the electrode[142]. This is often addressed by using very thin, crosslinked brushes or by incorporating the antifouling polymer into a conductive composite network[234].

2.9 Multifunctional coatings

While antifouling coatings are highly effective against non-specific protein adsorption, they may be insufficient to prevent the adhesion of certain hardy microbes or the eventual colonization by bacteria that secrete adhesive extracellular polymeric substances (EPS)[235]. For applications with a high risk of microbial contamination, such as indwelling medical devices or environmental monitors in wastewater, active antibacterial coatings are necessary[219]. A prominent strategy involves the use of cationic polymers, such as those containing quaternary ammonium compounds (QACs), CS, or poly(lysine)[142,236,237]. These materials exert a contact-killing effect. Their positively charged groups interact electrostatically with the negatively charged bacterial cell membrane, leading to membrane disruption, leakage of cytoplasmic contents and eventual cell lysis[237]. While effective, a significant challenge with cationic coatings is their potential cytotoxicity to host mammalian cells and their propensity to be fouled by the debris of dead bacteria, which can mask the active sites and diminish long-term efficacy[142]. Among contact-killing chemistries, representative examples include polymers derived from (3-acrylamidopropyl)trimethylammonium chloride (APTAC), poly(diallyldimethylammonium chloride) (PDADMAC), quaternized polyethyleneimine (qPEI) and cationic methacrylate copolymers, all of which have demonstrated broad antibacterial efficacy when immobilized on solid surfaces[142]. APTAC have been widely investigated for surface functionalization because they combine facile polymerization chemistry with strong cationic charge density that induces membrane destabilization in bacteria[238]. APTAC is a cationic (quaternary ammonium) monomer used in copolymers and hydrogels; copolymerization or grafting of APTAC units onto surfaces generates permanently cationic films that demonstrate broad antibacterial activity in many substrate contexts (textiles, hydrogels, coatings) and can be integrated into electrode coatings to add contact-killing functionality without continuous release of biocides[238]. Evidence from materials and antimicrobial studies indicates that increasing the fraction of permanently charged APTAC moieties in a copolymer enhances bactericidal efficacy, although the optimal charge density must be balanced against cytotoxicity and effects on protein adsorption relevant to biosensor operation[238].

An alternative active approach is the controlled release of antibacterial agents, such as silver ions (from silver nanoparticles or complexes), antibiotics, or nitric oxide[239]. These agents diffuse from the coating to kill planktonic bacteria in the vicinity[239]. However, release-based systems have a finite reservoir and can raise concerns about environmental impact, bacterial resistance and potential interference with the biosensor's biochemical recognition layer[221].

Given the complementary nature of these mechanisms, the most promising path forward lies in multifunctional or "smart" coatings that integrate both passive antifouling and active antibacterial properties[240]. For instance, a coating might consist of a zwitterionic polymer matrix embedded with contact-killing cationic moieties or silver nanoparticles[241]. Advanced designs aim for stimuli-responsive behaviour, where an antibacterial function is triggered only in the presence of an infection marker[242,243]. Integrating such coatings onto the complex, porous and electrochemically active surfaces of modern interfaces is non-trivial[234]. The coating must be conformal, adhere strongly, maintain permeability to the target analyte and not increase

charge transfer resistance prohibitively[219]. Research is increasingly focused on novel deposition techniques, such as electrochemically mediated polymerization or layer-by-layer assembly, to build these sophisticated, multifunctional interfaces that can ensure the long-term stability and reliability of interfaces, particularly in biosensors in the challenging, fouling-rich environments of their intended use[142,219].

Thus, these material classes provide complementary approaches for tailoring the physicochemical and electrochemical properties of LIG. But, achieving a stable and functional interface depends not only on the choice of material but also on the method used for its integration with the LIG surface. Therefore, various surface modification techniques have been developed to immobilize functional materials while preserving electrical communication, structural integrity and long-term operational stability and are discussed in the following section.

2.10 Surface modification techniques

The successful implementation of surface-engineered LIG depends not only on the selection of appropriate functional materials but also on the method used to integrate these materials onto the electrode surface[145,148]. The immobilization strategy governs the morphology, uniformity, adhesion, electrochemical accessibility and long-term stability of the resulting interface[136,173,244]. Thereby, selecting an appropriate surface modification technique is a critical step in constructing multifunctional electrochemical platforms capable of combining high analytical sensitivity with robust operational performance[12].

Surface modification techniques can generally be classified into physical, electrochemical and chemical approaches[12]. Each method offers distinct advantages and limitations with respect to fabrication simplicity, spatial control, film uniformity, loading efficiency, electrical communication and mechanical stability[216]. In many cases, these approaches are employed sequentially or in combination to fabricate multifunctional interfaces that integrate catalytic nanomaterials, polymers, hydrogels and biological recognition elements within a single platform[216,245].

2.10.1 Physical immobilization techniques

Physical adsorption represents the simplest approach for modifying LIG surfaces[246]. Typically, a suspension containing polymers, nanomaterials, enzymes, or other functional components is deposited onto the electrode by drop-casting or spin-coating, followed by solvent evaporation to produce the desired surface layer[96,246]. Owing to its simplicity, low cost and minimal instrumentation requirements, physical adsorption remains widely employed during proof-of-concept sensor fabrication[247]. However, these coatings generally rely on relatively weak intermolecular interactions, including van der Waals forces, hydrophobic interactions, or physisorption[136]. Consequently, physically adsorbed layers frequently exhibit non-uniform thickness, limited mechanical adhesion and susceptibility to leaching or delamination during prolonged electrochemical operation, thereby compromising reproducibility and long-term stability[136,247].

2.10.2 Electrochemical modification techniques

Electrochemical methods provide substantially greater control over interface formation by generating functional materials directly on the electrode surface[248]. Among these approaches, Electropolymerization (EP) enables the in-situ formation of conducting polymer films through electrochemical oxidation or

reduction of dissolved monomers[249]. Because polymer growth occurs only on electrically connected regions of the electrode, electropolymerization allows precise regulation of film thickness, morphology and spatial distribution through adjustment of the applied potential or transferred charge[250]. Furthermore, biomolecules may be incorporated within the growing polymer matrix during deposition, enabling simultaneous immobilization and formation of the electrochemically active interface[251]. The electrochemical conditions required for polymer growth may not always be compatible with sensitive biological components, while excessively dense polymer films may restrict analyte diffusion and increase mass-transport resistance[252].

Electrodeposition constitutes another widely employed electrochemical technique, particularly for the immobilization of metallic and metal oxide nanostructures[253]. In this method, dissolved metal ions are electrochemically reduced onto the LIG surface under controlled potential or current conditions, allowing precise control over nanoparticle loading, morphology and catalytic surface area[253,254]. Compared with conventional physical deposition methods, electrodeposition provides intimate electrical contact between the deposited nanostructures and the conductive graphene substrate, thereby improving charge transfer efficiency and catalytic activity[202,253]. However, successful electrodeposition requires careful optimization of deposition parameters to minimize nanoparticle aggregation, improve adhesion and ensure uniform coverage across the porous LIG architecture[253,254].

The method of nanoparticle integration onto the electrode transducer is as critical as the choice of material itself, dictating the catalyst's loading, dispersion, adhesion and ultimately, the sensor's reproducibility[195,197]. Electrodeposition techniques, including CA and CP, are highly favoured for their direct, maskless and controllable nature[1,255,256]. In CA, a constant potential is applied to reduce metal ions from solution onto the working electrode[1]. The total charge passed controls the mass deposited, allowing for precise tuning of nanoparticle loading[1]. CP, applying a constant current, offers an alternative route[1]. These electrochemical methods enable the nucleation and growth of nanoparticles directly onto complex, porous substrates, ensuring intimate electrical contact a significant advantage over physical drop-casting of pre-synthesized nanoparticles, which often rely on weak van der Waals forces for adhesion[257].

However, electrodeposition presents inherent challenges related to morphological control and stability[1,198]. The stochastic nature of nucleation can lead to polydisperse particle size distributions and aggregation, especially at high loadings[257]. Aggregated nanoparticles have reduced effective surface area and can clog the pores of a 3D substrate, hindering mass transport. Deposition of nanomaterials is a crucial step in fabrication[258]. Furthermore, weakly adhered nanoparticles are prone to detachment during electrochemical cycling or under flow conditions, leading to signal drift and device failure[258]. This detachment risk is when a secondary hydrogel or polymer membrane is applied over the nanoparticles for bioreceptor immobilization or fouling protection; the coating process can physically dislodge particles or create interfacial stresses[221,259].

The prerequisite to a stable biosensor is the immobilization of the bioreceptor at the surface of the transducer using a reversible or irreversible immobilization method[138,244,259]. To achieve this, different strategies may be used, which are classified into surface adsorption, covalence binding, cross-liking, entrapment (beads or fibers), bioaffinity and chelation or metal binding based on such criteria as a type of sample, desired selectivity, difficulty and ranging[2,259]. Addressing these challenges requires sophisticated interface design. Strategies include:

1. Pulsed Electrodeposition: Using pulsed potentials or currents to allow for diffusion of metal ions at the electrode surface, promoting smaller and more uniform nanoparticle sizes[254].
2. Surface Pre-Treatment: Functionalizing the carbon substrate with specific nucleation sites to obtain more uniform nanoparticles[12,13].
3. Formation of Conductive Hybrid Layers: co-depositing nanoparticles within a conductive polymer matrix (e.g., PEDOT) or a carbon nanomaterial ink. The polymer or carbon mesh acts as a mechanical binder, physically entrapping the nanoparticles and preventing aggregation and detachment while maintaining electrical connectivity[164].
4. Post-deposition Annealing: Mild thermal or electrochemical treatments to strengthen the metal-substrate bond and improve crystallinity, thereby enhancing both catalytic activity and adhesion[260].

In conclusion, the strategic deployment of noble metal nanoparticles represents a powerful route to catalytic amplification in electrochemical interfaces[257]. Their successful implementation, however, hinges on a holistic design philosophy that carefully selects the catalytic material, employs controlled fabrication to optimize morphology and adhesion and engineers the surrounding interface to ensure long-term structural and functional stability within the complete biosensing assembly[261,262]. In summary, metal nanoparticles, particularly noble metals such as platinum and iridium, are widely employed to enhance electrochemical biosensor performance through catalytic amplification.

2.10.3 Chemical immobilization strategies

In addition to physical and electrochemical approaches, chemical immobilization methods provide robust attachment of functional materials through covalent bonding or molecular self-assembly[247]. Covalent immobilization generally exploits reactive functional groups naturally present on LIG or introduced during surface functionalization to anchor biomolecules, polymers, or catalytic species through stable chemical linkages[169]. Self-assembled molecular layers represent another strategy for producing highly ordered interfacial architectures with controlled orientation and improved long-term stability[263]. Compared with physical adsorption, these chemically bonded interfaces exhibit superior mechanical robustness and resistance to leaching, making them particularly attractive for biosensors intended for prolonged operation in complex biological environments[169].

Although LIG possesses excellent electrical conductivity, hierarchical porosity and mechanical flexibility, its intrinsic physicochemical properties are often insufficient to satisfy the increasingly demanding requirements of advanced electrochemical applications[121,147]. Practical electrochemical platforms require not only efficient electron transport but also selective molecular recognition, catalytic activity, antifouling behaviour, biocompatibility, mechanical robustness and long-term operational stability[66,214]. Consequently, significant research efforts have shifted from the development of LIG itself toward engineering its surface to introduce application-specific functionalities while preserving its favourable electrochemical characteristics due to its hierarchical porous architecture and abundant surface defects of LIG[8,145]. These modifications transform LIG from a passive conductive substrate into an active multifunctional electrochemical interface capable of addressing the diverse requirements of biosensing, electrocatalysis, flexible electronics and biointegrated devices[245,264].

The functionalization of an electrode surface with biorecognition elements, catalysts, or protective layers is the definitive step in constructing a biosensor, transforming an inert transducer into a selective analytical device[45]. The method chosen to accomplish this modification governs the morphology, stability and ultimately the performance of the bioactive interface[10]. A suite of techniques is available, each with distinct physical and electrochemical foundations, advantages and inherent trade-offs[204]. Broadly, these methods can be categorized into physical adsorption, electrochemically driven processes (electro polymerization and electrodeposition) and chemical grafting (e.g., covalent bonding via self-assembled monolayers)[45]. The selection of an appropriate strategy is a critical design decision that must balance fabrication simplicity, spatial control, film uniformity, the electrochemical accessibility of immobilized species and the long-term operational stability of the resulting composite interface[121].

Physical adsorption, primarily through drop-casting, represents the most straightforward approach[12]. A solution containing the modifier be it enzyme, nanomaterial, or polymer is applied to the electrode surface and allowed to dry, forming a film through physisorption, van der Waals forces, or hydrophobic interactions[138]. However, this technique suffers from significant drawbacks. The resulting films are often non-uniform in thickness and distribution, leading to spatial variations in sensitivity across the electrode[218]. The adhesion is typically weak, making such layers prone to leaching or delamination under hydrodynamic flow or during extended electrochemical cycling, which compromises both reproducibility and long-term stability[218,245]. While spin-coating can improve uniformity for some polymeric films, it does not fundamentally address the weak interfacial adhesion[218].

In contrast, Electropolymerization is an in-situ, electrochemically driven synthesis where dissolved monomers are oxidized (or reduced) at the electrode surface, forming an adherent, cross-linked polymer film directly on the conductor[265]. This technique, used for polymers like polypyrrole, polyaniline and PEDOT, offers exceptional spatial and temporal control[266,267]. Film thickness can be precisely regulated by the total charge passed during polymerization and the growth can be confined to the energized working electrode, enabling micropatterning[268]. The resulting films are intrinsically adherent and conformal, as they are chemically grafted onto the substrate during synthesis[265]. Furthermore, the process can simultaneously entrap biological elements like enzymes or DNA within the growing polymer matrix, creating a one-step immobilization and transduction layer[266]. The primary limitation lies in the stringent electrochemical conditions required for polymerization (specific potential windows, electrolyte pH, monomer concentration), which may be incompatible with some sensitive biomolecules[251]. Additionally, the dense morphology of some electropolymerized films can hinder mass transport and the need for accessible conductive pathways can limit loading capacity[269].

Electrodeposition shares the electrochemical control of electropolymerization but is focused on the reduction of metal ions to form conductive or catalytic layers, typically of noble metals like platinum, gold, or their oxides[257]. By controlling the applied potential or current density and the deposition charge, one can precisely govern the loading, size and morphology of metallic nanostructures[132]. This allows for the creation of high-surface-area catalytic coatings directly onto complex, porous substrates like carbon foams or nanofibers, ensuring excellent electrical contact[256]. Techniques such as pulsed electrodeposition can further refine nanostructure, yielding more uniform and active catalytic sites[253]. The challenge with electrodeposition lies

in ensuring the mechanical stability of the deposited layer and the achievement of a uniform deposit on highly non-planar or heterogeneous surfaces requires careful optimization of the electrokinetic parameters[45].

The choice among these techniques is not mutually exclusive and hybrid or sequential approaches are often most effective[12]. For instance, a porous, nanostructured metal catalyst may first be electrodeposited to enhance sensitivity, followed by the electropolymerization of a conducting polymer that both entraps an enzyme and stabilizes the underlying nanoparticles[12,256]. Alternatively, a robust, covalently anchored self-assembled monolayer may provide a stable foundation for subsequent drop-casting of a hydrogel[263]. The optimal pathway is dictated by the specific demands of the application: a single-use, disposable sensor may tolerate the simplicity and imperfections of drop-casting, while an implantable, continuous monitor necessitates the robust, adherent interfaces afforded by electrochemical synthesis[101]. Consequently, the rational design of a biosensor interface mandates a holistic understanding of these fabrication tools, selecting and sequencing them to build a hierarchically structured surface that meets the multi-objective criteria of sensitivity, selectivity, stability and manufacturability[6].

Thus electropolymerization enables controlled, adherent coatings with tunable thickness, while electrodeposition provides precise control over metallic layer formation[2], which indicates selecting an appropriate modification strategy requires balancing ease of fabrication, film uniformity, electrochemical accessibility and long-term stability[45,270].

2.11 Stability and reproducibility concerns

A recurring limitation in LIG-based sensors and other platforms are variability in electrochemical performance arising from fabrication inconsistencies and surface contamination[105,115,271]. The most significant hurdles facing the commercialization and reliable use of LIG-based sensors are intertwined issues of long-term stability and device-to-device reproducibility[115,271]. Exposure to ambient conditions can alter surface chemistry, leading to changes in wettability and electrochemical response over time[88,90,102].

The minor fluctuations in laser focus, power stability, scan speed consistency, change in intervals, substrate properties, (e.g., PI film thickness, batch variation) can lead to measurable differences in LIG morphology, defect density and R_s[105,115,271]. These variations translate directly into variability in key electrochemical parameters like baseline current, charge transfer resistance and catalytic activity, making it difficult to produce sensors with identical calibration curves[83,115].

Stability concerns are twofold: environmental and operational[63,101]. The defect-rich, functional group-laden surface of LIG is chemically dynamic[51]. Upon exposure to ambient atmosphere over time, the surface can undergo further oxidation, adsorb atmospheric contaminants, or experience changes in hydrophilicity[50,136]. This alters the electrochemical interface, leading to signal drift. In operational settings, especially in biological fluids, surface fouling is a major threat[222,234]. Proteins and other biomolecules can irreversibly adsorb onto the high-surface-area porous network, blocking active sites and increasing impedance[136]. This fouling not only degrades sensitivity but can also alter selectivity by creating a non-specific biofilm[221]. Moreover, the mechanical integrity of the porous LIG structure under repeated electrochemical cycling or flow conditions in microfluidic devices is not always guaranteed; delamination or cracking of the LIG layer from the underlying polymer substrate can occur[106]. These issues highlight the need for robust surface engineering strategies to stabilize LIG interfaces for practical sensing applications[12]. Addressing these

limitations is an active area of research focused on surface engineering and encapsulation strategies[78]. Post-laser treatments, such as brief plasma exposure or thermal annealing in controlled atmospheres, can stabilize the surface chemistry[112,113]. Conformal coatings of ultra-thin, permeable polymers (e.g., parylene-C) or self-assembled monolayers can passivate the surface against non-specific adsorption and environmental aging while allowing analyte diffusion[204,222]. Developing standardized pre- and post-laser processing protocols, along with rigorous quality control metrics (e.g., in-line Raman monitoring during fabrication), will be crucial for advancing LIG from fascinating laboratory curiosities to reliable analytical tools[272].

2.12 LIG-based electrochemical interfaces: reported applications and limitations

The translation of LIG from a novel material into a functional platform has been vigorously explored, yielding a diverse portfolio of electrochemical interface demonstrations[7,101]. These applications leverage LIG's inherent structural and electrochemical properties high surface area, defect-mediated activity and facile patterning to detect targets ranging from biomolecules to environmental contaminants[273]. These studies demonstrate the use of LIG-based electrodes for the detection of biomolecules such as glucose, dopamine and H_2O_2, as well as environmental targets including heavy metals and organic contaminants, energy storage and biomedical applications[60,83,95,104,274].

Despite these promising developments, the transition from proof-of-concept demonstrations to reliable, field-deployable devices remains challenging[65,89]. LIG-based sensors often exhibit limitations related to long-term stability, selectivity in complex biological or environmental matrices and variability arising from fabrication conditions[63,105,115,129,]. In particular, the sensitivity of LIG properties to laser processing parameters can lead to batch-to-batch inconsistencies, complicating reproducibility and standardization[88,115]. Furthermore, biofouling, non-specific adsorption and signal drift remain significant obstacles in real-world applications[130,222]. A critical examination of both the successes and shortcomings of LIG-based platforms is essential to chart a path toward their maturation and practical adoption, which is essential for guiding future research toward robust, scalable and application-oriented systems[78].

2.13 Research gaps identified in the literature

Based on the comprehensive review of the current literature, it is evident that the field of LIG for electrochemical sensing applications, while exceptionally promising, is characterized by several critical and interconnected research gaps. These gaps span from fundamental materials science to applied analytical performance and their collective resolution is supreme for transitioning LIG-based biosensors from compelling laboratory prototypes to reliable, standardized analytical tools. The following synthesis delineates these gaps in detail, underscoring the necessity for a systematic, interdisciplinary approach to interface engineering that correlates fabrication parameters with interfacial chemistry and ultimate electrochemical performance.

A primary and pervasive gap is the striking absence of standardized protocols and reporting frameworks for LIG fabrication. The synthesis of LIG is influenced by a complex interplay of laser parameters like wavelength, power, scan speed, pulse duration, number of passes, intervals of lasing and precursor material properties (polymer type, foil/substrate thickness)[115,271]. The literature reveals a wide, often incomparable, range of these parameters, leading to significant variance in reported LIG properties such as porosity, R_s,

defect density and functional group composition[79,105]. Crucially, the electrochemical properties including heterogeneous electron transfer rates, double-layer capacitance and background current are directly dictated by this structural and chemical heterogeneity[1,83]. Several studies have proposed standardisation frameworks normalisation, these have not yet been universally adopted, leading to difficulty in cross-study comparison[105,139,271]. This parameters often cannot be directly transferred between different laser systems or substrate batches due to the diversity of laser systems, experimental conditions, variability in precursors[105,271]. This lack of standardization severely hinders the reproducibility of results across different research groups and impedes the establishment of robust structure-property relationships. Therefore, there is an urgent need for systematic parametric studies that not only optimize for performance but also define a minimum set of reported fabrication conditions and corresponding electrochemical characterization data (e.g., Raman D/G band ratio, XPS, voltammetric kinetics with standard redox probes) to enable meaningful comparison and replication.

When it comes to the surface engineering of LIG, the integration of hydrogels employed for biomolecule immobilization, size exclusion, or antifouling onto porous LIG electrodes introduces a complex, three-dimensional interface that is remains largely unexplored. How do hydrogel thickness, mesh size, ionic conductivity and swelling kinetics precisely modulate the mass transport of analytes, redox mediators and ions to the underlying LIG surface. Besides, how do the charges of the hydrogel (e.g., amine, carboxyl, hydroxyl groups) and its crosslinking density affect the electrical communication between the electrode and encapsulated biorecognition elements is poorly understood. The porous nature of LIG adds another layer of complexity, as hydrogels may infiltrate the pores, potentially block active sites or create diffusion barriers[164]. A significant gap exists in explaining these effects. Research is needed that combines controlled hydrogel modification, characterization and optimization of signal response based on defined hydrogel physicochemical properties.

The electropolymerization and electrodeposition on LIG is a common strategy to enhance biocompatibility and facilitate direct electron transfer. However, the mechanistic pathway of growth is largely inferred from studies on flat electrodes. The nucleation, growth morphology and adhesion on high-surface-area, defective carbon are likely distinct. Key unknowns include how LIG's surface energy and defect sites influence monomer adsorption and initial nucleation, how the evolving polymer structure affects subsequent ion and solvent ingress/entrance and how co-deposited biomolecules or doping ions alter the polymerization mechanism and the resulting conductivity. Addressing this gap requires spectroscopic and microscopic techniques coupled with electrochemical analysis to visualize and quantify the deposition process and modification according to the intended application.

A major challenge in advanced biosensor design is the integration of multiple functional layers such as catalytic nanoparticles conducting polymers and antifouling polymers into a coherent, high-performance architecture on LIG. Individually, these components enhance specific attributes: nanoparticles boost electrocatalytic activity, hydrogels and polymers improve biocompatibility and antifouling layers reject non-specific adsorption. However, their sequential integration often leads to deleterious trade-offs. For instance, a dense antifouling layer may insulate the electrode, increasing impedance and attenuating signal from nanoparticle-catalyzed reactions[234]. The literature lacks systematic studies on strategies and nanostructuring approaches that preserve the electrochemical accessibility and activity of catalytic sites while providing

robust fouling resistance. Research must focus on interface design, where the sequence, chemistry and nanostructure of each layer are co-optimized.

Finally, there is a pronounced deficiency in rigorous, systematic studies evaluating the long-term operational and storage stability of LIG biosensors, particularly when deployed in complex, real-world matrices such as blood serum, urine, wastewater, or food products. Most proof-of-concept demonstrations are validated in simple, clean buffer solutions. The gaps here are multifaceted: (i) The physicochemical stability of the LIG interface itself under prolonged electrochemical measurements or biofouling; (ii) The immobilized biorecognition elements on the unique LIG surface; (iii) The long-term efficacy of antifouling strategies against the diverse, adsorbent cocktail of proteins, cells and organic matter found in real samples; and (iv) The performance variance between individually fabricated LIG electrodes, which speaks to manufacturing reproducibility.

In conclusion, these collectively underscore a central, overarching need for dedicated research work in systematic surface and interface engineering. Such an approach must deliberately and quantitatively link controlled LIG fabrication parameters to defined surface chemical and morphological states and subsequently to measurable electrochemical and bioanalytical performance metrics. By addressing, the field can move beyond empirical optimization and toward the predictive design of robust, high-performance and commercially viable LIG-based electrochemical platforms.

Based on the literature reviewed, major things addressed in this study:

1. Systematic understanding of how laser fabrication parameters and precursor properties collectively influence LIG formation, graphitic structure and the resulting electroanalytical performances.
2. Understanding of how multifunctional polymer interfaces influences properties of porous LIG electrodes.
3. Understanding of APTAC and SBMA polymerization mechanism, polymer growth under biologically relevant conditions on LIG.
4. Challenges in integrating catalytic nanoparticles with polymeric and antifouling layers and incorporation onto LIG surface.
5. Systematic sequential surface engineering framework capable of integrating catalytic enhancement, multifunctional polymer engineering and functionality into single LIG interface without compromising electrochemical performance.
6. Systematic studies evaluating long-term stability and antifouling performance of functionalized LIG electroanalytical platforms.

CHAPTER 3 - OBJECTIVES AND SCOPE

As already introduced, the unique properties of LIG make it an attractive candidate for different applications including sensing. The realization of a functional biosensor requires the integration of appropriate surface modifications that enable specific biorecognition, controlled interfacial interactions and efficient signal transduction[9,12]. In this context, surface engineering plays a critical role in tailoring LIG interfaces to achieve desired performance[144]. Functionalization strategies, including the incorporation of catalytic nanomaterials, conducting polymers and hydrogel or antifouling layers, are essential for enhancing charge transfer kinetics, improving selectivity, stabilizing bioreceptors and enabling reliable operation in complex environments[12,144]. Therefore, the performance of LIG-based platforms is not solely determined by the intrinsic properties of the material, but by the deliberate design of its surface and interface[6,7].

Despite the promising properties of LIG, several challenges remain that limit its consistent application in electrochemical biosensing[275,276]. In particular, issues related to long-term stability, reproducibility of electrochemical performance and variability in material properties have been widely reported[122,275]. These challenges arise in part from the strong dependence of LIG structure and chemistry on laser processing conditions, as well as from an incomplete mechanistic understanding of the relationships between fabrication parameters, microstructure and electrochemical behaviour[276]. As a result, LIG electrodes produced under nominally similar conditions can exhibit significant variations in conductivity, surface functionality and interfacial response, which directly impact sensing performance[11]. The core of this work is to develop and validate interface engineering strategies that make LIG electrodes functional to improve overall performance.

3.1 Central research questions and hypothesis

Addressing these limitations requires the development of systematic surface engineering strategies that combines laser fabrication with targeted interface engineering to tailor the structural, electrochemical and biological properties of LIG. Accordingly, the primary objective of this thesis is to develop and validate a sequential surface-engineering methodology capable of systematically tuning the electroanalytical performance, functional reliability and long-term operational stability of LIG-based electrochemical interfaces to serve later for different electroanalytical requirements. Therefore, the central research question is:

How can laser fabrication parameters and targeted surface engineering strategies on LIG electrodes be employed to systematically tailor electroanalytical performance and functional reliability of multifunctionally modified LIG platforms?

To answer this question, the LIG surface was systematically engineered through sequential optimization of laser fabrication, catalytic nanozyme functionalization and multifunctional polymer modification, with each step designed to address specific limitations of the preceding interface. The hypothesis behind is:

The electrochemical performance and functional reliability of LIG-based interfaces are governed not only by the intrinsic properties of LIG but can be systematically tailored through controlled laser fabrication, precursor selection and surface-engineering strategies. As a result, rational integration of catalytic nanomaterials and multifunctional polymer interfaces is expected to enhance charge transfer behaviour, catalytic activity, interfacial stability and biological functionality independently, without

compromising electrochemical accessibility, thereby enabling electroanalytical platforms adaptable to diverse application-relevant environments. To evaluate this hypothesis experimentally, the proposed surface-engineering strategy was investigated through a series of measurable research questions that progressively examine the influence of fabrication parameters and surface engineering protocols on the performance of LIG

1. How do laser fabrication parameters influence the structural characteristics, graphitization behaviour and electrochemistry of PI-derived LIG?
2. How do surface modification using catalytic nanomaterials and multifunctional polymer interfaces influence properties and performance of LIG?
3. Can multifunctional copolymers be electropolymerized on LIG to simultaneously provide stable enzyme immobilization together with antifouling and antibacterial functionalities?
4. Can nanozyme- functionalized LIG interfaces provide robust catalytic amplification for while preserving electrochemical accessibility and long-term operational stability?

Each experimental result in later chapters will comprehensively map back to one or more of these questions. Additionally, the scope this work will also account on the:

1. The systematic optimization of laser parameters (power, scan speed, number of passes, intervals) while lasing on PI foil of different thickness and selection of different precursors. This accounts for the relationships between fabrication conditions, effect of substrate dependency, resulting electrochemical properties and supports the development of rapidly manufactured scalable, customizable and sustainable fabrication approaches.
2. To elucidate how variations in LIG microstructure and surface chemistry influence charge transfer kinetics, mass transport and overall electrochemical behaviour.
3. Understanding the effect by the integration of all surface engineering protocols.
4. To evaluate post-fabrication interface engineering strategies for improving the operational stability and biological robustness of LIG through multifunctional polymer interfaces incorporating antifouling and antibacterial functionalities. Hydrogen peroxide and glucose were employed as proof-of-concept electroanalytical systems to validate the proposed surface-engineering strategy under application-relevant sensor platforms in relevant sensing applications, such as glucose and H_2O_2 detection.

Collectively, these investigations indicate a dual focus of this work: i) to understand the formation mechanisms and properties of LIG and ii) to develop a systematic surface engineering strategies that enhance its functionality and applicability as a reliable multifunctional electrochemical interfaces. The electroanalytical performance demonstrated using hydrogen peroxide and glucose serves as proof-of-concept validation of the proposed engineering strategy instead of its sole application.

CHAPTER 4 - MATERIALS AND METHODS

4.1 Materials

The materials employed throughout this dissertation were selected according to the specific requirements of LIG fabrication, surface engineering, physicochemical characterization and electrochemical evaluation. To improve clarity and emphasize their functional roles within the experimental workflow, the materials are grouped according to their application in the different stages of the research.

4.1.1 Carbon precursor substrates and processing materials.

Commercial Kapton- PI foils with thicknesses of 50µm and 100µm (DuPont, USA) were employed as the primary precursor substrates for LIG fabrication. Whatman No. 40 cellulose filter paper (Cytiva, UK) was used as the biomass-derived precursor for cellulose-based LIG, while polytetrafluoroethylene (PTFE or Teflon) foil served as the fluoropolymer precursor for the preliminary investigation of fluorinated laser-derived architectures. BurnBlock flame retardant (FR) was applied as a pretreatment agent to improve thermal stability during laser irradiation and to facilitate controlled graphitization of the cellulose substrate.

4.1.2 Hydrogel and polymer materials

Hydrogel materials employed for surface modification and transfer studies included chitosan (CS), sodium alginate (Alg), agar and poly(ethylene glycol) diacrylate (PEGDA) with average molecular weights of 250, 500 and 700 Da. Glutaraldehyde solution (50%) was used as the crosslinking agent for CS while calcium chloride ($CaCl_2$) served as the ionic crosslinker for alginate hydrogels. Acetic acid was used for preparation of CS solutions. PEGDA photopolymerization was initiated using diphenyl(2,4,6-trimethylbenzoyl)phosphine oxide (TPO), which served as the UV photoinitiator during the development of transferable LIG platforms.

4.1.3 Monomers and polymerization reagents

For the fabrication of multifunctional electropolymerized interfaces, the zwitterionic monomer [2-(methacryloyloxy)ethyl]dimethyl-(3-sulfopropyl)ammonium hydroxide (SBMA) and the cationic monomer (3-acrylamidopropyl)trimethylammonium chloride (APTAC) were employed. Ammonium persulfate (APS) was used where applicable as the radical initiator during polymer synthesis. Prior to use, the APTAC solution was purified by passing it through a basic alumina column to remove the polymerization inhibitor and ensure reproducible electropolymerization.

4.1.4 Electrodeposition precursors

Iridium(III) chloride hydrate ($IrCl_3 \cdot xH_2O$) and hexachloroplatinic acid hydrate ($H_2PtCl_6 \cdot xH_2O$) were used as precursor salts for electrodeposition of Ir-Pt nanozymes. All electrodeposition electrolytes were prepared using deionized (DI) water immediately before use.

4.1.5 Electrochemical reagents

Electrochemical characterization was performed using phosphate-buffered saline (PBS), sodium sulfate (Na_2SO_4), potassium ferricyanide ($K_3[Fe(CN)_6]$), potassium ferrocyanide ($K_4[Fe(CN)_6]$), hexaammineruthenium(III) chloride (RuHex), poly(sodium 4-styrenesulfonate) (PSS), hydrochloric acid (HCl) and sodium hydroxide (NaOH). Unless otherwise specified, all aqueous solutions were prepared using DI water.

4.1.6 Other reagents

Glucose oxidase (GOx, Aspergillus niger), D-(+)-glucose, bovine serum albumin (BSA) and the reagents required for preparation of artificial sweat-including sodium chloride (NaCl), potassium chloride (KCl), urea and sodium lactate-were used for electroanalytical evaluation, operational stability studies, antifouling assessment and validation under physiologically relevant conditions.

Unless otherwise specified, all chemicals were of analytical grade and were used as received without further purification.

4.2 Experimental instrumentation

The experimental investigations presented in this dissertation required a combination of laser-processing equipment together with physicochemical, electrical and electrochemical characterization techniques. The instrumentation employed throughout this work is summarized below according to its function within the overall experimental workflow.

4.2.1 Laser fabrication system

LIG was fabricated using a computer-controlled CO_2 laser engraving system (Gweike Cloud 50 W CO_2 laser cutter, wavelength: 10.6 μm) equipped with a sealed CO_2 laser source operating at a wavelength of 10.6μm. The electrodes were designed and the laser system was controlled using LightBurn 1.7.08 software, which enabled independent adjustment of laser power, scanning speed, hatch interval, focal position and lasing/scribing mode during fabrication. Unless otherwise stated, all LIG structures were fabricated under ambient laboratory conditions.

The laser system was employed throughout this dissertation for fabrication of polyimide-derived LIG, cellulose-derived LIG, preliminary fluoropolymer-derived carbon architectures and laser-patterned electrodes used for subsequent surface engineering.

4.2.2 Physicochemical characterization

Morphological characterization of the fabricated materials was performed using Quanta 250 FEG SEM microscope (ThermoFisher Scientific) equipped with a Schottky field emission gun to evaluate the surface topology and porous microstructure of LIG before and after surface modification.

Structural characterization was carried out using Raman spectroscopy using an Xplora system (HORIBA) to assess the degree of graphitization and defect formation within the laser-processed carbon structures. Nanostructural characterization of electrodeposited Ir–Pt nanozymes was performed using transmission electron microscopy (TEM). TEM investigations were carried out using an FEI Tecnai G20 microscope

operating at an accelerating voltage of 200 kV, either in scanning transmission electron microscopy mode equipped with a high-angle annular dark-field detector (HAADF-STEM) or in high-resolution transmission electron microscopy (HRTEM) mode, depending on the specific analysis. Surface chemical composition and elemental bonding states were investigated by XPS Escalab 250Xi (ThermoFisher Scientific) multi-spectroscope, while a PerkinElmer Frontier FT-IR/FIR spectrometer was employed for identification of characteristic functional groups present in hydrogel and polymer-modified interfaces. The contact angle was measured to investigate changes in surface energy following laser processing and surface modification with a DSA100 goniometer (Kruss, Germany), at room temperature, with 2 µL drops of water applied. The contact angle was recorded with a CCD camera and the average value of the wetting angle was determined using ADVANCE software, with the Young-Laplace method. Each measurement was repeated several times.
Electrical conductivity of selected LIG samples was assessed using four-point probe resistance measurements to evaluate conductive network formation following laser fabrication and transfer.

4.2.3 Electrochemical instrumentation

Electrochemical experiments were performed using a BioLogic potentiostat/galvanostat controlled through EC-Lab software. Unless otherwise specified, all measurements were carried out using a conventional three-electrode electrochemical cell consisting of the fabricated LIG electrode as the working electrode, an Ag/AgCl reference electrode and a platinum wire counter electrode.
Electrochemical characterization included CV, CA, CP and electrochemical impedance spectroscopy (EIS), depending on the specific objective of each investigation.

4.2.4 Optical characterization

Optical characterization was performed throughout the optimization studies to evaluate the macroscopic appearance, laser-processing quality and transfer integrity of fabricated LIG structures. Digital photography and optical microscopy were employed for rapid visual assessment of graphitic pattern formation prior to the detailed structural characterization.

4.3 Methods - fabrication and translational strategies

The experimental investigations presented in this dissertation were designed as a systematic engineering methodology for the development of multifunctional LIG electrochemical platforms by surface engineering. More than treating individual experiments as independent studies, the methodology was structured as a sequential workflow in which each stage progressively builds upon the preceding one. This approach enabled systematic investigation of the LIG formation on different substrates, same substrate having different thickness, influence of laser parameters, different surface engineering protocols and the resulting physicochemical, electrochemical and electrochemical properties of LIG.
The experimental methodology consists of different stages. The first stage involves fabrication of LIG through systematic optimization of laser processing parameters using PI as the primary precursor material. The second stage focuses on multifunctional surface engineering of the optimized LIG electrodes through hydrogel modification, electrodeposition of catalytic nanozymes and electropolymerization of multifunctional polymer interfaces. The third stage comprises comprehensive structural, physicochemical,

electrical and electrochemical characterization to establish structure-property relationships. Finally, the engineered interfaces were validated through electroanalytical and biological investigations, including hydrogen peroxide and glucose sensing, operational stability, artificial sweat evaluation, antifouling assessment and antibacterial activity. Later building upon the optimized fabrication strategy, the methodology was subsequently translated to alternative precursor systems, including cellulose-derived LIG (Paper-LIGs) to investigate the influence of substrate chemistry on graphitization and electrochemical behaviour and as an extension of current study using fluoropolymer (PTFE)-derived architectures to explore the feasibility of fluorine-containing laser-derived materials. In parallel, preliminary studies on PEGDA-assisted LIG transfer were undertaken to investigate the translation of engineered LIG from rigid substrates towards flexible hydrogel-supported architectures, which points towards the future directions.

The methodology described in this chapter therefore establishes the experimental foundation for the engineering protocols developed throughout this dissertation, demonstrating not only systematic fabrication and multifunctionalization of LIG but also its translation towards alternative precursor materials and flexible electrochemical platforms.

4.3.1 Fabrication of polyimide-derived LIG

LIG was fabricated on Kapton foil of different thickness 50µm, 100µm using CO_2 laser cutting device as described in the section 4.2.1. In the first step, the geometry of LIG-based electrodes was designed using the built-in software Lightburn 1.7.08 provided with the laser cutting system. The electrode design is as shown in Figure 12 imported into the laser software, after which laser processing parameters including laser power, scanning speed, hatch interval, focal position and processing mode were adjusted according to the experimental design. The electrodes include a circular working electrode (WE) of diameter 3mm, which is encompassed by an incomplete ring of 0.5mm thickness. The spacing between WE and counter electrode (CE) was fixed at 0.5mm. Lasing was operated under ambient conditions and raster mode was used to engrave patterns over PI sheets. The laser speed (S) is expressed in unit of mm/s and laser power (P) is in %, (% represent the % portion of total power of the machine, 40W). Before the lasing process, no pretreatment was applied to PI sheets, but was cleaned with isopropyl alcohol (IPA) to remove any contaminants.

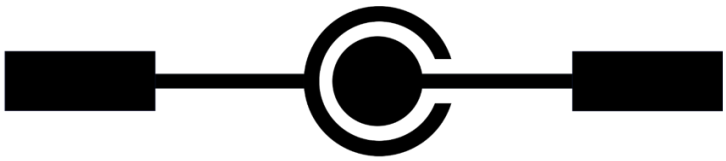


Figure 12: Electrode designed in Lightburn 1.7.08 software. The electrodes include a circular working electrode (WE), 3mm in diameter, which is encompassed by an incomplete ring of 0.5mm thick. The spacing between WE and counter electrode (CE) was fixed at 0.5mm.

This simplified geometry was employed to systematically evaluate the influence of individual laser processing parameters, including laser power, scanning speed, hatch interval and focal position, on LIG formation. The use of a square test pattern enabled rapid fabrication and direct comparison of processing conditions while minimizing material consumption and fabrication time. Following identification of suitable processing windows, the optimized laser parameters were subsequently applied to fabricate the complete electrochemical platform.

Following routine maintenance and recalibration of the laser system, a preliminary investigation was undertaken to examine the influence of laser focus position (Z-offset) on LIG fabrication. LIG electrodes were fabricated using identical laser power and scan speed while varying only the focal position (Z-offset). The resulting electrodes were subsequently characterized by SEM and CV to obtain a preliminary assessment of the influence of laser focus position on the morphology and electrochemical behaviour of the fabricated LIG. The present investigation provides an initial technical assessment of the potential influence of laser focus position. A comprehensive investigation involving systematic variation of the Z-offset together with detailed structural and electrochemical characterization, is currently being conducted within our research group and therefore lies beyond the scope of this thesis. It should be noted that intentional adjustment of the Z-offset was performed exclusively for the preliminary investigation described in this section. Unless otherwise stated, all LIG electrodes employed throughout the optimization studies, surface engineering investigations and electrochemical sensing experiments presented in this thesis were fabricated using the standard focal position of the laser system (Z = 0), which is considered as default position.

4.3.2 Fabrication of cellulose-derived LIG

Cellulose derived, Whatman No. 40 cellulose filter paper was selected as the precursor substrate, as it does not contains any chemicals and interfering agents. Prior to laser processing, the paper substrates were treated with a Burn Block FR using an ultrasonic spray-coating system to improve thermal stability during laser irradiation and minimize excessive combustion of the cellulose matrix. The treated paper was subsequently dried and secured onto a glass support substrate to ensure dimensional stability and consistent focal positioning throughout the laser fabrication process. A 5mm × 5mm square test patterns were fabricated to rapidly evaluate the influence of processing conditions on graphitic structure formation and substrate integrity. To identify suitable processing conditions for graphene formation while preserving substrate integrity, a range of laser parameters was systematically investigated, including laser power, scanning speed, pulse interval and laser scribing mode.

The effects of these parameters on carbonization, graphitization, pattern integrity and electrical conductivity were evaluated. The resulting laser-treated structures were initially assessed through visual inspection and resistance measurements, followed by structural characterization using Raman spectroscopy. Graphitization window for processing parameters enabled the fabrication of stable and electrically conductive paper-based LIG structures suitable for further physicochemical and electrochemical investigations.

4.3.3 Preliminary fabrication of PTFE-derived laser-induced carbon structures

The Teflon sheets were secured onto the flat glass platform and subjected to laser irradiation under various processing conditions. To investigate the feasibility of graphene formation on fluoropolymer substrates, a systematic optimization study was conducted by varying laser power, scanning speed, interval and scribing mode. The objective was to identify processing conditions capable of inducing localized carbonization and graphitization while maintaining the structural integrity of the substrate. 5 mm × 5 mm square test patterns were fabricated to rapidly assess the influence of individual processing parameters on laser-induced transformation of the PTFE substrate. The resulting laser-treated regions were initially evaluated through visual inspection, focusing on pattern continuity, surface appearance, substrate damage and evidence of graphitization. Following laser processing, the fabricated samples were visually inspected to assess the

continuity and macroscopic appearance of the laser-written structures. Selected samples were subsequently characterized using optical microscopy and SEM to evaluate their morphology. Preliminary Raman spectroscopy and electrical resistance measurements were also performed to assess graphitic structure formation and electrical behaviour.

As this investigation represents an exploratory extension of the fabrication methodology, comprehensive structural, chemical, electrical and electrochemical characterization of the PTFE-derived laser-induced carbon structures remains beyond the scope of the present dissertation. The experimental methodology established in this section provides the foundation for the preliminary investigations presented in Chapter 6 and for ongoing optimization studies aimed at evaluating the feasibility of developing fluorine-containing laser-derived carbon materials.

4.3.4 PEGDA-assisted transfer of LIG (LIGT)

Preliminary investigations were performed to evaluate the feasibility of transferring LIG (LIG) from rigid polyimide substrates onto flexible PEGDA hydrogel supports, a PEGDA-assisted transfer strategy was developed. The objective of this exploratory study was to establish an initial transfer methodology and assess whether the structural integrity of the laser-written graphene network could be preserved following substrate removal.

4.3.4.1 Preparation of PEGDA formulations and transfer procedure

PEGDA precursors with different molecular weights (PEGDA-250, PEGDA-550 and PEGDA-700) were selected to evaluate the influence of polymer chain length on transfer efficiency, mechanical integrity and preservation of the graphene architecture. The photopolymerizable precursor solution was prepared by mixing PEGDA with the photoinitiator TPO. Various PEGDA ratios and UV curing times were systematically investigated.

Optimized polyimide-derived LIG fabricated according to section served as the parent substrate for all transfer experiments. The resulting precursor solution was deposited onto the surface of the this electrode. Then it is allowed to uniformly infiltrate the porous graphene network. Following deposition, the samples were exposed to ultraviolet (UV) irradiation to initiate photopolymerization and form a crosslinked PEGDA matrix. After complete curing, the polymerized PEGDA film was carefully peeled off manually from the substrate.

The transferred samples obtained from parent LIG after peeling was designated as LIG Transfer (LIGT). The transfer continuity and structural preservation of transferred structures were initially assessed by visually inspection. Out of different samples, a candidate who yields more flexibility will be chosen for further studies.

4.3.4.2 Preliminary characterization

Transferred samples were examined using optical microscopy and SEM to evaluate the preservation of the porous LIG architecture following transfer. Preliminary electrical resistance measurements were also performed to assess conductive continuity after transfer. A systematic optimization for the transfer methodology is required before comprehensive physicochemical and electrochemical characterization can be performed.

4.3.4.3 Proposed experimental design for future optimization

Subsequently, optimization matrices were constructed to investigate the combined influence of TPO concentration and UV curing time on transfer quality. Transfer performance was evaluated using the Transfer Quality Score (TQS) developed in this work. The scoring system provides a qualitative assessment of transfer efficiency based on the continuity and integrity of the transferred LIG structure following separation from the parent substrate. The proposed TQS ranges from 0 to 5 and provides a qualitative classification of the structural integrity of the transferred LIG following separation from the parent substrate. A score of 0 corresponds to unsuccessful transfer, where the LIG either remains completely on the Kapton substrate or detaches without forming a recognizable pattern on the PEGDA support, indicating the absence of effective mechanical anchoring. A score of 1 represents very poor transfer, characterized by less than 25% pattern retention accompanied by severe cracking or fragmentation, suggesting insufficient polymer infiltration and/or crosslinking. A score of 2 indicates poor transfer, with approximately 25-50% of the pattern transferred together with discontinuous features and significant delamination, reflecting only partial mechanical integration. A score of 3 corresponds to moderate transfer, where approximately 50-75% of the LIG pattern is preserved despite localized defects or missing regions, demonstrating that transfer is feasible but requires further optimization. A score of 4 represents good transfer, with more than 75% of the pattern successfully transferred and only minor edge defects or isolated cracks, indicating effective preservation of the LIG architecture. Finally, a score of 5 corresponds to excellent transfer, characterized by nearly complete (>95%) preservation of the LIG pattern with negligible defects and excellent peel integrity, demonstrating successful transfer while maintaining the macroscopic LIG structure.

The preliminary investigations presented in this dissertation demonstrate the feasibility of PEGDA-assisted transfer of LIG and establish the experimental foundation for systematic optimization and comprehensive physicochemical, electrical and electrochemical evaluation in future studies.

4.4 Research methodology - surface engineering protocols

Following fabrication of the optimized LIG electrodes, the surface engineering strategies were employed to tune the physicochemical, electrochemical, catalytic and biological properties of the electrode interface. Surface modification protocols were developed according to the specific objective of each investigation and included hydrogel coating, catalytic nanozyme electrodeposition, electropolymerization of multifunctional copolymers and enzyme immobilization. Depending on the experimental objective, these modification strategies were applied individually or sequentially to produce multifunctional electrochemical interfaces for subsequent physicochemical characterization and electroanalytical evaluation.

4.4.1 Development of hydrogel membrane (HM) coated LIG electrodes

Aqueous CS solution (1 wt.%) was prepared by dissolving CS in an aqueous solution of acetic acid by rigorous mixing for 5 h. 2 µL of the CS solution was dispensed over the WE and allowed to dry under ambient conditions. After that, 2 µL of the aqueous solution of glutaraldehyde (3 wt.%) was dispersed on the electrode surface for a few hours to crosslink CS. Before electrochemical measurements, the electrodes were washed 3 times with deionized water to remove impurities. Alg was dissolved in DI water by rigorous mixing for 5 h. 2µL of solution drop-casted on to the electrode surface. After drying, 2 µL of 100mM $CaCl_2$ aqueous solution

was drop-casted for crosslinking. Agar was dissolved in hot water by maintaining a temperature of 90 °C under stirring to obtain a transparent solution. 2 µL of this solution was dispersed over WE. No crosslinking agent is used for agarose, because this non-ionic PSA undergoes physical crosslinking via multiple hydrogen bonding interactions.

The electrochemical properties of the hydrogel-modified electrodes were evaluated using 5mM of $K_3[Fe(CN)_6]$ and $K_4[Fe(CN)_6]$ in 10mM PBS electrolyte containing as the redox probes. The PBS solution was prepared by dissolving one commercially available PBS tablet in 200 mL of deionized water according to the manufacturer's instructions. EIS measurements were done at open circuit potential (OCP) conditions, using perturbation peak-to-peak amplitude 10 mV and frequencies from 100 kHz to 100 mHz, 12 points per decade, after 5 min initial conditioning. CV measurements were carried over potential window of -0.2 to 1.0 V, vs Ag/AgCl at scan rates from 10 to 1000 mV/s. CA tests were performed at applied voltages of +300 mV, +400 mV and +500 mV and 100 µL of 10mM PBS solution containing 5mM $Fe(CN)_6^{4-}$ redox probe was used for CA experiments for 2 minutes.

4.4.2 Electrodeposition of nanomaterials - Ir and Pt decorated LIGs

The Ir and/or Pt nanoparticles were electrodeposited on to the optimized P19%S220mm/s LIG electrode surface. Separate precursor solutions were prepared by dissolving 2mM H_2PtCl_6 and 2mM $IrCl_3$ in 0.5 M HCl for electrodeposition of Pt and Ir on LIG structures respectively. Fresh precursor solutions were prepared prior to each deposition experiment. Prior to electrodeposition, 50 µL of the corresponding precursor solution was drop-cast onto the electrode surface and allowed to remain on the surface for 5 min to facilitate infiltration into the porous LIG structure. Electrodeposition was subsequently carried out using CP at constant applied currents of 50, 100 and 150 µA for deposition times of 5 and 10 min. Monometallic electrodes were prepared by electrodeposition of either Ir or Pt individually and are designated as Ir(current, time) and Pt(current, time), respectively. Ir-decorated LIG (Ir@LIG), Pt-decorated LIG (Pt@LIG) and co-deposited bimetallic Ir-Pt coated LIG electrodes were prepared to study their properties.

To fabricate bimetallic Ir-Pt@LIG, Ir was first electrodeposited onto the LIG surface, followed by rinsing and subsequent electrodeposition of Pt nanoparticles. The resulting electrodes are denoted as Ir-Pt (applied current in µA, deposition time in min) and the optimized bimetallic electrode selected designated as (Ir-Pt@LIG).

The theoretical metal loading was estimated from the total charge passed during CP deposition using Faraday's law. The delivered charge (q) is defined as the product of applied current and deposition time (q=It). Assuming 100% current (Faradaic) efficiency, the theoretical metal loading was estimated using Faraday's law,$m = \frac{QM}{nF}$ (where M is the molar mass of the metal, n is the number of electrons involved in the reduction process and F is the Faraday constant). Based on the calculated charge, the theoretical metal loading was estimated for each deposition condition. These values represent nominal deposited masses calculated assuming 100% current efficiency and were used only to compare the electrodeposition conditions. The Electrochemical characterization of the modified electrodes was subsequently performed. The estimation of EASA using a modified Randles-Ševčík equation and the k^0 calculated using the Nicholson method[1].

4.4.3 Electropolymerization of APTAC and SBMA

Electropolymerization was employed to fabricate multifunctional copolymer films directly on the optimized LIG electrodes. The individual monomer coatings prepared on bare and metal nanoparticle-decorated LIG electrodes. A 20mM aqueous solution of SBMA or a 5mM solution of APTAC in 0.1 M Na_2SO_4 (supporting electrolyte) was used as the precursor electrolyte. For copolymer formation, equal volume of precursor solutions of SBMA and APTAC were mixed in a single precursor solution prior to electropolymerization to produce a copolymer coating in which both monomers were polymerized simultaneously during a single CV deposition process.

For comparison, SBMA and APTAC were also electropolymerized individually on bare LIG to produce polySBMA and polyAPTAC coatings, respectively. These electrodes served as control samples, whereas the mixed precursor solution was electropolymerized to form poly(APTAC-co-SBMA). The same copolymerization procedures were subsequently applied to metal nanoparticle-decorated LIG electrodes. To initiate the electropolymerization of SBMA, 0.2mM APS was added to the SBMA-containing electrolyte as a redox initiator. Before electropolymerization, a 50 µL droplet was drop-cast onto the LIG surface and allowed to rest for 5 min. Then CV was performed. Polymer growth was achieved by repeatedly cycling the electrode potential between -0.2 and +1.2 V (vs. Ag/AgCl) for 50 cycles. Then, the modified electrodes were washed with distilled water and dried under argon flow. The copolymer (or poly(APTAC-co-SBMA)) was labelled as CoP@LIG when deposited on bare optimized LIG. If deposited on Ir-Pt-decorated LIG electrodes, it was named as Ir-Pt-CoP@LIG.

4.4.4 GOx immobilization

The electropolymerized copolymer-modified electrodes were subsequently functionalized with glucose oxidase (GOx) to construct enzymatic electroanalytical platforms. GOx was immobilized onto the modified electrode surface by electropolymerization within the multifunctional copolymer matrix, followed by chemical stabilization using glutaraldehyde. For GOx incorporation, 0.5 mg of GOx dissolved in a mixture containing 50 µL of SBMA and 50 µL of APTAC precursor solutions in 0.1 M Na_2SO_4, resulting in final monomer concentrations of 10mM SBMA and 2.5mM APTAC. A 50 µL droplet out of this solution was drop-cast onto the Ir-Pt@LIG surface and allowed to rest for 5 min prior to CV at a scan rate of 50 mV/s for 50 cycles within a potential range of -0.2 to 1.2 V vs. Ag/AgCl. The resulting electrode was denoted as Ir-Pt-CoP-GOx@LIG. The electrodes without GOx entrapment are also prepared and are designate as Ir-Pt-CoP@LIG.

For the fabrication of CS-coated Ir-Pt@LIG electrode (named Ir-Pt-CS-GOx@LIG) 2 µL of GOx solution (20 mg/mL in 10mM PBS, pH 7.4) mixed with CS was drop-cast onto the Ir-Pt@LIG surface and incubated at 4 °C for 2 h and after drying followed by crosslinking using 3 wt.% aqueous glutaraldehyde solution. In order to avoid rapid evaporation, the electrode was placed in a sealed Petri dish. Before sealing, several water droplets were added to the Petri dish to saturate the environment with water vapor. After drying, the electrodes were stored in a freezer before using them. In order to investigate the effect of crosslinking, comparison between normal crosslinked CS-LIG uncrosslinked (CS without glutaraldehyde treatment, double-crosslinked CS (two time glutaraldehyde application after drying), triple-crosslinked CS (three time glutaraldehyde application after drying).

4.4.5 Physicochemical characterization

The electrical resistance of LIGs and the modified LIGs was measured using a four-point probe equipped with a Keithley 2400, UK. SEM analysis was conducted using a Quanta 250 FEG microscope (ThermoFisher Scientific) equipped with a Schottky field emission gun. The microscope operated at an accelerating voltage of 30 kV. SEM analysis was performed to investigate the porous morphology of bare LIG, hydrogel-coated electrodes, nanozyme-modified surfaces, electropolymerized copolymer films and PEGDA-transferred LIG structures. Depending on the experiment, SEM observations were used to evaluate changes in pore morphology, nanoparticle distribution, polymer coverage and structural preservation following surface engineering.

TEM was performed using a FEI Tecnai G20 microscope operating at 200 kV in a scanning mode using a high-angle annular dark-field detector (HAADF-STEM) or in a high-resolution TEM mode (HRTEM). Specimens for TEM observation were prepared by scratching LIG electrodes decorated with Ir, Pt and Ir-Pt nanoparticles, then preparing a solution of the scratch powder in tetrahydrofuran. The resulting solution was deposited on copper grids covered with amorphous carbon foil.

Raman spectroscopy measurements were conducted using an Xplora system (HORIBA). XPS analyses were carried out using Escalab 250Xi (ThermoFisher Scientific) multi-spectroscope, operating an AlKα x-ray source with a spot diameter of 650 μm. The pass energy for the high-resolution scans was 20 eV. Low-energy electron and Ar+ ions bombardment was used for charge compensation, with a final peak calibration using adventitious carbon C1s at 284.6 eV. The deconvolution was carried out using Avantage 5.9931 software Fourier transform infrared (FTIR) spectra were recorded using a PerkinElmer Frontier FT-IR/FIR spectrometer.

Static water contact angle measurements were performed to evaluate changes in the surface wettability of LIG following fabrication and surface engineering. A DSA100 goniometer (Kruss, Germany), at room temperature, with 2 μL drops of water applied. The contact angle was recorded with a CCD camera and the average value of the wetting angle was determined using ADVANCE software, with the Young-Laplace method. Each measurement was repeated 20 times. A sessile water droplet was deposited onto the electrode surface and the contact angle was measured using the instrument described previously. The obtained values were used to compare changes in surface hydrophilicity and hydrophobicity resulting from different fabrication parameters and surface modification strategies.

4.4.6 Electrochemical evaluation and electroanalytical validation

Electrochemical studies were carried out on Biologic VSP-300 potentiostat/galvanostat. The solution of 10mM PBS containing 5mM of $K_3[Fe(CN)_6]$ and $K_4[Fe(CN)_6]$ used as the redox probes. A three-electrode setup, with LIG as both the working electrode (WE, A = 0.085 cm^2) and CE and silver/silver chloride (Ag/AgCl) as reference electrode (RE), was used. All measurements were performed under ambient conditions (22 °C). For electrochemical procedures, the electrolyte droplet was applied, completely covering both the WE (3mm diameter) and CE and a thin layer of nail polish/ glue ring was used to prevent spillage. CV was employed as the primary electrochemical technique for evaluating the electrochemical behaviour of the fabricated electrodes. Depending on the objective of each experiment, CV measurements were performed over the appropriate potential window at scan rates ranging from 10 to 1000 mV/s. The resulting

voltammograms were subsequently used for evaluation of electrochemical activity, EASA and k^0. EIS measurements were performed at the open-circuit potential using a sinusoidal perturbation amplitude of 10 mV over the frequency range from 100 kHz to 100 mHz, with 12 points per decade following an initial conditioning period of 5 min. The impedance spectra were used to investigate interfacial charge transfer behaviour following fabrication and surface engineering. CA measurements were performed at selected applied potentials depending on the electroanalytical application under investigation. The technique was employed to evaluate catalytic activity, operational stability, biofouling behaviour and electroanalytical performance through continuous monitoring of the current response following successive additions of the target analyte. CP was employed for electrodeposition of catalytic nanoparticles under galvanostatic conditions. The technique was additionally used where appropriate to investigate the electrochemical behaviour of the fabricated interfaces.

The electroanalytical performance of the fabricated and surface-engineered electrodes was evaluated using H_2O_2 and enzymatic glucose as model analytes. The electrocatalytic activity of the fabricated electrodes toward H_2O_2 oxidation was evaluated using CV and CA. Calibration curves for different concentrations were subsequently constructed by plotting the steady-state current against H_2O_2 concentration. The analytical performance of the fabricated electrodes was evaluated in terms of sensitivity, linear response range and limit of detection.

The electrochemical performance of the GOx-functionalized electrodes toward glucose detection was evaluated by CA. CA measurements were carried out at the selected applied potential while successive additions of glucose. The resulting steady-state current responses were used to construct calibration curves and evaluate the analytical characteristics of the fabricated electrochemical interfaces. Analytical performance was assessed in terms of sensitivity, linear range, limit of detection, repeatability and operational stability. These proof-of-concept studies were employed to validate the effectiveness of the developed interface-engineering strategies and to investigate their influence on analytical sensitivity, electron-transfer behaviour, operational stability and analytical selectivity.

4.4.6.1 Interference and operational stability

The selectivity of the developed platform was evaluated by CA in the presence of 1mM solution of commonly occurring electroactive interferents like dopamine, ascorbic acid, paracetamol, cysteine, cysteamine, fructose. Solutions containing glucose together with the 1mM of selected interfering agents dopamine, ascorbic acid, cysteine, cysteamine, paracetamol, fructose were prepared in 10mM PBS and the chronoamperometric response was recorded under identical experimental conditions at applied potential of +0.3V and +0.6V vs. Ag/AgCl . The influence of the interfering species on the glucose response was subsequently evaluated by comparing the current responses with those obtained for glucose alone.

The operational stability of Ir-Pt modified and copolymer modified electrodes were evaluated by recording the H_2O_2 and glucose response once per day over a 13-day period using the same electrode at an applied potential of +0.6V vs. Ag/AgCl. Ir-Pt-CS-GOx modified electrode is also measured and considered as a control. After each measurement, the electrodes were rinsed with PBS and stored in a freezer until the following day.

4.4.6.2 Practical applicability under physiologically relevant conditions - Artificial sweat test

Artificial sweat was prepared according to a modified EN1811:2012 protocol[277]. The prepared artificial sweat was used as the electrolyte matrix to evaluate the practical applicability of the developed glucose biosensor under physiologically relevant conditions. The solution contained 0.5 wt% NaCl, 0.1 wt% KCl, 0.1 wt% urea and 2.0mM D-lactate dissolved in DI water. The pH was adjusted to 6 using 0.1 M HCl solution. In parallel, a 100mM glucose stock solution was prepared in DI water. Glucose-spiked artificial sweat samples were prepared by adding appropriate volumes of the glucose stock solution to the artificial sweat matrix to obtain final glucose concentrations of 0.5, 1, 2, 3, 4, 5, 7.5 and 10mM. Measurements were conducted at an applied potential of 0.6 V (vs. Ag/AgCl) in different pH environment. The recorded current responses were plotted as a function of glucose concentration.

4.4.7 Evaluation of antifouling and antibacterial functionalities

The antifouling performance of the developed final electropolymerized copolymer interface was indirectly evaluated using BSA as a model protein fouling agent[278]. The electrodes were directly incubated in a solution containing 1mM glucose and 1% (w/v) BSA, which acted as a functional probe to evaluate protein fouling. CA measurements were performed both in the presence and absence of BSA at different applied potentials of +0.3, +0.4, +0.5 and +0.6 V vs. Ag/AgCl. The current response was recorded for 2 min at 30 min intervals over a total incubation period of 4 h. After each measurement, the electrodes were stored in a freezer until the following measurements. The responses were monitored as a function of incubation time to assess resistance to protein-induced surface fouling. Identical measurements were carried out in BSA-free glucose electrolyte under identical conditions to serve as controls. This comparative protocol accounts for the effect of protein adsorption and the antifouling behaviour imparted by the polymer-modified LIG interface.

The antibacterial activity of the modified electrodes was assessed against gram-negative *E. coli* K12 and gram-positive methicillin-resistant Staphylococcus aureus (MRSA) ATCC®43300 strains according to the protocol by Swebocki et al[279]. Overnight bacterial cultures were diluted to an OD600 of ~0.1 and further diluted to a bacterial concentration of ~106 CFU/mL. That obtained suspension was then added to a microtiter plate in the presence of serially diluted samples. After overnight incubation at 37 °C, the plate was read using a Sunrise microplate reader (Tecan). The data obtained was then plotted (n=3). To determine the minimum inhibitory concentration (MIC), a modified Gompertz model was used where possible.

4.4.8 Data processing and electrochemical calculations

The electrochemical parameters reported throughout this dissertation were calculated using established electrochemical models and analytical methods. Unless otherwise stated, all data processing and statistical analysis were performed using OriginPro, EC-Lab and Microsoft Excel. Accordingly, established theoretical models, numerical fitting procedures and electrochemical equations were employed to determine diffusion coefficients, EASA, heterogeneous electron-transfer kinetics, theoretical metal loading and analytical performance parameters.

4.4.8.1 Chronoamperometric modelling

CA measurements were employed throughout this dissertation to investigate diffusion-controlled mass transport, catalytic activity and electroanalytical performance of the fabricated electrochemical interfaces. Current-time transients were recorded following the application of a constant potential under quiescent conditions. Depending on the specific experiment, CA was performed either in ferri/ferrocyanide electrolyte for diffusion studies or in analyte-containing electrolyte for electroanalytical measurements.

For diffusion coefficient (D) determination, chronoamperometric responses were acquired using the ferri/ferrocyanide redox couple under diffusion-controlled conditions. These experimental current transients formed the basis for the subsequent quantitative modelling described in the following sections. The measured current contains contributions from diffusion, electron-transfer kinetics, capacitive charging and background currents, mathematical modelling was required to distinguish the contribution of each process. For reversible electrochemical systems, diffusion-controlled current can be described using the Cottrell equation as shown in Equation (1):

$$I_F(t) = \frac{nFAC\sqrt{D}}{\sqrt{\pi t}} \quad (1)$$

where n is the number of transferred electrons, F is Faraday's constant, A is electrode surface area, C is concentration of electroactive species and D is the diffusion coefficient.

Although the Cottrell equation provides a useful description of diffusion-controlled processes, the measured current depends simultaneously on the product A*C*√D. Therefore, changes in current cannot distinguish whether observed differences arise from variations in diffusion coefficient, electroactive surface area, or local analyte concentration.

To overcome this limitation, a modified Delahay model was employed. Unlike the Cottrell equation, the Delahay formulation incorporates the heterogeneous electron-transfer rate constant and allows independent estimation of diffusion and kinetic parameters through non-linear fitting of chronoamperometric transients.

Moreover, in the case of irreversible process the Cottrell equation is not valid. Instead, Delahay equation can be used to describe the faradaic current is shown below as Equation (2):

$$I_F(t) = nFACk \times \exp\left(\frac{k^2}{D}t\right) \times erfc\left(\frac{k}{\sqrt{D}}t\right) \quad (2)$$

where k is in principle independent of the electrode potential and concentration. It is to be noted that the prefactor is now linked to the product A*C*k. Additionally, it is worth mentioning that the measured current consists of the sum of capacitive, faradaic and residual currents, thus the final equation describing the total current in the CA experiment can be given as Equation (3):

$$I_{total}(t) = nFACk \times \exp\left(\frac{k^2}{D}t\right) \times erfc\left(\frac{k}{\sqrt{D}}t\right) + I_c \times exp\left(\frac{-t}{\tau}\right) + I_s \quad (3)$$

It is to be noted that further modifications of this expression can be required for some systems. Nevertheless, this model was sufficient to describe the CA responses presented in this work.

By non-linear least squares fitting using e.g. Levenberg – Marquardt algorithm one can obtain the following constants show in Equation (4):

$$A' = nFACk$$
$$B' = \frac{k}{\sqrt{D}} \quad (4)$$

which can subsequently be used to determine diffusion coefficients, heterogeneous electron-transfer rate constants and electroactive surface areas.

The major advantage of this approach is that diffusion effects can be separated from surface-area effects. Consequently, changes in electrochemical response can be attributed to specific physicochemical phenomena and not being inferred solely from peak-current variations. This led to various assumptions and thus an experimental strategy developed according to that assumptions. The EASA of the commercial screen-printed carbon electrode (SPCE) was assumed to be equal to its geometric area because of its relatively smooth and non-porous surface. Hydrogel deposition on SPCE was assumed not to alter the intrinsic electron-transfer characteristics of the underlying carbon electrode. Consequently, changes observed following hydrogel deposition were attributed primarily to modifications in diffusion and partitioning phenomena.

Diffusion coefficients (D) determined for hydrogel-coated SPCEs were assumed to represent the intrinsic transport characteristics of the corresponding hydrogel matrices when subsequently deposited on porous LIG electrodes. The diffusion environment surrounding bare SPCE and bare LIG electrodes was assumed to be identical because neither contained a hydrogel layer.

Partitioning effects occurring within bare LIG pores were assumed to be negligible compared with the stronger partitioning phenomena expected within hydrogel networks.

Prior to application of the proposed fitting methodology to hydrogel-modified electrodes, the analytical procedure was validated using the well-established ferri/ferrocyanide redox couple in 0.1 M KCl. Potassium chloride was selected because the diffusion coefficient of ferri/ferrocyanide ions in this electrolyte is well documented in the literature, thereby providing an appropriate reference system for evaluating the reliability of the fitting procedure. CA measurements were first performed using commercially available SPCEs possessing a well-defined and reproducible geometric area. The experimentally determined diffusion coefficient was subsequently compared with literature values to verify the validity of the analytical methodology before its application to hydrogel-modified systems.

4.4.8.2 Determination of EASA

EASA of the fabricated electrodes was determined from CV measurements using the reversible ferri/ferrocyanide redox couple. Since the electrochemical response of porous LIG is governed by the electrochemically accessible surface in preference to its geometric dimensions, determination of EASA provides a more representative parameter for evaluating the influence of laser fabrication and subsequent surface engineering on the active electrode interface.

CV were recorded at different scan rates in 10mM PBS containing Fe probe, 5mM $K_3[Fe(CN)_6]/K_4[Fe(CN)_6]$. The anodic peak current obtained at each scan rate was plotted against the square root of the scan rate ($v^{1/2}$). The calculation of EASA according to the modified Randles-Ševčík Equation (5):

$$i_{(a,p)} = (2{,}99 \cdot 10^5)\alpha^{(1/2)}ACD^{(1/2)}\upsilon^{(1/2)} \quad (5)$$

where $i_{(a,p)}$ denotes the anodic peak current , υ denotes the CV scan rate, α is the charge transfer symmetry factor (assumed to be 0.5) and D represents the diffusion coefficient. The Randles-Ševčík plots for the bare

and metal-coated LIG electrodes have CV recorded at different scan rates (200, 150, 100, 80, 60, 40, 20) for the selected samples.

4.4.8.3 Heterogeneous electron transfer rate constant (k^0)

The k^0 was determined to quantitatively evaluate the electron-transfer characteristics of the fabricated LIG interfaces. The k^0 offers a quantitative measure of the intrinsic kinetics governing electron exchange between the electrode surface and the electroactive species. The heterogeneous electron-transfer rate constant was estimated from CV using the Nicholson method, which correlates the peak-to-peak potential separation (ΔEp) with the electron-transfer kinetics of a quasi-reversible electrochemical system. CV were recorded at different scan rates in 10mM PBS containing 5mM potassium ferri/ferrocyanide as the reversible redox probe.

4.4.8.4 Charge transfer resistance (R_{ct})

The R_{ct} represents the resistance associated with electron transfer across the electrode-electrolyte interface. The R_{ct} was determined from EIS by fitting the experimental impedance spectra using an equivalent electrical circuit model implemented in EC-Lab software. Impedance measurements were performed under open-circuit potential (OCP) conditions using a sinusoidal perturbation amplitude of 10 mV over a frequency range from 100 kHz to 100 mHz, with 12 points per decade following an initial equilibration period of 5 min. Unless otherwise specified, measurements were conducted in 10mM PBS containing 5mM $K_3[Fe(CN)_6]/K_4[Fe(CN)_6]$ as the reversible redox probe.

4.4.8.5 Electroanalytical performance calculations

The analytical performance of the developed electrochemical platforms was evaluated in terms of sensitivity, linear response range and limit of detection (LOD) using calibration curves obtained from CA measurements. Calibration curves were constructed by plotting the steady-state current response against the corresponding analyte concentration and linear fit performed.

Sensitivity was determined from the slope of the corresponding calibration curve. The linear detection range was defined as the concentration interval over which the calibration curve exhibited a significant linear relationship between analyte concentration and electrochemical response. The lower and upper limits of the linear range were established from the experimental calibration data and confirmed by the corresponding coefficient of determination (R^2) obtained from linear fit analysis. The limit of detection (LOD) was calculated according to Equation (6):

$$LOD = \frac{3\sigma}{S} \quad (6)$$

Where σ is the standard deviation of the blank response and S is the slope of the calibration curve.

The calculated LOD represents the lowest analyte concentration that can be reliably distinguished from the background signal under the experimental conditions employed in this dissertation.

CHAPTER 5 - RESULTS AND DISCUSSION

5.1 Fundamentals of LIG formation and performance evolution (results from[280,281])

The objective of this chapter is to establish the fundamental relationships between laser processing conditions, graphitization, morphology development, electrical conductivity and electrochemical performance of LIG. Additionally, this chapter aims to develop a mechanistic understanding of how laser-material interactions govern the formation of electrochemically active graphene architectures.

5.1.1 The influence of lasing parameters and effect of thickness of Kapton foil (results from[280,281])

The successful formation of LIG strongly depends on the energy delivered to the PI substrate during laser irradiation. Because the laser energy density is governed primarily by laser power and scanning speed, systematic optimization of these parameters was performed to identify the processing window that enables stable graphitization while avoiding substrate damage. Even though both 50 μm and 100 μm Kapton substrates exhibited successful LIG formation, graphitization was achieved only within specific combinations of laser power and scanning speed, indicating that each substrate thickness possesses a distinct but limited processing window.

The optimization matrices were constructed for 50 μm and 100 μm Kapton substrates demonstrated that successful LIG formation occurs only within a specific processing window as shown in Figure 13. Three distinct processing regions can be identified, corresponding to insufficient, optimal and excessive energy delivery. At insufficient laser fluence, incomplete carbonization was observed, resulting in discontinuous conductive structures. Conversely, excessive laser fluence resulted in delamination, substrate burning and hole formation due to excessive thermal stress. The existence of an optimal processing region highlights the importance of balancing graphitization and substrate integrity during LIG fabrication. At low laser powers or excessively high scanning speeds, insufficient thermal energy is generated to induce complete carbonization of the polyimide substrate. Under these conditions, incomplete graphitization occurs and discontinuous carbon structures are formed. The resulting electrodes exhibit poor conductivity and limited electrochemical activity.

As power increases or speed decreases, a transition region is observed in which graphitization becomes increasingly effective. Within this operating window, the thermal energy supplied to the substrate is sufficient to drive extensive carbonization and graphitization while maintaining structural integrity of the resulting carbon framework. The generated LIG structures exhibit uniform morphology, high conductivity and robust mechanical stability. Further increases in laser energy density result in excessive localized heating. Under these conditions, thermal stresses generated during rapid gas evolution promote delamination of the carbonized layer from the underlying substrate. In extreme cases, complete burnout of the polyimide film occurs, producing holes and catastrophic failure of the electrode structure.

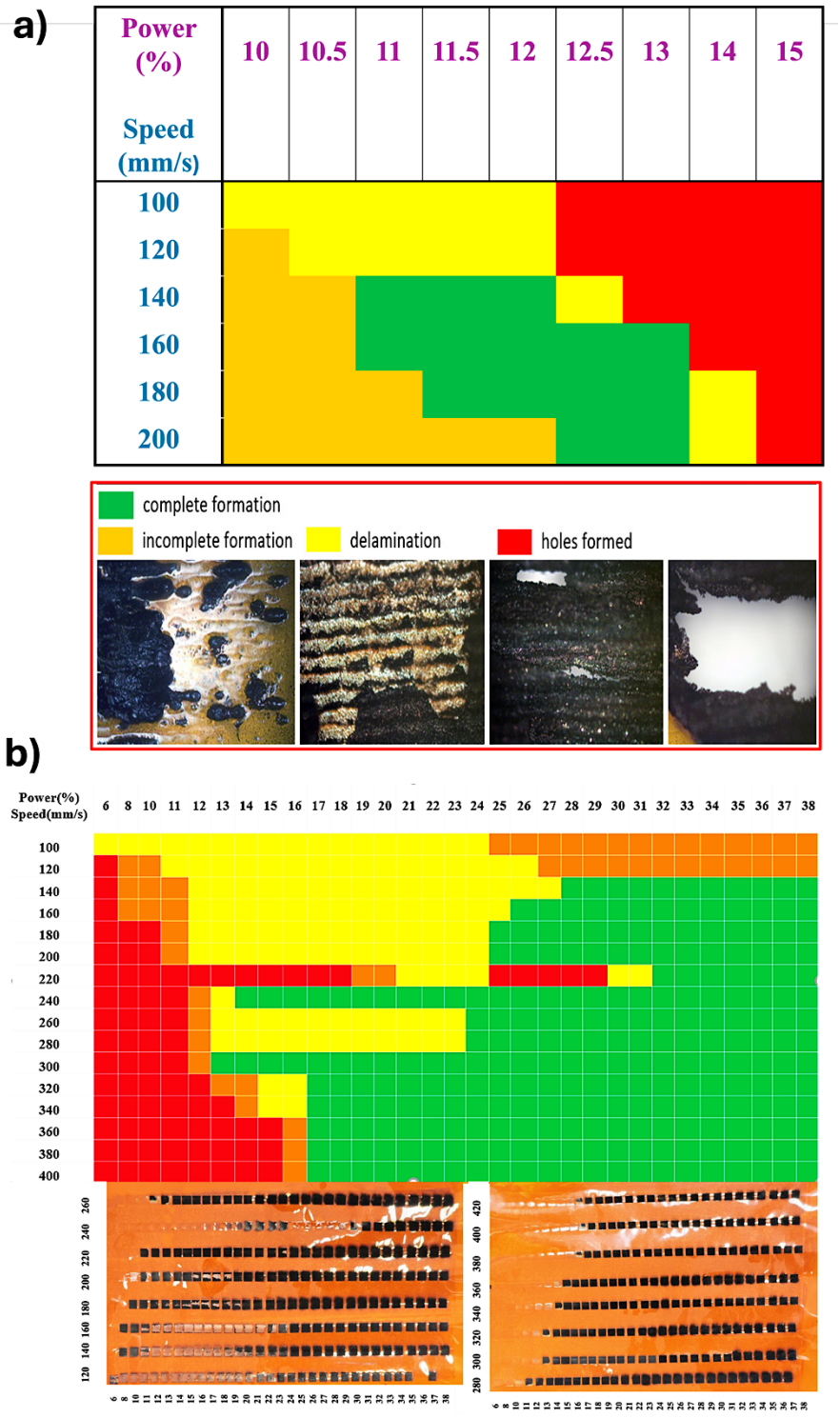


Figure 13: Optimization matrix of Kapton-LIG with representative photographs for LIG fabrication on 50 µm and 100 µm Kapton substrates, showing representative surface morphologies obtained under different combinations of laser power and scanning speed. The matrices identify the processing window for successful LIG formation together with the characteristic failure modes observed under insufficient and excessive energy input[280,281]**.**

The optimization matrix therefore illustrates the narrow balance required between insufficient and excessive laser energy. This behaviour highlights the importance of controlling laser fluence during fabrication. The

identified operating window served as the basis for all subsequent electrode preparation and characterization studies.

During laser irradiation, the PI substrate undergoes rapid pyrolysis, in which cleavage of C–O, C–N and C=O bonds is followed by the rearrangement of carbon atoms into interconnected sp^2-rich graphitic domains. Graphitization requires a minimum temperature threshold. Below this, carbonization remains incomplete resulting in poorly interconnected networks, whereas excessive temperatures promote structural degradation through ablation and material removal. Consequently, precise control of laser processing conditions is essential for producing reproducible LIG electrodes with consistent physicochemical properties.

The observed defects provide valuable insight into the physical mechanisms governing LIG formation. Incomplete graphitization indicates insufficient bond cleavage and carbon rearrangement, whereas delamination originates from internal stresses generated by rapid gas evolution during pyrolysis. Hole formation reflects localized overheating where material removal exceeds graphitization. Collectively, these observations demonstrate that LIG formation is governed by a delicate interplay between heat generation, polymer decomposition kinetics, gas evolution, carbon restructuring and heat dissipation.

Moreover, a comparison of the two polyimide substrate thicknesses further highlights the influence of thermal management during laser processing. Although both the 50 µm and 100 µm Kapton films exhibited a distinct processing window for successful LIG formation, the thicker 100 µm substrate demonstrated greater resistance to laser-induced thermal damage. As evident from both the optimization matrices and the representative optical photographs, complete perforation of the substrate was observed only for the 50 µm Kapton foil under excessive laser energy input, whereas the 100 µm foil predominantly exhibited delamination and partial formation (no formation) without hole formation.

This improved thermal tolerance can be attributed to the larger thermal mass of the 100 µm foil, which enhances heat dissipation and reduces localized overheating during laser irradiation. Additionally, the processing window for the 100 µm Kapton substrate is broader and more tolerant to variations in laser processing conditions than 50 µm foil.

Even though the comparative analysis of the two substrates provides insight into the role of heat transfer during laser irradiation and its impact on graphene formation, This potential graphitization window matrices is not alone sufficient to assess the quality of formed LIGs. Several LIG formed visually appeared uniform and continuous were produced under the conditions closer to the boundaries of optimal region, where the degree of graphitization, structural continuity and electrical conductivity can vary significantly without being detectable by visual assessment.

Therefore the next section addresses the morphological characteristics of LIGs formed. A detailed investigation of the surface architecture is required to establish the relationship between laser processing conditions and electrochemical activity. Therefore, the following section focuses on the morphological characterization of bare LIG using SEM, providing insight into the pore development, graphene connectivity and hierarchical microstructure responsible for the superior performance of the LIG.

5.1.2 Morphological characteristics of LIG (results from[280,281])

The morphology of LIG plays a fundamental role in determining its electrochemical behaviour. The rapid photothermal decomposition of PI involves simultaneous occurrence of carbonization, graphitization and gas release generates a highly porous three-dimensional architecture of LIG. Since morphology directly governs electrolyte accessibility, electrical connectivity and EASA, SEM characterization provides the first direct evidence linking fabrication conditions to electrochemical performance by establishing the relationship between laser processing conditions and the development of the porous graphene architecture.

Representative SEM micrographs revealed a three dimensional highly interconnected porous network composed of irregularly distributed pores and graphitic domains. The morphology exhibited a hierarchical pore distribution extending from the submicrometer to micrometer scale. Such morphology originates from rapid gas evolution during laser-induced pyrolysis, which expands the carbon matrix and generates a foam-like structure[8]. The observed porous structure is characteristic of LIG.

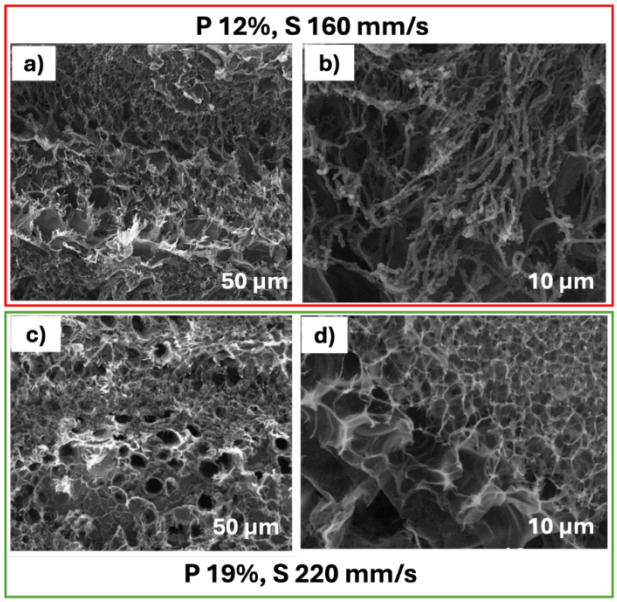


Figure 14: SEM images for LIG formed on substrate of different thickness. a),b) LIG fabricated on 50µm Kapton foil-P12%S160mm/s; and c), d) LIG formed on 100µm Kapton foil- P19%S220mm/s at different magnifications[280,281]**.**

At lower magnification, the LIG surface exhibited a continuous porous morphology extending throughout the irradiated region. The interconnected nature of the carbon framework suggests the formation of electrically conductive pathways across the electrode surface. Such connectivity is important for efficient charge transport during electrochemical measurements.

At higher magnification, additional structural features become evident. The surface contains numerous cavities, channels and edge-rich carbon domains that collectively increase the accessible surface area of the electrode. Laser irradiation generated foam like graphitic scaffold than forming a film. These structural features are particularly important because electrochemical reactions occur predominantly at accessible surface sites rather than within the bulk material. Consequently, the porous morphology contributes directly to the enhanced electroactive surface area observed for LIG electrodes.

The hierarchical porous morphology observed in both thicknesses with interconnected pores facilitate rapid penetration of electrolyte solutions throughout the electrode structure. The increased surface area provides a larger number of active sites available for electron-transfer reactions. The rough architecture offers abundant

locations for subsequent immobilization of hydrogels, conductive polymers, metallic nanostructures and biological recognition elements. Therefore, the observed morphology serves as an important structural foundation for the surface engineering strategies investigated in later chapters of this thesis.

Despite the difference in the substrate thicknesses, the 50µm and 100µm PI-LIGs exhibited well developed hierarchical porous structure. structurally continuous LIGs. Collectively, the SEM reveals both substrates successfully produce highly porous graphitic architecture capable of supporting efficient mass transport, enhanced charge transfer and subsequent functionalization processes. These morphological characteristics provide the structural basis for the physicochemical properties discussed in the following sections, including graphitic ordering, surface chemistry, wettability, electrical conductivity and electrochemical behaviour.

5.1.3 Structural and surface characterization of LIG (results from[280,281])

Although SEM clearly demonstrates the successful formation of the hierarchical porous graphene architecture, it cannot determine the degree of graphitization or distinguish between well-ordered graphitic domains and structurally defective carbon. Since the electrical and electrochemical properties of LIG depend strongly on its structural ordering, Raman spectroscopy was subsequently employed to evaluate the graphitic nature of the electrodes and to establish how laser processing parameters and substrate thickness influence the structural evolution of LIG, whereas XPS reveals the elemental composition and chemical bonding environment of the electrode surface. Together, these techniques enable correlation of the observations presented in this section. Comparative analyses were performed for electrodes fabricated on both 50µm and 100µm PI substrates in order to evaluate the influence of laser processing conditions and substrate thickness on the formation of graphitic carbon.

All the Raman spectra exhibited the characteristic D (~1350 cm^{-1}), G (~1580 cm^{-1}) and 2D (~2700 cm^{-1}) bands associated with graphene-derived materials. The D band originates from defect-activated breathing modes of six-membered carbon rings and reflects the presence of structural defects, edge-plane sites and lattice disorder generated during laser-induced graphitization. Conversely, the G band corresponds to the in-plane stretching vibration of sp^2-hybridized carbon atoms and is considered a characteristic signature of graphitic carbon. The presence of a distinct 2D band further confirms the formation of graphene-like domains within the laser-carbonized material.

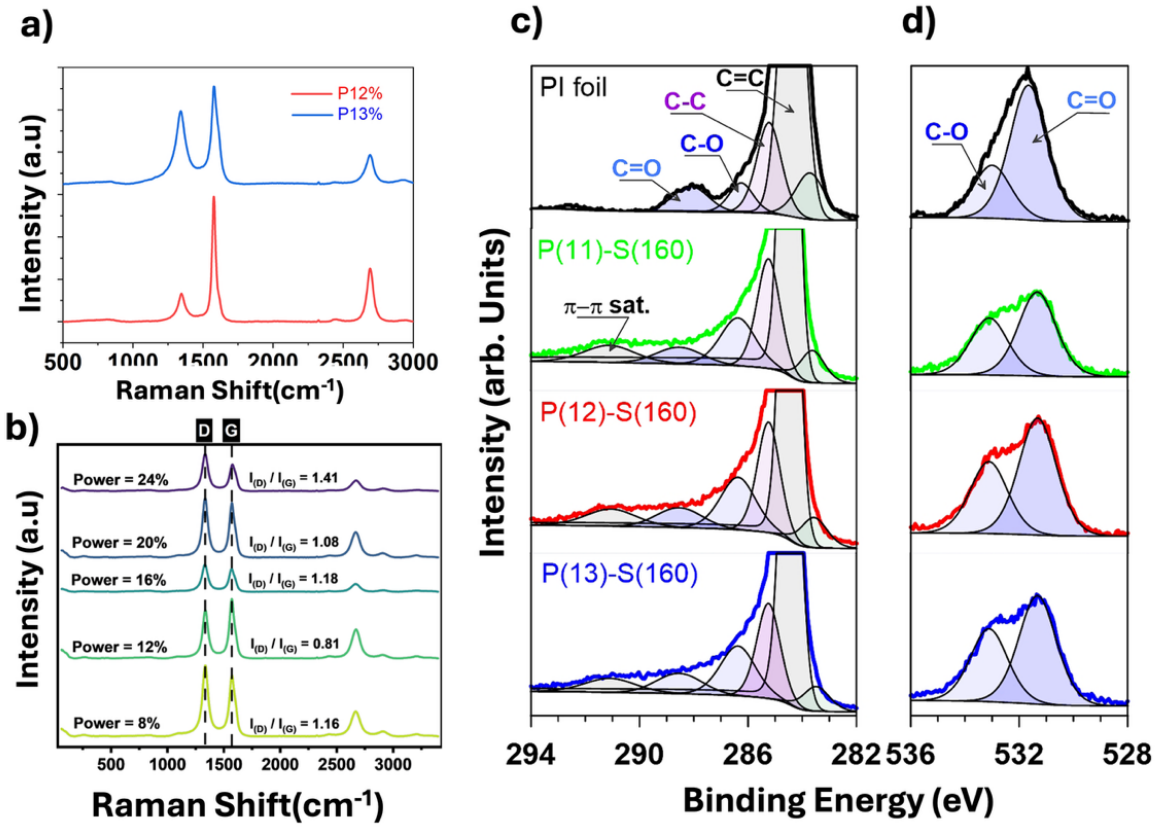


Figure 15: Structural and surface characterization of LIG. Raman spectra of LIG fabricated on (a) 50µm Kapton at P12%S160 and P13%S160 and (b) 100µm Kapton under different laser powers of 100µm thickness High-resolution XPS spectra of (c) C 1s and (d) O 1s regions for pristine Kapton and LIG fabricated on 50µm polyimide under different laser powers at a constant scanning speed of 160mm/s[280,281]**.**

For electrodes formed from 50µm PI- derived LIGs, A comparison between the P12% and P13% samples demonstrates that a relatively small increase in laser power substantially influences the structural quality of the resulting graphene. The higher I_D/I_G ratio observed for the P12% sample suggests a greater degree of graphitic ordering and a lower defect density compared with the P13% electrode.

The influence of laser processing was further investigated using the 100µm Kapton substrate. Similar to the thinner substrate, all investigated laser powers produced the characteristic D, G and 2D bands, confirming that laser-induced graphitization occurred over the entire range of investigated processing conditions. However, comparison of the spectra reveals that the degree of structural disorder varies with laser power. Although no simple linear relationship exists between the I_D/I_G ratio and laser power, increasing the laser power beyond the optimum processing window generally results in a higher degree of structural disorder, as reflected by the increased intensity of the D band and changes in the I_D/I_G ratio. It is noteworthy that all investigated samples exhibit a pronounced D band, indicating that the synthesized material is not pristine graphene but rather consists of defect-rich multilayer graphene. Such defects are considered beneficial for electrochemical applications because they serve as active sites for charge transfer reactions. The Raman results further demonstrate that increasing laser power beyond an optimal threshold increases structural disorder. Therefore, optimization of laser parameters is necessary to achieve a balance between graphitization and defect generation.

While Raman spectroscopy provides information regarding the structural ordering of the graphene framework, XPS enables detailed investigation of the chemical transformations occurring during laser-induced graphitization. High-resolution C 1s and O 1s spectra obtained from the LIG fabricated on the 50µm Kapton substrate.

The C 1s spectra reveal a complex carbon chemistry arising from both the original polyimide precursor and the graphitized carbon produced during laser irradiation. The dominant component centred at approximately 284.2 eV corresponds to sp^2-hybridized C=C bonds originating from graphitic carbon. Following laser-induced graphitization, this peak exhibits the characteristic asymmetric line shape accompanied by a distinct π–π^* shake-up satellite at approximately 291.1 eV, confirming the formation of conjugated aromatic carbon structures. Additional components observed at approximately 286.3 eV and 288.6 eV are assigned to carbon atoms bonded to oxygen or nitrogen (C–O/C–N) and carbonyl species associated with the imide structure, respectively. A lower binding-energy component located near 283.4 eV corresponds to C–C bonds associated with the pentagonal rings of the original Kapton structure, while the component near 285.1 eV is attributed to adventitious carbon contamination and residual C–N bonds.

The corresponding O 1s spectra were successfully deconvoluted into two principal contributions located at approximately 531.4 eV and 533.1 eV, assigned to carbonyl oxygen (C=O) and ether oxygen (C–O–C), respectively. These components reflect the residual oxygen-containing functionalities remaining after laser processing and provide valuable insight into the degree of carbonization achieved during graphitization. The deconvolution results of high-resolution XPS spectra in the core-level binding energy range of C 1s and O 1s, in at. % is shown in Table 6.

Table 6. Peak deconvolution details from high-resolution XPS spectra of LIG in the core-level binding energy range of C 1s and O 1s, in at. % (LIGs fabricated with laser speed: 160mm/s).

Species		BE (eV)	PI foil	P11%	P12%	P13%
C 1s	pentagonal	283.4	7.94	4.12	4.20	3.8
	C=C	284.2	53.69	60.55	56	54.72
	C-C	285.1	13.52	13.35	13.17	12.98
	C-O	286.6	4.77	8.90	9.72	10.2
	C=O	288.6	5.53	3.89	4.63	5.25
O 1s	C-O	533.1	4.10	3.72	4.68	5.25
	C=O	531.4	10.44	5.47	7.6	7.80

Comparison of the P12% and P13% samples demonstrates that laser power influences not only the structural ordering but also the surface chemistry of LIG. The P12% electrode exhibits a slightly higher fraction of graphitic carbon, whereas increasing the laser power to P13% promotes further oxidation of the electrode surface. Quantitative XPS analysis indicates that the combined concentration of oxygen-containing species increases from approximately 26 at.% for the P12% sample to 28.5 at.% for the P13% sample, accompanied by a slight reduction in the contribution associated with the pentagonal carbon rings of the original polyimide.

These observations suggest that higher laser fluence promotes more extensive cleavage of the imide structure while simultaneously increasing surface oxidation, most likely due to the elevated temperatures generated during laser processing.

The XPS results closely complement the Raman observations. Whereas Raman spectroscopy demonstrates that excessive laser power increases structural disorder within the graphene lattice, XPS confirms that the same processing conditions also modify the surface chemistry by increasing the concentration of oxygen-containing functional groups. Together, these findings confirm that the fabricated material should not be considered pristine graphene and demonstrate that optimization of laser processing parameters requires balancing graphitic ordering with surface oxidation in order to obtain LIG possessing both high electrical conductivity and favourable electrochemical properties.

From an electrochemical perspective, this combination is highly advantageous. Numerous studies have demonstrated that edge-plane sites exhibit substantially faster electron-transfer kinetics than basal-plane graphite. Furthermore, oxygen-containing functionalities can enhance analyte adsorption and facilitate charge transfer by increasing the density of electrochemically active surface sites.

These complementary observations establish a clear relationship between laser processing conditions, graphitic structure and surface chemistry, providing the physicochemical basis for the wettability, electrical conductivity and electrochemical characteristics discussed in the subsequent sections.

5.1.4 Wettability and surface properties (results from[280,281])

Following the structural and surface characterization of LIG, the wettability of the fabricated electrodes was evaluated using contact angle measurements. Surface wettability plays an important role in determining the electrochemical performance of porous carbon electrodes because it governs electrolyte spreading, interfacial contact and accessibility of electrochemically active sites.

The influence of laser processing parameters on the wettability of 50µm Kapton-derived LIG and measured contact angle values are summarized in Table 7, while representative contact angle images are presented in Figure 16. The contact angles above 117° indicate that all fabricated LIG samples exhibit pronounced hydrophobic behaviour. The hydrophobicity originates from the combination of graphitic surface chemistry and hierarchical micro/nanostructured roughness generated during laser processing. The porous morphology amplifies the intrinsic hydrophobicity through a Cassie-Baxter wetting mechanism, often referred to as the lotus effect.

Table 7. Contact angle measurements for electrodes with different power and speed

Sample	Contact Angle(°)
P11-S160	**128.51**
P12-S160	**121.25**
P13-S160	**121.81**
P12-S180	**119.29**
P12-S170	**117.73**

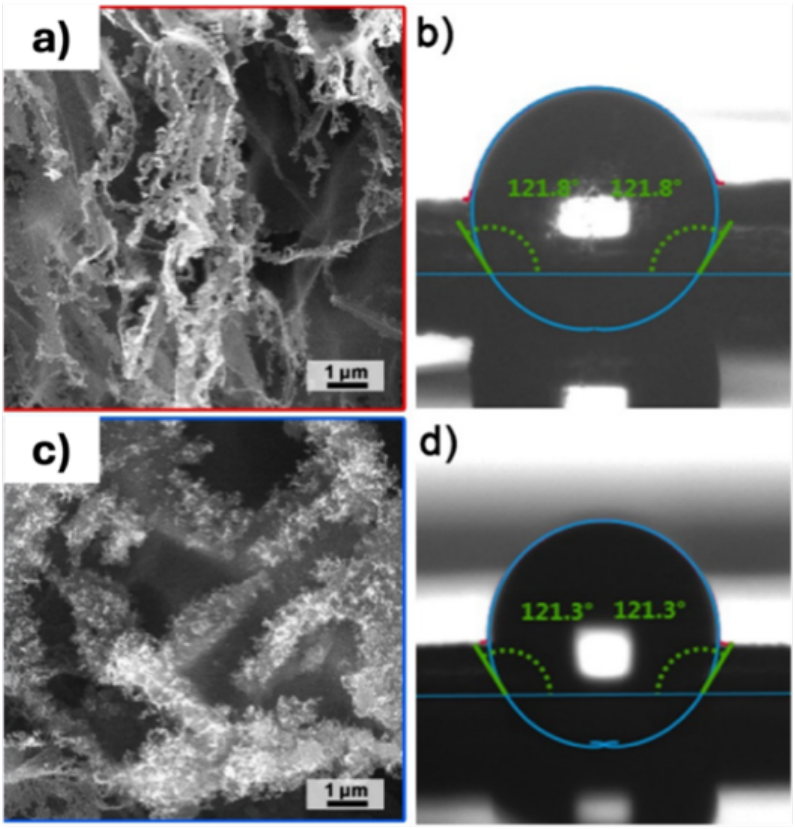


Figure 16: Contact angle measurement for sample 50µm Kapton foil a) P 12%, c)P13% and their corresponding measurements b),d) respectively[280]**.**

In this state, air pockets become trapped beneath the water droplet, thereby reducing the solid–liquid contact area and increasing the apparent contact angle. As a result, the combined effects of graphitic surface chemistry and hierarchical roughness contribute to the highly hydrophobic character of the LIG electrodes. Although hydrophobic surfaces exhibit excellent water repellence, excessive hydrophobicity may not be advantageous for electrochemical sensing applications. Limited electrolyte spreading can reduce the effective contact area between the electrolyte and the electrode surface, thereby restricting utilization of the available porous network and decreasing the effective EASA. This observation further highlights the importance of the subsequent surface modification strategies. Therefore, the wettability of LIG should not be viewed solely as a surface property but rather as a consequence of the underlying hierarchical structure generated during laser-induced graphitization.

For the 100µm Kapton-derived LIG, the influence of laser processing on wettability was investigated by varying the laser interval spacing (hatch spacing). Increasing interval spacing further increases roughness and trapped air pockets, producing higher apparent contact angles. the primary objective of this investigation was to determine how overlap between adjacent laser scan lines influences the surface characteristics by wettability study of the resulting graphene.

As shown in Figure 17, the water contact angle increases markedly once the interval spacing exceeds a critical threshold. This behaviour indicates that increasing the spacing between adjacent laser scan lines alters the surface microstructure sufficiently to enhance surface hydrophobicity.

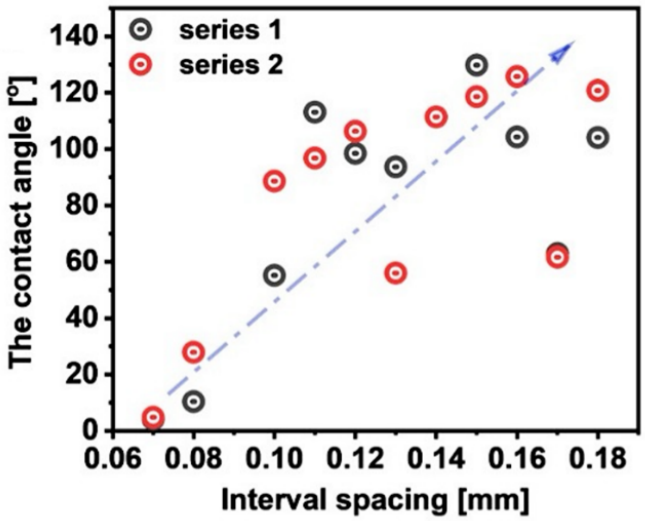


Figure 17: Effect of interval spacing on a water contact angle for LIGs fabricated on 100µm Kapton-derived LIG[281].

At larger interval spacings, neighbouring LIG tracks overlap less effectively, producing a more heterogeneous surface topography that favours air entrapment beneath the water droplet. This behaviour is again consistent with the Cassie-Baxter wetting model, where increased surface roughness and reduced solid-liquid contact area lead to larger apparent contact angles. As a result, an interval spacing of 50µm (0.05mm) was selected for subsequent experiments.

Overall, the wettability studies demonstrate that the interfacial properties of LIG are governed by the combined influence of surface chemistry and hierarchical surface morphology. While the 50µm study highlights the effect of laser power and scanning speed on the hydrophobic behaviour of LIG, the 100µm study demonstrates that interval spacing represents an additional processing parameter capable of tailoring the wetting characteristics of the graphene surface. Together, these results emphasize that optimization of laser processing conditions is essential not only for achieving desirable structural and electrical properties but also for controlling the interaction between the electrode surface and aqueous electrolytes.

Since surface wettability determines how effectively the electrolyte interacts with the electrode surface, efficient electrochemical performance also requires rapid electron transport throughout the interconnected graphene network. The electrical conductivity of LIG is therefore another critical parameter that reflects the quality of graphitization and the continuity of the porous carbon. Consequently, the following section examines the influence of laser processing parameters on the electrical resistance and conductivity of LIG. While surface wettability provides insight into the interaction between the electrode surface and aqueous media, the practical performance of LIG also depends on its ability to efficiently transport electrons throughout the interconnected carbon framework. Therefore, the following section investigates the electrical conductivity of LIG by examining the influence of laser processing parameters on the electrical resistance of the fabricated electrodes.

5.1.5 Electrical conductivity of LIG (results from[280,281])

Electrical conductivity represents one of the most important performance indicators of LIG. The electrical conductivity of LIG is directly related to the degree of graphitization, continuity of the carbon network,

overlap between neighbouring laser tracks or connectivity between adjacent graphene domains. and the density of structural defects introduced during laser processing and as a result, measurements of R_s and electrical conductivity provide valuable information regarding the efficiency of the laser-induced conversion of polyimide into electrically conductive graphene. Therefore, electrical resistance measurements were performed to identify the laser processing conditions that produce highly conductive graphene structures on both 50µm and 100µm Kapton substrates.

The lowest R_s was obtained for P12 %, indicating optimum graphitization. Similar resistance values in the longitudinal and transverse directions demonstrate effective overlap of adjacent laser scan tracks and formation of a continuous conductive network. The conductivity trends further indicate that excessive laser power introduces structural damage and increased disorder, which partially offsets the benefits of graphitization. The conductivity optimization requires balancing carbon conversion and structural preservation. Table 8 shows the R_s, Ω/sq, measured using a four-probe technique.

The results demonstrate that the electrical properties of LIG are highly dependent on the applied laser power. Among the investigated samples, the P12%S160 electrode exhibited the lowest R_s of 1.91 Ω/sq, whereas increasing the laser power to P13%S160 resulted in an increase to approximately 2.50 Ω/sq. These values are comparable to those reported for highly conductive LIG fabricated under optimized processing conditions. The measured R_s values in both the longitudinal and transverse directions are summarized in Table 8.

Table 8. Longitudinal and transverse sheet resistance of LIG fabricated on 50µm Kapton foil at different laser powers (laser scanning speed is 160mm/s)

Samples	Longitudinal sheet resistance (Ω/sq)	Traverse sheet resistance (Ω/sq)
P11%	**2.33**	**2.57**
P12%	**1.91**	**2.04**
P13%	**2.50**	**2.71**

The relatively small difference between the longitudinal and transverse R_s indicates that the laser-written graphene tracks overlap sufficiently during raster scanning to produce a continuous conductive network. During laser fabrication, the laser beam scans the substrate sequentially in the longitudinal direction and inadequate overlap between neighbouring scan lines would normally produce significantly higher resistance in the transverse direction. However, the similar resistance values obtained in both orientations demonstrate that the selected processing conditions generated a well-connected graphene with effective electrical continuity across the electrode surface.

The minimum R_s observed for the P12%S160 sample is consistent with the structural characterization presented in the previous sections. Raman spectroscopy demonstrated that this sample possessed the highest graphitic quality, as evidenced by the narrower G-band and higher graphitic ordering, while SEM revealed a continuous porous graphene architecture capable of supporting uninterrupted conductive pathways. The increase in the laser power to P13%-S160 resulted in a measurable increase in R_s, corresponding to the increased structural disorder identified by Raman spectroscopy. These observations indicate that although

higher laser power promotes carbonization, excessive thermal energy introduces defects that reduce the overall electrical conductivity of the graphene network.

For the 100µm Kapton substrate, the electrical properties were further evaluated by investigating the influence of the interval spacing between adjacent laser scan lines. As shown in Figure 18, the R_s in both the longitudinal and transverse directions increases rapidly once the interval spacing exceeds a critical value. This behaviour reflects the progressive reduction in overlap between neighbouring laser-scribed graphene tracks. At small interval spacings, adjacent LIG grooves overlap sufficiently to produce a continuous conductive pathway throughout the electrode. However, increasing the interval spacing reduces this overlap, interrupting the electrical connectivity between neighbouring tracks and thereby increasing the measured R_s.

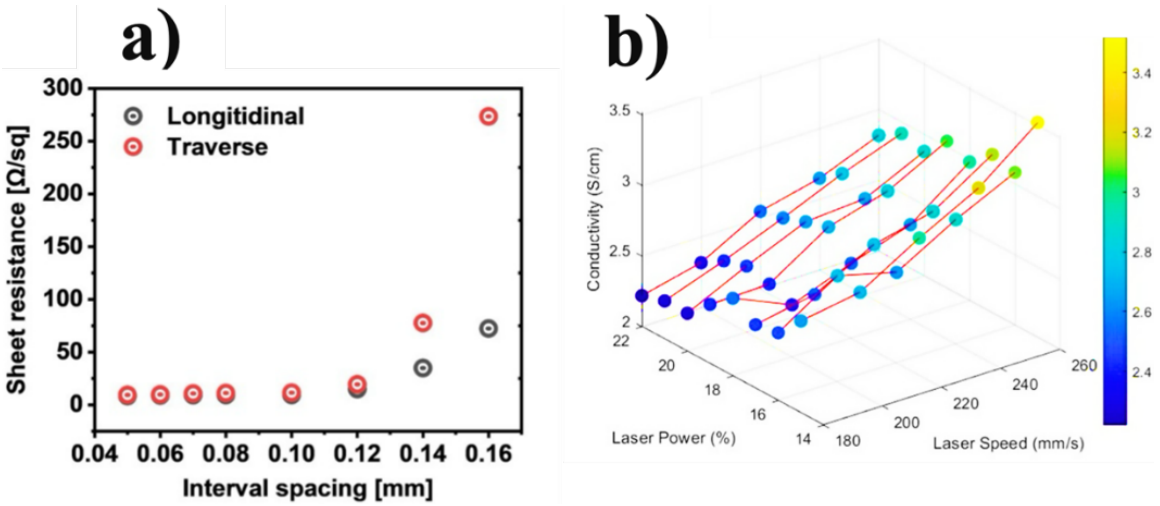


Figure 18: Effect of interval spacing and effect of power and speed on the electrical conductivity of the LIG. a) Effect of interval spacing on electrical conductivity of LIG; b) Effect of power and speed on the electrical conductivity of the LIG at a fixed interval of 50 µm (or 0.05mm)[281].

Based on these observations, an interval spacing of 50µm was selected from the investigated over the range of 50-180µm for all subsequent experiments involving the 100µm substrate, ensuring adequate overlap between neighbouring laser scan lines and preserving the electrical continuity of the graphene network.

The influence of laser power and scanning speed on the electrical conductivity of LIG fabricated on the 100µm Kapton substrate was investigated. The results indicate that electrical conductivity gradually decreases with increasing laser power, whereas increasing the laser scanning speed produces a noticeable improvement in conductivity. These observations suggest that excessive laser energy does not necessarily improve electrical transport within the graphene framework. Instead, maintaining an appropriate balance between laser power and exposure time is essential for producing a highly conductive interconnected carbon network.

The dependence of conductivity on laser processing parameters further confirms that optimization of LIG fabrication requires simultaneous control of laser power, scanning speed and interval spacing. Collectively, these parameters determine the extent of graphitization, the continuity of neighbouring graphene tracks and the overall quality of the conductive network produced during laser irradiation.

The exceptionally low R_s values obtained for the investigated LIG structures confirm the formation of a highly interconnected graphitic network capable of supporting rapid electron transport. Since the electrochemical performance of porous carbon electrodes depends not only on electrical conductivity but also on the number of accessible electroactive sites, EASA of the LIG electrodes was subsequently evaluated.

5.1.6 Electrochemical characterization of LIG (results from[280,281])

Following the physicochemical characterization of LIG, the electrochemical behaviour of the fabricated electrodes was investigated using CV. The previous sections established the influence of laser processing on the morphology, graphitic structure, surface chemistry, wettability and electrical conductivity of LIG, these properties alone do not fully describe its behaviour as an electrochemical electrode. The practical applicability of LIG depends on its ability to efficiently exchange electrons with electroactive species at the electrode-electrolyte interface. The CV of $[Fe(CN)_6]^{4-/3-}$PBS system was used for the evaluation of influence of laser processing parameters on the electrochemical performance of LIG electrodes.

CV is one of the most widely employed electrochemical techniques for evaluating electrode performance because it provides information regarding the reversibility of electrochemical reactions, electron-transfer efficiency and the accessibility of electroactive surface sites. The $[Fe(CN)_6]^{4-/3-}$ redox couple was selected as the electrochemical probe due to its well-established reversible behaviour and sensitivity to changes in electrode surface properties. The influence of laser processing parameters on the electrochemical characteristics of LIG was assessed by analysing two key electrochemical descriptors: the anodic peak current density and the peak-to-peak separation While the peak current density reflects the electrochemical activity and accessible surface area of the electrode, the peak separation provides an indication of the reversibility and efficiency of electron-transfer processes. Together, these parameters were used to identify the optimum laser processing conditions for both 50µm and 100µm Kapton substrates before undertaking detailed electrochemical characterization.

For the 50µm Kapton substrate, CV response was found to influence strongly on the applied laser power and scanning speed. The effect of power and speed of LIGs fabricated on 50µm is show in Figure 19. Variations in the laser processing conditions produced noticeable changes in peak currents together with differences in the peak-to-peak separation, indicating that the quality of the graphene network directly influences the electrochemical behaviour of the electrode.

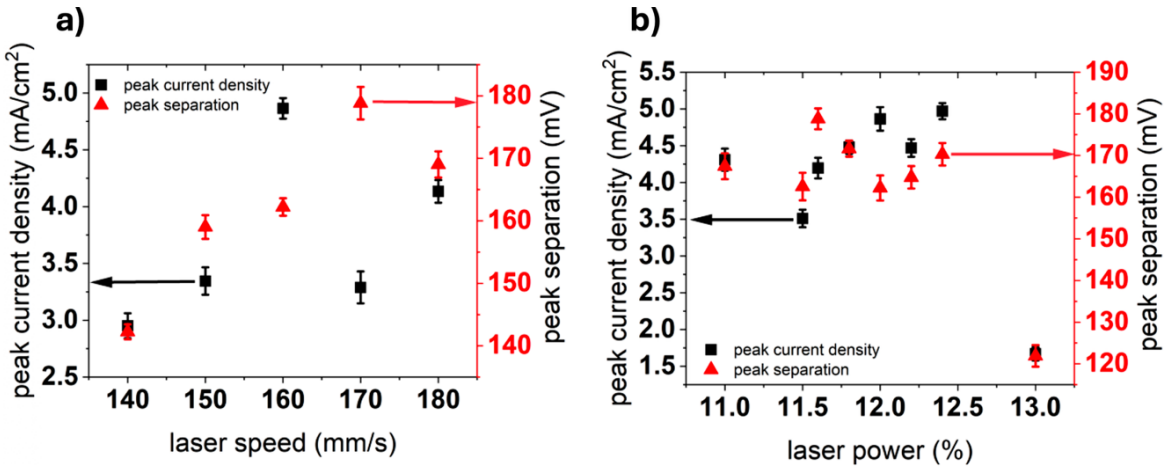


Figure 19: Effect of laser power and laser speed of LIGs fabricated on 50µm substrate. Effect of a) laser power and b) laser speed of LIGs fabricated on 50µm substrate in 5mM solution of $[Fe(CN)_6]^{4-}$ in PBS[280].

Variation of the laser scanning speed as shown in Figure 19 revealed that the anodic peak current density initially increased with increasing scanning speed, reaching a maximum at 160mm/s, before decreasing at higher speeds. Simultaneously, the peak-to-peak separation remained comparatively low near the optimum

processing conditions but increased at higher scanning speeds, indicating a gradual reduction in electron-transfer efficiency. These observations suggest that an optimum balance exists between laser exposure time and graphitization. Excessively slow scanning speeds increase thermal exposure of the substrate, whereas excessively rapid scanning reduces the energy available for complete graphitization, resulting in deterioration of the electrochemical response. Overall, the electrochemical optimization of the 50µm substrate identified P12%S160 electrode as the optimum processing condition, providing the highest electrochemical activity.

Reproducibility is an essential requirement for practical electrochemical electrodes because variations introduced during fabrication directly influence analytical performance. To evaluate the repeatability of the optimized laser processing conditions, CVs were recorded for three independently fabricated P12%S160 electrodes under identical experimental conditions. All three electrodes exhibit nearly identical anodic and cathodic peak currents together with comparable peak potentials and voltammetric profiles. The excellent agreement between independently fabricated electrodes demonstrates that the optimized laser processing conditions produce highly reproducible graphene structures with consistent electrochemical behaviour.

The optimized P12%S160 electrode exhibits substantially higher anodic and cathodic peak currents than the P13%S160 sample, demonstrating enhanced electrochemical activity toward the ferri/ferrocyanide redox couple. In addition, the voltammetric response of the P12%S160 electrode is characterized by a smaller peak-to-peak separation, indicating a more reversible electrochemical process and more efficient electron transfer at the electrode/electrolyte interface. The poorer electrochemical response observed for the P13%S160 electrode is consistent with the physicochemical characterization presented in the previous chapter sections. Considering all these observations suggest that excessive laser fluence compromises the quality of the conductive graphene, thereby reducing electrochemical performance, which is confirmed by the CV of the P12% and P13% electrodes having same speed and intervals. Even a 1% fluence has importance and influence on physicochemical properties and LIG electrochemical characteristics.

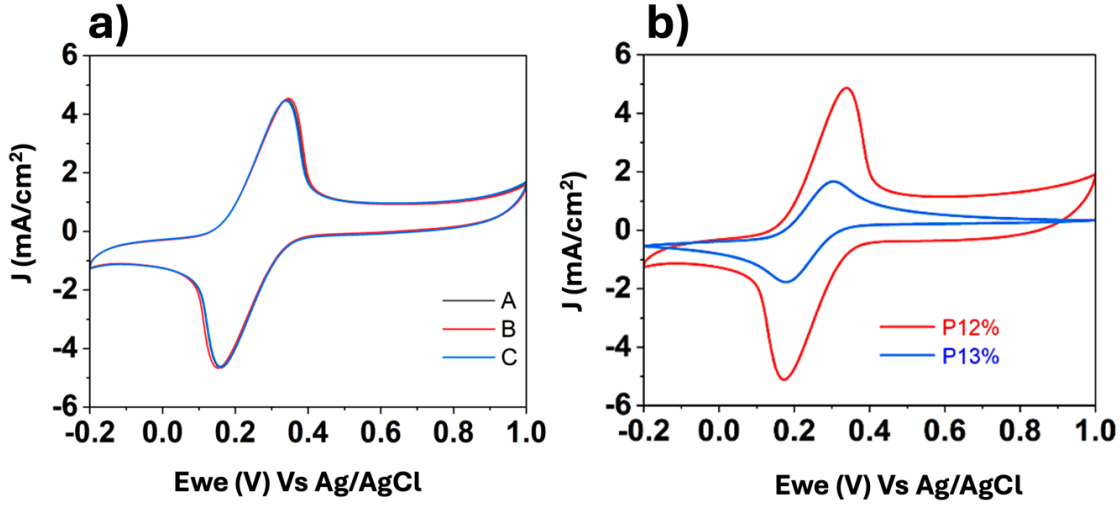


Figure 20: Repeatability and CV plot showing influence of Laser fluence. a) Repeatability of three P12% LIG electrodes for 1mM $[Fe(CN)_6]^{4-}$ in PBS solution, b) CV graphs for LIGs formed at various lasing powers (P12% and P13%) and with lasing speed 160mm/s[280].

Similarly evaluation of influence of laser parameters on electrochemical behaviour of 100µm Kapton was carried out and the response provided a more comprehensive visualization of the electrochemical processing

window and clearly illustrates the synergistic influence of laser power and scanning speed on electrode performance. The general trend for different laser power is that peak current density reaches a maximum at around 220mm/s and then decreases slowly. Similarly peak separation reaches a minimum as this speed for different laser powers. Accordingly laser speed of 220mm/s and power of 19% was selected as the best candidate from the investigated electrodes.

Thus the electrochemical performance of investigated LIG electrodes is highly dependent on laser processing conditions. Optimization of laser power and scanning speed produced a distinct processing window in which the fabricated electrodes exhibited the highest J_p and the smallest ΔEp). For the 50µm Kapton substrate, the optimum electrochemical response was obtained for the P12%S160mm/s electrode, while for 100µm substrate, it is P19%S220mm/s. This further highlighted the combined influence of laser power and scanning speed, effect of substrate on electrochemical behaviour.

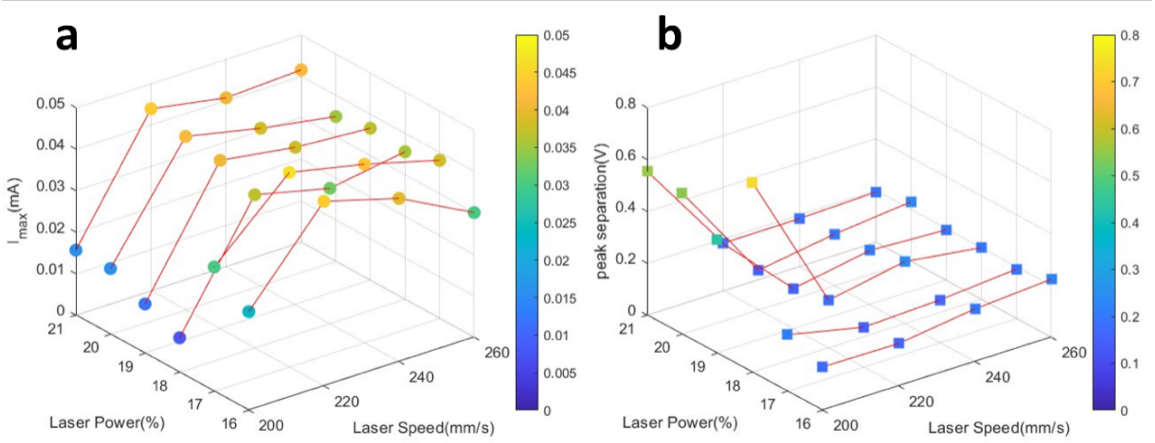


Figure 21: Effect of laser power and laser speed on a) max current density and b) peak separation of LIGs fabricated on 100µm in 5 mM solution of $[Fe(CN)_6]^{4-}$ in PBS[281].

Although both substrate thicknesses produced electrochemically active LIGs exhibiting well-defined ferri/ferrocyanide redox behaviour, the optimum laser processing conditions differed. This demonstrates, that substrate thickness influences the laser-material interaction and consequently the processing window required to achieve the best electrochemical performance. The excellent repeatability obtained for independently fabricated electrodes confirms the reliability of the optimized fabrication protocol and confirms suitability for subsequent electrode modifications.

Even though CV identifies the optimum laser processing conditions and qualitatively evaluates the electrochemical behaviour of LIG, it does not quantify the electrochemically accessible surface responsible for the observed current response. Since porous graphene electrodes possess a surface area substantially larger than their geometric dimensions, determination of the EASA is essential for understanding the origin of the enhanced electrochemical activity. As a result, the following section quantitatively evaluates the EASA of the optimized LIG electrodes using the Randles-Ševčík relationship.

5.1.7 Electroactive surface area (EASA) (results from[280,281])

The electrochemical response of an electrode is governed not only by its intrinsic electrical conductivity but also by the fraction of the electrode surface that is electrochemically accessible to the electrolyte. For highly

porous carbon materials such as LIG, the EASA generally exceeds the geometric area because the 3D interconnected architecture exposes a significantly larger number of electrochemically active sites. EASA represents one of the most important parameters describing electrode performance, where heterogeneous electron transfer occurs at the electrode-electrolyte interface. Therefore, the EASA of the optimized LIG electrodes fabricated on both 50µm and 100µm Kapton substrates was quantitatively determined using the Randles-Ševčík equation and scan-rate-dependent CV measurements in ferri/ferrocyanide electrolyte. The geometric area of the fabricated working electrode was approximately 0.085 cm².

$$i_{(p)} = (2.69 * 10^5) n^{(3/2)} A D^{(1/2)} C v^{(1/2)}$$

where $i_{(p)}$ denotes the anodic peak current (A), n is the number of electrons transferred, A is the electroactive surface area (cm²), D is the diffusion coefficient (cm²/s), C is the concentration of the electroactive species (mol/cm³) and ν is the scan rate (V/s). Under diffusion-controlled conditions, the peak current varies linearly with the square root of the scan rate, allowing the electroactive surface area to be calculated from the slope of the resulting linear relationship. CV recorded at different scan rates from 10 to 1000 mV/s for the electrodes P12%S160 on 50µm and P19%S220 on 100µm as shown in Figure 22.

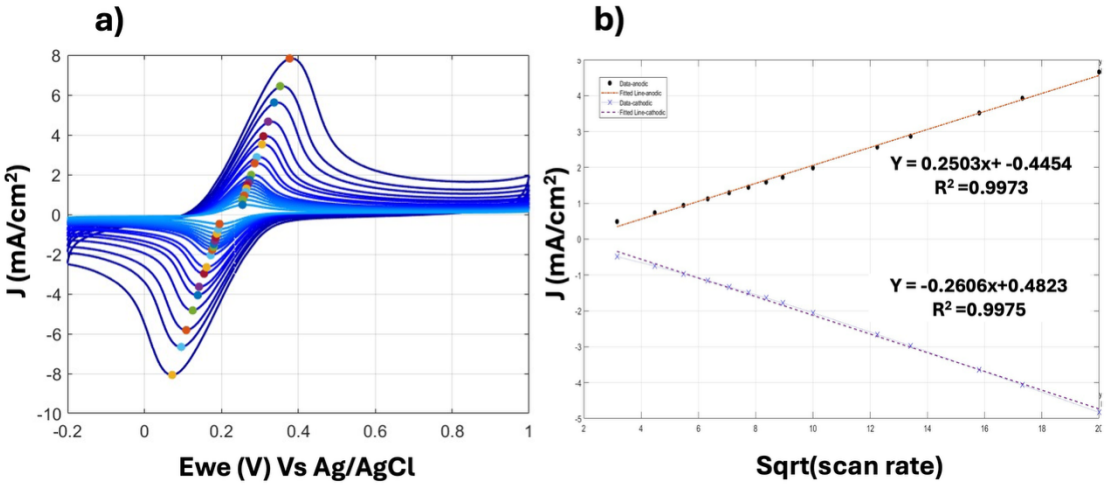


Figure 22: EASA of P12%S160 on 50µm Kapton. :a) CV recorded at different scan rates in 5mM ferri/ferrocyanide dissolved in PBS, (b) Linear dependence on the square root of scan rate[280].

For both the P12%S160 electrode fabricated on the 50µm Kapton substrate and the P19%S220 electrode fabricated on the 100µm Kapton substrate, the anodic and cathodic peak currents increased progressively with increasing scan rate while maintaining well-defined and symmetric voltammetric profiles. The systematic increase in peak current without significant distortion of the voltammograms indicates stable electrochemical behaviour and confirms that the electrochemical response is predominantly governed by diffusion of the ferri/ferrocyanide species toward the electrode surface.

The preservation of the characteristic redox peaks over the investigated scan-rate range further demonstrates that the optimized laser processing conditions produce electrochemically stable graphene electrodes capable of sustaining rapid electron exchange with the redox species. These observations also indicate that the interconnected porous graphene network provides efficient electrolyte accessibility throughout the electrode surface while maintaining continuous electrical pathways for charge transport. The high coefficients of

determination (R^2) confirm the validity of applying the Randles–Ševčík equation for calculating the EASA of the optimized LIG electrodes.

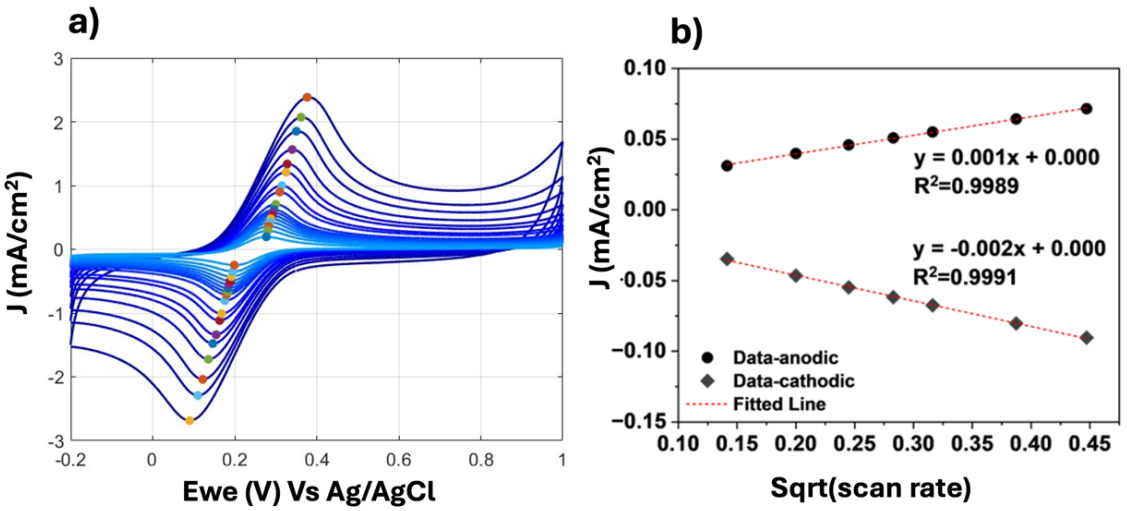


Figure 23: EASA of P19%S220 on 100µm Kapton. a) CV recorded at different scan rates in 5mM ferri/ferrocyanide dissolved in PBS, (b) Linear dependence on the square root of scan rate[280].

The P12%S160 exhibited an EASA of 0.250 cm², corresponding to approximately 2.9 times its geometric surface area (0.085 cm²) and P19%S220) exhibited an EASA of 0.195 cm², representing approximately 2.3 times its geometric area. Although the optimized electrode fabricated on the 50µm substrate exhibited a somewhat higher EASA than that produced on the 100µm substrate, both values greatly exceeded the geometric electrode area, confirming that appropriate optimization of the laser processing conditions produces highly accessible electrochemical interfaces irrespective of substrate thickness. Simply this indicates that the electrochemically accessible interface is substantially larger than the geometric footprint of the fabricated electrode. These confirmed that the optimized laser processing conditions successfully generated a hierarchically porous graphene network capable of providing abundant electrochemically accessible active sites.

Following the determination of the EASA, the standard heterogeneous electron-transfer rate constant (k^0) of the optimized LIG electrodes was evaluated to assess the intrinsic charge transfer capability of the graphene-electrolyte interface.

5.1.8 Electron transfer kinetics (results from[280,281])

The EASA determines the number of electrochemically accessible reaction sites, the overall electrochemical performance of an electrode is equally dependent on the rate at which electrons are transferred across the electrode-electrolyte interface. Even though the electrodes possessing comparable EASA, may still exhibit different performances if their interfacial electron-transfer kinetics differ. Therefore, the intrinsic ability of an electrode material to exchange electrons with electroactive species, the k^0 was evaluated from CV measurements using Nicholson analysis of the ferri/ferrocyanide redox system[282].

The P12%S160 electrode fabricated on the 50µm Kapton substrate exhibited a k^0 value of 4.12×10^{-3} cm/s, whereas P19%S220 electrode fabricated on the 100µm Kapton substrate exhibited a slightly lower value of 1.50×10^{-3} cm/s. Although both electrodes demonstrated efficient heterogeneous electron transfer, the higher k^0 obtained for the 50µm substrate indicates a faster electron-transfer process at the graphene-electrolyte

interface. The difference can be correlated with the physicochemical characteristics established in the previous sections. The P12%-S160 electrode exhibited a slightly higher degree of graphitization together with lower R_s, providing more efficient conductive pathways for charge transport. These structural characteristics facilitate faster electron exchange between the electrode surface and the ferri/ferrocyanide redox couple, resulting in the higher k^0.

Together, these results demonstrate that LIG provides an electrochemically active interface that is highly suitable for subsequent surface modification and customizable functionalization. Although information regarding the EASA and k^0, it does not distinguish the individual resistive and capacitive processes occurring at the electrode-electrolyte interface. EIS complements CV by separating these contributions over a wide frequency range, thereby providing detailed insight into the charge transfer resistance, double-layer capacitance and mass-transport characteristics of the electrode system. Therefore, EIS was subsequently employed to further evaluate the interfacial electrochemical behaviour of the optimized bare LIG electrodes.

5.1.9 Charge transfer resistance and electrochemical impedance analysis (results from[280])

EIS was employed to evaluate the interfacial electrochemical behaviour of the optimized P12%S160 LIG electrode. The impedance spectra were recorded in 5mM $K_3[Fe(CN)_6]/K_4[Fe(CN)_6]$ containing 0.1 M KCl and the corresponding Nyquist and Bode plots are presented in Figure 24.

As shown in Figure 24a, the Nyquist plot exhibits a depressed semicircular feature in the high-to-medium frequency region followed by a gradual increase in impedance at lower frequencies. The deviation from an ideal semicircle indicates non-ideal capacitive behaviour, which is characteristic of porous carbon electrodes. Such behaviour originates from the heterogeneous architecture of LIG, where interconnected graphitic domains, structural defects, edge sites and hierarchical porosity produce a distribution of electrochemical time constants more than a single homogeneous electrode-electrolyte interface.

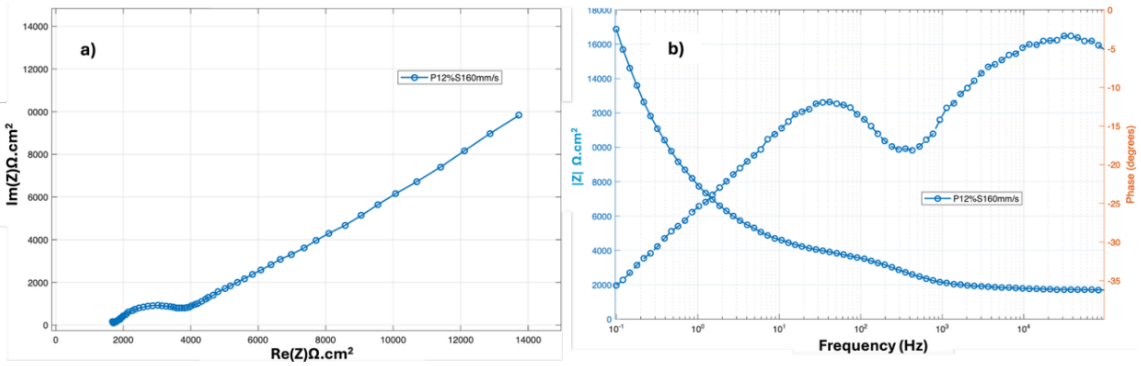


Figure 24: EIS spectra for P12%S160mm/s in 5mM $K_3[Fe(CN)_6]/K_4[Fe(CN)_6]$: a) Nyquist plot and (b) Bode plots showing the impedance magnitude (|Z|) and phase angle as a function of frequency[280].

The corresponding Bode plots further demonstrate the frequency-dependent electrochemical response of the optimized electrode. The impedance magnitude progressively decreases with increasing frequency, indicating that low-frequency behaviour is increasingly influenced by interfacial polarization and ion transport within the porous architecture, whereas the response at higher frequencies is governed predominantly by the intrinsic conductivity of the graphitic network. Similarly, the broad phase-angle response confirms that the

electrochemical behaviour cannot be described by an ideal resistor-capacitor system but instead reflects the distributed interfacial properties associated with the three-dimensional porous structure of LIG.

The observed impedance behaviour is consistent with the structural and electrochemical characteristics established in the preceding sections. Raman spectroscopy confirmed successful graphitization through the formation of interconnected sp^2 carbon domains, while electrical measurements demonstrated low R_s, indicating efficient electronic conduction throughout the carbon. Furthermore, SEM analysis revealed a hierarchically porous morphology that facilitates electrolyte infiltration and the defect-rich graphitic structure provides electrochemically active edge-plane sites that are known to promote electron transfer with solution-phase redox species. These complementary structural characteristics collectively account for the favourable impedance response observed for the optimized electrode.

The EIS results are further supported by CV, EASA and heterogeneous electron-transfer analyses, all of which demonstrated improved electrochemical performance under the optimized laser processing conditions. Therefore, the laser-induced graphitization successfully transforms the insulating polyimide precursor into a conductive porous carbon interface with favourable interfacial electrochemical characteristics. Consequently, the optimized P12%S160 electrode provides a robust bare LIG platform for subsequent surface engineering and functionalization toward advanced electrochemical interfaces.

5.1.10 Preliminary assessment of influence of laser focus position (Z-offset) on LIG fabrication

Preliminary assessment of laser focus position (Z-offset) on LIG Fabrication outlines why the LIG fabrication requires parametric optimization and systematic investigation on parameters is important. Failed or undesirable synthesis is generally a consequence of deviations from the optimal processing window, highlighting the importance of identifying suitable fabrication conditions.

The optimization presented in the preceding sections identified the optimum laser power and scanning speed for the fabrication of LIG electrodes on Kapton substrates under the standard focal conditions employed in this work (Z = 0). However, in laser-material processing, the position of the laser focus relative to the substrate surface (Z-offset) represents an additional processing parameter that can influence energy delivery during irradiation. This Z-height/Z-level represents an additional parameter capable of influencing the graphitization process. Because the Z-offset directly modifies the distance between the laser's focus lens and the substrate surface, it alters the laser energy density delivered to the precursor and consequently affects the photothermal conversion process responsible for graphene formation. As a result, assessment of the Z-offset provides further insight into the complexity of laser parameter optimization and illustrates that successful LIG synthesis depends on the combined influence of multiple processing variables more than laser power and scan speed alone.

To obtain a preliminary understanding of this effect, SEM characterization and CV measurements were performed on bare LIG electrodes fabricated using P19%S220mm/s while differing only in the Z-parameters as taking Z=0 (default) and Z= -2.5. This preliminary investigation was conducted in collaboration with Ms. Angelika Łępek (PhD student, Department of Electrochemistry and Surface Physicochemistry, Gdańsk University of Technology) and Ms. Kornelia Ciurzyńska (Research Scholar, Gdańsk University of Technology). SEM was first employed to examine whether variation of the laser focus position produced

observable differences in the morphology of the fabricated LIG. Representative micrographs are presented in Figure 25.

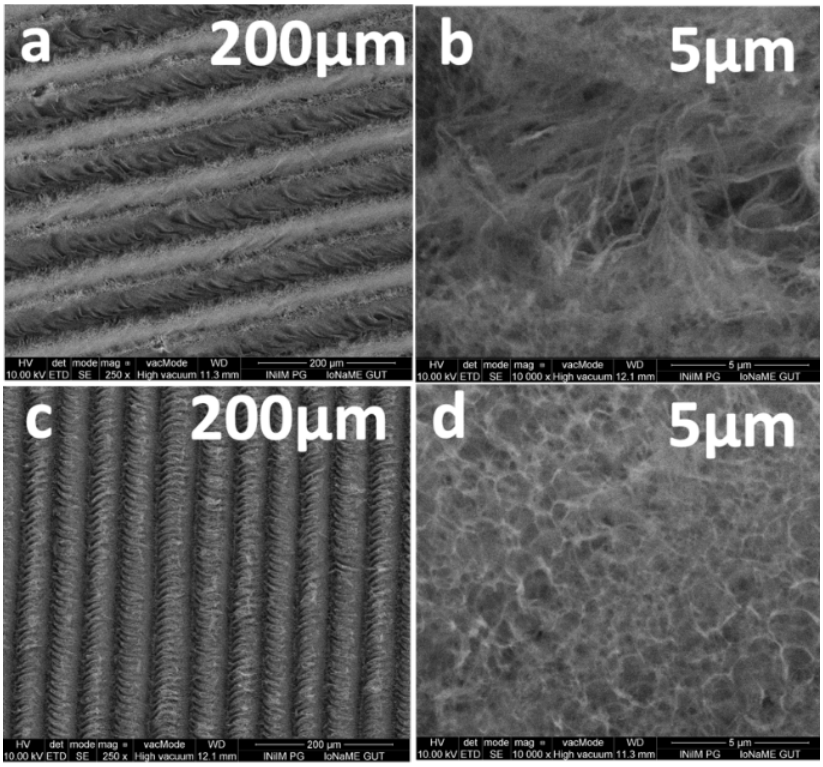


Figure 25: SEM images illustrating the influence of laser focus position (Z-offset) on the morphology of LIG P19%S220mm/s (a,b) Electrode fabricated using a negative Z-offset (Z = -2.5mm); (c,d) electrode fabricated under the standard focal condition (Z = 0). Low-magnification images (a,c) show the morphology of the laser-written tracks, whereas high-magnification images (b,d) reveal differences in the surface microstructure of the resulting graphene layer. The images qualitatively indicate that laser focus position influences the morphology of the LIG formed during irradiation.

The electrode fabricated using a negative Z-offset (Z = -2.5mm) exhibited a highly porous and interconnected fibrous network at higher magnification, whereas the electrode produced under the standard focal condition (Z = 0) displayed a comparatively denser and more compact surface morphology. At lower magnification, differences in the morphology of the laser-written tracks were also observed, suggesting that laser focus position influences the local energy distribution during irradiation and consequently affects the microstructural development of the LIG layer. Owing to the preliminary nature of this investigation, these observations are qualitative and serve only to illustrate that laser focus position can influence the morphology of the resulting material.

To examine whether these morphological differences were accompanied by changes in electrochemical behaviour, CV was performed using Fe redox probe. Representative voltammograms are shown in Figure 26. The electrode fabricated using a negative Z-offset (Z = -2.5mm) exhibited higher anodic and cathodic peak currents than the electrode produced under the standard focal condition (Z = 0). As all other fabrication and measurement parameters were maintained constant, the observed difference suggests that laser focus position influences the characteristics of the LIG. The defocusing of the laser beam may modify the effective laser fluence delivered to the substrate, thereby influencing the extent of laser-induced material transformation.

The increased current response suggests enhanced electrochemical activity, indicating that the laser focus position influences the quality of the graphene network produced during laser irradiation.

Since all other fabrication and measurement parameters were maintained constant, the observed improvement is attributed to differences in the effective laser fluence associated with the modified focal position. These preliminary observations further demonstrate that successful LIG fabrication depends not only on laser power and scanning speed but also on accurate control of the laser focus. Consequently, optimization of the Z-offset represents an additional route for improving the electrochemical performance and reproducibility of LIG electrodes.

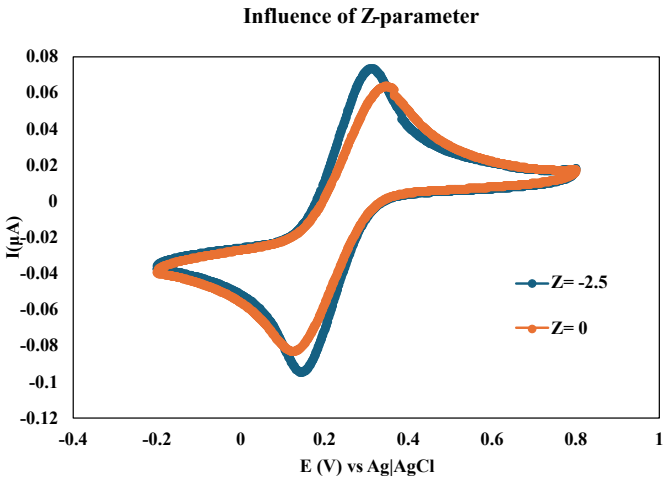


Figure 26: Preliminary assessment of the influence of laser focus position (Z-offset) on the electrochemical behaviour of LIG electrodes. CV of bare LIG 19%S220mm/s electrode under the standard focal condition (Z = 0) and with a negative laser focus offset (Z = –2.5mm). Measurements were performed in 5mM $K_3[Fe(CN)_6]$ prepared in 10mM PBS at a scan rate of 100 mV/s. The increased peak currents observed for the defocused condition suggest that laser focus position influences the properties of the laser-induced carbon network. The comparison is presented as a preliminary technical assessment and does not represent a systematic optimization of the Z-offset parameter.

It should be emphasized that the observations presented here are intended only as a preliminary assessment of the influence of laser focus position and do not constitute a systematic optimization of the Z-offset parameter. Owing to the limited dataset, no definitive conclusions regarding the optimum focal position can be drawn. Additionally, these initial results indicate that laser focus position represents an additional processing variable capable of influencing LIG properties and therefore warrants comprehensive investigation through systematic variation of Z-offset, accompanied by detailed morphological, structural, electrical and electrochemical characterization.

Accordingly, all optimized LIG electrodes discussed throughout the remainder of this thesis were fabricated under the standard focal conditions of the laser system (Z = 0), unless otherwise stated. The observations presented in this section should therefore be regarded as a technical note highlighting the potential influence of laser focus position and not as a modification of the fabrication methodology established in this work. Owing to the limited dataset, no systematic conclusions regarding the effect of Z-offset can be drawn. The preliminary results indicate that laser focus represents an additional process variable capable of influencing electrode properties and therefore merits comprehensive investigation in future studies.

The optimization studies presented throughout this chapter demonstrate that the electrochemical performance of LIG is governed by a combination of fabrication parameters that collectively determine the morphology, structure and electrical properties of the resulting graphene network. Having established the optimum LIG electrodes for both 50µm and 100µm Kapton substrates, the following chapter investigates surface engineering protocols based on hydrogel coatings and polymers to further enhance the electrochemical performance of the optimized LIG platform.

5.2 Hydrogel-LIG interface engineering (results from[280])

The previous chapter established the optimum laser processing conditions required to fabricate highly conductive and electrochemically active LIG electrodes. Even though LIG possesses excellent electrical properties, its surface alone does not provide an ideal interface for the immobilization of biological recognition elements or for controlling the physicochemical interactions occurring at the electrode-electrolyte interface. In order to enhance the properties and to tailor the surface, modification play crucial role. Surface engineering through hydrogel membranes offers an effective strategy for tailoring the interfacial properties of LIG without significantly altering its underlying conductive architecture. Owing to their hydrated three-dimensional polymeric network, hydrogels provide a biocompatible microenvironment capable of accommodating biomolecules while simultaneously influencing the transport of electroactive species toward the electrode surface. In addition to serving as immobilization matrices, hydrogel coatings may modify electrochemical behaviour through changes in surface chemistry, permeability, diffusion characteristics and electrostatic interactions occurring within the hydrogel layer. These combined effects directly influence the charge transfer process and consequently the analytical performance.

Therefore, this section investigates the influence of three naturally derived hydrogel membranes- CS, Agar and Alg on the physicochemical and electrochemical properties of the optimized unmodified /bare LIG electrode. These materials were deliberately selected because they represent distinct chemical classes and possess different charge characteristics, functional groups and transport properties. Figure 27 shows the chemical structure of these hydrogels. The discussion focuses on understanding how the hydrogel coatings modify the surface morphology, wettability and electrochemical characteristics of LIG prior to the immobilization of biological recognition elements.

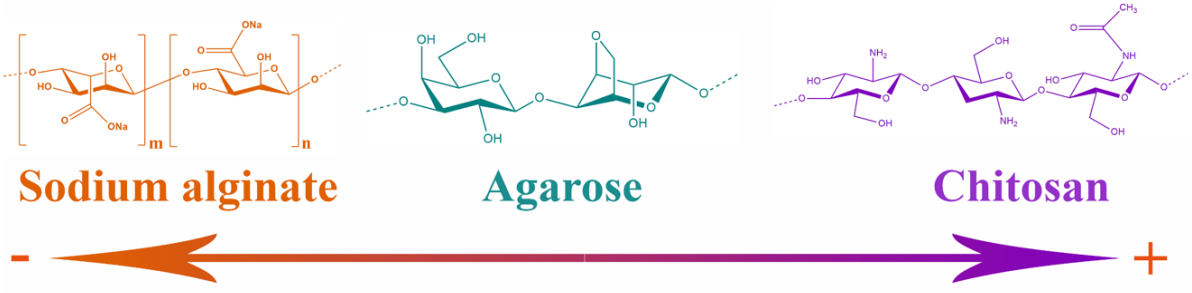


Figure 27: Chemical structure of hydrogels[280].

They provide an opportunity to systematically investigate how hydrogel chemistry influences the electrochemical properties of LIG. The P12%S160 electrode was subsequently selected as the substrate for hydrogel surface engineering in order to investigate how naturally derived hydrogel membranes influence the physicochemical and electrochemical behaviour of LIG.

5.2.1 Morphological characteristics of hydrogel-coated LIGs (results from[280])

SEM was employed to investigate the morphological changes induced by hydrogel deposition on the porous LIG surface. The electrochemical behaviour of hydrogel-modified electrodes depends strongly on the morphology of the coating layer and its interaction with the underlying porous graphene network Representative SEM micrographs of bare and chitosan-coated (CS-LIG) electrodes are shown in Figure 28. Compared with the bare LIG, CS-LIG forms a continuous layer over the graphene surface while preserving the overall porous architecture of the underlying LIG. Instead of completely masking the graphene network, the deposited hydrogel conforms to the rough topography of the LIG. The structure consisted of interconnected graphitic platelets and pore channels generated during the rapid pyrolysis of polyimide.

SEM images reveal at higher magnification, the chitosan coating exhibits the presence of surface cracks distributed across the membrane. These cracks originate from solvent evaporation during atmospheric drying of the deposited polymer solution and expose portions of the underlying porous LIG structure. Upon hydration, however, the CS coating is expected to swell and form a 3D hydrogel network, thereby covering these drying-induced discontinuities and providing a hydrated interface for electrochemical measurements.

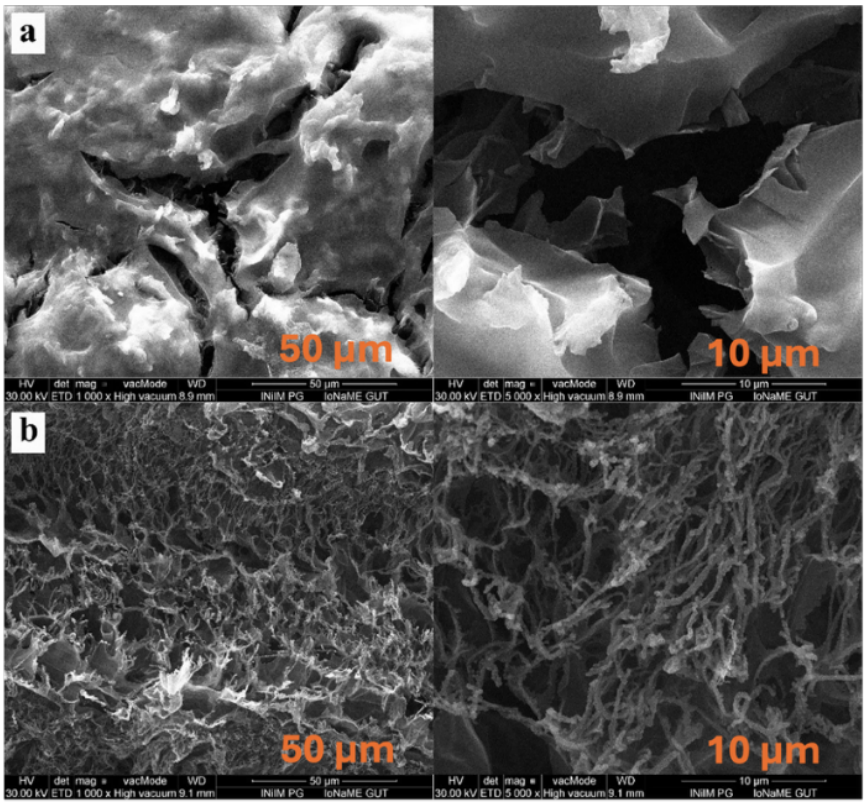


Figure 28: SEM images at two different magnifications for comparison of CS with Bare. a) CS-LIG and b) bare LIG. The images illustrate the preservation of the porous graphene architecture following hydrogel deposition and reveal the morphology of the polymer coating after drying[280].

Overall, the SEM observations confirm successful deposition of the CS membrane on the optimized LIG electrode while maintaining the underlying porous graphene architecture. This morphology is expected to facilitate interaction between the hydrogel and the conductive substrate, providing a suitable platform for investigating how hydrogel coatings influence the wettability and electrochemical behaviour of LIG. This

observation is critical because it explains why hydrogel coatings can influence electrochemical properties without completely blocking electron transfer at the underlying graphene surface.

While SEM demonstrates the successful deposition of the hydrogel and its interaction with the porous LIG substrate, morphological observations alone cannot confirm the chemical modification of the electrode surface. Therefore, the following section investigates the structural and surface chemical changes induced by hydrogel deposition using spectroscopic characterization techniques.

5.2.2 Surface chemistry of hydrogel-coated LIG (results from[280])

XPS was employed to verify successful hydrogel modification and to identify the chemical functionalities introduced by each hydrogel system. High-resolution C 1s, O 1s and N 1s spectra for hydrogel-modified LIG electrodes are presented in Figure 29 and corresponding deconvolution results are summarized in Table 9.

The C 1s spectra of all hydrogel-modified electrodes exhibited significant increases in oxygen-containing functionalities relative to bare LIG. This confirms the presence of polysaccharide coatings at the electrode surface. However, distinct chemical signatures were observed for each hydrogel system. For CS-LIG, the dominant carbon species consisted of C–C bonds (39.5 at.%), followed by C–O groups (19.5 at.%) and carbonyl functionalities (10.6 at.%). In addition, a distinct OC=O contribution was observed at 289.0 eV. The N 1s spectrum revealed characteristic nitrogen-containing species corresponding to amine groups (C–NH_2, 1.8 at.%) and protonated ammonium groups (NH_4^+, 1.0 at.%). These nitrogen functionalities originate exclusively from CS and therefore provide direct evidence for successful CS modification on the electrode surface.

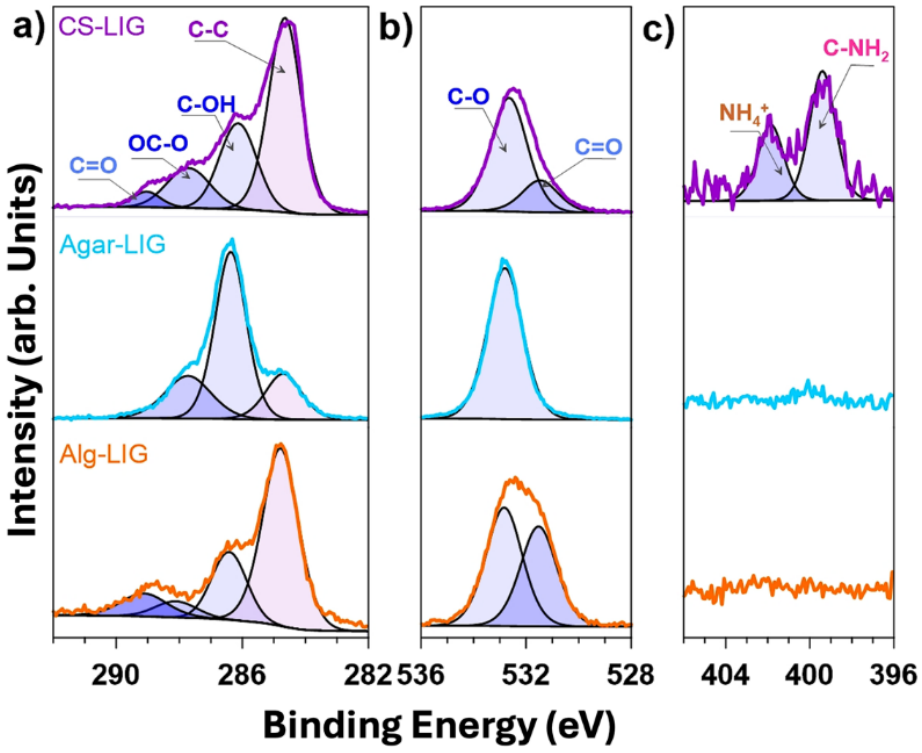


Figure 29: High-resolution XPS spectra of hydrogel-modified LIG. (a) C 1s, (b) O 1s and (c) N 1s regions for chitosan (CS-LIG), agarose (Agar-LIG) and sodium alginate (Alg-LIG) coated electrodes. The spectra demonstrate changes in surface chemical composition following hydrogel deposition[280].

The Agar-LIG electrode exhibited the highest concentration of C–O species (36.9 at.%), consistent with the hydroxyl-rich structure of agarose. Unlike CS, no N-containing functionalities were detected. This reflecting the chemically neutral nature of this hydrogel. The O 1s spectrum was dominated by O-containing functionalities associated with polysaccharide chains.

For ALG-LIGs, a significant contribution from carboxylate-containing species was observed, evidenced by the OC=O peak (5.6 at.%). The presence of abundant oxygenated groups in both C 1s and O 1s spectra reflects the highly anionic character of alginate and confirms successful immobilization of the hydrogel network.

Table 9. Peak deconvolution details from high-resolution XPS spectra different hydrogels in the core-level binding energy range of C 1s and O 1s, in at. %.

	Species	BE [eV]	CS- LIG	Agar- LIG	Alg- LIG
C 1s	C-C	284.7	39.5	11.7	33.3
	C-O	286.4	19.5	36.9	12.0
	C=O	287.7	10.6	13.9	3.4
	OC=O	289.0	2.7	-	5.6
O 1s	C-O	532.8	19.5	-	24.8
	C=O	531.5	5.5	37.5	20.9
N 1s	$C\text{-}NH_2$	399.6	1.8	-	-
	NH_4^+	402.1	1.0	-	-

The XPS results are consistent with successful surface modification by substantially alters the chemical environment of the LIG surface. These modification introduce additional O- and, in the case of CS, nitrogen-containing functional groups at the electrode surface. These chemically active functionalities are expected to influence the interfacial interactions between the electrode and the electrolyte and therefore play an important role in determining the subsequent wettability and electrochemical behaviour of the modified electrodes. These chemically active functionalities are expected to influence the interfacial interactions between the electrode and the electrolyte and therefore play an important role in determining the subsequent wettability and electrochemical behaviour of the modified electrodes.

5.2.3 Wettability and hydrophilicity (results from[280])

The wettability of an electrode surface governs its interaction with aqueous electrolytes and directly influences electrolyte penetration into the porous electrode architecture. Since hydrogel deposition introduced functional groups onto the LIG surface, contact-angle measurements were performed to evaluate the influence of hydrogels on the interfacial wetting behaviour of the modified electrodes.

Representative contact angle images for bare and modified LIG electrodes are shown in Figure 30. The measured water contact angles significantly exceeding 90°, confirm the strongly hydrophobic nature of bare LIG.

Following hydrogel deposition, a pronounced decrease in contact angle was observed for all investigated hydrogel coatings, demonstrating a substantial increase in surface wettability. Compared with bare LIG, CS, Alg, Agar, all transformed the hydrophobic graphene surface into a considerably more hydrophilic interface.

This behaviour is consistent with the incorporation of polar functional groups confirmed by XPS analysis in the previous section.

Although all three hydrogels improved wettability, differences in the measured contact angles indicate that each hydrogel establishes a distinct surface environment. These variations arise from the different chemical compositions and functional groups of the individual polysaccharides, resulting in different interactions with water at the electrode surface. The dynamic wetting behaviour of CS by studying the water droplet soaking rate, further illustrates the effectiveness of CS hydrogel surface modification. As shown in Figure 30c, the deposited water droplet spreads rapidly across the CS-LIG electrode and is progressively absorbed within approximately 20 ms. This rapid water uptake demonstrates the strong affinity of the hydrogel membrane towards aqueous media and confirms the formation of a highly hydrophilic interface capable of facilitating electrolyte transport to the underlying porous graphene structure.

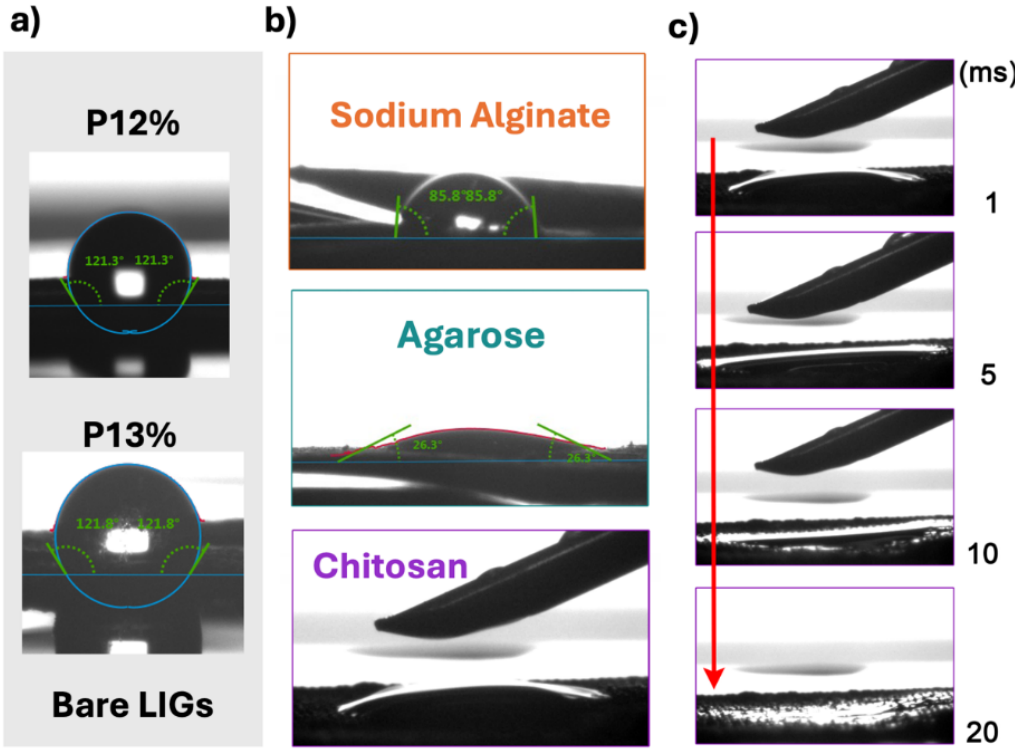


Figure 30: Wettability of bare and hydrogel-modified LIG. a) Contact angle of Bare electrode P12% and P13%,b) contact angle measured for P12% with different HMs (CS, Agar, Alg); c) water droplet soaking rate into CS HM at P12%S160 LIG[280].

Hydrogel surface engineering substantially modifies the interfacial properties of optimized LIG by transforming the initially hydrophobic graphene surface into a highly hydrophilic interface. Static and dynamic contact-angle measurements demonstrate that all the investigated hydrogel coatings improve water affinity. The rapid absorption of water by the CS-LIG confirms its ability to promote efficient electrolyte transport toward the underlying porous graphene architecture.

The improved wettability demonstrated in this section suggests that hydrogel modification enhances the interaction between the electrode surface and aqueous electrolytes. To determine how these interfacial changes influence electrochemical performance, the following section evaluates the effect of hydrogel coatings on the CV response of the electrodes under various experimental conditions.

From an electrochemical perspective, the enhanced wettability introduced by hydrogel modification is expected to improve electrolyte penetration into the porous graphene structure and increase utilization of internal electroactive sites. Improved hydration facilitates ion transport within the diffusion layer and promotes access of redox species to regions that may be inaccessible in the hydrophobic bare LIG electrode. Consequently, the wettability transformation induced by hydrogel modification provides a mechanistic explanation for the substantial increases in electroactive surface area and changes in electrochemical behaviour observed in the following sections.

5.2.4 Electrochemical behaviour of hydrogel-modified LIG electrodes (results from [280])

The influence of hydrogel modification on the electrochemical performance of LIG was investigated using CV in the presence of the ferri/ferrocyanide redox probe. Ferri/ferrocyanide was selected because it is highly sensitive to changes in EASA, charge transfer kinetics and interfacial transport processes, making it a suitable model system for evaluating the electrochemical consequences of hydrogel modification. The CV plots in Figure 31 reveals that hydrogel deposition influences the electrochemical response of the optimized LIG electrode. All electrodes exhibited well-defined oxidation and reduction peaks, indicating that the hydrogel coatings did not completely block access of the redox probe to the conductive graphene network.

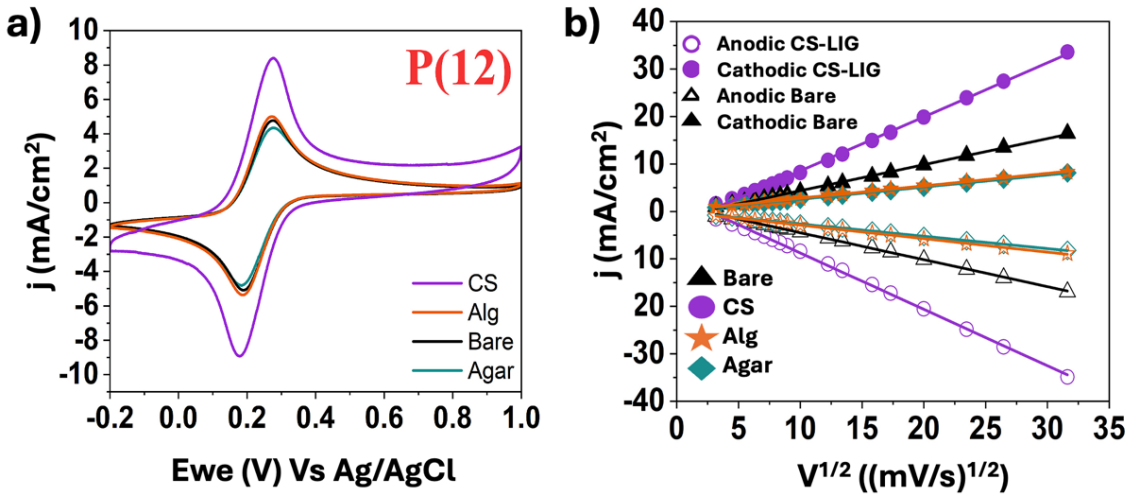


Figure 31: Electrochemical behaviour of bare P12%S160 and HM-coated LIG in 5mM $Fe(CN)_6^{4-}$;a) CV at scan rate, ν = 50 mV/s); b) RS plot for bare and HM-coated LIGs to understand dependence of anodic and cathodic peak currents on the square root of scan rate used for electroactive surface area estimation[280].

Among the investigated hydrogel coatings, CS-LIG exhibited the highest anodic and cathodic peak currents. In contrast, Agar-LIG and Alg-LIG electrodes produced voltammetric responses comparable to, or only slightly different from, the bare LIG electrode. This observation demonstrate that the hydrogel layers actively influence the electrochemical environment surrounding the electrode. This observation is consistent with the wettability studies discussed in the previous section, where CS transformed the initially hydrophobic graphene surface into a highly hydrated interface capable of rapidly absorbing water. The enhanced electrochemical response produced by CS-LIG suggests that the hydrogel network facilitates penetration of electrolyte species into the porous graphene architecture. These indicate that improved wettability alone

cannot fully explain the electrochemical response. Rather, the specific chemical nature of the hydrogel, including its charge characteristics and interactions with electrolyte species, appears to play an important role in determining electrode performance.

Following the comparative electrochemical evaluation of the hydrogel-coated electrodes, EASA was determined to quantify the influence of hydrogel surface engineering. Prior to EASA determination, D of the ferri/ferrocyanide redox probe within each HM-modified interface was estimated from CA measurements according to the procedure described in experimental section. The calculated D varied among the investigated hydrogel coatings, indicating that the HM influence the transport of electroactive species toward the underlying LIG surface. Among the investigated hydrogels, the CS-LIG electrode exhibited the lowest D, whereas Agar and Alg produced comparatively higher D. This behaviour demonstrates that diffusion through the hydrogel layer depends strongly on the chemical nature of the deposited hydrogel than solely on its physical presence. The representative CA together with calculated D are presented Table 10.

Table 10. Estimated values for D for bare and HM-coated SPCE (CS, Alg, Agar).

Electrode	D $\times 10^{-6}$ (cm^2 s^{-1})
Bare SPCE	**6.98**
Alg-SPCE	**3.99**
Agar-SPCE	**2.40**
CS-SPCE	**0.38**

The reduced D observed for CS should not be interpreted as inferior electrochemical performance. Instead, the positively charged chitosan matrix promotes favourable interactions with the negatively charged ferri/ferrocyanide redox species, increasing their partitioning within the hydrogel while simultaneously reducing their diffusion rate. So a larger concentration of electroactive species becomes available at the electrode interface despite the slower apparent diffusion through the modification layer. This behaviour is consistent with the electrochemical response observed in the previous CV studies and provides an important mechanistic basis for interpreting the calculated EASA values.

To further evaluate the electrochemical behaviour, the corresponding Randles-Ševčík plots are presented in and the calculated EASA values are summarized in Table 11. The determination of EASA provides insight into the fraction of the electrode surface that actively participates in the electrochemical reaction and therefore helps explain the differences in voltammetric response observed among the HM-coated LIG electrodes. For all investigated electrodes, both anodic and cathodic peak currents increased linearly with the square root of the scan rate, indicating that the electrochemical process remained predominantly diffusion controlled within the investigated experimental conditions.

Agar-LIG and Alg-LIG exhibited EASA values of 0.20 cm^2 and 0.16 cm^2, respectively. This reveals these hydrogel coatings did not increase the accessible electrochemical surface relative to the bare LIG. Instead, both coatings produced slightly lower EASA values than the bare electrode.

In contrast, the CS-LIG electrode exhibited a remarkably larger EASA of 2.34 cm^2, representing an approximately 9-fold increase compared with bare LIG and nearly 28 times larger than the geometric electrode area (0.085 cm^2). This substantial increase demonstrates that CS surface engineering enables

significantly greater electrochemical utilization of the hierarchical porous graphene structure than either Agar or Alg modifications Table 11.

Table 11. EASA of bare and HM LIG electrodes estimated from the Randles-Ševčík relationship.

Electrode	k ×10⁻³ (cm s⁻¹)	EASA(a) (cm²)	EASA(c) (cm²)
Bare LIG	**4.12**	**0.25**	**0.26**
Alg-LIG	**7.99**	**0.16**	**0.17**
Agar-LIG	**6.78**	**0.20**	**0.20**
CS-LIG	**3.88**	**2.34**	**2.33**

This superior EASA observed for CS-LIG can be attributed to the favourable interaction between the positively charged CS chains and the oxygen-containing functional groups present on the LIG surface. Together with mechanical interlocking within the hierarchical porous graphene network. These interactions promote intimate contact between the hydrogel and the conductive substrate, allowing a larger fraction of the porous graphene surface to participate in the electrochemical process.

The contrasting behaviour of the three hydrogel modifications indicates that the electrochemical response is governed not only by the presence of a hydrogel layer but also by the interaction between the polymer and the porous graphene substrate. While Agar and Alg do not translate into an increase in electrochemically accessible surface area. Conversely, the chitosan coating allows the underlying porous graphene network to be utilized much more effectively during the electrochemical process, consistent with the enhanced current response observed in the CV studies. The enhanced EASA may also be associated with improved partitioning of ferri/ferrocyanide species within the CS matrix, increasing the effective availability of electroactive species at the electrode interface.

5.2.5 Heterogeneous electron transfer kinetics (results from[280])

Heterogeneous electron transfer represents the fundamental process through which electrons are exchanged between an electrode surface and electroactive species in solution. The rate at which this process occurs significantly influences electrochemical response, determining peak separation, current density, charge transfer resistance and overall performance. The k^0 was determined for bare and HM LIG electrodes using data presented in the previous section. The calculated k^0 values are summarized in Table 12.

The k^0 demonstrate that hydrogel surface engineering influences the charge transfer kinetics differently depending on the deposited polymer. Among the investigated electrodes, Alg and Agar exhibited larger k^0 values than the bare LIG electrode, whereas the CS-LIG produced a slightly lower k^0. Initially the lower k^0 for CS appears inconsistent with its superior voltammetric response and substantially larger electroactive surface area.

Table 12. Heterogeneous electron-transfer rate constants of bare and HM-coated LIG electrodes.

Electrode	$k^0 \times 10^{-3}$ (cm s^{-1})
Bare LIG	**4.12**
Alg-LIG	**7.99**
Agar-LIG	**6.78**
CS-LIG	**3.88**

However, this behaviour reflects the different physicochemical processes governing electron transfer and mass transport within the hydrogel layer. Unlike agarose and alginate, chitosan contains protonatable amino groups that interact favourably with the negatively charged ferri/ferrocyanide redox species. These electrostatic interactions increase the partitioning of the redox probe into the hydrogel matrix while simultaneously reducing its diffusion rate through the polymer layer. Consequently, although the apparent k^0 decreases slightly, the local concentration of electroactive species at the electrode interface increases, producing significantly larger voltammetric currents and a markedly greater EASA. This observation demonstrates that the electrochemical performance of hydrogel-modified LIG cannot be evaluated solely on the basis of k^0. Instead, the overall response results from the combined influence of surface chemistry, electrolyte accessibility, redox-probe partitioning and electrochemically accessible surface area. Therefore, the substantial increase in EASA associated with CS outweighs the modest reduction in the apparent electron-transfer rate constant, leading to the most favourable overall electrochemical performance among the investigated hydrogel coatings.

The behaviour of Agar-LIG and Alg-LIG further supports this interpretation. Although these hydrogels exhibited comparatively larger k^0 values, their EASA remained similar to or lower than that of bare LIG. Therefore, the apparent discrepancy between the EASA and k^0 results underscores the importance of evaluating multiple electrochemical descriptors when assessing hydrogel-modified electrodes. That is no single parameter is sufficient to explain electrode performance.

5.2.6 Electrochemical impedance spectroscopy analysis (results from[280])

EIS was employed to further investigate the influence of hydrogel surface engineering on the interfacial electrochemical properties. All electrodes exhibit the characteristic impedance response consisting of a high-frequency semicircle followed by a low-frequency linear region associated with diffusion-controlled transport. Comparison of the EIS spectra demonstrates that hydrogel modification significantly alters the interfacial electrochemical behaviour of the LIG electrode. The bare LIG electrode exhibits the largest impedance response, indicating a relatively higher resistance to interfacial charge transfer. Following hydrogel deposition, the impedance characteristics change depending on the hydrogel used for modification.

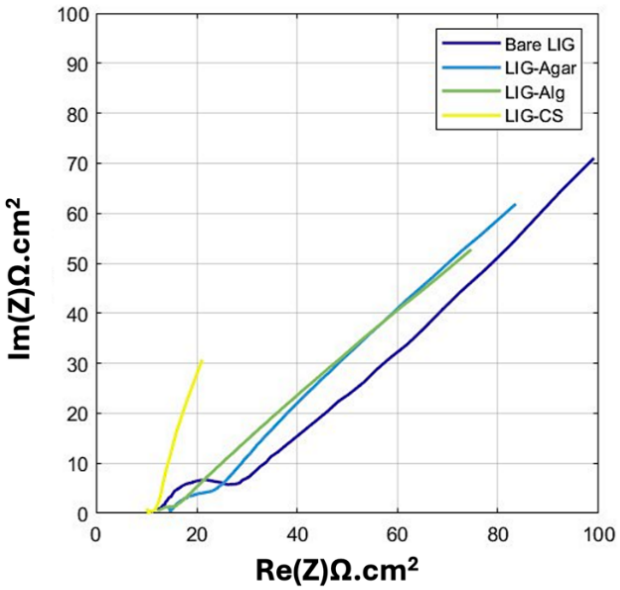


Figure 32: Comparison of EIS spectra for bare and hydrogel modified LIGs[280].

Among the investigated modifications, the CS-LIG electrode exhibits the smallest impedance response, indicating the lowest charge transfer resistance and the most favourable interfacial electron-transfer behaviour. In contrast, Agar-LIG and Alg-LIG exhibit intermediate impedance responses, demonstrating that although both hydrogels modify the electrode interface, they do not reduce the interfacial resistance to the same extent as CS. The reduced impedance observed for CS-LIG therefore complements the EASA and CV results, confirming that CS provides the most effective hydrogel interface for surface engineering of LIG. Therefore CS was selected for further optimization studies focused on improving the stability of CS through glutaraldehyde crosslinking.

5.2.7 Effect of chitosan crosslinking density on electrochemical performance (results from[280])

Crosslinking density affects the structure of the hydrogel thereby it can affect the kinetic of electrochemical processes. In case of CS, Glutaraldehyde crosslinking stabilizes the CS network by forming covalent linkages between polymer chains, thereby improving the mechanical integrity of the hydrogel coating To investigate the effect of crosslinking To evaluate this effect, CV was performed for uncrosslinked, single-crosslinked, double-crosslinked and triple-crosslinked CS- LIG electrodes. The corresponding CVs recorded at different scan rates are presented in Figure 33.

The electrochemical response varied considerably with the degree of crosslinking. The uncrosslinked CS-LIG exhibited voltammetric behaviour closely resembling that of bare LIG, indicating that the deposited CS layer contributed little to the electrochemical response in the absence of glutaraldehyde treatment.

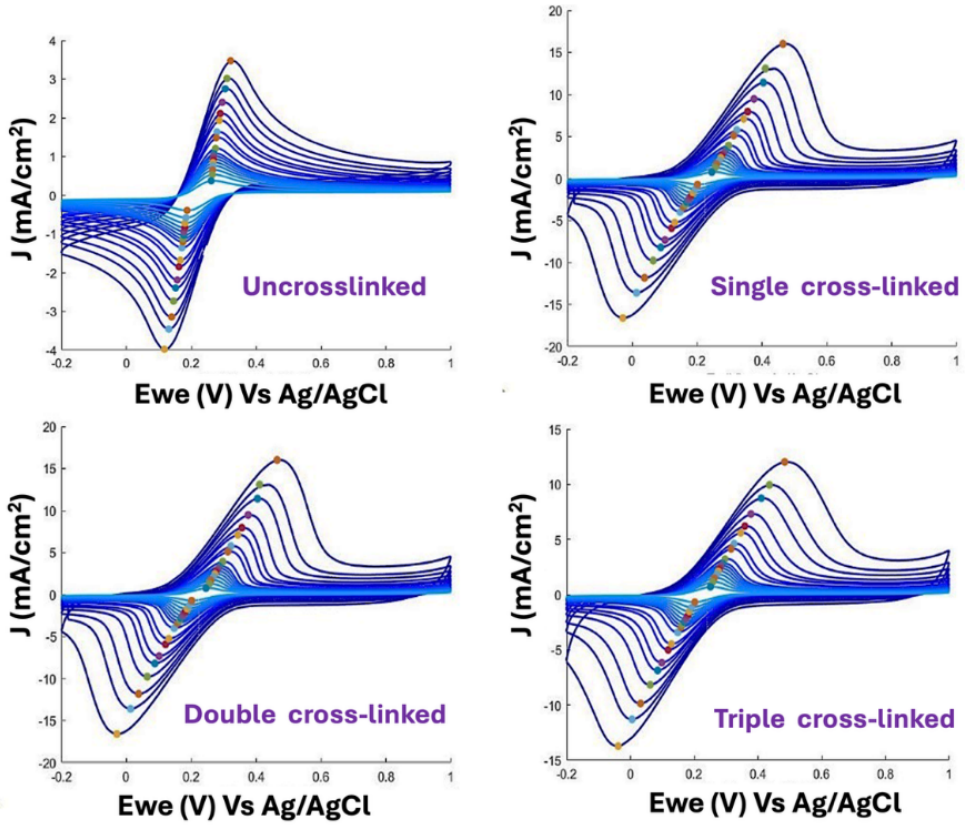


Figure 33: Effect of crosslinking in CS. of CS-LIG with different glutaraldehyde crosslinking densities: (a) uncrosslinked, (b) single-crosslinked, (c) double-crosslinked and (d) triple-crosslinked, recorded in 5mM $K_4[Fe(CN)_6]$ electrolyte at different scan rates[280].

This observation suggests that, without chemical crosslinking, adsorbed CS chains are insufficiently stabilized on the electrode surface and are likely to dissolve or detach during electrochemical measurements. Consequently, the beneficial effects of hydrogel surface engineering cannot be maintained under these conditions.

Following glutaraldehyde treatment, a pronounced enhancement of the voltammetric response was observed. Both the single- and double-crosslinked CS-LIG electrodes exhibited substantially higher peak currents compared with the uncrosslinked electrode, indicating that crosslinking effectively stabilizes the hydrogel while preserving efficient charge transfer through the electrode-electrolyte interface. The similarity of the CV obtained for the single- and double-crosslinked electrodes further indicates that a second crosslinking treatment does not produce a significant additional improvement in electrochemical performance.

In contrast, the triple-crosslinked electrode exhibited a noticeable reduction in peak current compared with the single- and double-crosslinked electrodes. This behaviour indicates that excessive crosslinking produces a denser network, which can restrict the transport of electroactive species through the hydrogel layer and consequently reduces the rate of the electrochemical process. Although increased crosslinking improves structural stability, excessive network densification introduces an additional barrier for mass transport, thereby limiting the electrochemical performance of the modified electrode.

This observation indicates that excessive crosslinking can negatively influence electrochemical performance. This depends on achieving an appropriate balance between hydrogel stability and electrolyte accessibility. Insufficient crosslinking results in poor membrane stability, whereas excessive crosslinking limits the

diffusion of electroactive species through the polymer network. Under the investigated experimental conditions, the single-crosslinked CS-LIG electrode provided the most favourable compromise between structural integrity and electrochemical performance and was therefore selected for subsequent immobilization. The optimized single-crosslinked CS-LIG provides a stable, hydrophilic and electrochemically active interface that is well suited for subsequent surface functionalization. The presence of abundant amino functionalities together with the improved structural stability of the hydrogel offers a versatile platform for further chemical modification and, where required, immobilization of catalytic or biological recognition elements in subsequent stages of electrode development.

5.2.8 Transition from hydrogel interphase engineering to metallic functionalization

However, the electrochemical analyses also revealed that improvements in EASA do not necessarily translate into proportional enhancements in intrinsic charge transfer kinetics. Although CS-LIG electrodes exhibited the highest EASA, the k^0 remained comparable to that of bare LIG. This observation indicates that optimization of mass transport and electrolyte accessibility alone is insufficient to fully exploit the electrochemical potential of LIG.

The results therefore suggest that additional surface-engineering approaches can be employed to improve catalytic activity and facilitate more efficient electron-transfer processes. One promising strategy involves the incorporation of metallic nanostructures onto the graphene surface. Noble and transition metal nanomaterials can provide highly active electrochemical sites, reduce charge transfer resistance, accelerate redox reactions and enhance signal transduction. Moreover, metallic coatings can provide a versatile surface for subsequent functional interfaces for subsequent chemical modification.

The focus of this thesis now shifts from hydrogel-mediated interfacial engineering toward metallic functionalization of LIG. While hydrogels primarily influence mass transport, wettability and analyte partitioning, metallic nanostructures are expected to directly influence charge transfer kinetics and electrocatalytic activity. In preference to representing competing strategies, hydrogel engineering and metallic functionalization address complementary aspects of electrode design. The integration of these complementary surface-engineering approaches provides a rational methodology for developing advanced electrochemical interfaces capable of supporting a broad range of electroanalytical applications.

5.3 Nanozyme-based bimetallic surface engineering (results from[283])

Among the available surface modification approaches, electrodeposition of metallic nanostructures offers a versatile and controllable route for tailoring the electrochemical properties. In contrast to hydrogel coatings, which primarily regulate the physicochemical environment surrounding the electrode surface, metallic nanostructures introduce catalytically active sites capable of accelerating interfacial electron-transfer reactions, reducing charge transfer resistance. Thereby promoting electrochemical oxidation and reduction processes. The morphology, composition and oxidation state of electrodeposited metals can be precisely controlled through electrochemical deposition parameters. This enables the systematic optimization of catalytic performance while preserving the porous architecture and high conductivity of LIG.

Ir and Pt based nanomaterials are among the most widely investigated electrocatalysts because of their excellent chemical stability, high electrical conductivity and outstanding catalytic activity toward a wide

range of electrochemical reactions. Platinum exhibits rapid heterogeneous electron-transfer kinetics and excellent catalytic performance for numerous oxidation reactions, whereas iridium and its oxide species possess exceptional electrochemical stability and catalytic activity toward oxygen-containing intermediates. Combining these two noble metals within a single bimetallic interface offers the possibility of integrating the favourable properties of both materials, while electronic interactions between the two components may further modify the catalytic behaviour beyond that of the corresponding monometallic systems.

Ir was selected due to its exceptional electrochemical stability and the formation of robust IrO_2 surface species under oxidative conditions. Pt was selected because of its well-established catalytic activity toward hydrogen peroxide oxidation and its rapid electron-transfer kinetics. The combination of these two metals was hypothesized to generate a stable bimetallic nanozyme interface capable of enhancing catalytic activity while simultaneously preserving long-term operational stability.

5.3.1 Electrodeposition of Iridium and Platinum nanostructures (results from[283])

The sequential electrodeposition of Ir and Pt NPs is employed to introduce metallic nanostructures onto the selected P19%S220mm/s LIG electrode surface. Thus, metallic nanostructures were fabricated using a two-step galvanostatic electrodeposition process. IrNPs were first deposited onto the LIG surface at a constant current, followed by Pt deposition onto the pre-formed Ir layer. CP curves recorded during electrodeposition provide valuable insight into the nucleation and growth mechanisms occurring at the electrode surface. The CP deposition curves recorded during both electrodeposition steps are presented in Figure 34.

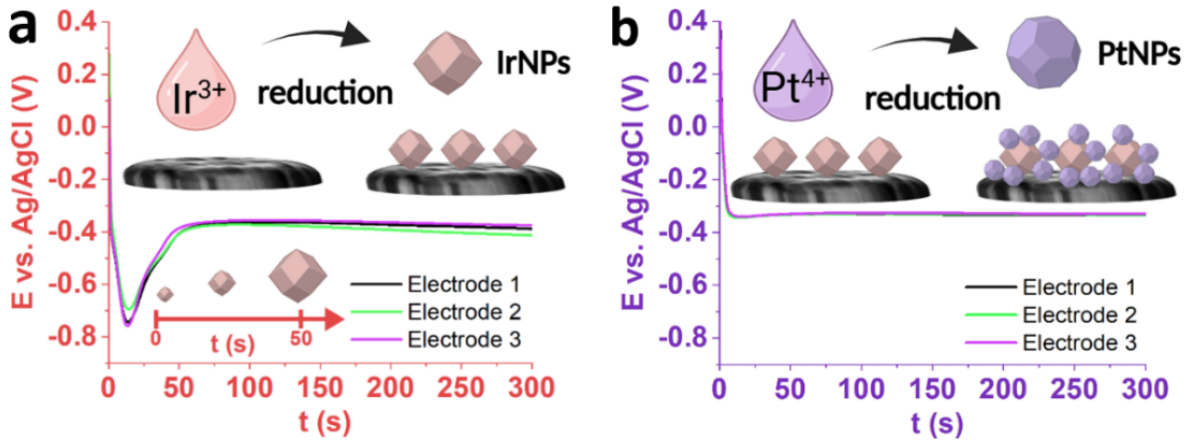


Figure 34: Electrodeposition of Iridium and Platinum nanostructures (a) and (b) CP curves recorded during the electrodeposition of Ir and Pt, respectively, using deposition parameters of (100 µA, 5 min) on three different LIG electrodes. Insets show schematic illustrations of the reduction of metal cations (Ir^{3+} and Pt^{4+}) and the subsequent formation of metal nanoparticles on the LIG surface during electrodeposition[283].

The Ir deposition curves obtained from independently prepared electrodes exhibit nearly identical profiles. This demonstrating excellent reproducibility of the electrodeposition process. During the initial stage of Ir deposition, the applied potential initially exhibited a pronounced negative minimum before gradually stabilizing into a plateau after approximately 50 s. This behaviour indicates an initial nucleation barrier associated with IrNP formation on the electrode surface. The temporary increase in overpotential suggests that additional driving force was required to initiate nucleation of Ir clusters on the porous LIG substrate.

The Pt deposition on the pre deposited Ir-layer ,that is on Ir-coated LIG designated as Ir@LIG surface exhibited a significantly reduced nucleation barrier. The characteristic voltage valley observed during Ir deposition became almost negligible during Pt electrodeposition. This behaviour suggests that pre-existing Ir nanostructures acted as energetically favorable nucleation centers for Pt growth. This facilitating rapid and uniform formation of PtNPs throughout the porous LIG structures. The improved nucleation behaviour suggests that the pre-deposited Ir layer facilitates subsequent Pt deposition, supporting the formation of sequential bimetallic nanostructures. The nearly identical CP responses obtained from three independently fabricated electrodes further demonstrate excellent reproducibility of the electrodeposition process.

To investigate the influence of electrodeposition conditions on the electrochemical behaviour of the modified electrodes, a systematic matrix of deposition currents and deposition times was evaluated. These parameters together with the corresponding electrode codes are summarized in Table 13.

Table 13. Electrodeposition parameters

Electrode	Current (µA)	Time (min)	Metal loading * ($\mu g/cm^2$)
Bare LIG	**0**	**0**	**0**
Ir (50, 5)	**50**	**5**	**140.88**
Ir (100, 5)	**100**	**5**	**281.75**
Ir (150, 5)	**150**	**5**	**422.63**
Ir (100, 10) or Ir@LIG	**100**	**10**	**563.51**
Pt (50, 5)	**50**	**5**	**214.43**
Pt (100, 5)	**100**	**5**	**429.01**
Pt (150, 5)	**150**	**5**	**643.42**
Pt (100, 10) or Pt@LIG	**100**	**10**	**857.99**
Ir-Pt (100,5)	**Ir: 100;Pt: 100**	**Ir: 5;Pt: 5**	**710.75**
Ir-Pt (100,10) or Ir-Pt@LIG	**Ir: 100;Pt: 100**	**Ir: 10;Pt: 10**	**1421.50**

5.3.2 Morphological characterization of Ir-Pt NPs (results from[283])

To determine how sequential electrodeposition modifies the morphology of optimized LIG and to understand the structural evolution of the Ir-Pt catalytic interface, Morphological characterization was carried out. Since the catalytic activity of metallic nanomaterials is strongly influenced by particle morphology and distribution, SEM, TEM, high-angle annular dark-field scanning transmission electron microscopy (HAADF-STEM) were employed. The SEM micrographs presented in Figure 35 illustrate the progressive morphological evolution of the LIG surface during metallic functionalization.

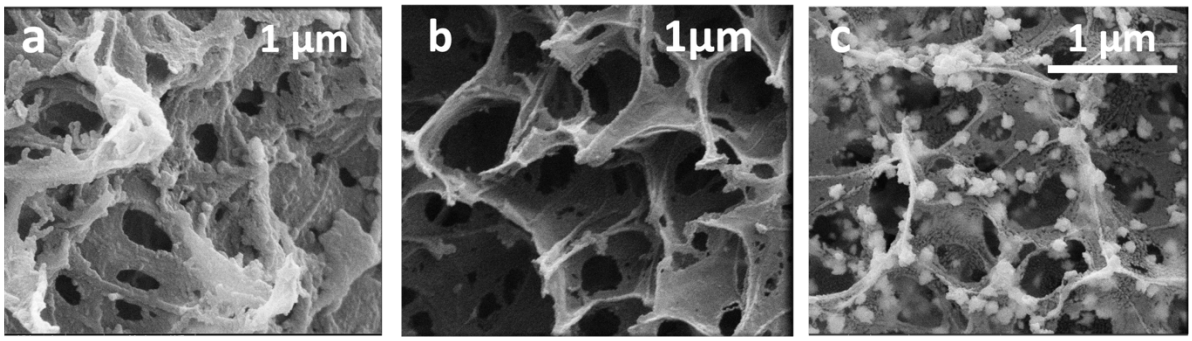


Figure 35: SEM images illustrating the morphological evolution of bimetallic functionalized LIG.(a) (Ir@LIG, (c) Ir-Pt@LIG. The images demonstrate the formation and distribution of metallic nanostructures on the porous graphene framework[283].

SEM reveals the porous LIG architecture serves not only as a conductive support but also as a scaffold capable of accommodating high densities of catalytically active nanostructures. Following electrodeposition of Ir, discrete NPs are uniformly distributed across the graphene framework without obstructing the interconnected porous architecture. The deposited particles preferentially decorate exposed graphene edges and defect-rich regions, indicating that these energetically favourable surface sites act as nucleation centres during the electrodeposition process. The porous morphology of the underlying graphene scaffold remains preserved after Ir deposition, demonstrating that the electrodeposition process modifies the surface chemistry while maintaining the structural characteristics responsible for the high surface area of LIG.

Subsequent Pt deposition further modifies the electrode surface through the formation of additional metallic nanostructures. Compared with the monometallic electrodes, the sequentially deposited Ir-Pt electrode exhibits a more uniformly decorated graphene framework, with metallic NPs distributed throughout the porous architecture. The Pt nanostructures appear more densely distributed throughout the graphene framework and exhibit a finer nanoparticulate appearance compared with the Ir-modified surfaces. Despite the increased NP coverage, the interconnected graphene network remains clearly visible, indicating that sequential electrodeposition produces a conformal catalytic coating than a continuous metallic film. Preservation of the porous graphene morphology is particularly advantageous because it maintains efficient electrolyte penetration while simultaneously increasing the density of catalytically active surface sites. To obtain further insight into the morphology of the electrodeposited nanostructures, TEM characterization was performed and TEM images are presented in Figure 36.

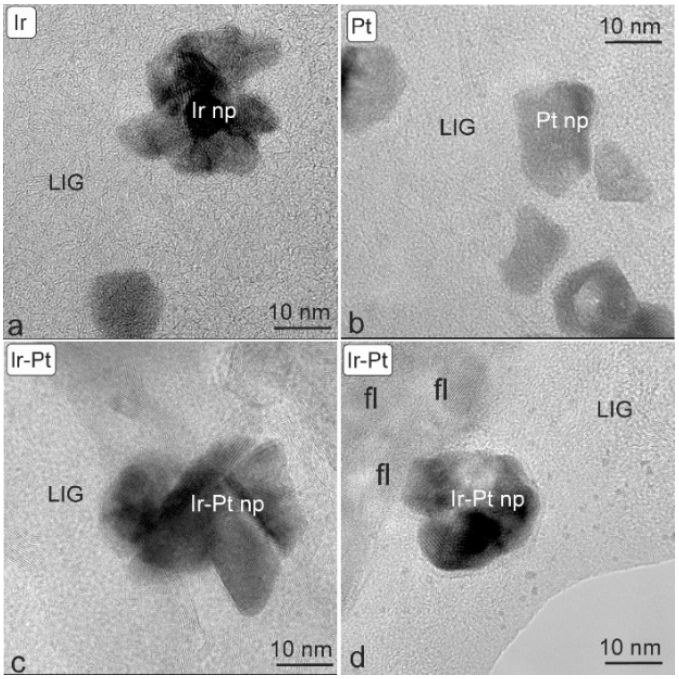


Figure 36: TEM images of electrodeposited metallic nanostructures: a) Ir@LIG, (b) Pt@LIG, (c) and (d) Ir-Pt@LIG. In all specimens, the porous structure of LIG is visible with sections of layered graphene together with crystalline nanoparticles of Ir (a) and Pt (b). In the Ir-Pt@LIG specimen, additionally, the thin flake-like (fl) few-nanometer crystals are observed next to the Ir-Pt NP[283].

TEM reveal that both Ir and Pt are deposited in the form of nanoscale crystalline particles. The NPs are well dispersed and exhibit intimate contact with the graphene substrate, facilitating efficient electrical communication between the metallic phase and the conductive LIG framework. The sequential Ir-Pt sample displays closely associated metallic nanostructures distributed over the graphene support, suggesting successful formation of the bimetallic catalytic interface through the sequential electrodeposition strategy. Higher-resolution structural characterization using HAADF-STEM further confirms the successful incorporation of both metallic components.

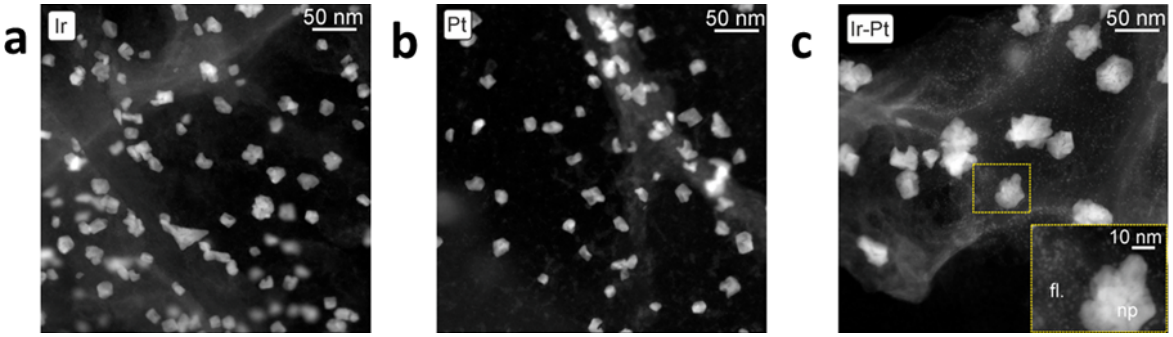


Figure 37: HAADF-STEM for nanozyme electrode. (a-c) HAADF-STEM results for (a) Ir@LIG, (b) Pt@LIG and (c) Ir-Pt@LIG. Inset in (c) shows Ir-Pt nanoparticle and a few nanometer-diameter flakes observed in Ir-Pt specimen[283].

The HAADF-STEM images further reveal the formation of highly dispersed metallic structures integrated within the graphene architecture instead of localized agglomerates. Such distribution is advantageous because it maximizes exposure of catalytic sites while preserving access to the underlying conductive graphene framework. The strong atomic-number contrast observed in the HAADF image confirms the presence of

high-atomic-number metallic nanoparticles on the low-atomic-number graphene support, while elemental mapping verifies that both Ir and Pt are distributed across the modified LIG surface.

These observations confirm successful sequential electrodeposition and demonstrate that the adopted fabrication strategy produces a homogeneous bimetallic catalytic interface than isolated monometallic deposits. The observed morphology therefore provides direct structural evidence supporting the nucleation mechanism proposed from the CP electrodeposition experiments.

Overall, these results demonstrate the homogeneous distribution of NPs throughout the porous graphene network ensures that electrocatalytic activity is not confined to the external electrode surface but instead porous graphene substrate enables uniform NP deposition throughout the three-dimensional architecture, thereby maximizing catalyst utilization. Simultaneously, the nanoparticulate morphology prevents complete blockage of the pore network and maintains electrolyte accessibility. This characteristic is particularly advantageous for electroanalytical applications, where efficient electron transfer and rapid catalytic conversion of enzymatically generated species are essential for signal amplification.

5.3.3 Structural and surface chemical characterization of Ir-Pt interfaces (results from[283])

XPS was employed to determine the chemical composition and oxidation states of the electrodeposited Ir-Pt nanostructures and to establish the chemical basis for the catalytic properties of the modified LIG interface. Whereas electron microscopy confirmed the successful formation and spatial distribution of the nanoparticles, XPS provides information regarding their surface chemical environment and oxidation states, both of which strongly influence electrocatalytic performance. High-resolution XPS spectra of the C 1s, Ir 4f and Pt 4f regions are presented in Figure 38 below.

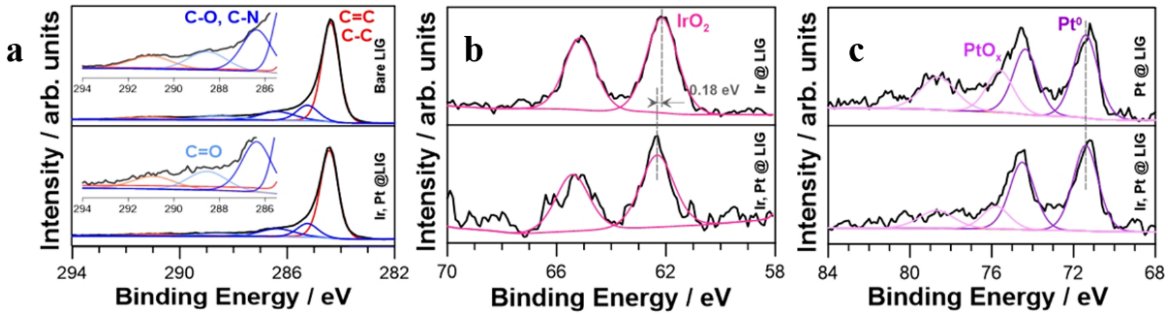


Figure 38: XPS of nanozymes. a) High-resolution C 1s spectra of bare LIG and Ir-Pt@LIG. b) High-resolution Ir 4f spectra of Ir (50, 5) and Ir-Pt@LIG. c) High-resolution Pt 4f spectra of Pt (50,5) and Ir-Pt@LIG[283].

The XPS survey spectra confirms successful incorporation of both Ir and Pt species onto the LIG. The survey spectrum of bare LIG is dominated by carbon and oxygen signals associated with the graphene framework and residual oxygen-containing functional groups generated during laser-induced graphitization. Following electrodeposition, additional peaks corresponding to Ir and Pt become clearly visible, confirming successful formation of bimetallic modified electrodes. The appearance of these characteristic metallic signals verifies successful fabrication of the intended bimetallic nanozyme interface by electrodeposition process and are effectively introduces catalytically active species onto the porous graphene architecture.

The high-resolution Ir 4f spectra shown in Figure 38b reveal that the deposited Ir exists predominantly in an oxidized chemical state and not as metallic Ir^0. The Ir 4f doublet is dominated by IrO_2-related species,

demonstrating that oxidation of the deposited Ir occurs following electrodeposition and exposure to the electrochemical environment. The predominance of IrO_2 is particularly significant because it indicates that the deposited Ir functions as an electrochemically active oxide than merely increasing the metallic surface coverage. The presence of catalytically active iridium oxide species is expected to contribute to both the electrochemical stability and catalytic performance of the modified electrode, providing active surface sites capable of participating in oxidation reactions. The comparison of the Ir 4f spectra obtained before and after Pt deposition demonstrates that the characteristic IrO_2 chemical state is retained following sequential electrodeposition, indicating that the subsequent Pt deposition does not alter the chemical identity of the underlying Ir layer. Instead, both metallic components coexist within the final bimetallic interface.

In addition to catalytic activity, the presence of IrO_2 may improve long-term electrode stability by protecting the underlying graphene architecture from degradation during repeated electrochemical cycling. Ir component of the bimetallic system contributes both catalytic and structural advantages to the overall nanoparticle functionalized platform.

The chemical environment of platinum was investigated through analysis of the Pt 4f region, the spectra indicate the coexistence of metallic Pt and oxidized platinum species on the electrode surface. The simultaneous presence of Pt^0 and PtOx species is commonly observed for electrodeposited Pt nanostructures and reflects partial surface oxidation upon exposure to air and electrochemical environments. Metallic Pt provides highly conductive pathways that facilitate rapid heterogeneous electron transfer, whereas oxidized platinum introduces additional oxygen-containing surface-active sites capable of participating in electrochemical oxidation processes. The mixed-valence platinum surface is expected to provide a chemically versatile catalytic interface suitable for a broad range of electrochemical reactions.

The XPS results demonstrate that the fabricated Ir-Pt interface consists of a chemically complex surface containing both oxidized iridium species and mixed platinum species. Such a composition is expected to provide catalytic advantages beyond those achievable with either metal alone. The IrO_2 component contributes electrochemical stability and catalytic activity, whereas platinum provides highly efficient electron-transfer pathways and strong electrocatalytic activity. Thus, XPS analysis confirms that sequential electrodeposition does not simply increase metal loading but instead generates a chemically sophisticated NP based multifunctional catalytic interface.

The combined morphological and XPS analyses demonstrate that sequential electrodeposition successfully produced a porous Ir-Pt nanozyme interface consisting of uniformly distributed metallic nanostructures and catalytically active IrO_2/PtOx surface species. These reveals important structural and chemical evidence for the formation of a multifunctional electrocatalytic platform. However, the presence of catalytically active nanostructures alone does not necessarily guarantee improved electrochemical performance. Therefore, it is necessary to evaluate how the introduction of Ir and Pt nanostructures influences the electrochemical behaviour.

5.3.4 Electrochemical behaviour of bimetallic functionalized LIG (results from[283])

To identify the most suitable nanozyme platform and to study the influence of bimettalic functionalization on LIG, CV measurements were performed in a 5mM $[Fe(CN)_6]^{3-/4-}$ redox probe prepared in 0.1 M PBS (pH 7.4) at different scan rates and electrodes were systematically investigated. The comparison of the CV

responses shown in Figure 39 provides direct insight into the influence of Ir and Pt nanostructures on the reversibility of the redox process, electron-transfer efficiency and overall electrochemical activity of the modified electrodes.

The bare LIG electrode exhibits the characteristic reversible redox behaviour of the ferri/ferrocyanide couple with relatively low anodic and cathodic peak currents. Following electrodeposition of Ir, a pronounced increase in the peak current density is observed together with a noticeable enhancement of the overall CV response, indicating that incorporation of Ir nanostructures increases the electrochemically active interface available for electron transfer.

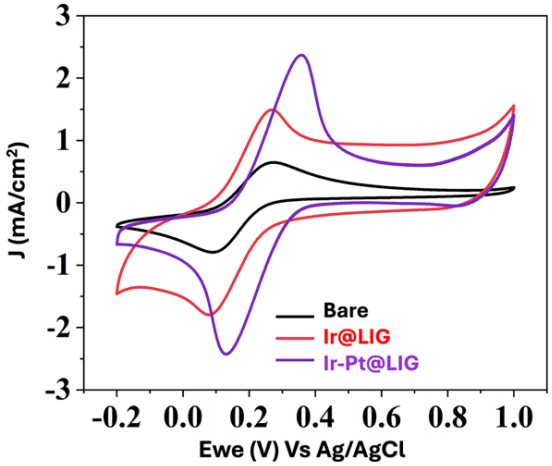


Figure 39: Comparison of CV plots of bare and nanozymes modified electrodes (Ir@ LIG and Ir-Pt@LIG) recorded in 5mM $[Fe(CN)_6]^{3-/4-}$ redox probe prepared in 0.1 M PBS at a scan rate of 50 mV/s. The comparison illustrates the influence of metallic functionalization on the electrochemical behaviour of the optimized P19%S220 electrode.

Subsequent deposition of Pt onto the Ir-modified electrode produces a further enhancement of the electrochemical response. Among the investigated electrodes, the Ir-Pt-modified LIG exhibits the highest anodic and cathodic peak currents. The increased current response reflects the combined contribution of the conductive graphene framework and the catalytically active metallic nanostructures, which together facilitate more efficient charge transport across the electrode-electrolyte interface.

The progressive increase in peak current from bare LIG to Ir@LIG and finally to Ir-Pt@LIG indicates that sequential electrodeposition successfully transforms the optimized graphene electrode into a more electrochemically active interface. Importantly, the voltammetric profiles remain well defined after metallic functionalization, indicating that the electrodeposition process enhances the electrochemical response while preserving the reversible behaviour of the ferri/ferrocyanide redox couple.

To further investigate the electrochemical characteristics of the modified electrodes, CV was subsequently performed over a range of scan rates (200, 150, 100, 80, 60, 40, 20). For all electrodes, both anodic and cathodic peak currents increase systematically with increasing scan rate while maintaining the characteristic voltammetric shape. Besides, the peak current exhibits an excellent linear relationship with the square root of the scan rate, confirming that the electrochemical process remains predominantly diffusion-controlled following metallic functionalization.

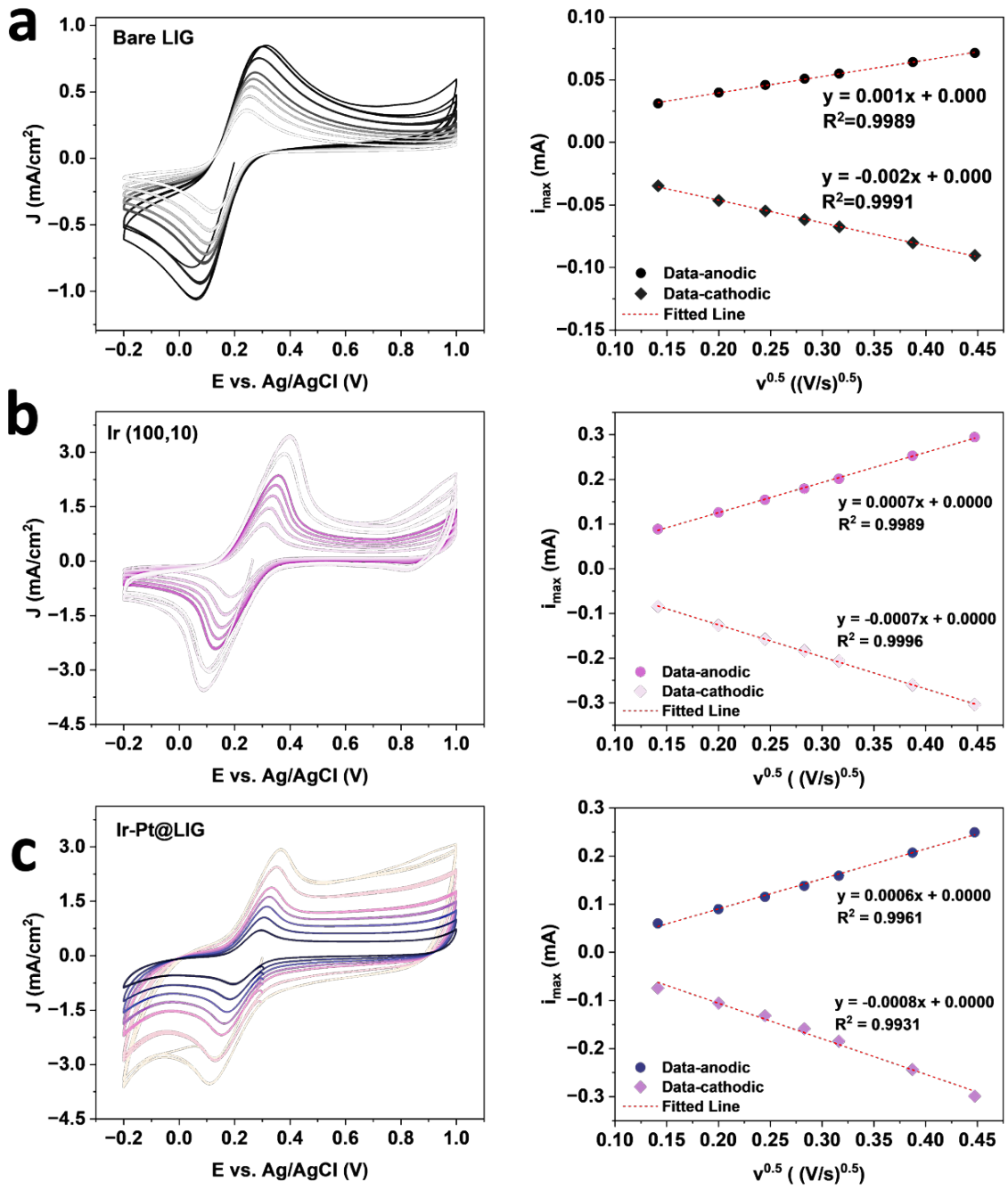


Figure 40: Estimation of EASA bare vs nanozymes. CV recorded at different scan rates (left) and corresponding Randles-Ševčík (RS) fitted plots (right) for (a) bare LIG, (b) Ir@LIG and (c) Ir-Pt@LIG. All the measurements were carried out in 5mM $[Fe(CN)_6]^{3-/4-}$ in PBS[283].

The higher slopes obtained for the Ir- and Ir-Pt-modified electrodes indicate an increase in electrochemically accessible surface area compared with bare LIG. Since the slope of the Randles-Ševčík relationship is directly proportional to the EASA, these results suggest that metallic functionalization substantially increases the number of electrochemically accessible reaction sites. Quantitative estimation of the EASA using Randles–Ševčík plots and k^0, determined using Nicholson's method is summarised in Table 14.

Table 14. EASA and k^0 of the bare and nanozyme modified electrodes

Electrode	EASA (cm^2)	K^0 cm/s
bare LIG	0.195	0.0015
Ir (50, 5)	0.280	0.0052
Ir (100, 5)	0.250	0.0030
Ir (150, 5)	0.125	0.0039
Ir (100, 10)/Ir@LIG	0.245	0.0025
Pt (50, 5)	0.330	0.0026
Pt (100, 5)	0.157	0.0060
Pt (150, 5)	0.123	0.0076
Pt (100, 10) or Pt@LIG	0.164	0.0045
Ir-Pt (100,5)	0.141	0.0013
Ir-Pt (100,10) or Ir-Pt@LIG	0.226	0.0038

The unmodified LIG electrode exhibited an EASA of 0.195 cm^2 and a k^0 of 0.0015 cm/s. Considering that the geometric electrode area was only 0.085 cm^2, the porous graphene structure generated an electrochemically active area approximately 2.3 times larger than the projected geometric surface.

The results demonstrate that metallic functionalization substantially influences the EASA of the optimized LIG electrode. Compared with bare LIG, deposition of both iridium and platinum nanostructures increases the electrochemically accessible surface available for charge transfer. This increase is attributed to the introduction of nanoscale metallic features that provide additional electrochemically active sites while preserving the interconnected porous graphene architecture established during laser fabrication.

For Ir@LIG, the highest EASA was obtained at the lowest deposition current investigated. Specifically, Ir(50,5) exhibited an EASA of 0.280 cm^2 and k^0 of 0.0052 cm/s. Increasing the deposition current from 50 µA to 100 µA reduced the EASA to 0.250 cm^2, while a further increase to 150 µA caused a substantial decrease to only 0.125 cm^2. These results suggest that excessive Ir deposition progressively blocks the porous graphene architecture, reducing the accessibility of electrochemically active sites.

A similar tendency was observed for Pt deposition. The Pt(50,5) electrode displayed the highest EASA among all monometallic electrodes, reaching 0.330 cm^2. However, increasing deposition current resulted in a pronounced reduction of EASA, decreasing to 0.157 cm^2 for Pt(100,5) and 0.123 cm^2 for Pt(150,5). Unlike Ir, however, Pt deposition produced a substantial increase in electron-transfer kinetics. The k^0 value increased from 0.0026 cm/s for Pt(50,5) to 0.0076 cm/s for Pt(150,5), representing the highest electron-transfer rate observed among all investigated electrodes. These reveals that platinum primarily enhances charge transfer kinetics, whereas Ir contributes more strongly to surface area enhancement.

Interestingly, the bimetallic Ir-Pt electrodes combined characteristics of both individual metals. The Ir-Pt(100,10) electrode exhibited an EASA of 0.226 cm² and a k^0 value of 0.0038 cm/s. Although these values were not individually the highest among all tested samples, they represented a balanced combination of EASA and electron-transfer kinetics while simultaneously providing the highest theoretical metal loading and most extensive nanozyme coverage. Overall these results indicate that sequential electrodeposition provides an effective strategy for constructing multifunctional electrochemical interfaces that combine high surface area with catalytically active nanostructures.

5.3.4.1 Integrated correlation between theoretical metal loading, electroactive surface area and electron-transfer kinetics (results from[283])

In order to establish the relationship between theoretical metal loading, EASA and k^0, a graph was plotted where the theoretical metal loading is represented on the x-axis, the calculated EASA on the y-axis and the bubble diameter representing k^0 and obtained as Figure 41.

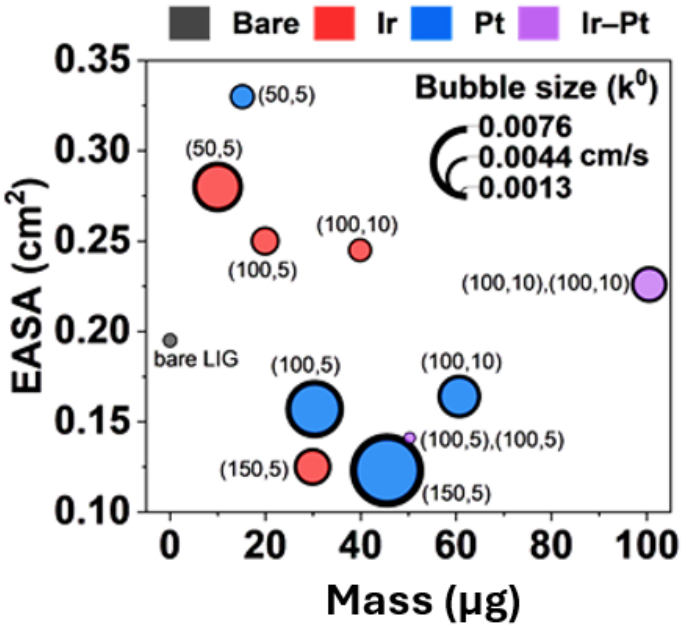


Figure 41: Bubble plot - Bubble plot illustrating the relationship between the theoretical metal loading (calculated using Faraday's law), electroactive surface area (EASA) and heterogeneous electron-transfer rate constant (k^0) for bare and nanozyme-modified LIG electrodes. Bubble diameter represents k^0 [283].

It should be noted that the metal loading shown in Figure 41 represents the theoretical loading estimated from Faraday's law assuming 100% current efficiency and therefore provides a comparative than experimentally measured parameter.

The integrated correlation reveals that EASA and electron-transfer kinetics do not scale linearly with theoretical metal loading. Instead, an optimum region exists where sufficient metal coverage is achieved without excessive blockage of the porous graphene framework. At higher deposition currents, thicker metallic deposits likely reduce pore accessibility and increase structural compactness, leading to lower EASA despite higher theoretical metal loading.

The correlation plot also highlights the distinct electrochemical roles of iridium and platinum within the fabricated catalytic interfaces. Ir-modified electrodes generally occupy the upper region of the plot, indicating their strong contribution toward increasing the EASA. In contrast, platinum-modified electrodes exhibit comparatively larger bubble diameters despite their more moderate EASA values, demonstrating that platinum contributes more significantly to the enhancement of heterogeneous electron-transfer kinetics than to the expansion of the electrochemically accessible surface itself. Overall, Ir-modified electrodes demonstrated superior EASA values, while Pt-modified electrodes exhibited faster heterogeneous electron-transfer kinetics.

The sequentially electrodeposition Ir-Pt interfaces occupy an intermediate region of the correlation plot, combining relatively high EASAs with enhanced heterogeneous electron-transfer rate constants. In place of maximizing either electrochemical descriptor individually, the bimetallic architecture provides a balanced combination of extensive electrochemically accessible surface area and rapid intrinsic electron-transfer kinetics. This balanced behaviour is consistent with the superior electrochemical performance observed during the preceding electrochemical characterization. Since bimetallic Ir-Pt hetero-nanostructures integrated both beneficial characteristics, they were therefore selected for subsequent investigations.

5.3.5 Electrochemical impedance spectroscopy and interfacial charge transfer (results from[283])

EIS was employed to evaluate interfacial charge transfer characteristics and EIS analysis confirms that Ir-Pt NP modification significantly enhances the electrochemical performance of LIG electrodes by reducing R_{ct} and improving electron transfer kinetics.

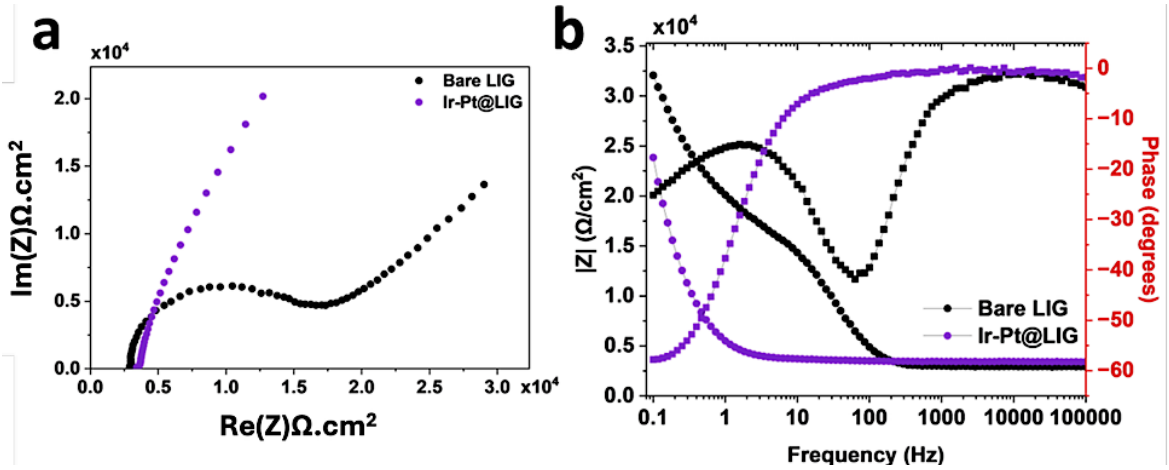


Figure 42: EIS Spectra; (a) Nyquist and (b) Bode plots comparing the EIS performance of bare LIG and Ir-Pt@LIG in 5mM $[Fe(CN)_6]^{3-/4-}$ redox system[283].

As shown in the Nyquist plot, the bare LIG electrode exhibits a prominent semicircle in the high-frequency region, which corresponds to a significant Rct. This indicates slower electron transfer kinetics at the electrode-electrolyte interface, likely due to limited catalytic activity or fewer active sites for redox exchange. In contrast, the Ir-Pt@LIG exhibits a nearly linear response without a distinct semicircle (or a very small one), indicative of a diffusion-controlled process with minimal charge transfer resistance (Rct). Additionally, the inclined line observed in the low-frequency region suggests a combination of capacitive behaviour and

Faradaic processes occurring at the electrode interface. This behaviour signifies enhanced electron transfer kinetics, suggesting that the presence of Ir and Pt nanoparticles effectively catalyzes the redox reaction and significantly lowers the interfacial resistance.

From the Bode plot, the |Z| magnitude of the Ir-Pt@LIG electrode is generally lower than that of the bare LIG across low to mid frequencies, indicating improved charge transfer. At higher frequencies ($f > 10^3$ Hz), the |Z| magnitude becomes slightly higher for the coated electrode, which may be attributed to increased surface roughness or interfacial capacitance effects resulting from the bimetallic layer.

The Ir-Pt@LIG exhibits a broader phase angle response in the mid-to-high frequency region ($f > 10^1$ Hz), with values approaching 0°, indicative of predominantly resistive behaviour. At low frequencies, the phase angle becomes more negative (~ -50°) compared to bare LIG, showing the presence of C_{dl} and Faradaic charge transfer due to redox reactions. This behaviour suggests a more capacitive and stable interfacial environment, likely resulting from the homogeneous and highly conductive surface provided by the bimetallic nanoparticle coating. The extended phase angle range also implies more efficient charge storage and reduced resistive losses.

The phase response of bare LIG reveals two distinct time constants, which can be attributed to separate adsorption-desorption and diffusion-controlled processes occurring at the electrode-electrolyte interface. For nanozyme-based platforms, the low charge transfer resistance is important because efficient electron transfer directly influences catalytic activity, analytical sensitivity and signal generation. Consequently, impedance analysis provides valuable insight into the effectiveness of the deposited metallic nanostructures in facilitating interfacial electrochemical processes. These characteristics establish the fabricated bimetallic electrode as a favourable electrocatalytic platform for subsequent evaluation of catalytic oxidation reactions.

5.3.6 Electrocatalytic activity towards hydrogen peroxide oxidation (results from[283])

Having established that sequential Ir-Pt electrodeposition improves the structural, chemical and electrochemical characteristics of the optimized LIG electrode, it is now necessary to determine whether these improvements translate into enhanced electrocatalytic activity. Hydrogen peroxide was selected as a model electroactive species because its oxidation is widely employed for evaluating the catalytic performance of metallic nanozyme interfaces. As a result, CA measurements were performed to compare the catalytic responses of bare LIG, Ir-, Pt- and Ir-Pt-modified electrodes toward hydrogen peroxide oxidation. To investigate catalytic activity, CA measurements were performed at a constant potential of +0.6 V vs. Ag/AgCl in bare LIG and different electrodes including Ir@ LIG, Pt@ LIG and Ir-Pt@ LIG electrodes using PBS containing 5mM of H_2O_2 as shown in Figure 43.

The CA responses clearly demonstrate the influence of metallic functionalization on catalytic activity toward hydrogen peroxide oxidation. Compared with bare LIG, both Ir- and Pt-modified electrodes exhibit substantially higher oxidation currents, confirming that the deposited metallic nanostructures significantly enhance the catalytic activity of the porous graphene electrode. Among all investigated electrodes, the sequentially modified Ir-Pt@LIG exhibits the highest steady-state current response, demonstrating the superior catalytic performance of the bimetallic interface.

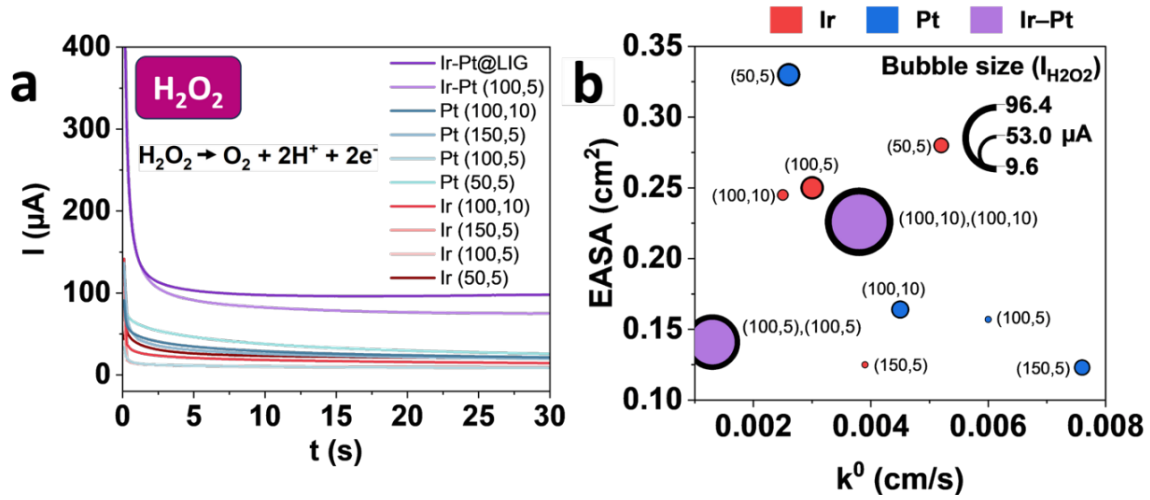


Figure 43: Electrocatalytic performance of nanozyme platform (a) CA recorded at +0.6 V (vs. Ag/AgCl) in 0.01 M PBS containing 5mM H_2O_2 for bare LIG, Ir-, Pt- and Ir-Pt-modified electrodes prepared under different electrodeposition conditions. (b) Integrated correlation between EASA, k^0 [283].

The enhanced response of Ir-Pt@LIG is likely related to the mixed surface chemistry of the bimetallic interface. The enhanced catalytic response cannot be attributed solely to an increase in EASA. Instead, the superior performance of the Ir-Pt electrode reflects the combined influence of multiple complementary factors established throughout this chapter. The porous graphene architecture provides efficient electrolyte accessibility, the homogeneous nanoparticle distribution observed by electron microscopy maximizes the availability of catalytic sites, the mixed $IrO_2/Pt^0/PtO_x$ surface chemistry identified by XPS creates chemically active interfaces, while the enhanced heterogeneous electron-transfer kinetics and reduced charge transfer resistance demonstrated by CV and EIS facilitate rapid interfacial electron exchange. Collectively, these factors produce a catalytic interface that is significantly more active than either bare LIG or the corresponding monometallic electrodes.

To further examine the relationship between the physicochemical and electrochemical characteristics of the fabricated electrodes, the H_2O_2 response was correlated with the electroactive surface area and heterogeneous electron-transfer rate constant, as illustrated in Figure 43b. Instead, the optimum electrocatalytic performance is obtained when both parameters are simultaneously optimized. While Ir deposition primarily increases the EASA and Pt predominantly enhances intrinsic electron-transfer kinetics, sequential electrodeposition of Ir-Pt successfully combines these complementary characteristics within a single catalytic interface. Therefore the synergistic nanozyme activity of the bimetallic electrode exhibits the most favourable balance between active surface area, electron-transfer efficiency and catalytic current response. Thus these points towards provide high catalytic performance.

5.3.7 Analytical performance and long term stability (results from[283])

To quantitatively evaluate catalytic performance, calibration experiments were performed using different concentrations of H_2O_2. The resulting calibration curves are presented in Figure 44a. Among the investigated platforms, Ir-Pt@LIG exhibited the highest current response, exceeding those of bare LIG as well as the monometallic Ir- and Pt-modified electrodes. On this basis, Ir-Pt@LIG was selected as the optimal nanozyme platform for subsequent modifications.

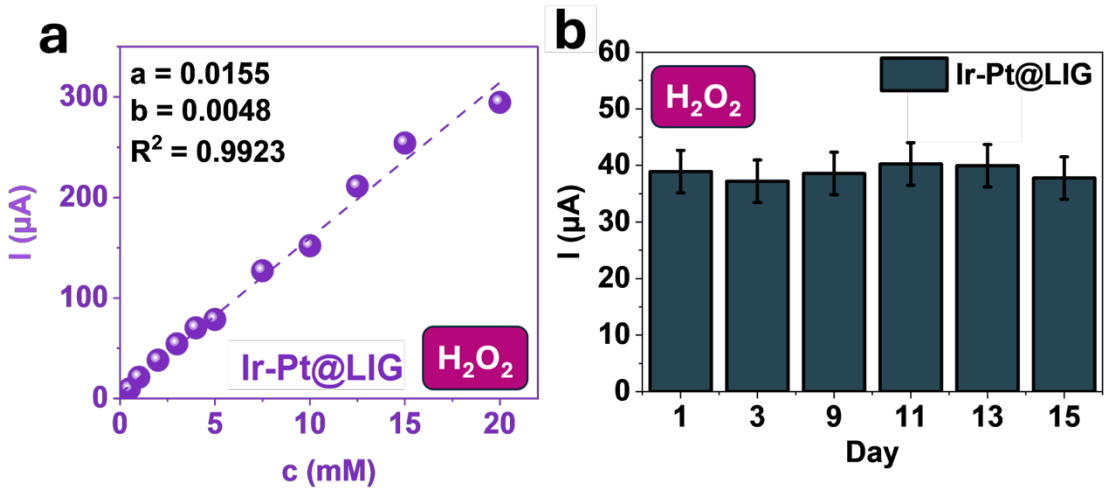


Figure 44: Analytical performance and operational stability a) calibration curve showing a linear relationship between current and H_2O_2 concentration; b) long-term stability performance over 13 days[283].

The Ir-Pt@LIG electrode also exhibited a concentration-dependent increase in current with increasing H_2O_2 concentration yielding a linear calibration over the investigated concentration range. This result confirms that the bimetallic, Ir-Pt@ LIG can serve as an effective nanozyme-based transduction platform for peroxide detection.

The operational stability of the optimized electrode was further evaluated over a 13-day period using repeated CA measurements under identical experimental conditions. As shown in Figure 44b, Ir-Pt@LIG electrodes exhibited minimal variation in current response during repeated measurements over 13 days using the same electrode reveals stable catalytic behaviour and good long-term operational stability. Together, these results validate the Ir-Pt heteronanostructures as a robust nanozyme-based transduction layer for H_2O_2. While these characteristics provide an excellent catalytic foundation, practical electroanalytical interfaces additionally require stable biomolecule immobilization together with resistance to nonspecific adsorption and biological fouling. As a result, the next chapter investigates the incorporation of functional hydrogel interfaces onto the Ir-Pt@LIG electrodes via electropolymerization (EP) to enable stable enzyme immobilization and impart antifouling and antibacterial functionalities while preserving the favourable catalytic properties established in the present chapter.

5.4 Multifunctional copolymer based surface engineering of Ir-Pt decorated LIG (results from[283])

Engineering the biological interface represents a critical step in translating an optimized electrocatalytic electrode into a functional electrochemical platform. Two functional copolymers with complementary physicochemical properties were investigated through electropolymerization onto the optimized Ir-Pt@LIG platform. APTAC was selected to introduce antibacterial functionality through its permanently charged quaternary ammonium groups, whereas SBMA, a zwitterionic sulfobetaine-based copolymer, was employed to impart antifouling properties. This chapter demonstrates how catalytic surface engineering can be integrated with multifunctional polymer interfaces to produce advanced electrochemical platforms suitable for practical electroanalytical applications.

5.4.1 Electropolymerization of functional copolymers - APTAC and SBMA (results from[283])

5.4.1.1 Electropolymerization strategy (results from[283])

The individual electropolymerization studies of APTAC and SBMA monomers were performed to establish the electrochemical behaviour and optimum polymerization conditions of each monomer. Based on the knowledge obtained from the individual electropolymerization studies was subsequently applied to the co-electropolymerization (copolymerization) of the mixed precursor solution and adapted for the fabrication of the multifunctional copolymer interface (poly(APTAC-co-SBMA) interface) on the Ir-Pt-decorated LIG electrode. The corresponding CV responses of polymerization of APTAC and SBMA is shown in Figure 45 below.

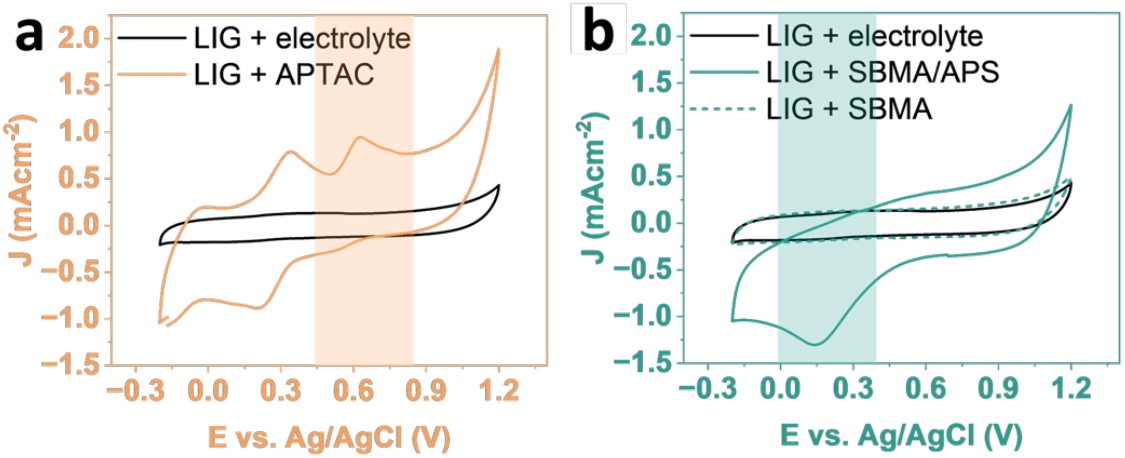


Figure 45: CV plots of Electropolymerization of functional polymers. a) APTAC compared with supporting electrolyte Na_2SO_4. B) SBMA in presence and absence of initiator (APS) compared with Na_2SO_4, supporting electrolyte[283].

The CV recorded during electropolymerization of APTAC are presented in Figure 45a. Compared with the supporting electrolyte (Na_2SO_4), the APTAC-containing solution exhibits a pronounced anodic peak centred at approximately +0.6 V vs. Ag/AgCl. This oxidation process may be attributed to electrochemical activation of the APTAC monomer, generating radical cation intermediates that initiate polymer chain growth directly at the electrode surface. Besides the oxidation peak responsible for polymer initiation, an additional pair of quasi-reversible peaks appears at approximately +0.30 V and +0.20 V vs. Ag/AgCl. As the deposited poly(APTAC) film (designated as pAPTAC) is electrochemically inactive within this potential window, these peaks cannot be assigned to intrinsic polymer redox reactions and therefore required further investigation.

5.4.1.2 Polymer growth and redox peaks (results from[283])

In order to examine the evolution of polymer growth the CV recorded during 4th and 50th cycles were compared as shown in Figure 46a. The oxidation peak at approximately +0.6 V gradually decreases with successive potential cycles, indicating progressive consumption of electroactive APTAC molecules near the electrode surface during formation of the polymer film. Simultaneously, a gradual increase in capacitive current is observed, reflecting continuous growth of a surface-confined polymer layer.

The origin of the additional voltammetric features observed between 0.2 and 0.3 V was subsequently investigated using different supporting electrolytes. As shown in Figure 46, voltammograms recorded in 0.1 M Na_2SO_4 and 0.1 M NaCl exhibit comparable electrochemical behaviour, demonstrating that chloride ions alone are not responsible for these peaks. The increasing the ionic strength by employing 0.3 M NaCl markedly suppresses the intermediate redox features in Figure 46, indicating that they arise primarily from changes in electrolyte composition and ionic strength than from specific chloride adsorption-desorption processes. These observations suggest that the peaks originate from interfacial ion transport accompanying polymer growth than from electrochemical activity of the deposited p(APTAC) film.

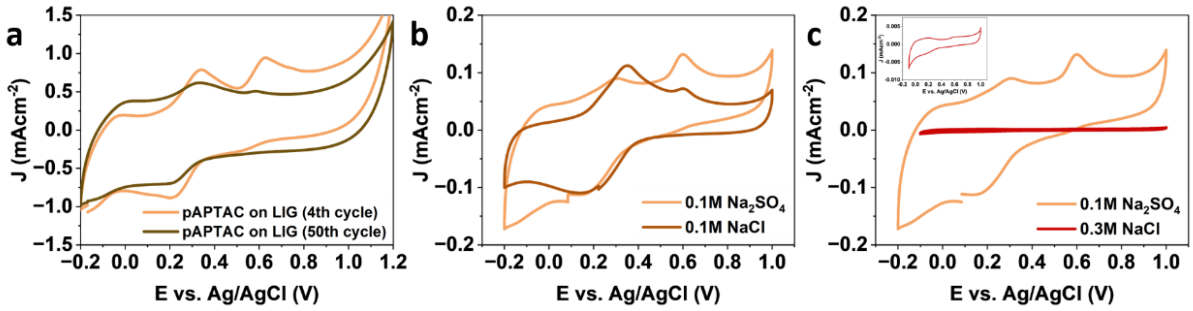


Figure 46: Evolution of polymer growth. (a) CV during 50 cycles of electropolymerization of APTAC at scan rate of 50mv/s. (b, c) CV plots of APTAC modified LIG in 0.1M Na_2SO_4 and 0.1M NaCl aqueous electrolytes at identical concentration, c) Comparison of voltammograms recorded at identical ionic strength using 0.1M Na_2SO_4 and 0.3M NaCl ionic strength[283].

The electropolymerization of SBMA differs significantly from that of APTAC. As shown in Figure 46b, the voltammograms recorded for SBMA solutions in the absence of ammonium persulfate (APS) are nearly identical to those obtained for the supporting electrolyte, indicating that direct electrochemical oxidation of SBMA is insufficient to initiate polymerization.

Following the addition of APS, however, a distinct cathodic feature appears at approximately +0.15 V vs. Ag/AgCl, corresponding to electrochemical reduction of persulfate species and generation of sulfate radical intermediates capable of initiating free-radical polymerization. Unlike APTAC, complementary oxidation-reduction peaks are not observed throughout the polymerization process. Instead, successful formation of the polymer coating is evidenced by the progressive increase in capacitive current, indicating development of a thin polymer film on the electrode surface.

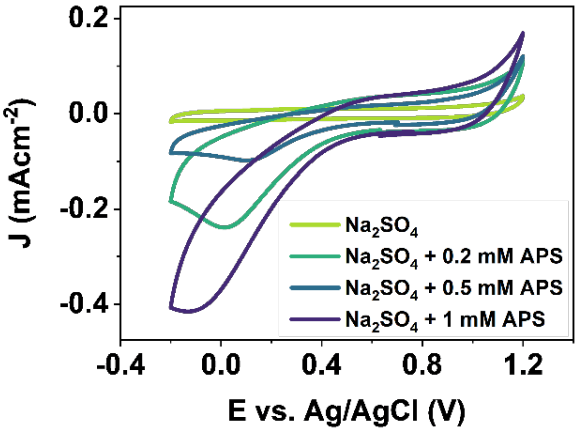


Figure 47: Influence of ammonium persulfate (APS) concentration on electropolymerization of SBMA. CV plots during the electropolymerization of SBMA in the supporting electrolyte containing 0, 0.2, 0.5 and 1.0mM APS during electropolymerization of SBMA[283].

To optimize the polymerization conditions, APS concentrations of 0, 0.2, 0.5 and 1.0mM were systematically investigated and shown in Figure 47. In the absence of APS, no measurable evidence of polymer formation was observed. Introduction of 0.2mM APS was sufficient to reproducibly initiate polymerization, whereas increasing the initiator concentration to 0.5 and 1.0mM produced only minor additional changes in the voltammetric response. As a result, 0.2mM APS was selected as the optimum initiator concentration for all subsequent copolymerization experiments, providing efficient initiation while minimizing unnecessary radical generation and possible side reactions.

5.4.1.3 Proposed electropolymerization mechanisms of APTAC and SBMA (results from[283])

The experimental observations described in the previous sections indicate that APTAC and SBMA undergo fundamentally different electrochemical initiation pathways despite producing similar surface-confined polymer films. In order to better understand the distinct electrochemical behaviour observed during the electropolymerization of APTAC and SBMA, a mechanistic interpretation of the polymerization process is proposed based on the voltammetric observations and the established free-radical polymerization pathways of methacrylate-based monomers. The proposed initiation, propagation and termination steps for both monomers are illustrated schematically in Figure 48.

Polymerization of APTAC proceeds through direct anodic oxidation of the monomer, generating radical cation intermediates that initiate chain growth at the electrode surface. Subsequent propagation occurs through successive addition of APTAC monomers, followed by radical termination to produce surface-bound poly(APTAC). In contrast, SBMA polymerization proceeds through an indirect initiation pathway. Electrochemical reduction of APS first generates sulfate radical species, which subsequently attack the SBMA monomer to produce reactive radicals capable of initiating chain propagation.

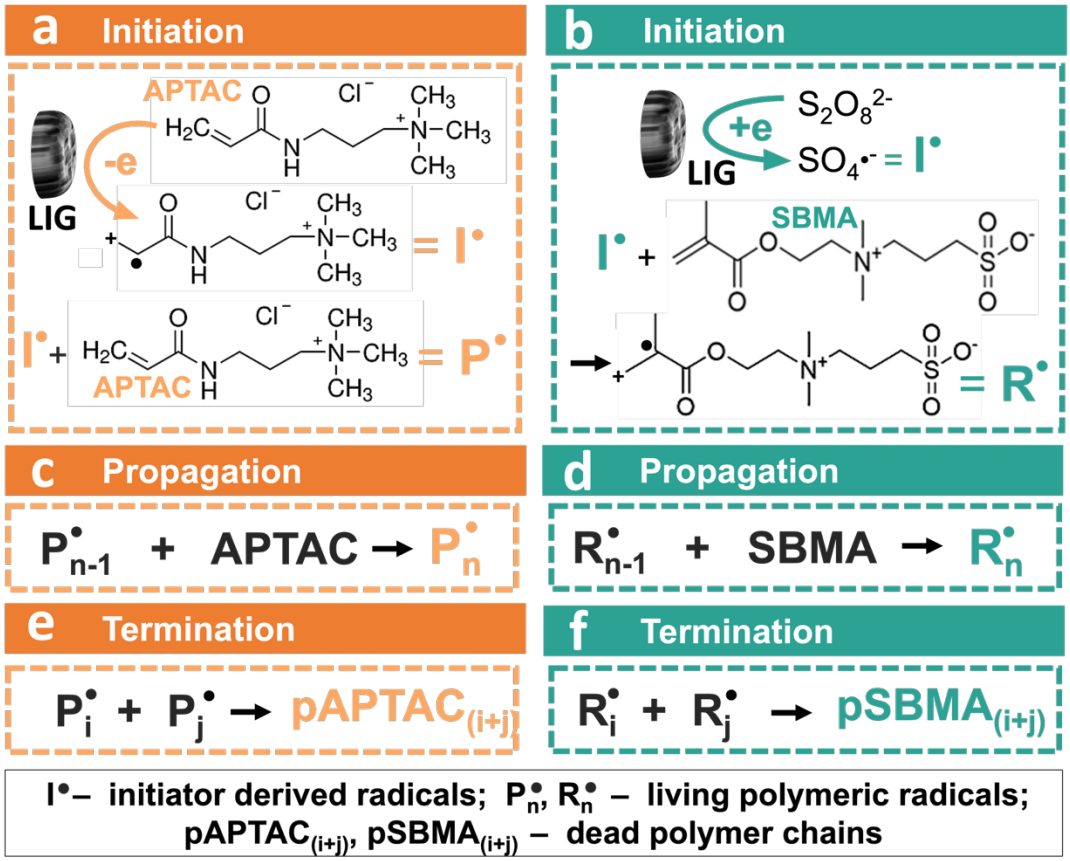


Figure 48: Proposed electropolymerization mechanisms of APTAC and SBMA. Schematic illustration of the initiation, propagation and termination stages during electropolymerization of (a,c,e) APTAC and (b,d,f) SBMA, leading to formation of surface-confined polymer films on the Ir-Pt-decorated LIG electrode[283].

Although the initiation pathways differ, both polymerization processes ultimately proceed through conventional free-radical propagation and termination reactions, producing polymer chains that are partially anchored to the Ir-Pt-decorated LIG surface while the remaining fraction remains dispersed within the electrolyte.

The mechanistic understanding gained from the individual electropolymerization studies followed by copolymerization of a mixed-monomer solution for the actual copolymer synthesis established in this section provides the foundation for controlled fabrication of multifunctional copolymer interfaces. Regulation of polymer initiation and growth is essential for controlling film thickness, preserving efficient electrical communication with the underlying catalytic interface and creating a stable surface suitable for subsequent enzyme immobilization and multifunctional biointerface engineering. The proposed mechanisms provide a rational explanation for the distinct electrochemical signatures observed during polymer growth and establish the fundamental basis for controlled fabrication of multifunctional copolymer interfaces. Understanding these initiation pathways is essential for regulating polymer film formation, preserving electrical communication with the underlying Ir-Pt catalytic layer and creating stable interfaces suitable for subsequent enzyme immobilization and multifunctional electroanalytical applications.

The electrochemical investigations described above established the individual polymerization behaviour of APTAC and SBMA and identified the experimental conditions required for reproducible polymer growth. Based on these results, the optimized electropolymerization parameters were subsequently employed to

fabricate multifunctional copolymer coatings on the Ir-Pt-decorated LIG electrodes. APTAC and SBMA were electropolymerized from its mixed monomer solution under the optimized conditions, with 0.2 mM APS incorporated to facilitate initiation of the SBMA polymerization and promote formation of a uniform copolymer interface. The resulting electropolymerized copolymer film integrates the complementary functionalities of both monomers within a single surface-confined coating, combining the antibacterial characteristics associated with APTAC and the antifouling properties imparted by SBMA. The electrochemical investigations confirmed successful formation of APTAC- and SBMA-based polymer films and established the optimum conditions required for controlled electropolymerization. Having defined the fabrication strategy and polymerization mechanisms, the next section examines how these electropolymerized coatings influence the surface morphology of the Ir-Pt-decorated LIG.

5.4.2 Morphological characterization of polymer-modified electrodes (results from[283])

SEM analysis was employed to investigate the surface morphology of the electropolymerized multifunctional copolymer coatings and verify that polymer deposition uniformly covers the Ir-Pt-decorated LIG while preserving the underlying porous graphene architecture. The intrinsic surface morphology of the individually electropolymerized polymers deposited on LIG was examined to establish their characteristic structural features and shown in Figure 49. The differences in film morphology between the two homopolymers is revealed as pAPTAC formed a thicker, more continuous hydrogel-like layer. pSBMA produced a thinner and more uniform surface coverage.

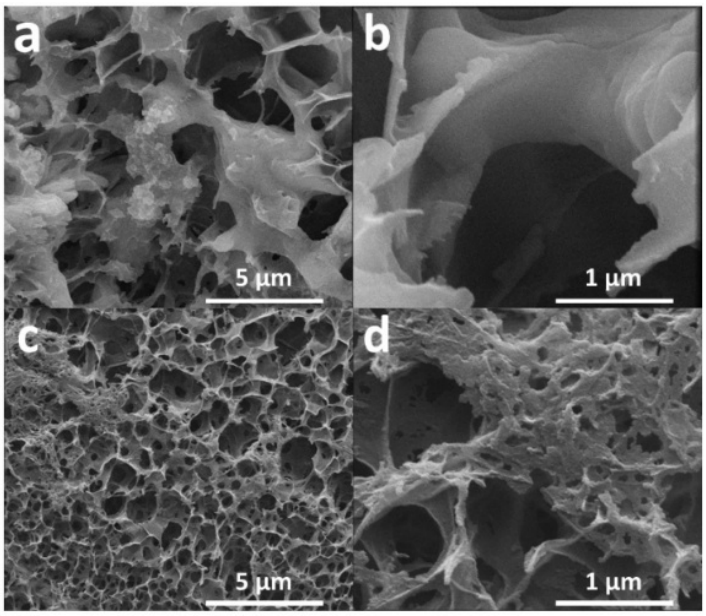


Figure 49: SEM micrographs of individually electropolymerized polymer coatings on LIG at two different magnifications polymer-coated LIG electrodes at two different magnifications: (a, b) pAPTAC@LIG, shows a porous continuous film formation; higher magnification reveals partial surface coverage and localized aggregation. (c, d) pSBMA-coated LIG, showing a uniform surface coverage[283].

The pAPTAC coating forms a relatively continuous polymer layer that extends across the porous graphene. At higher magnification, the deposited film appears comparatively smooth with localized polymer

aggregation and partial coverage of the underlying pores, indicating successful formation of a surface-confined polymer coating while preserving the characteristic 3D architecture of the LIG substrate. In contrast, as shown in Figure 49c and 49d the pSBMA coating exhibits a markedly different morphology. The electropolymerized polymer forms a highly porous and interconnected network distributed uniformly throughout the graphene scaffold. Compared with pAPTAC, the SBMA coating displays a more open microstructure with numerous interconnected pores, reflecting the intrinsic characteristics of the zwitterionic polymer network. Such porous morphology is advantageous for electrochemical interfaces because it facilitates electrolyte penetration and diffusion of electroactive species while maintaining intimate contact with the conductive graphene substrate.

The observed morphological differences demonstrate that the polymer architecture can be tailored through appropriate monomer selection, producing interfaces with distinct structural characteristics while preserving the porous nature of LIG. Having established the intrinsic morphology of the individual polymer coatings, the optimized electropolymerization strategy was subsequently applied to the Ir-Pt-decorated LIG electrodes to fabricate the multifunctional catalytic polymer interface.

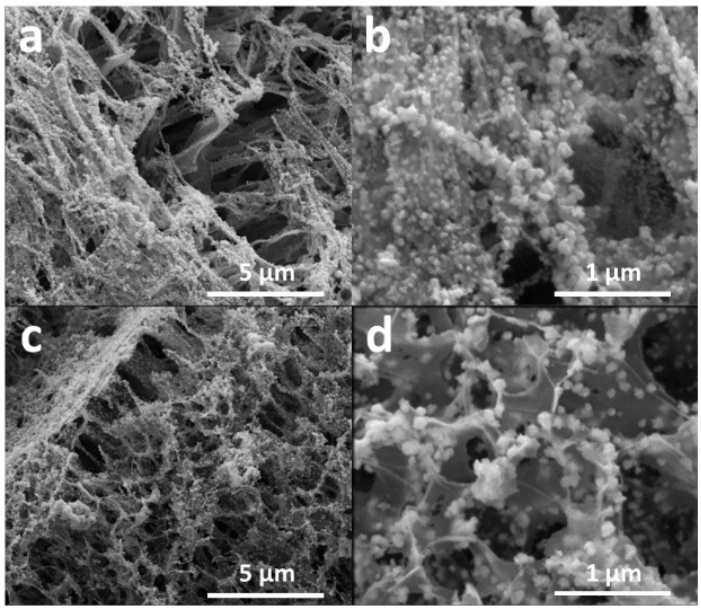


Figure 50: SEM micrographs of multifunctional copolymer at two different magnifications. (a, b) Ir-Pt-pAPTAC@LIG, showing a hydrogel network covering nanoparticles. Higher magnification highlights uniform covering nanoparticles. (c, d) Ir-Pt-SBMA@LIG, exhibiting a highly porous and interconnected morphology with homogeneous nanoparticle distribution. The hydrogel layer appears well-integrated with the underlying bimetallic nanostructures[283]**.**

Following electropolymerization onto the optimized Ir-Pt-decorated LIG electrodes, both polymer systems formed continuous multifunctional surface coatings while preserving the structural integrity of the catalytic platform as shown in Figure 50. The Ir-Pt-pAPTAC@LIG electrode exhibits a continuous polymer network conformally covering the Ir-Pt-decorated graphene surface. At higher magnification, the polymer matrix uniformly surrounds the deposited nanoparticles without evidence of cracking, delamination, or significant disruption of the underlying porous graphene architecture. This observation indicates strong integration between the electropolymerized polymer layer and the catalytic nanostructures.

The Ir-Pt-pSBMA@LIG electrode as shown in Figure 50c and Figure 50d retains the characteristic porous morphology observed for the individual SBMA coating while simultaneously accommodating the Ir-Pt nanostructures within the polymer network. The interconnected porous architecture remains clearly distinguishable and the metallic nanoparticles appear homogeneously distributed throughout the polymer-coated graphene framework. Preservation of this porous morphology is expected to facilitate efficient electrolyte transport and maintain electrochemical accessibility of the catalytic interface.

Comparison of Figures 49 and 50 demonstrates that incorporation of Ir-Pt nanostructures does not significantly alter the characteristic morphology of either electropolymerized polymer. Instead, both APTAC and SBMA form coatings that integrate effectively with the underlying bimetallic catalyst while maintaining the hierarchical porous architecture established during laser-induced graphitization. Such structural integration is particularly important because it combines the electrocatalytic functionality of the Ir-Pt nanostructures with the biological functionalities introduced by the polymer coatings, thereby establishing a multifunctional interface suitable for subsequent electroanalytical applications.

SEM confirms successful formation of functional copolymer over LIG. The successfully formed copolymer on Ir-Pt denoted as Ir-Pt-Cop@LIG.

5.4.3 Surface chemical characterization of copolymer modified Ir-Pt decorated LIGs (results from[283])

In order to verify successful electropolymerization of the multifunctional polymer coatings through surface-sensitive chemical analysis and identify the characteristic chemical functionalities introduced by APTAC and SBMA onto the LIG surface, XPS was employed.

XPS analyses revealed the details about surface chemistry of all polymer and copolymer modified electrodes. The slight decrease observed in the π-π* satellite implies that pAPTAC, but in particular, pSBMA and copolymer, can form a thin film covering the LIG surface. A similar conclusion is drawn by tracking the sp^2 C=C share, which contributes 70-72% of the total [C], for bare and NP-modified LIGs, while only 65% for polymer-covered LIGs.

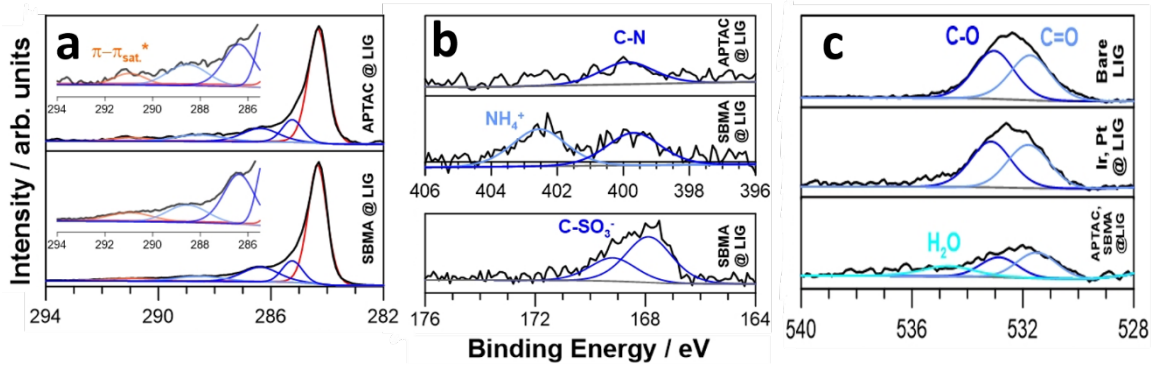


Figure 51: High-resolution XPS spectra of electropolymerized polymer-coated LIGs recorded in the core-level binding energy regions of a) C1s; b) N1s and S2p; c) O1s. Samples: bare LIG, Ir-Pt@LIG, pAPTAC@LIG, pSBMA@LIG and Ir-Pt-CoP@LIG[283].

The high-resolution C 1s spectra presented in Figure 51a confirm that the graphitic carbon remains the dominant surface component following electropolymerization. In detail, For both pAPTAC- and pSBMA-

coated electrodes, the spectra are dominated by the characteristic sp^2 C=C/C–C component originating from the underlying LIG, while additional contributions assigned to C–N, C–O and carbonyl-containing species demonstrate the introduction of polymer-derived functional groups. The persistence of the graphitic carbon peak indicates that electropolymerization modifies only the outer surface without disrupting the conductive graphene established during laser graphitization.

The presence of pAPTAC and pSBMA polymer at the LIG surface is further evidenced via nitrogen chemistry as shown in Figure 51b. In the case of pAPTAC, the N 1s region shows a weak component at approx. ~399.9 eV (C–N), but the quaternary ammonium N^+ is not clearly resolved above the noise. This observation is consistent with a very thin polymer layer. On the contrary, SBMA-modified surfaces reveal both amide-type C-N as well as quaternary ammonium N^+ (at 402.5 eV) features. Moreover, the *S 2p* region as shown in Figure 50c, pSBMA shows a clear doublet (S $2p_{3/2}$ at 167.9 eV) assignable to sulfonate moieties ($–SO3^–$). Since sulfur is absent from the pristine graphene substrate, the detection of this signal provides direct chemical evidence for successful incorporation of the zwitterionic polymer onto the electrode. Thus, both N and S chemistry strongly support the presence of pSBMA.

Changes in the oxygen chemical environment are observed in the O 1s spectra as shown. Bare LIG exhibits the expected oxygen-containing functionalities originating from residual oxygen groups formed during laser-induced graphitization. Following Ir-Pt electrodeposition, the overall oxygen environment remains similar, indicating that the metallic modification does not substantially alter the oxygen chemistry of the graphene surface. After electropolymerization, however, a noticeable increase in the contribution associated with hydroxyl and oxygen-containing polymer functionalities is observed. These are consistent with oxygen-containing functionalities expected from the polymer coating. In the polymer- or copolymer-modified samples, there is a notable increase in the relative contributions of C=O to C–O species and an easily recognizable tail that is typically assigned to chemisorbed water (at ~534.6 eV). This observation was expected for a hydrated polymer film present on the surface overlay. Thus testifying that the oxygen chemistry changes primarily reflect the polymer, not the underlying metal or LIG as shown in Figure 51c.

Thus, XPS results provide surface-sensitive evidence consistent with successful polymer deposition on the LIG surface. Polymer-derived nitrogen-, sulfur- and oxygen-containing functionalities were detected to the extent supported by the resolved core-level spectra, while the graphitic carbon signal remained dominant, indicating that the underlying LIG framework remained exposed through the relatively thin polymer coating. That is this electropolymerized films are sufficiently thin to preserve electrical communication with the conductive substrate introducing additional surface functional groups for subsequent surface modification studies.

The morphological and surface chemical characterization presented in the preceding sections collectively confirms the successful fabrication of multifunctional polymer interfaces on the Ir-Pt-decorated LIG electrodes. SEM demonstrated the formation of homogeneous polymer coatings that preserved the porous catalytic architecture, while XPS verified the incorporation of the characteristic chemical functionalities associated with APTAC and SBMA. The combined SEM and XPS analyses indicate that the polymer coating was deposited on the Ir-Pt-modified LIG surface while preserving the porous morphology of the underlying substrate.

However, the structural and surface-chemical characterization confirms successful surface modification, these analyses do not by themselves establish the functional performance of the engineered interface. Therefore, electrochemical evaluation is required to determine how the polymer coating influences the electroanalytical behaviour of the modified electrodes.

5.4.4 Proof-of-concept validation: electroanalytical performance of the multifunctional copolymer for glucose sensing (results from[283])

The ultimate objective of the present work is not merely to modify the electrode surface, but to determine whether these sequential surface-engineering strategies translate into improved electroanalytical performance. For this purpose, enzymatic glucose sensing was selected as a representative proof-of-concept electroanalytical application. Glucose sensing provides an appropriate proof-of-concept system because it simultaneously evaluates the catalytic activity of the Ir-Pt nanozyme, the ability of the electropolymerized copolymer to support enzyme entrapment and the efficiency of electron transfer across the engineered electrode-electrolyte interface.

The selection of glucose as the proof-of-concept analyte is closely linked to the electrocatalytic properties established in the previous chapter. In first-generation enzymatic glucose biosensors, GOx catalyses the oxidation of β-D-glucose to D-glucono-δ-lactone while simultaneously reducing molecular oxygen to H_2O_2. As a result, the analytical signal is generated through electrochemical oxidation of the enzymatically produced H_2O_2 than through direct oxidation of glucose itself. Therefore, the excellent H_2O_2 electrocatalytic activity demonstrated for the Ir-Pt nanozyme interface in previous chapter provides the fundamental basis for the glucose sensing strategy employed here.

To validate the electroanalytical performance of the optimized multifunctional platform, enzymatic electrodes was fabricated using the optimized electropolymerization conditions established in the preceding sections. GOx was incorporated directly into the electropolymerization precursor solution, enabling simultaneous in situ enzyme entrapment and copolymer formation on the Ir-Pt-decorated LIG surface. This one-step electropolymerization strategy produces an integrated biofunctional interface in which the catalytic Ir-Pt nanozyme, multifunctional copolymer and recognition element are assembled into a single surface-engineered Ir-Pt-CoP-GOx@LIG sensing platform.

For comparison, a reference electrode (Ir-Pt-CS-GOx@LIG) was prepared using the conventional approach of drop-casting a CS-GOx mixture onto the Ir-Pt-decorated LIG surface. This control provides an appropriate benchmark for evaluating the multifunctional copolymer as an alternative enzyme-entrapment matrix. Thus a systematically engineered electrochemical interface, verified every modification using complementary characterization techniques is finally subjected the fully engineered platform to a demanding electroanalytical proof-of-concept.

5.4.4.1 Electroanalytical glucose sensing

To evaluate the performance of developed multifunctional platform, Ir-Pt-CS-GOx@LIG is evaluated with in PBS containing different glucose concentrations. CA calibration curves were recorded at +0.6 V vs. Ag/AgCl. Since CS is a well-established matrix for enzyme immobilization and serves as a control sample. In both cases, the steady-state current increased proportionally with glucose concentration, yielding linear

calibration relationships over the investigated range. The linear detection ranges for the Ir-Pt-CS-GOx@LIG and Ir-Pt-CoP-GOx@LIG electrodes were 0.01-7.5mM and 0.5-7.5mM, respectively. The LODs were calculated as 8.14 µM and 6.55 µM for the CS- and copolymer-coated electrodes, respectively.

Representative CA responses are presented in Figure 52. In both sensing platforms, successive additions of glucose produced rapid stepwise increases in oxidation current followed by stable steady-state responses, demonstrating efficient enzymatic oxidation of glucose and subsequent electrocatalytic oxidation of the generated hydrogen peroxide on the Ir-Pt nanozyme interface. The rapid stabilization of the current following each glucose addition indicates efficient coupling between enzymatic recognition and electrochemical signal transduction.

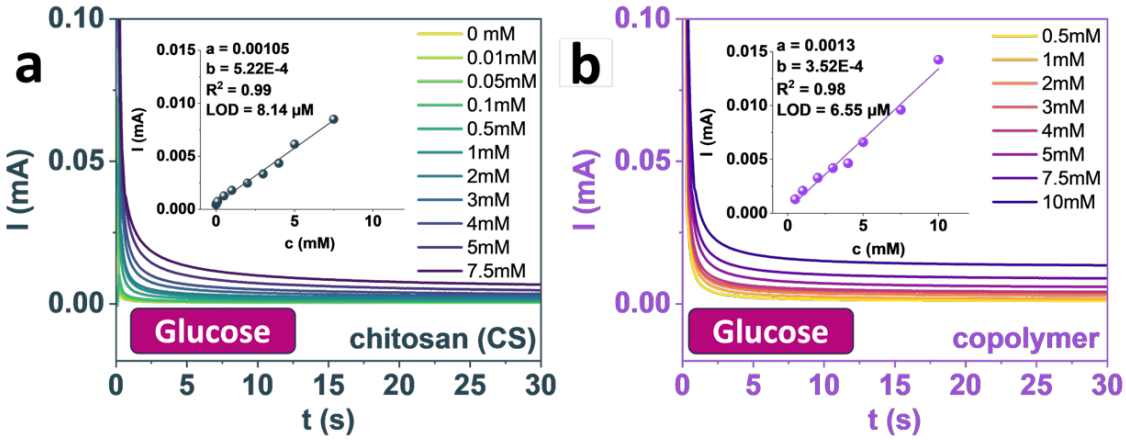


Figure 52: Glucose sensing performance. CA evaluation of glucose sensing at +0.6 V vs. Ag/AgCl. (a) CA responses of Ir-Pt-CS-GOx@LIG following successive additions of different concentration of glucose. Inset: corresponding calibration curve. (b) CA of Ir-Pt-CoP-GOx@LIG recorded under identical experimental conditions. Inset: corresponding calibration curve[283].

The corresponding calibration curves demonstrate a linear dependence of the oxidation current on different concentrations of glucose solutions. The Ir-Pt-CS-GOx@LIG and Ir-Pt-CoP-GOx@LIG electrodes exhibited linear detection ranges of 0.01-7.5mM and 0.5-7.5mM, respectively. The calculated limits of detection were 8.14µM for the CS-based electrode and 6.55µM for the copolymer-modified platform. Based on the geometric electrode area (0.085 cm²), the corresponding sensitivities were 12.4 and 15.4 µA/mM/cm², respectively.

The slightly higher sensitivity observed for the multifunctional copolymer platform demonstrates that the integrated surface-engineering strategy enhances electroanalytical performance. This improvement is attributed to the combined contribution of the highly conductive LIG scaffold, the catalytic Ir-Pt nanozyme interface and the multifunctional copolymer, which provides a hydrated microenvironment favourable for enzyme entrapment while maintaining efficient mass transport and charge transfer.

The investigated concentration range encompasses physiologically relevant glucose concentrations encountered in human blood, indicating the practical potential of the developed platform for electroanalytical applications. Even though the sensing at +0.6V provided excellent analytical sensitivity, practical electroanalytical applications additionally require high selectivity toward the target analyte. Therefore, the influence of common electroactive interfering species was investigated to evaluate the analytical specificity of the developed sensing platform.

5.4.4.2 Selectivity of the glucose sensing platform (results from[283])

The selectivity of the developed glucose sensing platform was evaluated using common interference like ascorbic acid, fructose, dopamine, paracetamol, cysteamine, cysteine. Since the analytical performance established in the previous section was obtained at +0.6 V vs. Ag/AgCl, the selectivity of the sensor was initially assessed under the same operating conditions.

As shown in Figure 53, glucose generated the dominant current response at +0.6 V, whereas most interfering species produced only negligible signals. However, dopamine exhibited a noticeable oxidation current, indicating that it undergoes direct electrochemical oxidation on the Ir-Pt-modified electrode surface. This behaviour is expected because dopamine is an electroactive molecule that can be oxidized at relatively high anodic potentials, independently of the enzymatic sensing mechanism. Even though dopamine is typically present in physiological fluids at concentrations considerably lower than glucose, the observed response indicates that operation at +0.6 V may introduce contributions from non-specific electrochemical oxidation, thereby reducing analytical selectivity.

To investigate whether this interference originated primarily from the relatively high operating potential, the selectivity measurements were subsequently repeated at +0.3 V vs. Ag/AgCl. As illustrated in Figure 53, lowering the operating potential markedly suppressed the responses of the interfering species while preserving the response toward glucose. These results demonstrate that reducing the applied potential effectively minimizes non-specific oxidation reactions and significantly improves analytical selectivity.

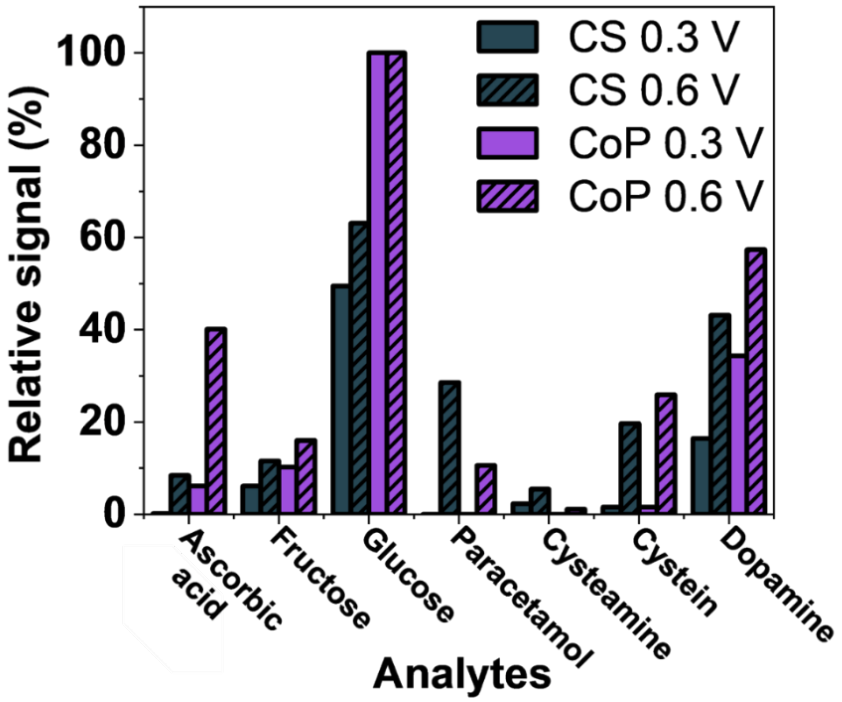


Figure 53: Selectivity of the multifunctional glucose biosensor evaluated at two operating potentials. Relative current responses of the Ir-Pt-CS-GOx@LIG and Ir-Pt-CoP-GOx@LIG electrodes toward glucose and representative electroactive interfering species (1mM each) measured at +0.3 V and +0.6 V vs. Ag/AgCl. The glucose response at each operating potential was normalized to 100% and the responses of the interfering species are expressed relative to the corresponding glucose signal[283].

Motivated by the selectivity results obtained at +0.6 V, glucose sensing was subsequently evaluated at a reduced operating potential of +0.3 V vs. Ag/AgCl to suppress oxidation of electroactive interferents while preserving enzymatic signal generation.

As shown in Figure 54, the re-evaluated sensing performance at a lower potential of +0.3V, both sensing platforms retained concentration-dependent current responses over the investigated glucose concentration range. The multifunctional copolymer electrode again exhibited higher sensitivity than the CS -based control, with calibration slopes corresponding to sensitivities of 7.1 and 2.35 μA/mM/cm² respectively.

Compared with the performance at +0.6 V, the analytical sensitivity decreased, accompanied by lower coefficients of determination, indicating a reduced linearity. This behaviour is expected because H_2O_2 oxidation proceeds less efficiently at lower anodic potentials. But the operation at +0.3 V substantially reduced oxidation of interfering electroactive species while maintaining satisfactory analytical performance.

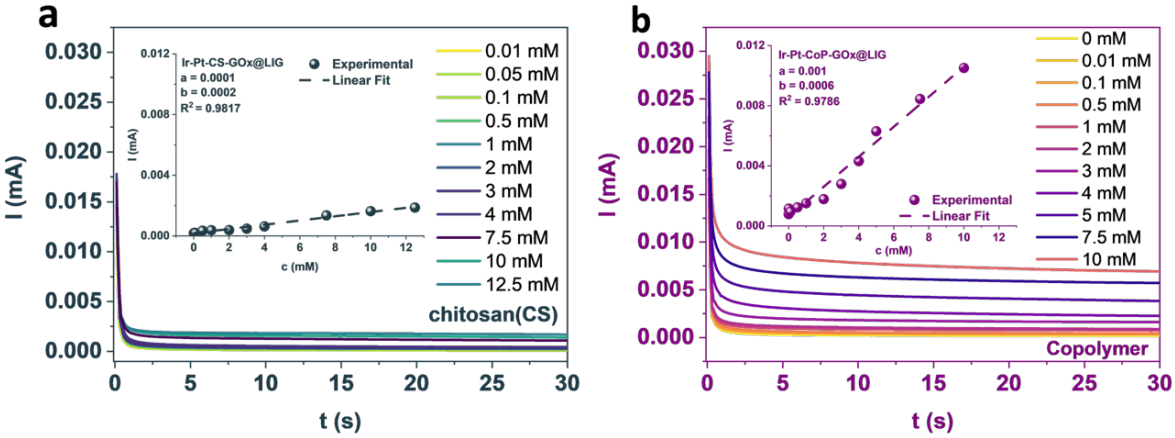


Figure 54: Glucose sensing at lower potential. Chronoamperometric glucose sensing performed at +0.3 V vs. Ag/AgCl. (a) CA responses and calibration curve of Ir-Pt-CS-GOx@LIG (b) CA responses and calibration curve of Ir-Pt-CoP-GOx@LIG[283].

These results suggest the compromise or the inverse relationship between analytical sensitivity and selectivity that is commonly encountered in electrochemical biosensors. Even though the operation at +0.6 V maximizes the analytical response, the reduced operating potential offers improved selectivity and may therefore be preferable for analyses performed in complex biological matrices.

5.4.4.3 Operational stability (results from[283])

Long-term stability is an important performance criterion for electrochemical biosensors because gradual enzyme deactivation, loss of immobilized biomolecules and deterioration of the electrode interface can progressively reduce the analytical response during repeated use. Therefore, the ability of the multifunctional copolymer matrix to preserve sensor performance over time was investigated and compared with the CS-based immobilization strategy.

Operational stability was evaluated over 13 days by repeated CA measurements 1mM glucose solution using the same sensing electrodes to assess electrode-to-electrode reproducibility. Both the CS- and copolymer-modified electrodes retained a substantial fraction of their initial response, indicating acceptable stability of the enzyme/nanozyme sensing interface. The copolymer-modified electrode showed better signal retention than the CS-based system, suggesting a beneficial role of the copolymer matrix in preserving sensor performance over time.

The gradual decrease in current observed for both platforms over time may result from partial loss of enzyme activity during repeated measurements, as well as gradual release of physically entrapped GOx from the polymer matrices. The copolymer-based platform exhibited improved signal retention compared with the conventional CS system. This improved stability observed for the multifunctional copolymer suggests that the electropolymerized matrix provides a more favourable microenvironment for preserving enzymatic activity during prolonged operation.

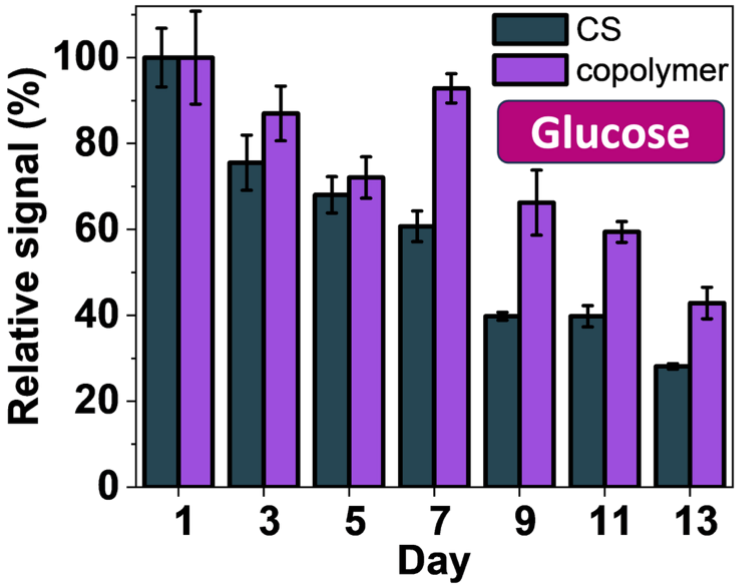


Figure 55: Operational stability. Ir-Pt-CS-GOx@LIG and Ir-Pt-CoP-GOx@LIG evaluated over 13 days using repeated CA measurements +0.6 V vs. Ag/AgCl in 1mM glucose. Error bars represent the standard deviation obtained from measurements of three independently fabricated electrodes[283].

Additionally indicates that the multifunctional electropolymerized network more effectively stabilizes the entrapped enzyme while preserving the electrochemical communication between the biological recognition layer and the underlying Ir-Pt nanozyme interface. Together, these results show that the copolymer-modified Ir-Pt@LIG platform provides effective glucose sensing and slightly improved signal retention compared with the conventional CS-based control. Simply, the multifunctional copolymer contributes not only to improved analytical sensitivity but also to enhanced durability of the electroanalytical interface during prolonged operation.

Even though the sensing platforms demonstrated analytical performance and operational stability under controlled laboratory conditions, practical electroanalytical applications require reliable performance validation. To further test practical applicability of developed sensing platform, it was evaluated in artificial sweat under mildly acidic conditions, which accounts on the next section.

5.4.4.4 Validation in artificial sweat (results from[283])

Evaluation in physiologically relevant model media represents an important intermediate step between measurements performed in simple buffer solutions and future investigations in more complex biological samples. Artificial sweat was therefore employed as a representative synthetic biofluid to perform a preliminary assessment of the developed sensing platform under chemically more demanding conditions.

Unlike phosphate-buffered saline (PBS), artificial sweat contains physiologically relevant electrolytes and low-molecular-weight organic constituents that may influence enzyme activity, analyte transport and electrochemical signal generation. Consequently, measurements performed in artificial sweat provide a more representative assessment of sensor behaviour than those conducted in simple buffer solutions.

In order to examine the preliminary feasibility of glucose detection in a representative synthetic sweat matrix, the electrochemical response of Ir-Pt-CoP-GOx@LIG electrode was evaluated in artificial sweat at pH 5.4 and pH 6.0, reflecting the range of pH values commonly reported for human sweat. Representative chronoamperometric responses obtained in artificial sweat are presented in Figure 56.

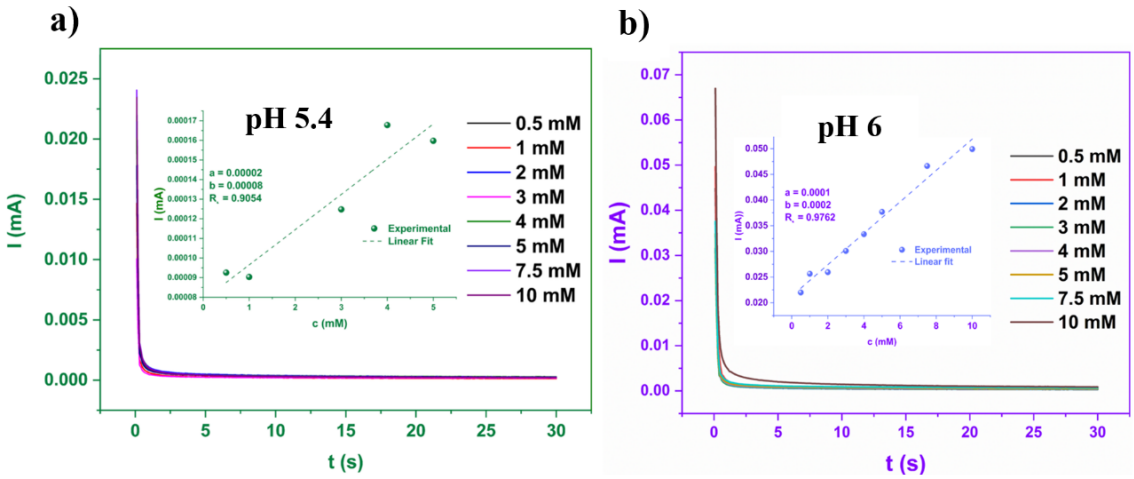


Figure 56: Electroanalytical performance of the multifunctional Ir-Pt-CoP-GOx@LIG sensing platform in artificial sweat. CA curves shows performance of the Ir-Pt-CoP-GOx electrode in artificial sweat at an applied potential of 0.6 V. (a) pH 5.4 , b) pH 6; Insets calibration curve constructed from the steady-state current responses as a function of glucose concentration[283]**.**

At both pH values, successive additions of glucose produced concentration-dependent increases in the oxidation current, indicating that the modified electrode remained electrochemically responsive in the artificial sweat matrix. The corresponding calibration plots exhibited an approximately linear relationship between glucose concentration and current over the investigated concentration range. Although differences in the analytical response were observed between pH 5.4 and pH 6.0, the electrode maintained measurable glucose-dependent responses under both conditions.

Compared with measurements performed in PBS (pH 7.4), the measurements in artificial sweat showed lower sensitivity and a stronger dependence on pH. At pH 5.4, the glucose-dependent response was weak and less clearly concentration-resolved, whereas at pH 6.0, a more regular concentration-dependent response was obtained, although still with lower sensitivity than in PBS.

The ability of the modified electrode to produce concentration-dependent electrochemical responses in artificial sweat indicates that the surface-engineering strategy developed in this work remains functional in a chemically more complex model medium than PBS. Although reduced sensitivity and pH-dependent behaviour were observed, the results provide preliminary evidence that the integrated graphene, Ir-Pt nanozyme, copolymer coating and immobilized enzyme remain electrochemically active under representative synthetic sweat conditions. Hereby, demonstrate the preliminary feasibility of glucose detection in a physiologically relevant model medium.

It should be emphasized that artificial sweat represents a simplified synthetic model and does not reproduce the full complexity of native sweat, including proteins, metabolites and other biological constituents that may influence electrode performance. Thus, additional investigations involving authentic biological samples, long-term operational stability and comprehensive interference studies will be required before practical or wearable applications can be established.

While the artificial sweat experiments demonstrate that the sensing platform remains electrochemically functional in a representative synthetic physiological medium, prolonged operation in biological environments is also influenced by nonspecific adsorption of proteins and other biomolecules at the electrode interface. Such biofouling may progressively hinder analyte transport and electron transfer, leading to deterioration of the electrochemical response. Therefore, the influence of protein-containing conditions on the electrochemical behaviour of the multifunctional copolymer-modified electrode was investigated using BSA as a model protein.

5.4.5 Electrochemical response under protein-containing conditions (results from[283])

The long-term operation of electrochemical devices in biological environments is frequently limited by biofouling. Non-specific adsorption of proteins onto the electrode surface can block electroactive sites, affect mass transport and gradually deteriorate analytical performance. Accordingly, the antifouling properties of the multifunctional copolymer interface were evaluated using BSA as a representative model protein.

Indirect antifouling behaviour was assessed by CA measurements performed at different applied potentials in 1mM glucose solutions with and without 1% BSA at different potentials +0.3, +0.4, +0.5 and +0.6 V vs. Ag/AgCl. Because the copolymer contains the zwitterionic monomer SBMA, the experiment was designed to examine whether the electrochemical response could be retained during prolonged exposure to a protein-containing environment. Figure 57 compares glucose solutions containing and lacking 1% BSA at different applied potentials, during 4 h of incubation. The experiment was designed to provide an indirect assessment of the influence of protein-containing conditions on the electrochemical response of the multifunctional copolymer-modified electrode. Instead of directly measuring protein adsorption, the measurements evaluate the extent to which the electrochemical response is retained during prolonged exposure to BSA. This approach also suggests the foundation of the electrochemical consequences of biofouling by monitoring changes in the analytical response over time, thereby providing a practical assessment of the ability of the multifunctional interface to maintain sensor functionality under protein-rich conditions.

In the presence of BSA, a progressive decrease in current is observed at all applied potentials, indicating gradual surface fouling caused by nonspecific protein adsorption. This behaviour is consistent with progressive adsorption of BSA onto the electrode interface, which is expected to reduce the number of electrochemically accessible active sites and thereby resulting in a gradual decrease in current.

The most pronounced decrease in current was observed at +0.6 V, whereas operation at +0.3 V resulted in the smallest loss of analytical response over the four-hour evaluation period. These observations indicate that lower operating potentials mitigate the adverse influence of protein fouling on sensor performance, most likely by reducing non-specific electrochemical oxidation processes occurring at the electrode interface. In contrast, the BSA-free control measurements exhibited only minor changes in current throughout the experiment. The nearly constant responses observed in the absence of BSA confirm that the signal

deterioration recorded during protein exposure primarily originates from biofouling than from intrinsic instability of the platform.

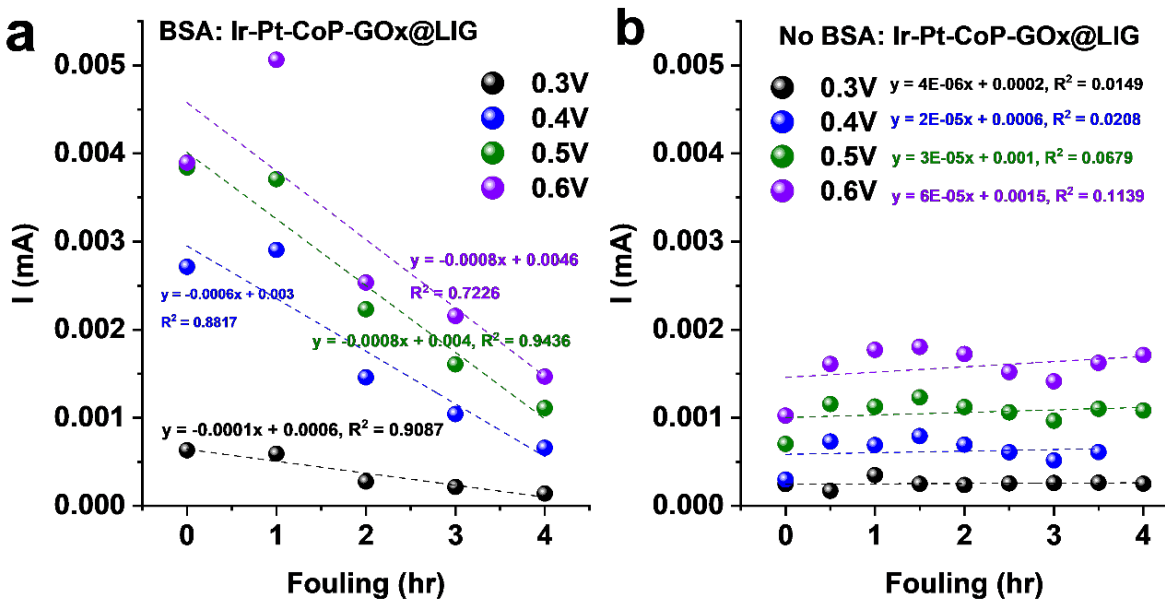


Figure 57: Time-dependent electrochemical response of the multifunctional copolymer-modified electrode in 1mM glucose solutions in the (a) presence and (b) absence of 1% BSA at applied potentials of +0.3, +0.4, +0.5 and +0.6 V (vs. Ag/AgCl) (control)[283].

Although a gradual decrease in current was observed during exposure to BSA, the electrode retained a measurable electrochemical response throughout the four-hour evaluation period. These results indicate that the multifunctional copolymer-coated electrode remained electrochemically active under protein-containing conditions. While this behaviour is consistent with partial preservation of sensor performance in the presence of BSA, the present measurements alone do not permit direct conclusions regarding the extent of protein adsorption or the antifouling properties of the coating. Direct evaluation of antifouling behaviour would require complementary surface-sensitive protein adsorption measurements.

The observed retention of electrochemical response is consistent with the intended incorporation of the zwitterionic SBMA component within the copolymer. However, the present measurements provide only indirect evidence of the coating's behaviour under protein-containing conditions and do not directly quantify protein adsorption.

In addition to evaluating the electrode behaviour under protein-containing conditions, the multifunctional copolymer was designed to incorporate antibacterial functionality through the APTAC component. Therefore, the antibacterial properties of the modified interface were subsequently investigated.

5.4.6 Antibacterial assays of multifunctional copolymer interface (results from[283])

In addition to protein adsorption, bacterial colonization represents another important consideration for electrochemical interfaces intended for operation in biological environments. Surface-associated bacteria may proliferate to form biofilms, potentially altering mass transport, modifying the interfacial properties of the electrode and affecting long-term electrochemical performance. To complement the physicochemical characterization of the multifunctional copolymer, its antibacterial potential was evaluated to determine whether the APTAC-containing polymer retained antibacterial activity following electropolymerization. It

should be noted that the antibacterial experiments presented in this section provide a semi-quantitative assessment of the polymer-derived material and do not represent a direct evaluation of bacterial adhesion or killing on the intact modified electrode surface.

5.4.6.1 Antibacterial assessment of individual polymers (results from[283])

Before investigating the multifunctional copolymer, the antibacterial characteristics of the individual electropolymerized polymers were examined to establish their respective contributions to the biological behaviour of the final coating. Polymer-containing suspensions were evaluated against *E. coli* and MRSA using the standard broth microdilution protocol and the corresponding results are presented in Figure 58.

The pAPTAC-derived material exhibited measurable antibacterial activity against both bacterial strains, whereas the pSBMA-derived material showed little or no inhibitory effect under the experimental conditions employed. This observation is consistent with the established role of quaternary ammonium-containing polymers, whose positively charged functional groups are known to interact with negatively charged bacterial membranes. In contrast, SBMA is a zwitterionic polymer primarily designed to modify interfacial hydration and reduce nonspecific adsorption than to provide intrinsic antibacterial activity.

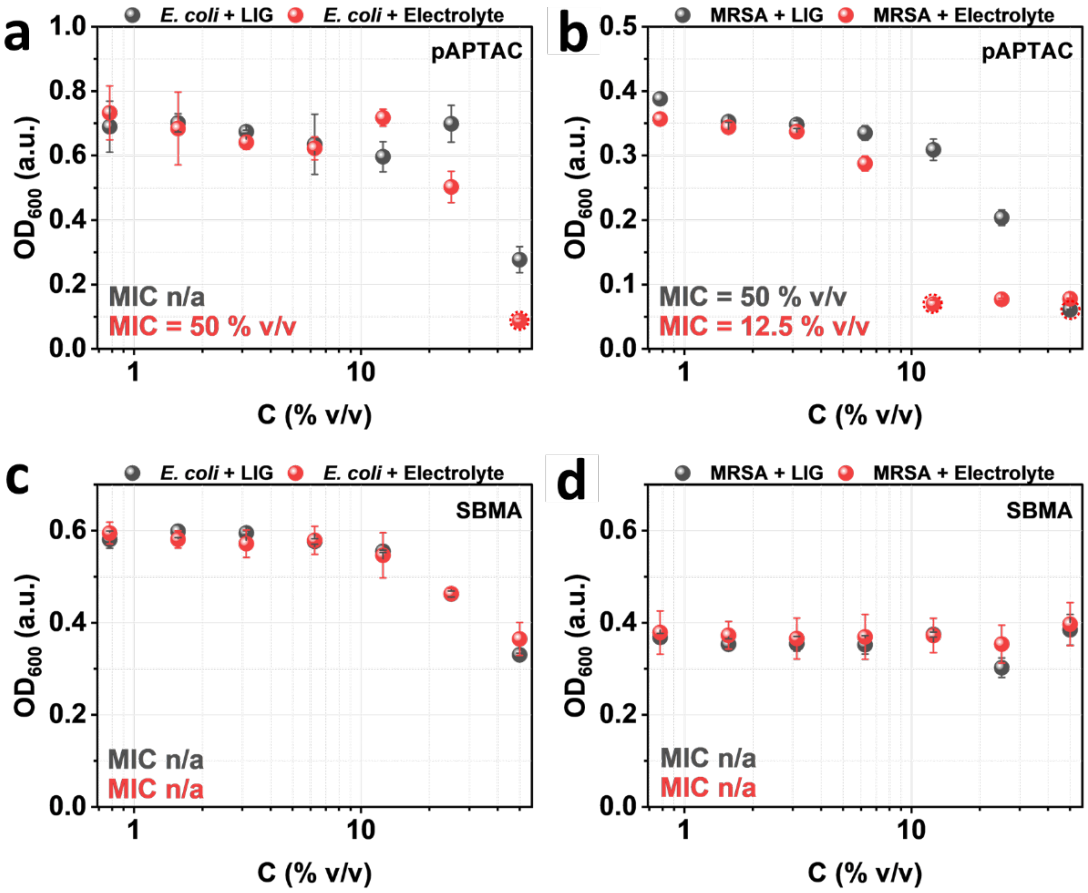


Figure 58: Semi-quantitative broth microdilution assessment of polymer suspensions derived from individually electropolymerized polymers. a) pAPTAC against *E. coli* (b) pAPTAC against MRSA (c), pSBMA against *E. coli* (d) pSBMA against MRSA[283].

Accordingly, the results indicate that the antibacterial potential of the multifunctional copolymer is predominantly associated with the APTAC component, whereas SBMA contributes a different surface functionality within the copolymer.

5.4.6.2 Semi-quantitative antibacterial assessment of the multifunctional copolymer (results from[283])

Following evaluation of the individual polymers, the antibacterial potential of the multifunctional copolymer was examined. As described in the experimental section, the antibacterial assay was performed using polymer-containing suspensions obtained either directly from the electropolymerization electrolyte or following ultrasonic desorption of the polymer coating from the modified LIG surface. As a result, the reported MIC values represent semi-quantitative indicators of the antibacterial activity of the recovered polymer material and should not be interpreted as direct measurements of the antibacterial performance of the intact sensing electrode or compared directly with conventional MIC values reported for soluble antimicrobial agents.

Representative results are shown in Figure 59. Under the experimental conditions employed, the polymer-containing suspensions produced greater inhibition of MRSA than *E. coli*. The electrolyte-derived polymer suspension exhibited a lower apparent MIC (7.36% v/v) than the ultrasonically recovered polymer suspension (approximately 15% v/v), whereas both samples exhibited comparatively weaker activity against *E. coli* (approximately 50% v/v). These observations indicate differences in antibacterial behaviour between the tested bacterial strains and between the two polymer-containing sample types.

The greater susceptibility of MRSA compared with *E. coli* is consistent with the structural differences between Gram-positive and Gram-negative bacterial cell envelopes. The additional outer membrane present in Gram-negative bacteria acts as a permeability barrier that may reduce interactions between cationic polymeric materials and the cytoplasmic membrane. Thus, Gram-positive bacteria are often more susceptible to membrane-active cationic materials.

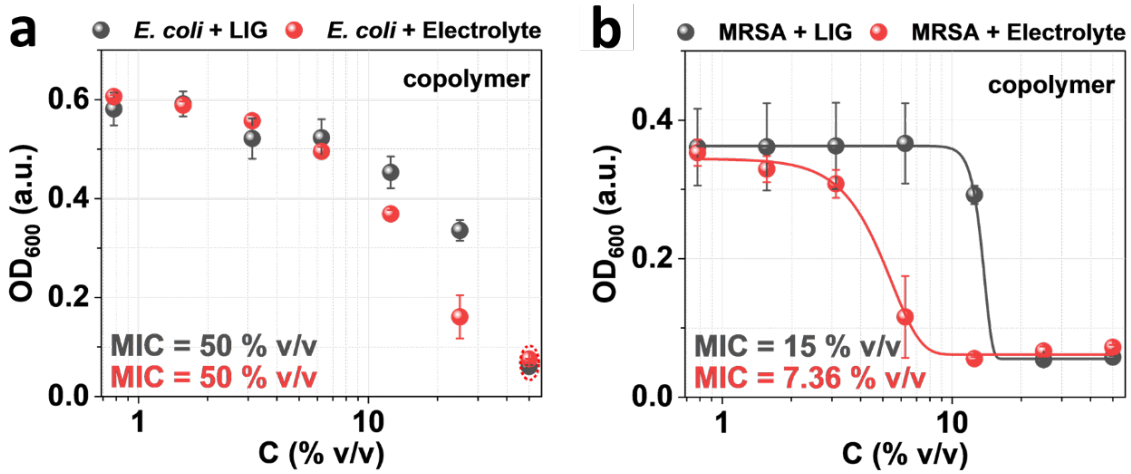


Figure 59: Semi-quantitative broth microdilution assessment of polymer suspensions derived from the multifunctional copolymer against: a) *E. coli* and b) MRSA[283].

Differences observed between the electrolyte-derived and ultrasonically recovered polymer suspensions may reflect variations in the amount or composition of the recovered polymer available for testing. However, because the polymer concentration in each suspension was not directly quantified, the present study does not permit quantitative comparison of antibacterial potency between the two sample preparation methods.

The observations obtained for the multifunctional copolymer are consistent with the individual polymer studies, which indicated that antibacterial activity is primarily associated with the APTAC component, while the SBMA component contributes the zwitterionic character of the copolymer than intrinsic antibacterial activity.

Direct evaluation of bacterial adhesion on the modified electrode surface was considered; however, recovery of surface-associated bacteria resulted in partial delamination of the polymer coating, preventing reliable quantitative analysis. Consequently, the antibacterial results presented here should be regarded as evidence that the electropolymerized polymer retains antibacterial potential following fabrication and not as a direct assessment of antibacterial performance at the intact electrode interface.

Collectively, the electrochemical characterization, protein-exposure experiments and antibacterial suspension assays indicate that incorporation of the multifunctional poly(APTAC-co-SBMA) coating introduces additional biologically relevant surface functionality while maintaining the electrochemical characteristics of the modified LIG platform. Further investigations involving direct bacterial adhesion, biofilm formation and surface-associated viability measurements will be required to comprehensively evaluate the antibacterial performance of the intact multifunctional electrode under application-relevant conditions.

This chapter investigated the development of a multifunctional surface-engineering strategy for Ir-Pt-decorated LIG through sequential electrodeposition, electropolymerization and enzyme immobilization. The resulting interface combined catalytic nanostructures with a multifunctional copolymer coating and enabled evaluation of electrochemical performance together with preliminary biological and physiologically relevant assessments. Electropolymerization of the copolymer not only preserved the electrochemical properties of the underlying Ir-Pt nanozyme but also provided an effective matrix for enzyme immobilization.

The resulting Ir-Pt-CoP-GOx@LIG biosensor exhibited favourable electroanalytical performance, achieving a sensitivity of 15.4 μA/mM/cm², a LOD of 6.55 μM and a linear detection range of 0.5-7.5mM at +0.6 V vs. Ag/AgCl, outperforming the conventional CS-based control. Optimization of the operating potential to +0.3 V reduced the influence of common electroactive interferents while maintaining concentration-dependent glucose responses. The sensor also retained electrochemical functionality over a 13-day evaluation period and remained responsive in artificial sweat at pH 5.4 and pH 6.0. Although the analytical response in artificial sweat was reduced compared with phosphate-buffered saline, the results provide preliminary evidence of sensor functionality in a representative synthetic physiological medium.

Beyond electrochemical characterization, the multifunctional copolymer was evaluated under protein-containing conditions and by antibacterial suspension assays. Chronoamperometric measurements demonstrated that the modified electrode retained a measurable electrochemical response during prolonged exposure to BSA, providing an indirect assessment of electrode behaviour in protein-containing media. The broth microdilution experiments further indicated that polymer-containing suspensions derived from the electropolymerized coating exhibited antibacterial activity, with greater inhibition observed against MRSA than against *E. coli*. These suggest that the APTAC-containing copolymer retained antibacterial potential following electropolymerization, while the overall multifunctional coating remained compatible with electrochemical sensing. Nevertheless, further studies involving direct bacterial adhesion, biofilm formation and quantitative protein adsorption measurements will be required to comprehensively evaluate the biological performance of the intact modified electrode.

Collectively, the results presented in this chapter demonstrate that sequential surface modification provides an effective approach for integrating catalytic nanostructures, polymer coatings and enzyme immobilization on LIG without compromising electrochemical functionality. The multifunctional interface developed in this work provides a foundation for further investigations of LIG-based biosensing platforms in increasingly complex biological environments while illustrating how complementary surface modifications can be combined to tailor electrode performance and functionality.

The preceding chapters established fabrication, surface modification and electrochemical characterization of the optimized polyimide-derived LIG platform. These investigations demonstrated how laser processing and subsequent surface modifications influence the structural, physicochemical and electrochemical properties of PI-derived LIG, leading to the development of multifunctional electrode interfaces. An important question that naturally arises from these results is, whether these engineering principles established can be extended beyond the current PI-derived LIG platform to compare the effect of substrate dependency, when the precursor material itself is fundamentally changed. Exploring different precursors materials and processing strategies provides insight into how the nature of the starting substrate influences the fabrication process and the properties of the resulting material. The next chapter therefore preliminarily investigates the influence of precursor chemistry on LIG formation by selecting an alternative precursor material using cellulose, investigate laser processing of PTFE and evaluate PEGDA-assisted transfer of LIG as an alternative processing strategy.

CHAPTER 6 – FUTURE PERSPECTIVES AND ONGOING RESEARCH

Extension of the LIG engineering to alternative precursors and translation towards next-generation LIG platforms

This chapter presents ongoing research activities and preliminary investigations that form the basis of future manuscripts. The presented studies evaluate the preliminary feasibility of the transferring the structure-property established in previous chapters to alternative substrate systems, emerging laser parameters, fabrication approaches and transferable material architectures.

Accordingly, this chapter presents three exploratory studies investigating different aspects of LIG extension and translation. The first examines cellulose as a renewable precursor to determine how substrate chemistry influences graphitization and conductive network formation. The second investigates laser processing of PTFE as a preliminary feasibility study towards fluoropolymer-derived carbon structures.

The central question is how can the engineering principles established in this thesis be extended beyond the current LIG platform to compare the effect of substrate dependency?

Finally, PEGDA-assisted LIG transfer (LIGT) is explored as an initial strategy for transferring LIG onto flexible hydrogel supports. Collectively, these studies evaluate the feasibility of extending laser-derived carbon materials to alternative precursor systems and substrate configurations while identifying the principal scientific and engineering challenges that remain to be addressed. These studies, ultimately enabling scalability, customizability and extend the applicability of LIG beyond conventional PI substrates and highlight future opportunities as promising platforms.

6.1 Influence of substrate chemistry: PI versus cellulose-derived LIG

Throughout this dissertation, PI served as the model precursor for investigating relationships between laser fabrication parameters, graphitic structure, electrochemical behaviour and for surface modifications. To determine whether similar laser-processing strategies could be applied to chemically distinct materials, the present study preliminarily investigates cellulose as an alternative precursor. Unlike PI, cellulose is a renewable, biodegradable and low-cost material, making it an attractive candidate for sustainable disposable laser-derived materials. The objective of this investigation is not simply to replace one precursor with another, but to understand how precursor chemistry influences laser-induced graphitization and the formation of conductive carbon networks. In particular, this study addresses the following scientific question:

How does precursor chemistry alter the graphitization mechanism and what fabrication strategy is required to produce conductive LIG on thermally sensitive cellulose substrates?

It is hypothesized that successful fabrication of conductive cellulose-derived LIG requires substrate-specific laser processing strategy, because precursor chemistry governs thermal decomposition, carbonization pathways, graphitic ordering and conductive network formation during laser processing. Unlike PI, cellulose exhibits fundamentally different thermal decomposition pathways during laser irradiation. Instead of undergoing direct graphitization, cellulose initially experiences dehydration, depolymerization, cleavage of glycosidic bonds and evolution of volatile oxygen-containing species before carbonaceous structures are

formed. Cellulose consists of linear polysaccharide chains connected through β-(1→4)-glycosidic linkages and contains a significantly higher oxygen content. Upon laser irradiation, the evolution of volatile species such as water, carbon monoxide and carbon dioxide. These competing reactions reduce the carbon yield available for graphitic reorganization and increase the susceptibility of the substrate to localized combustion and structural collapse. As a consequence, direct application of laser-processing parameters optimized for PI frequently resulted in excessive material ablation, discontinuous carbon formation, or complete destruction of the paper substrate. Therefore, this distinct thermal response of cellulose is making direct transfer of laser parameters tuned for PI unsuitable for cellulose-derived substrates.

Therefore, extending LIG fabrication from PI to cellulose is not simply a change of precursor material but represents a fundamentally different graphitization problem that requires careful regulation of energy delivery to balance carbonization and graphitic ordering while minimizing excessive thermal degradation. Thus, understanding how precursor chemistry governs LIG formation is essential for developing a promising foundation regarding substrate-specific fabrication strategies and for exploring the applicability of LIG towards sustainable electrochemical devices.

6.1.1 Preliminary assessments and development of the laser processing strategy

Among the available cellulose substrates, Whatman Grade 40 qualitative filter paper was selected as the model precursor because of its high cellulose purity, minimal inorganic impurities and excellent batch-to-batch uniformity. Unlike commercial paper products containing fillers, coatings, or sizing agents, laboratory-grade filter paper provides a well-defined cellulose matrix that enables the influence of precursor chemistry on laser-induced material transformation to be investigated with minimal interference from additional components. Prior to laser processing, the paper was uniformly coated with a flame-retardant (FR) solution using an ultrasonic spraying system to minimize excessive burning during laser irradiation. The spraying conditions were optimized to two spraying cycles at a flow rate of 0.02 mL/min, with the spray nozzle positioned 50mm (z direction) above the substrate to ensure homogeneous coating.

Preliminary laser-processing trials demonstrated that fabrication of conductive cellulose-derived LIG requires a different processing strategy from that established for polyimide. Initial experiments showed that direct focused laser irradiation frequently resulted in severe substrate ablation, discontinuous carbon formation, or complete destruction of the paper. Conversely, exclusively defocused irradiation produced only partial carbonization with irregular and poorly defined carbonized regions that exhibited limited electrical conductivity. These observations indicated that neither focused nor defocused laser processing alone was sufficient to produce continuous conductive structures on cellulose.

To overcome these limitations, a sequential two-step laser-processing strategy was investigated and shown in Figure 60. In the first step, defocused laser irradiation was employed to promote controlled carbonization over a larger irradiation area while minimizing localized overheating and catastrophic thermal degradation. The resulting carbonized layer subsequently served as a mechanically stable scaffold for a second focused laser treatment, which increased the local energy density and promoted graphitic ordering within the pre-carbonized region. The objective of this sequential approach was to improve conductive pathway formation while preserving the structural integrity of the cellulose substrate.

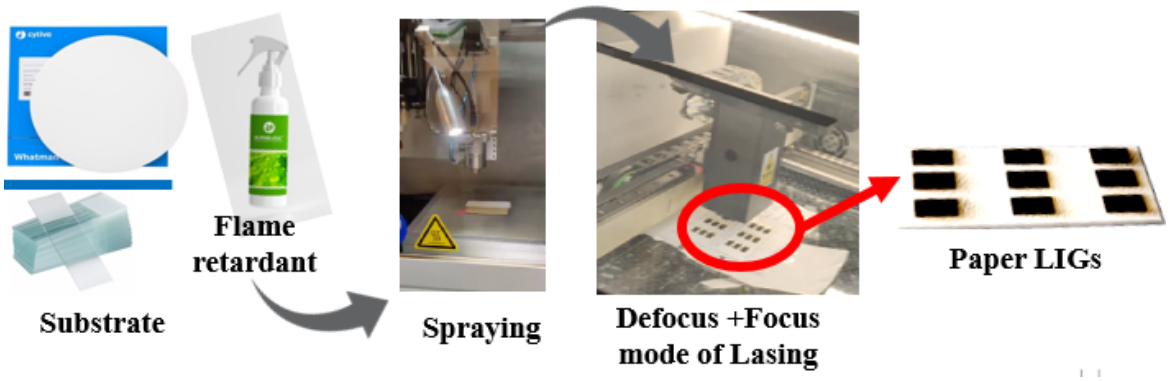


Figure 60: Schematic illustration of the substrate-specific laser-processing strategy developed for cellulose-derived LIG. The process comprises flame-retardant pretreatment followed by sequential defocused carbonization and focused laser treatment to promote graphitic ordering and conductive pathway formation.

Based on these preliminary observations, systematic optimization of laser processing was undertaken by varying laser power, scan speed, lasing mode and hatch interval. The following sections discusses the influence of these processing parameters on graphitic structure and conductive network formation in cellulose-derived LIG.

6.1.2 Influence of laser parameters - cellulose -derived LIGs/ Paper-LIGs

The objective and the primary step is to identify the laser processing conditions that maximize graphitic ordering while minimizing substrate degradation. The optimization strategy adopted in this work focused on identifying the combination of laser parameters capable of producing continuous laser-written tracks while maintaining the structural integrity of the cellulose matrix. Considering each laser parameter independently, Because laser power, scan speed, lasing mode and hatch interval collectively determine the effective energy delivered to the substrate, these parameters were systematically investigated to suggest a suitable processing window for cellulose-derived LIG.

As shown in Figure 61, initial experiments employed focused laser irradiation over a broad range of laser powers (5-20%) and scan speeds (40-200mm/s) while maintaining a constant hatch interval of 0.05mm. Under these conditions, direct focused irradiation frequently produced localized burning, ash formation, whole generation, or discontinuous carbon tracks. Resistance measurements were generally unstable or exceeded the measurable range, indicating that continuous conductive pathways were not established. These observations suggest that the localized energy density generated under focused irradiation exceeded the thermal tolerance of cellulose, resulting in rapid substrate degradation instead of controlled graphitic transformation.

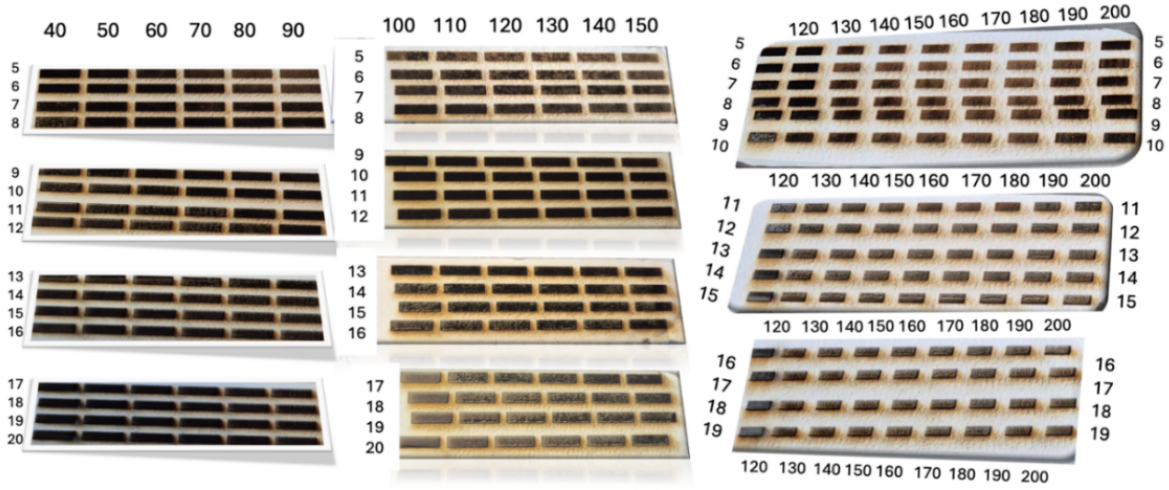


Figure 61: Photographs of cellulose-derived LIG fabricated using focused laser irradiation over a range of laser powers (5-20%) and scan speeds (40-200mm/s) with a constant hatch interval of 0.05mm. Direct focused irradiation resulted predominantly in localized burning, substrate perforation and discontinuous carbon formation.

To reduce localized thermal damage, the influence of defocused laser irradiation was investigated and shown in Figure 61 and Figure 62. Unlike focused processing, defocused irradiation generated broader carbonized regions with reduced substrate destruction. However, the resulting patterns remained discontinuous and exhibited poor electrical conductivity, indicating that defocused irradiation alone promoted carbonization but was insufficient to establish continuous graphitic networks. Increasing the defocused laser power beyond 10-15% again resulted in severe substrate damage, leading to refinement of the defocused power range to 3-8%.

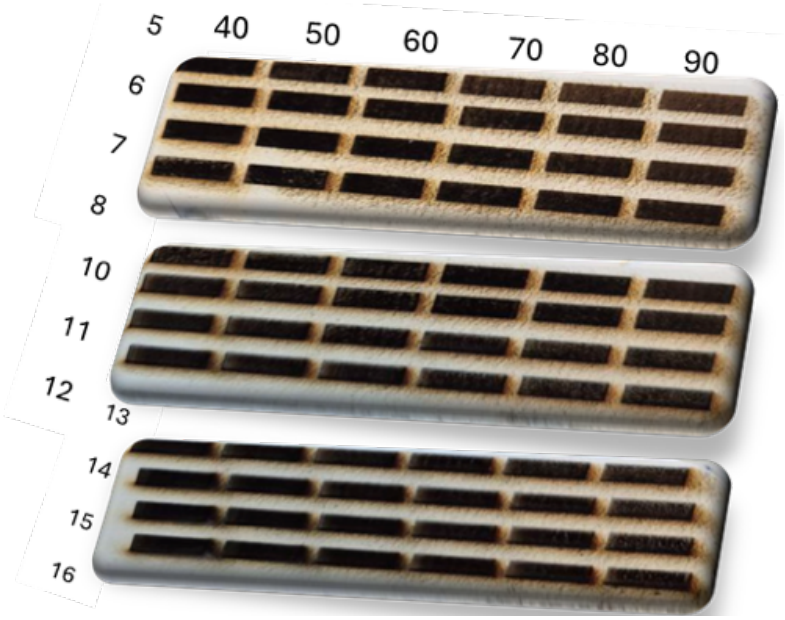


Figure 62: Photographs of cellulose substrates processed exclusively under defocused laser irradiation. Defocused processing reduced substrate burning but produced discontinuous carbonized regions with limited electrical conductivity. Samples prepared at different power from 5% and speed from 40 to 90mm/s, at interval 0.05mm.

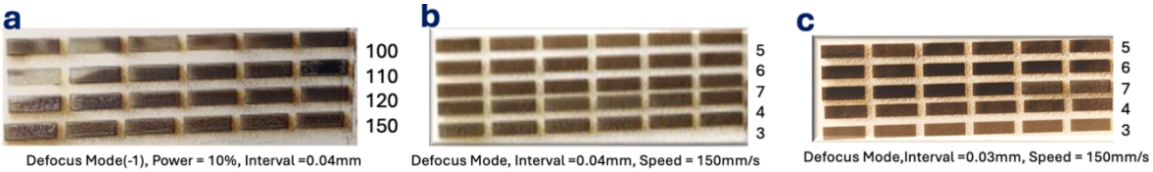


Figure 63: Defocused mode only lasing (-1mm) : a) same power and different speed with interval 0.04mm, b) same speed of 150mm/s and different powers, c) same speed of 150mm/s and different laser power with interval of 0.03mm.

The complementary behaviour observed during focused and defocused processing motivated the development of a sequential two-step laser strategy. In this approach, defocused irradiation was first employed to generate a carbonized scaffold, followed by focused irradiation to locally increase the energy density and promote graphitic ordering within the pre-carbonized layer. Visual examination demonstrated substantially improved pattern continuity and reduced substrate degradation compared with either focused-only or defocused-only processing, indicating that separating carbonization and graphitization into two consecutive processing steps provides a broader and more controllable processing window for cellulose-derived LIG.

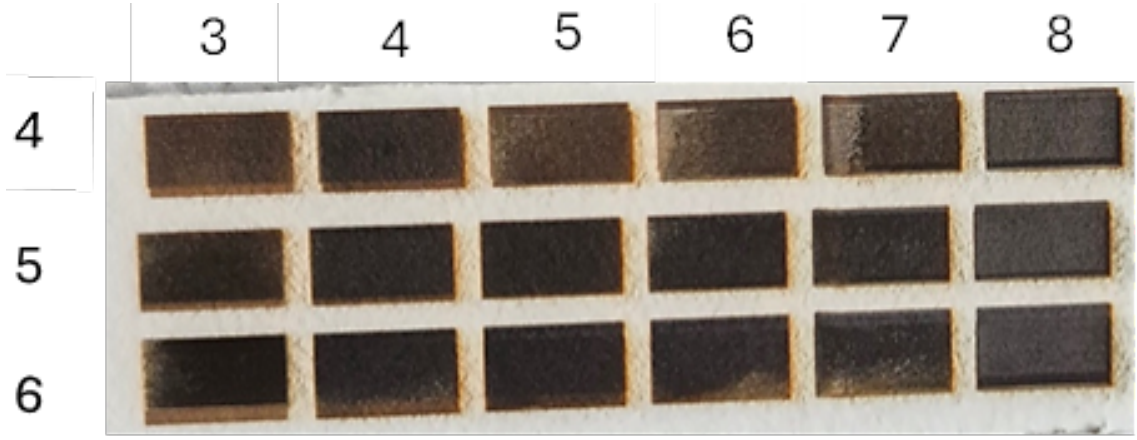


Figure 64: Representative cellulose-derived LIG fabricated using the sequential defocused-focused laser-processing strategy. Defocused laser powers (3-8%) were combined with focused laser powers (4-6%) at a scan speed of 150mm/s and a hatch interval of 0.02mm.

Following establishment of the sequential processing strategy, laser power combinations and hatch interval were further optimized to improve structural continuity. Preliminary resistance measurements indicated that although graphitic structures could be generated, the electrical response remained unstable, suggesting incomplete interconnection of the graphitic domains. Consequently, the influence of hatch interval was investigated by reducing the spacing from 0.05mm to 0.03mm and 0.02mm.

Optical observations obtained using Raman microscopy demonstrated that decreasing the hatch interval progressively increased the overlap between adjacent laser tracks as shown in Figure 65 and Figure 66. Smaller hatch intervals produced more continuous carbonized regions and reduced the presence of unprocessed areas between neighbouring scan lines.

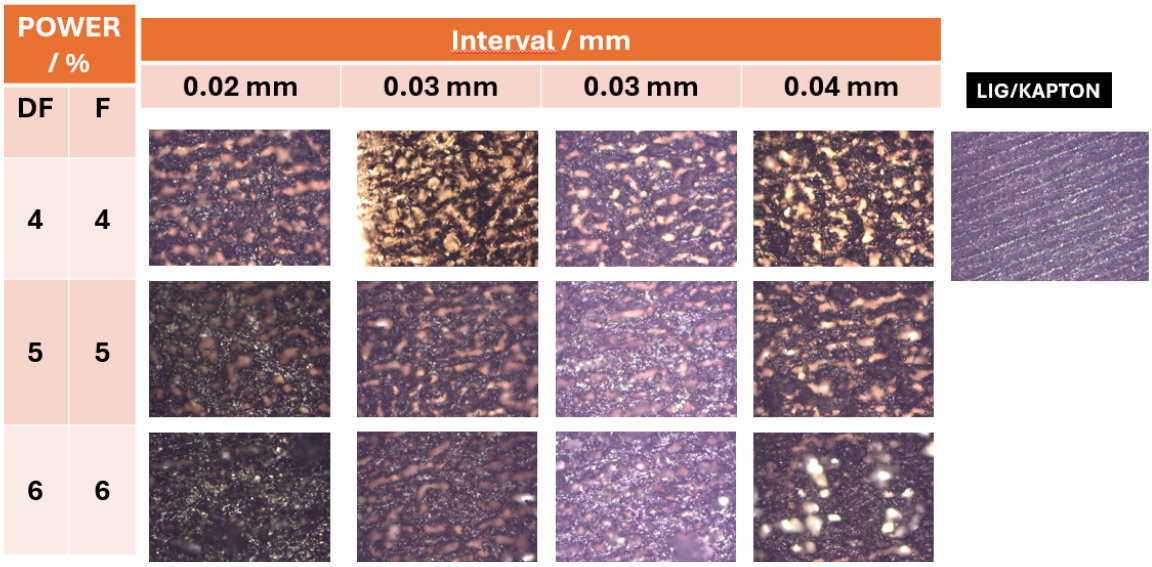


Figure 65: Raman optical micrographs illustrating the influence of hatch interval (0.05, 0.04, 0.03 and 0.02mm) on the continuity of cellulose-derived LIG. Progressive reduction of the hatch interval increased overlap between adjacent laser tracks and improved structural uniformity.

Based on these observations, a scan speed of 150mm/s together with a hatch interval of 0.02mm was selected for subsequent characterization, as these conditions provided the most uniform laser-written structures while minimizing excessive thermal damage.

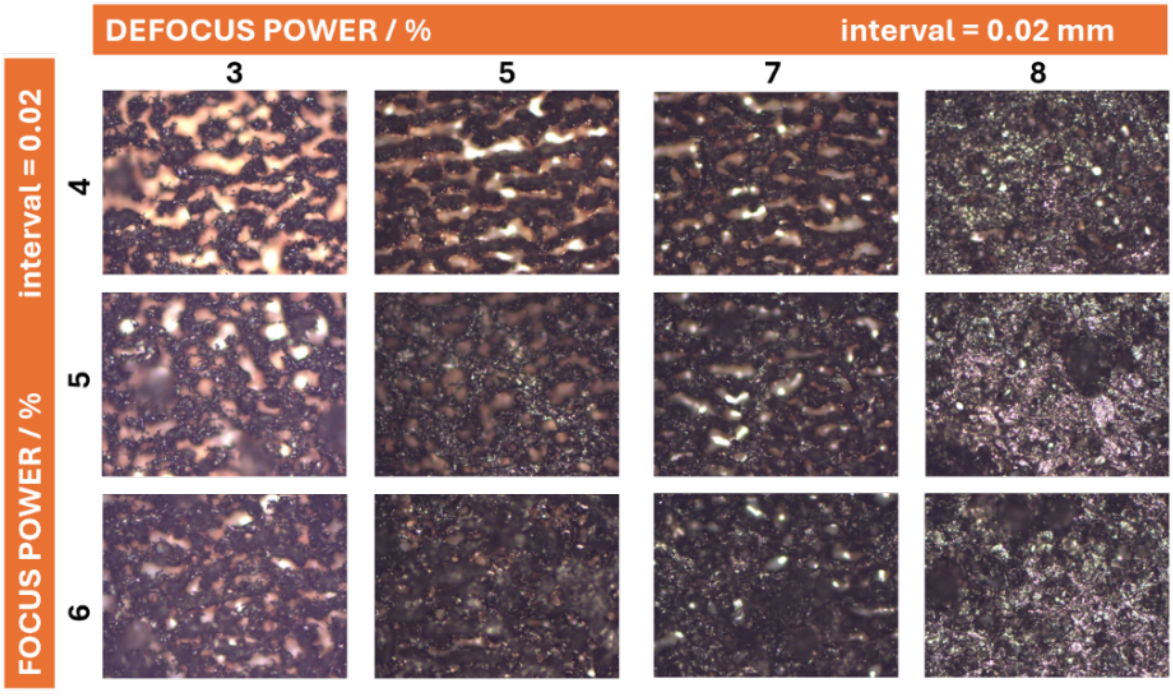


Figure 66: Raman optical micrographs of cellulose-derived LIG fabricated at a fixed scan speed of 150mm/s and a hatch interval of 0.02mm under different combinations of defocused and focused laser powers. The images illustrate the processing conditions selected for subsequent structural characterization.

As shown in Figure 66, combination of the defocus power of 8% with focus powers of 4, 5, 6% and defocus power of 7% with focus power of 6% is selected as they have dense structure formation. Additionally the set of 4,5,6% for both defocus and focus powers will be considered for further studies.

6.1.3 Structural evolution and graphitic ordering of cellulose-derived LIG

Visual observations alone cannot confirm graphitic ordering within the processed material. Therefore, Raman spectroscopy was employed to determine whether the sequential laser-processing strategy promoted the formation of graphitic carbon.

Representative Raman spectra obtained from samples fabricated under different processing conditions are presented in Figure 67 and Figure 68. Samples prepared exclusively by focused irradiation exhibited weak or poorly resolved D and G bands, indicating incomplete graphitic ordering. These observations are consistent with the extensive substrate degradation and unstable electrical behaviour observed during the preliminary optimization experiments.

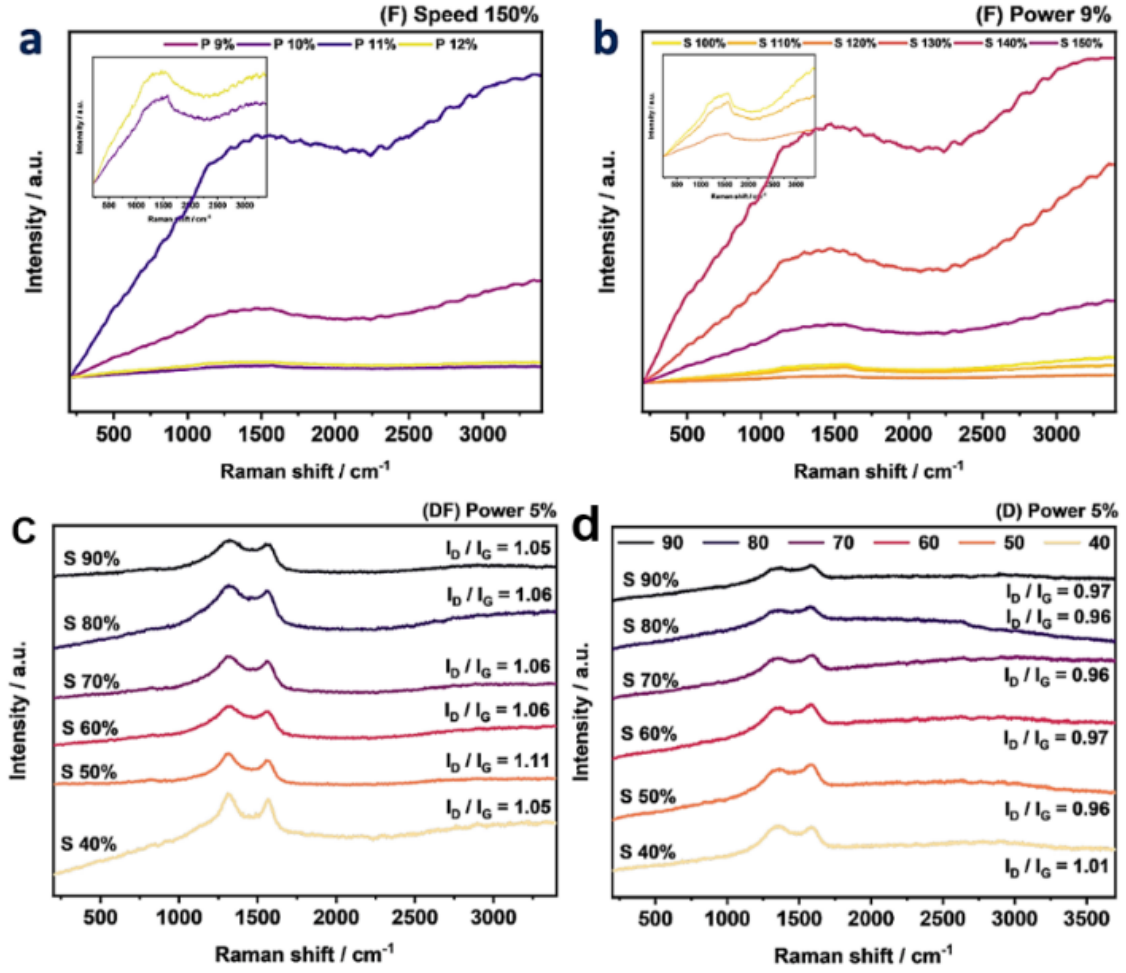


Figure 67: Representative Raman spectra of cellulose-derived LIG fabricated under different laser-processing conditions: (a) focused irradiation at different laser powers, (b) focused irradiation at different scan speeds, (c) sequential defocused-focused processing and (d) defocused irradiation at different scan speeds. The spectra illustrate the evolution of graphitic carbon as a function of the laser-processing strategy.

In contrast, samples fabricated using the sequential defocused-focused processing strategy exhibited well-defined D and G bands characteristic of graphitic carbon, confirming that the two-step processing approach promoted graphitic ordering while reducing excessive thermal degradation. Although the calculated I_D/I_G ratios generally remained close to or slightly above unity, indicating a defect-rich graphitic structure, the

spectra demonstrate successful conversion of the cellulose precursor into conductive graphitic carbon under the optimized processing conditions.

The graphitic features were successfully generated, the calculated I_D/I_G ratios generally remained close to or slightly above unity, indicating that the material consists predominantly of defect-rich graphitic carbon rather than highly ordered graphene. This behaviour is expected for cellulose-derived LIG because the precursor undergoes extensive dehydration, depolymerization and volatile evolution prior to graphitization, producing a carbon containing numerous structural defects and disordered sp^2 domains.

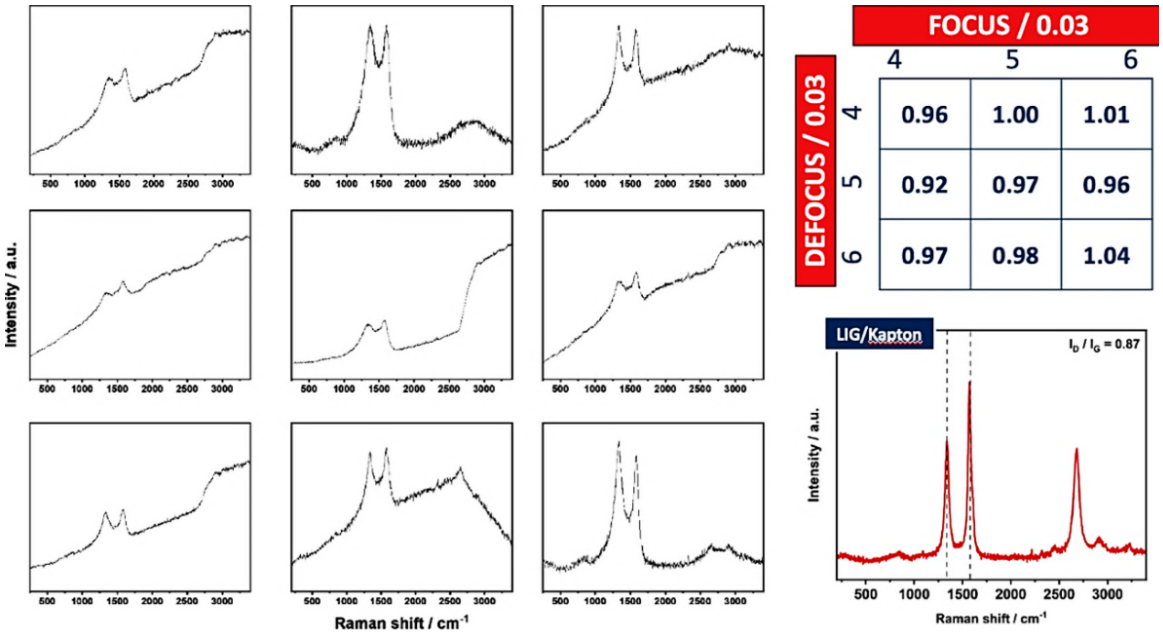


Figure 68: Representative Raman spectra of cellulose-derived LIG fabricated using the sequential defocused-focused laser-processing strategy (scan speed 150mm/s, hatch interval 0.03mm). Well-defined D and G bands indicate graphitic carbon formation, while the corresponding I_D/I_G ratios suggest the development of defect-rich graphitic structures. Focused-only processing produced weak graphitic features, whereas sequential processing resulted in improved structural ordering.

The Raman observations further indicate that reducing the hatch interval improves the continuity of the graphitic network by increasing overlap between adjacent laser tracks. These structural observations are consistent with the improved stability of the resistance measurements obtained under the optimized processing conditions and suggest that conductive performance depends not only on graphitic ordering but also on the continuity of the interconnected carbon network.

The sequential defocused-focused laser strategy appears to provide sufficient thermal energy to promote graphitic ordering while avoiding the extensive substrate degradation observed under direct focused laser irradiation.

Compared with the optimized Kapton-derived LIG, the Raman response of cellulose-derived LIG reflects the influence of precursor chemistry on graphitic network formation as shown in Figure 68. Although both materials exhibit the characteristic Raman features of laser-induced graphene, differences in the relative intensities, positions, and evolution of the Raman bands suggest differences in the graphitization process, consistent with the distinct thermal decomposition mechanisms and molecular structures of PI and cellulose.

These observations support the hypothesis that precursor chemistry governs the mechanisms of LIG formation and necessitates substrate-specific fabrication strategies.

The structural evolution observed by Raman spectroscopy provides the basis for understanding the electrical behaviour of the fabricated material. The graphitic ordering alone does not necessarily guarantee efficient electrical transport, as conductive performance additionally depends on the continuity of interconnected graphitic pathways throughout the laser-written network. Thus revealed the interval played a vital role in formation of dense conductive pathways and thus it accounts for the resistance measurements in the following chapter. Therefore, electrical characterization was subsequently performed to analyse the relationship between structural ordering and conductive network formation.

6.1.4 Electrical percolation and conductive network formation

Following structural characterization by Raman spectroscopy, the electrical properties of the optimized cellulose-derived LIG were evaluated through resistance measurements to determine whether graphitic ordering was accompanied by the formation of continuous conductive pathways. The electrical conductivity is governed not only by the presence of graphitic domains but also by their degree of interconnection, continuity and spatial distribution throughout the laser-written structure. Additionally, electrical characterization was performed to evaluate whether the optimized graphitization strategy provides complementary information regarding the effectiveness of the optimized laser-processing strategy. Based on the Raman optical images and the structural continuity observed under different processing conditions, samples fabricated using a scan speed of 150mm/s, a hatch interval of 0.02mm and a defocused laser power of 8% combined with focused laser powers of 3-6% exhibited the most uniform Paper LIGs with continuous dense graphitic networks.

Table 15. Sheet resistance of cellulose-derived LIG fabricated using the sequential defocused-focused laser-processing strategy at a scan speed of 150mm/s and different combinations of focused and defocused laser powers at interval spacing of 0.02mm.

Defocus Power (%)	Focus Power (%)	R_s (Ω/Sq)	Defocus Power (%)	Focus Power (%)	R_s (Ω/Sq)
3	5	1639.796	3	6	1122.932
4	5	1194.859	4	6	157.104
5	5	234.939	5	6	189.675
6	5	379.274	6	6	115.053
7	5	159.977	7	6	157.458
8	5	411. 587	8	6	104.969

Table 16. Sheet resistance of cellulose-derived LIG fabricated using the sequential defocused-focused laser-processing strategy at a scan speed of 150mm/s and different combinations of focused and defocused laser powers at interval spacing of 0.03mm.

Defocus Power (%)	Focus Power (%)	R_s (Ω/Sq)	Defocus Power (%)	Focus Power (%)	R_s (Ω/Sq)
3	5	1130.793	3	6	3494.453
4	5	366.853	4	6	237.6497
5	5	868.672	5	6	209.1505
6	5	68783.68	6	6	263.9906
7	5	63918.82	7	6	1443.712
8	5	888.727	8	6	289.7532

The electrical behaviour of the fabricated cellulose-derived LIG by resistance measurements provide a direct indication of conductive network formation by reflecting the effectiveness of graphitic domain interconnection throughout the laser-scribed architecture. In the context of LIG, a progressive reduction in electrical resistance is generally associated with improved graphitic continuity, enhanced electrical percolation and more efficient charge transport through the interconnected carbon network.

The resistance measurements demonstrated that electrical conductivity evolved progressively as the laser processing strategy was refined. Samples produced under non-optimized processing conditions exhibited comparatively high electrical resistance and unstable readings, indicating incomplete formation of interconnected conductive pathways. In contrast, implementation of the sequential laser processing strategy together with optimized fabrication parameters produced a substantial reduction in resistance, demonstrating that the graphitic domains generated during laser irradiation had developed into a continuous electrically conductive network.

The hatch interval have a significant influence on the electrical behaviour of the fabricated structures. Reducing the spacing between adjacent laser scan lines increased overlap between neighbouring graphitized regions, thereby improving conductive pathway continuity and decreasing resistance. The larger hatch intervals produced discontinuous conductive regions separated by partially carbonized cellulose. Thus, it demonstrate that electrical conductivity depends not only on the degree of graphitic ordering but also on the spatial continuity of the interconnected carbon network.

These observations of electrical measurements are consistent with the structural observations obtained from Raman spectroscopy. Samples exhibiting better-defined graphitic features and more continuous laser-written structures generally displayed lower and more stable resistance values. This correlation suggests that optimization of the laser-processing conditions promotes both graphitic ordering and conductive network formation within the cellulose-derived material.

Taken together with the Raman analysis, the electrical measurements establish a direct structure-property relationship for Paper-LIGs. These indicates, the optimization of laser-processing conditions is essential for

achieving continuous graphitic networks on cellulose substrates and provide the basis for future investigations into the physicochemical and electrochemical properties of cellulose-derived laser-induced materials.

6.1.5 Future characterization and scientific outlook

An important outcome of this work is the demonstration that successful fabrication of cellulose-derived LIG requires independent control of carbonization and graphitization by defocused-focused laser-processing strategy. Systematic optimization of laser power, scan speed, focal position and hatch interval was performed to identify processing conditions that promoted graphitic network formation while minimizing thermal degradation of the cellulose substrate.

The combined structural and electrical characterization demonstrates that optimization of laser-processing conditions is essential for achieving continuous conductive networks while preserving the structural integrity of the cellulose substrate. These provides an initial understanding of the relationship between laser-processing parameters, graphitic ordering and conductive pathway formation in cellulose-derived LIG. Further characterization would provide a more comprehensive understanding of the physicochemical properties of the material. Evaluation of electrochemical behaviour was beyond the scope of this investigation. Nevertheless, the formation of continuous graphitic structures with improved electrical conductivity provides a suitable foundation for future studies examining the electrochemical characteristics of cellulose-derived LIG, including its behaviour as an electrode material under different electrochemical environments. Overall, these findings demonstrate that cellulose represents a promising alternative precursor for laser-induced graphitic materials following appropriate optimization of the laser-processing conditions. Further investigation of the physicochemical and electrochemical properties of the resulting material will contribute to a broader understanding of precursor-dependent LIG formation and its potential for future functional material development.

The results presented here provides the experimental foundation for investigating additional precursor materials and their influence on laser-induced graphitic carbon formation. Additionally it indicates laser-processing conditions is strongly dependent on the characteristics of the precursor material. This approach motivated the preliminary investigation on laser processing of PTFE, undertaken to evaluate the feasibility of generating laser-induced carbon structures on a chemically distinct fluoropolymer substrate and to explore how differences in precursor chemistry influence laser-induced material transformation.

6.2 Exploration of fluoropolymer precursors: towards laser modified fluoropolymer-derived carbon architectures

The investigations presented in the previous chapter demonstrated that precursor chemistry constitutes an important engineering variable governing graphitization behaviour and conductive network formation during laser processing. Building upon this concept, the next step is to investigate whether along with precursor selection can be further exploited to introduce additional material functionalities directly during laser irradiation and processing. In place of modifying LIG exclusively through post-fabrication surface engineering, precursor engineering offers the possibility of tailoring the physicochemical properties of graphene during laser processing by selecting polymers that contribute chemically active elements to the evolving carbon.

Among the available fluoropolymer materials, polytetrafluoroethylene (PTFE) represents a promising precursor owing to its exceptionally high fluorine content, strong carbon-fluorine (C–F) bonds, excellent chemical stability and low surface energy. During laser irradiation, localized photothermal heating induces decomposition of PTFE through cleavage of C–F bonds, resulting in complex thermochemical transformations. The chemical state and retention of fluorine within the processed material, however, require confirmation by complementary spectroscopic analysis.

As a result, laser processing of PTFE provides an opportunity to investigate not only graphitization but also the possibility of developing fluorine-containing carbonaceous architecture or graphene-based architectures through precursor-directed substrate engineering with potential applications in electrochemical sensing, energy storage, catalysis and advanced electronic devices. The PTFE provides a unique platform for investigating fluoropolymer-derived carbon architectures, which have attracted increasing interest because fluorine incorporation can modify electronic structure, surface energy, wettability, corrosion resistance and electrochemical behaviour. Unlike polyimide or cellulose, PTFE possesses a carbon backbone fully surrounded by fluorine atoms, resulting in unique physicochemical characteristics that may influence both LIG formation and the resulting graphene surface chemistry.

Accordingly, a preliminary exploratory study was undertaken to establish the feasibility of producing fluoropolymer-derived carbon architectures and to explore how precursor chemistry influences laser-induced material transformation.

Unlike the investigations presented for PI- and cellulose-derived LIG, the objective of the present study was not to demonstrate the successful formation of conventional LIG or fluorinated graphene (FG). Thus, this work represents an exploratory feasibility study aimed at identifying suitable laser-processing conditions capable of inducing controlled transformation of PTFE and establishing an initial processing window for future investigations of fluoropolymer-derived carbon materials.

6.2.1 Preliminary establishment of the laser processing window

The primary objective of this preliminary investigation was to identify laser-processing conditions capable of inducing controlled transformation of PTFE while preserving sufficient structural integrity for subsequent characterization. A systematic optimization matrix was therefore developed by varying laser power, scan speed, scribing mode and hatch interval over a broad range of processing conditions as shown in Figure 68.

Visual examination of the processed samples revealed several distinct transformation regimes depending on the applied laser energy. Under selected conditions, localized black carbonaceous regions were observed, indicating partial thermal transformation of the PTFE surface. However, increasing the delivered laser energy frequently resulted in extensive melting, severe deformation, or complete perforation of the substrate, demonstrating that PTFE possesses a considerably narrower processing window than either PI or cellulose.

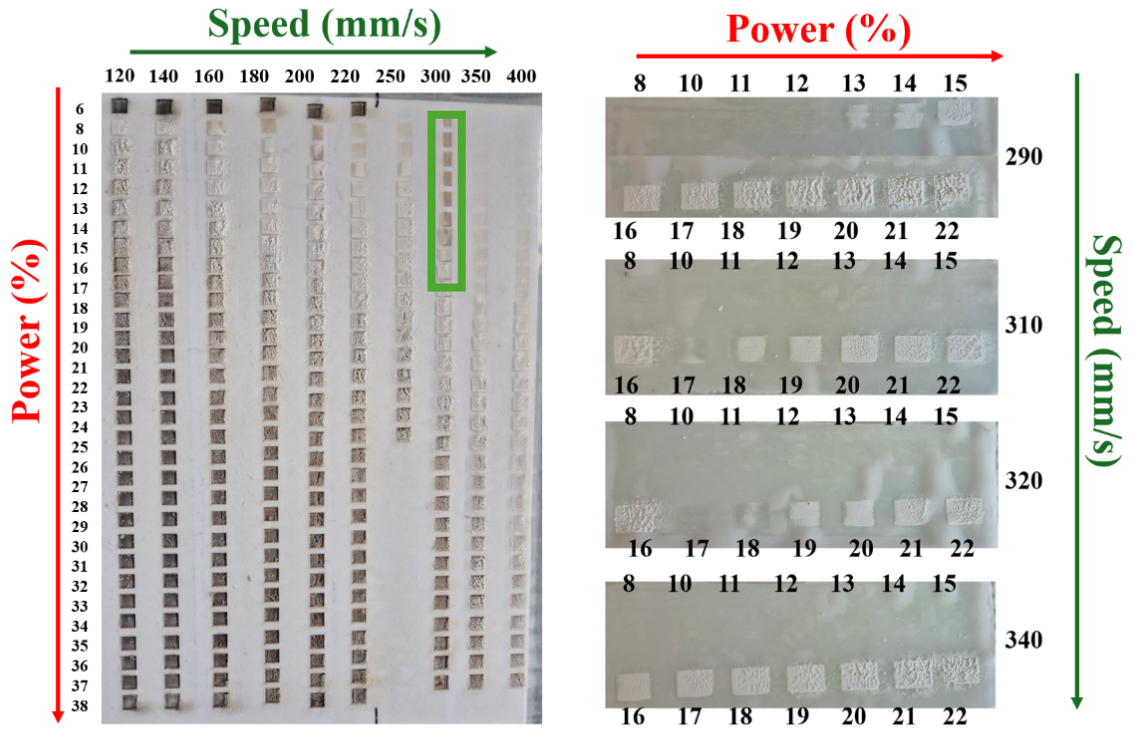


Figure 69: Preliminary processing matrix illustrating the influence of laser power and scan speed on the laser-induced transformation of PTFE under focused irradiation. Extensive melting and substrate perforation were observed under most processing conditions, whereas only a limited processing region (laser speed 300mm/s, laser power 6-15%) produced localized carbonaceous structures suitable for further investigation.

To further refine the processing conditions, the influence of positive and negative defocus together with hatch interval was subsequently evaluated and are shown in Figure 70. Adjustment of the focal position modified the spatial distribution of laser energy and influenced the extent of thermal transformation, whereas variation of the hatch interval affected the continuity of the processed regions. These observations establish an initial processing window that will serve as the basis for subsequent studies.

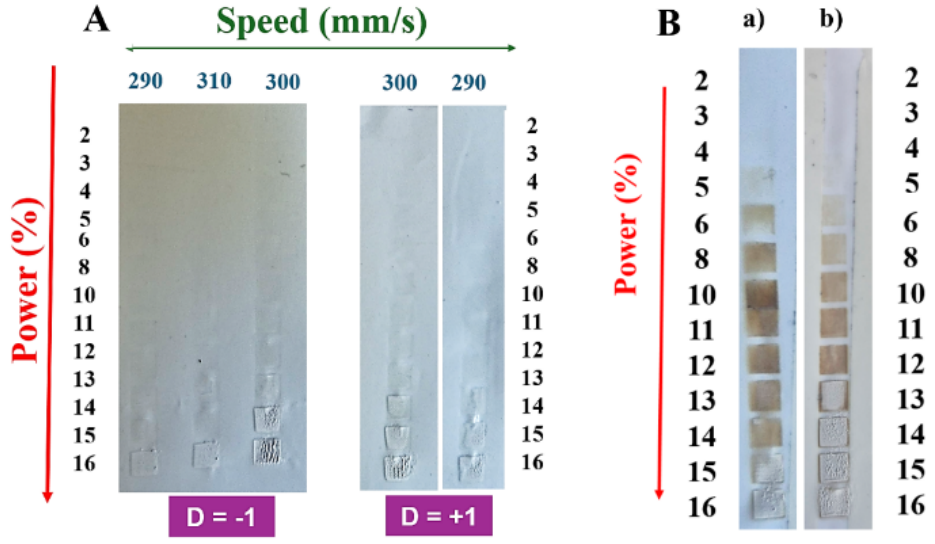


Figure 70: Preliminary evaluation of PTFE processing conditions showing the influence of scribing mode and intervals. A) Scribing mode (negative and positive defocus) and B) Intervals: a) 0.02mm and b) 0.05mm at laser speed of 300mm/s at focused scribing mode.

The photographic observations demonstrate that laser processing of PTFE proceeds through multiple transformation regimes as the delivered energy is varied. Changes in the visual appearance of the processed regions suggest progressive modification of the polymer surface during laser irradiation, although detailed structural characterization is required to determine the extent of carbonization, graphitic ordering and possible fluorine retention. Consequently, the optimization matrix presented here serves primarily to establish the processing conditions that will guide subsequent morphological, spectroscopic and electrical characterization of PTFE-derived carbonaceous architecture.

6.2.2 Preliminary physicochemical characterization

SEM was employed to examine the morphological changes induced by laser processing of PTFE under the preliminary optimized conditions. Representative micrographs obtained at different magnifications are presented in Figure 71a.

Laser irradiation produced pronounced morphological modification of the PTFE surface, resulting in the development of a heterogeneous porous carbonaceous morphology and irregular interconnected pores and partially fused regions, indicating substantial thermally induced transformation of the fluoropolymer. As observed in both micrographs, the processed regions exhibit an interconnected porous morphology consisting of irregular cavities and partially fused structural features distributed throughout the irradiated area.

The irregular pore distribution and partially collapsed regions suggest that localized melting, decomposition and material reorganization occurred during laser irradiation. Such behaviour is consistent with the complex thermal decomposition mechanism of fluoropolymers, where the exceptionally strong C–F bonds require substantially higher energy input than conventional LIG precursors. Consequently, the processed PTFE exhibits a heterogeneous carbonaceous morphology indicative of incomplete or localized carbonization than producing a well-developed graphitic foam-like architecture similar to PI-derived LIG. The observed morphology differs considerably from the highly interconnected graphene foam typically obtained from PI-derived LIG, also suggesting that precursor chemistry plays a decisive role in governing the laser-induced transformation pathway. Although the porous morphology suggests that laser irradiation induced significant modification of the fluoropolymer, SEM observations alone cannot confirm the formation of graphitic carbon or fluorinated graphene. Therefore, complementary structural and chemical characterization using Raman spectroscopy was employed.

Preliminary optical examination using Raman microscopic image revealed the presence of dark regions beneath the partially melted fluoropolymer surface PTFE layers as shown in Figure 71b, indicating localized laser-induced transformation. However, the optical appearance alone does not confirm the formation of graphitic carbon and must therefore be interpreted together with Raman spectroscopic analysis. However, Raman spectra acquired from the processed regions did not exhibit well-defined D and G bands characteristic of graphitic carbon under the investigated processing conditions. As a result, successful graphitization could not be confirmed at this stage.

Similarly, preliminary electrical measurements exhibited unstable resistance values, indicating that continuous conductive pathways had not yet been established. Although SEM revealed substantial morphological changes within the irradiated regions, the structural identity and chemical composition of the resulting material remain to be established through comprehensive physicochemical characterization.

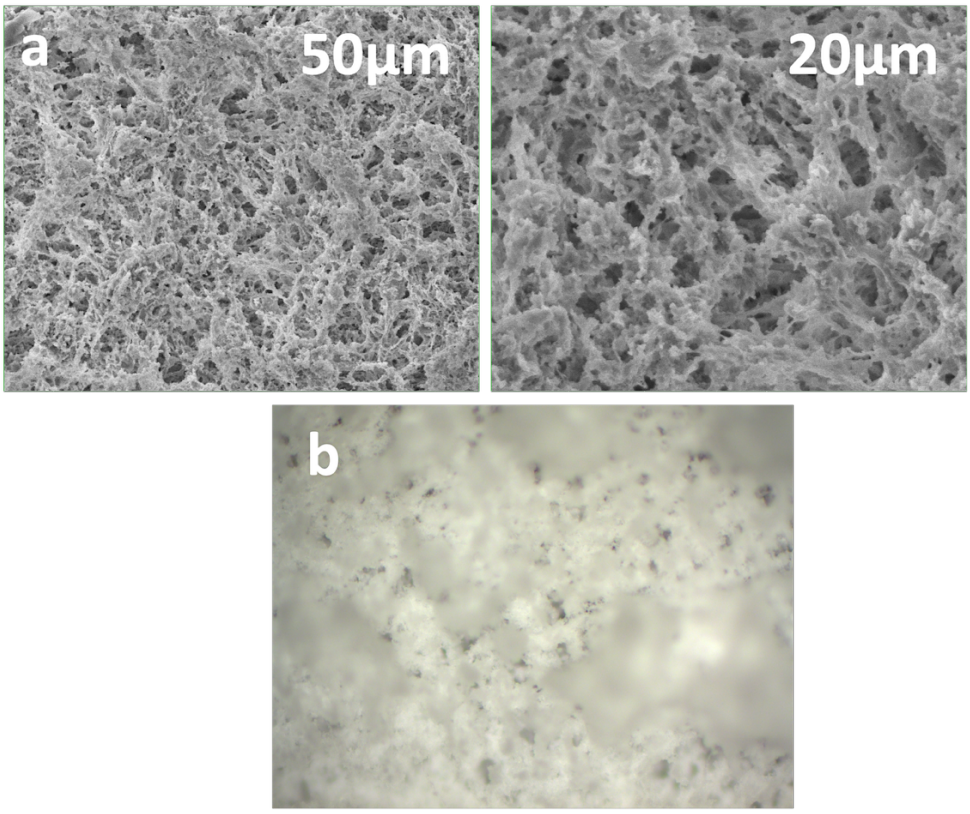


Figure 71: a) SEM of laser-processed PTFE fabricated under the preliminary optimized processing conditions at different magnifications corresponding to 50µm and 20µm scale bars; b) Raman microscopic image of laser-processed PTFE at P10% S300 and 0.05mm interval showing regions formed following preliminary optimization. Localized dark carbonaceous regions are observed beneath the partially melted fluoropolymer surface, indicating laser-induced material transformation; however, the formation of graphitic carbon cannot be confirmed from the present results.

Therefore, additional Raman spectroscopy, XPS, SEM and electrical conductivity measurements are required to determine the extent of carbonization, possible fluorine retention and the mechanisms governing laser-induced transformation of PTFE.

6.2.3 Significance and future outlook

Although the present investigation does not demonstrate the formation of conventional LIG or FG, it establishes an important first step towards understanding the laser-induced transformation of fluoropolymer precursors. The study identifies an initial laser-processing window for PTFE and demonstrates that localized carbonaceous structures can be generated under carefully controlled processing conditions. These findings provide the experimental basis for future optimization and detailed investigation of fluoropolymer-derived carbon architectures.

Unlike PI and cellulose, PTFE undergoes a fundamentally different laser-induced transformation because of the exceptional strength of C–F bonds and the complex decomposition behaviour of fluoropolymers. As a result, considerably more extensive structural, chemical and electrical characterization is required before the formation of graphitic or fluorine containing carbon materials can be confirmed. Future work will therefore focus on systematic optimization of laser-processing parameters combined with comprehensive

physicochemical and electrical characterization to elucidate the mechanisms governing carbonization, fluorine retention and conductive network formation.

Together with the cellulose- and PTFE-based studies illustrate that the strategy developed throughout this thesis is transferable beyond conventional PI substrates and can be adapted according to the chemical nature of the precursor material. While the degree of graphitization and material functionality is strongly dependent on precursor chemistry, these preliminary findings highlight the broader potential of precursor engineering as a route towards the future development of chemically tailored carbon architectures for multifunctional interfaces.

6.3 Exploratory PEGDA-assisted transfer of LIG (LIGT) onto flexible hydrogel substrates

The preceding chapters established systematic strategies for tailoring the structural, physicochemical and electrochemical properties of LIG through optimization of laser fabrication, precursor selection, nanomaterial functionalization and multifunctional interface engineering. Although these approaches successfully improved the electrochemical performance of LIG, the resulting electrodes remain intrinsically attached to the rigid substrate on which they are fabricated, limiting their mechanical adaptability. As a result, an important challenge is to determine whether the porous LIG architecture can be physically transferred onto mechanically compliant substrates while preserving its structural integrity.

Physical transfer of LIG from its parent substrate represents a promising strategy for overcoming this limitation. Such an approach could potentially enable the integration of laser-fabricated graphene with soft polymeric materials while maintaining the advantages of laser-based fabrication. However, successful transfer requires simultaneous preservation of the interconnected graphene architecture, adequate mechanical adhesion to the receiving substrate and retention of electrical continuity throughout the transferred network. Achieving these requirements remains a significant challenge.

To investigate the feasibility of this approach, preliminary transfer experiments were performed using PEGDA as a hydrogel support. PEGDA was selected because of its excellent biocompatibility, optical transparency, tunable mechanical properties and rapid UV-induced photopolymerization. Additionally, the uncured precursor can infiltrate the porous LIG architecture before crosslinking, providing a potential mechanism for mechanically anchoring the graphene network during substrate removal. The objective of this study was therefore not to demonstrate a fully functional flexible electrochemical electrode, but rather to evaluate the feasibility of physically transferring LIG while preserving its structural morphology.

6.3.1 Evaluation of feasibility of PEGDA-assisted LIG transfer

Initial proof-of-concept experiments demonstrated the transfer of LIG from the parent PI substrate onto PEGDA-supported hydrogel films as shown in Figure 72. Visual inspection showed that the macroscopic electrode geometry was retained after peeling, indicating that photopolymer-assisted transfer provides a feasible strategy for preserving the overall LIG architecture during substrate removal by physical/manual peeling off.

The influence of PEGDA molecular weight on the transfer behaviour was subsequently investigated. Distinct differences in mechanical flexibility were observed between the investigated formulations. PEGDA with a

molecular weight of 700 Da exhibited the greatest flexibility, whereas lower molecular-weight formulations produced progressively stiffer hydrogel supports with reduced mechanical compliance. The corresponding TQS value for the PEGDA with molecular weights of 700, 500 and 250 Da are 5, 3 and 1respectively. These preliminary observations suggest that the mechanical properties of the supporting hydrogel influence the integrity of the transferred graphene architecture and should therefore be considered as an important design parameter during transfer optimization.

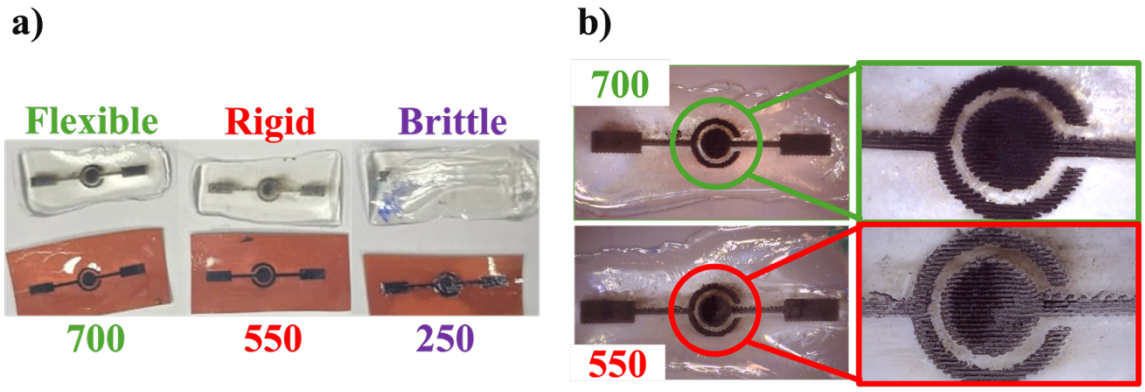


Figure 72: PEGDA-assisted transfer of LIG. (a) Digital photographs of parent LIG and PEGDA-supported transferred structures prepared using PEGDA with molecular weights of 700, 500 and 250 Da. (b) Optical microscopic images illustrating preservation of the transferred graphene patterns following substrate removal.

The transferred structures retained their macroscopic geometry after peeling, confirming that the transfer methodology is capable of mechanically supporting the porous LIG architecture. Still these experiments should be regarded as a preliminary demonstration of physical transfer rather than complete translation into a functional flexible electrode. The quality of the transferred structures is expected to depend on the balance between several competing parameters, including polymer infiltration into the porous graphene network, crosslinking density, mechanical cohesion of the hydrogel and adhesion between the graphene and polymer matrix.

Thus, further optimization is required before reliable electrical functionality can be achieved. The observed dependence on PEGDA molecular weight further indicates that hydrogel elasticity influences the transfer process. Increasing molecular weight produced progressively more compliant hydrogel supports, whereas lower molecular-weight formulations generated stiffer structures that exhibited reduced flexibility. These findings provide an initial basis for systematic optimization of the transfer methodology by correlating hydrogel composition with transfer efficiency and structural preservation.

6.3.2 Preliminary structural and electrical assessment of transferred LIG

To further evaluate the influence of the transfer process on the integrity of the graphene architecture, preliminary SEM was performed on the PEGDA-supported transferred structures. Representative micrographs obtained at different magnifications are presented in Figure 73.

The SEM observations demonstrate that the transferred material largely retains the characteristic porous morphology of the parent LIG following substrate removal. At lower magnification, the interconnected carbon remains continuous over relatively large areas without evidence of extensive delamination or complete structural collapse. Higher-magnification images further reveal preservation of the porous fibrous architecture

that is characteristic of the parent LIG, indicating that the transfer process does not completely disrupt the laser-generated microstructure.

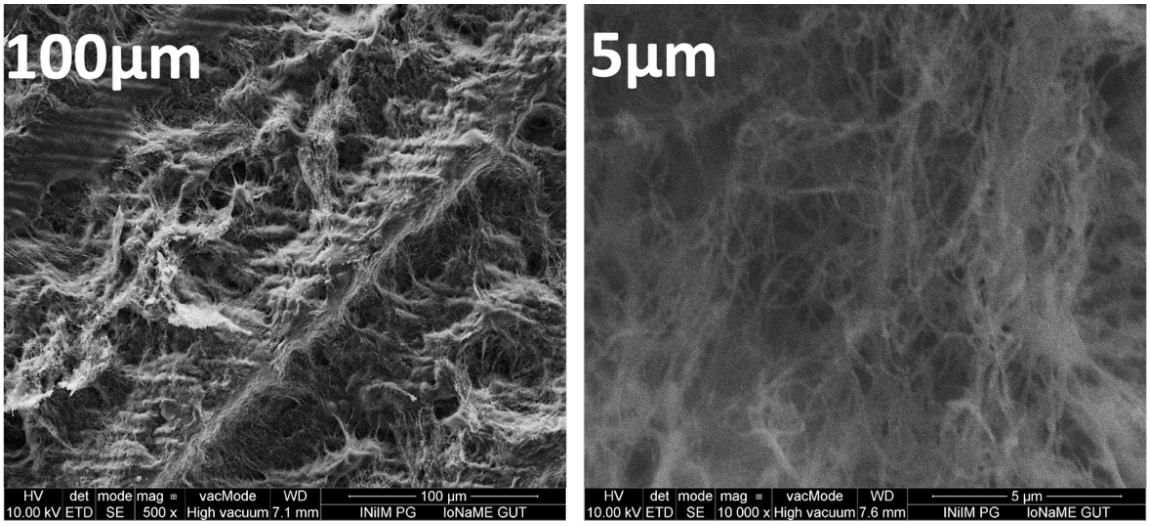


Figure 73: SEM micrographs of PEGDA-assisted transferred LIG at different magnifications. The transferred material retains the characteristic porous architecture of the parent LIG while remaining partially embedded within the PEGDA hydrogel matrix, indicating preservation of the laser-generated morphology following physical transfer.

Although the overall morphology is retained, SEM also reveals that portions of the porous graphene network are embedded within the surrounding PEGDA matrix. Such encapsulation is expected because the uncured PEGDA precursor infiltrates the porous LIG architecture prior to UV crosslinking, thereby mechanically anchoring the graphene during substrate removal. As a result, the transferred material should be regarded as a hydrogel-supported graphene composite more than a free-standing graphene film. The extent of polymer infiltration is expected to influence both the mechanical stability and the continuity of conductive pathways within the transferred structure.

The preservation of the porous morphology demonstrates that physical transfer can be achieved without complete destruction of the laser-generated architecture. However, SEM observations alone cannot determine whether the electrical connectivity of the graphene network has also been preserved. Therefore, complementary electrical characterization was performed to evaluate the continuity of the conductive network after transfer.

Preliminary resistance measurements revealed that the transferred structures currently exhibit unstable and poorly reproducible electrical behaviour. Measured resistance values frequently remained within the giga-ohm range or fluctuated substantially between repeated measurements, indicating that continuous conductive pathways were not consistently preserved following the transfer process.

The loss of electrical continuity is likely associated with several factors acting simultaneously. Partial infiltration of PEGDA into the porous graphene network may locally interrupt conductive pathways, while mechanical stresses generated during substrate removal may disrupt fragile graphitic connections within the three-dimensional architecture. In addition, excessive encapsulation of the graphene by the crosslinked hydrogel may reduce electrical contact between neighbouring graphitic domains. These observations indicate that preservation of morphology alone is insufficient to guarantee preservation of electrical functionality.

As a result, successful transfer of LIG should be considered as a multi-parameter engineering problem requiring simultaneous optimization of mechanical stabilization, polymer infiltration and electrical continuity. The present study therefore establishes the feasibility of physical transfer while identifying preservation of electrical conductivity as the principal challenge requiring further optimization.

To address this limitation, systematic optimization of the transfer process is planned through evaluation of the influence of PEGDA composition, water content, photoinitiator concentration, TQS and UV curing conditions. These parameters are expected to govern hydrogel viscosity, polymer infiltration, crosslinking kinetics and ultimately the structural and electrical integrity of the transferred graphene architecture.

The transfer mechanism further highlights the competing requirements governing successful transfer. Sufficient infiltration of the uncured PEGDA precursor is required to mechanically anchor the porous graphene network before polymerization. However, excessive penetration may partially fill the porous architecture and interrupt conductive pathways, whereas insufficient infiltration may reduce adhesion between the hydrogel and graphene, resulting in incomplete transfer or structural delamination during peeling. Optimization of these competing phenomena therefore represents a critical step toward improving both transfer efficiency and electrical continuity.

6.3.3 Future characterization and scientific outlook

The preliminary investigations presented in this chapter establish the feasibility of PEGDA-assisted physical transfer of LIG from the parent PI substrate onto flexible hydrogel supports while preserving the characteristic macroscopic geometry and porous microstructure of the original material. Although the transferred structures retain the morphological features of the parent LIG, the present results indicate that preservation of structural integrity alone does not ensure preservation of electrical functionality. Therefore, the current study should be regarded as an initial proof-of-concept demonstrating the feasibility of physical transfer rather than the realization of a fully functional flexible electrochemical electrode.

The findings further demonstrate that successful transfer depends on balancing several competing phenomena, including polymer infiltration into the porous graphene network, hydrogel crosslinking, mechanical adhesion and preservation of conductive pathways. These observations identify electrical continuity as the principal engineering challenge governing the development of transferable LIG architectures and establish a rational basis for future optimization of the transfer methodology.

Future investigations will therefore focus on systematic optimization of the transfer process through controlled variation of PEGDA composition, water content, TPO concentration and UV curing conditions. These parameters are expected to influence polymer viscosity, infiltration behaviour, crosslinking density and mechanical stability, thereby governing the structural and electrical integrity of the transferred material. Following optimization, comprehensive characterization will be performed to determine whether the structural, physicochemical and electrochemical properties of the parent LIG can be preserved following transfer.

The present investigation explores an additional strategy for physically transferring LIG onto flexible hydrogel supports by introducing substrate-independent transfer as an additional engineering strategy. Whereas the preceding chapters demonstrated how laser processing, precursor selection and surface engineering can be employed to tailor the properties of substrate-bound LIG, the present work explores the

feasibility of transferring these engineered materials onto mechanically compliant hydrogel supports. Although further optimization is required before functional electrochemical performance can be achieved, the study provides a systematic foundation for future investigations into transferable LIG architectures.

Rather than demonstrating a ready-to-use flexible electrochemical platform, this work establishes the key processing variables and engineering considerations governing PEGDA-assisted transfer of LIG. The insights obtained from this preliminary investigation contribute to the broader understanding of how fabrication methodology, material architecture and substrate engineering collectively influence the development of mechanically compliant graphene-based materials. Consequently, this proof-of-concept provides a scientifically grounded basis for future research aimed at developing transferable graphene architectures for flexible electrochemical systems.

Exploratory studies and future perspectives

The investigations presented in this chapter is the preliminary exploration of extension of the methodology developed for LIG beyond conventional PI-derived materials. These three exploratory studies were primarily designed to evaluate the feasibility of expanding the applicability of the laser processing to alternative precursor materials and transferable architectures. The studies presented here were intended to examine preliminary processing strategies and identify the principal scientific challenges associated with extending laser-derived carbon materials to new material systems.

The cellulose investigation demonstrated that fabrication of electrically conductive graphitic structures requires substrate-specific optimization of the laser-processing conditions. A sequential defocused-focused laser-processing strategy produced more uniform laser-written structures than single-step irradiation, while Raman spectroscopy indicated graphitic carbon formation and resistance measurements showed improved continuity of the conductive network. These findings highlight the importance of balancing carbonization and graphitic ordering during laser processing and demonstrate that the optimum processing conditions depend on the characteristics of the precursor material.

The preliminary investigation of PTFE demonstrated that laser irradiation induces significant transformation of fluoropolymer surfaces and established an initial processing window for the formation of fluoropolymer-derived carbonaceous structures. Although the present results do not demonstrate the formation of conventional LIG or FG, they provide important insights into the influence of fluoropolymer chemistry on laser-induced material transformation and identify the principal challenges associated with graphitization, fluorine retention and conductive network formation. These findings establish a scientific basis for future optimization of fluoropolymer-derived carbon architectures and further highlight the importance of precursor chemistry in governing laser-induced material evolution.

In comparison with polyimide-derived LIGs, these findings indicate that substrate-specific optimization is an essential component of LIG fabrication and that processing strategies cannot be directly generalized across chemically distinct precursor materials and varies with varying substrate/ precursor material. Thus, substrate selection becomes an additional engineering parameter that can be exploited alongside laser parameters potential graphitization window. Therefore the precursor chemistry itself is a controllable variable in the design of LIG.

Complementary to precursor engineering, the PEGDA-assisted transfer study explored the feasibility of transferring LIG onto flexible hydrogel supports. The preliminary results demonstrated preservation of the macroscopic geometry and porous morphology of the parent LIG following transfer, confirming that photopolymer-assisted transfer provides a viable strategy for producing hydrogel-supported graphene architectures. However, unstable electrical behaviour indicated that preservation of structural morphology alone is insufficient to ensure preservation of electrical continuity. As a result, the study identifies electrical connectivity as the principal engineering challenge governing the development of transferable LIG architectures and establishes a rational future optimization of the transfer methodology.

Together, these exploratory investigations demonstrate that the engineering concepts developed throughout this dissertation are transferable beyond conventional PI-derived LIG. More importantly, they illustrate that both precursor chemistry and substrate engineering represent additional design variables that can further expand the versatility of laser-derived carbon materials. While these studies remain preliminary and require further optimization and comprehensive characterization, they provide valuable scientific insight into the challenges associated with extending LIG to alternative precursor materials and mechanically compliant supports.

Overall, these investigations should be regarded as proof-of-concept studies that broaden the scope of the approach established in this dissertation rather than as fully optimized material systems. Collectively, they reinforce the central conclusion of this work that the performance and functionality of laser-derived carbon materials are governed by the synergistic interaction between processing conditions, precursor chemistry, material architecture, surface engineering and substrate selection as these parameters are heavily interrelated. Future work should focus on comprehensive physicochemical characterization of the developed materials, together with systematic evaluation of their electrical, mechanical and electrochemical properties. These findings establish a scientifically grounded foundation for future investigations aimed at developing advanced laser-derived carbon materials for multifunctional electrochemical interfaces. The knowledge gained from these studies will contribute to the continued development of laser-derived carbon materials across a broader range of precursor systems and supporting architectures.

CONCLUSIONS

Through this dissertation it was aimed to fabricate LIGs with optimal properties and to modify their surface using various bio- and nanomaterials for targeted applications. It was found that laser fabrication parameters, such as laser power and speed, can drastically affect the final properties of the fabricated LIG. Electrical and electrochemical properties, morphological features and hydrophilicity of LIGs fabricated under different laser parameters were found to be highly different and intercorrelated. Although, most of the research work was performed on polyimide foils, as the substrate for LIG fabrication, the lasing procedure was extended to include paper or cellulose as a sustainable and biodegradable substrate for disposable LIG-based materials. It was found that utilization of a flame-retardant material and meticulous selection of lasing parameters, especially defocusing, are necessary to make LIGs on the cellulose-based substrates. This allows for carbonization and graphitization without burning the paper during lasing.

LIGs are powerful electrode materials, with favourable inherent characteristics, the surface engineering strategies can further enhance its applicability in different fields from energy storage to environmental and health applications. Accordingly, metal nanoparticles decoration was utilized as the first surface modification strategy. It was found that noble metal nanoparticles, especially Pt and Ir, can significantly enhance the electrocatalytic properties of LIGs. It was observed that the best procedure for electrodeposition of nanoparticles is through Chronopotentiometric mode, i.e., a constant reductive current and using a sequential procedure because various nanoparticles, even Pt and Ir which are next to each other in the periodic table, have different reduction potential making it challenging to co-deposit them. This procedure can be extended to decorate LIG surface with other metallic nanoparticles, as well. It was found that, compared to individual nanoparticles, Pt-Ir heteronanostructures show enhanced catalytic activity toward H_2O_2 compared to either unmodified LIG or LIG that are modified by individual metal nanoparticles. Electrodeposition of nanoparticles also impacts the EASA and heterogeneous electron transfer rate constant.

While metal nanoparticles, are interesting candidates to induce electrocatalytic properties, soft electrochemical interfaces can result in further functionalities. Accordingly, specific functional monomers were selected to induced antibacterial and antibiofouling features to the LIG electrodes that can be helpful when utilized in environmental and biological media. It was observed that electropolymerization of APTAC monomer is easily possible on bare or metal nanoparticles-decorated LIGs while SBMA require a redox initiator to proceed. The corresponding initiation and propagation steps of polymerization can be discriminated via the cyclic voltammograms. Furthermore, it is possible to entrap biological macromolecules, like enzymes, in the hydrogel layer during electropolymerization process indicating that the copolymer also serves as enzyme immobilization matrix. The copolymer layer is expected to change charge transfer processes through changes in hydration, analyte diffusion and partitioning, because of functional groups and electrostatic charges of constituents. Electropolymerization was successful both on the bare and metal NPs decorated LIG indicating that decoration is not inhibiting the polymerization. As compared to traditional chitosan hydrogel as enzyme immobilization, this copolymer not only can immobilize enzyme without requirement for toxic crosslinkers, but also can induce further functionalities that cannot be attained via simple hydrogels. This electrochemical polymerization procedure can be extended toward other monomers to make electrochemical interfaces with tailored functionalities.

These showed the application of electrochemical procedures as a powerful technique to engineer the surface of LIG toward inducing or enhancing favourable properties or reducing unfavourable features. As a proof-of-concept, the obtained engineered LIG platforms were utilized to detect H_2O_2 and also glucose. The developed platform exhibited a broad linear glucose detection range of 0.5-7.5mM, a detection limit of 6.55μM and a sensitivity of 15.4 μA/mM/cm². Moreover, the copolymer-modified interface provided partial resistance to protein fouling and exhibited antibacterial potential associated primarily with the APTAC component.

In parallel to surface modification strategies, more interests were raised toward making LIGs on fluoropolymer-based substrates for special application. Furthermore, LIG transfer using polymerization-induced shrinkage can be harnessed to have LIG electrodes as more flexible, skin conformable and even stretchable platforms. Preliminary investigations showed the possibility to fabricate fluoropolymer-derived LIG and PEGDA-assisted LIG transfer.

Collectively, this thesis addressees the research gaps identified in the literature by:

1. Establishing a systematic methodology for optimization of LIG fabrication.
2. Improved understanding of relationships between laser parameters, LIG formation and precursor dependency, structural and electrochemical behaviour.
3. Elucidated the successful integration of catalytic nanozymes with multifunctional polymer interfaces while preserving electrochemical accessibility.
4. Validated the influence of these surface engineering protocols on operational stability, antifouling behaviour, antibacterial functionality and reliability of engineered LIG platforms

The principal scientific contribution of this thesis therefore extends beyond the development of an enzymatic glucose sensing platform. This work establishes a systematic and transferable multifunctional surface-engineering strategy for tailoring the electrochemical properties of LIG through rational integration of optimized laser fabrication, catalytic nanozyme functionalization and multifunctional polymer interfaces. The proof-of-concept hydrogen peroxide electrocatalysis and enzymatic glucose detection studies validate the effectiveness of the proposed engineering framework, while the underlying design principles provide a transferable foundation for the rational development of advanced LIG-based electrochemical interfaces. Beyond the proof-of-concept systems investigated in this work, the laser processing strategies developed in this dissertation and established surface engineering protocols has the potential to be extended to flexible and wearable electrochemical devices, microfluidic platforms, bioelectronic interfaces, electrocatalytic systems and other application-specific electrochemical technologies.

Furthermore, the intrinsic advantages of LIG, including its rapid direct-write fabrication, mask-free processing, scalability and exceptional design flexibility, provide a versatile manufacturing platform that can be readily customized for diverse application requirements. As advances in precursor engineering, laser processing and multifunctional surface modification continue to emerge, the application landscape of LIG is expected to expand progressively, creating new opportunities for future electrochemical and bioelectronic technologies.

REFERENCES

(1) Bard, Allen J; Faulkner, Larry R. *Electrochemical Methods: Fundamentals and Applications*, 2nd ed.; John Wiley & Sons: New York (or Hoboken, NJ), 2001.

(2) Wang Joseph. *Analytical Electrochemistry*, 3rd ed.; Wiley-VCH: Hoboken, NJ (or New York), 2006.

(3) Turner, A. P. F. Biosensors: Sense and Sensibility. *Chem. Soc. Rev.* **2013**, *42* (8), 3184–3196.

(4) Wang, C.; Liu, M.; Wang, Z.; Li, S.; Deng, Y.; He, N. Point-of-Care Diagnostics for Infectious Diseases: From Methods to Devices. *Nano Today* **2021**, *37*, 101092.

(5) Lin, J.; Peng, Z.; Liu, Y.; Ruiz-Zepeda, F.; Ye, R.; Samuel, E.; Yacaman, M.; Yakobson, B.; Tour, J. Laser-Induced Porous Graphene Films from Commercial Polymers. *Nature communications* **2014**, *5*, 5714.

(6) D. Crapnell, R.; Bernalte, E.; A. Muñoz, R. A.; E. Banks, C. Electroanalytical Overview: The Use of Laser-Induced Graphene Sensors. *Analytical Methods* **2025**, *17* (4), 635–651.

(7) Aftab, S.; Koyyada, G.; Mukhtar, M.; Kabir, F.; Nazir, G.; Memon, S. A.; Aslam, M.; Assiri, M. A.; Kim, J. H. Laser-Induced Graphene for Advanced Sensing: Comprehensive Review of Applications. *ACS Sens.* **2024**, *9* (9), 4536–4554.

(8) Avinash, K.; Patolsky, F. Laser-Induced Graphene Structures: From Synthesis and Applications to Future Prospects. *Materials Today* **2023**, *70*, 104–136.

(9) Ronkainen, N. J.; Halsall, H. B.; Heineman, W. R. Electrochemical Biosensors. *Chem. Soc. Rev.* **2010**, *39* (5), 1747–1763.

(10) Grieshaber, D.; MacKenzie, R.; Vörös, J.; Reimhult, E. Electrochemical Biosensors - Sensor Principles and Architectures. *Sensors* **2008**, *8* (3), 1400–1458.

(11) Obeid, P. J.; Sari-Chmayssem, N.; Yammine, P.; Homsi, D.; El-Nakat, H.; Matar, Z.; Hamieh, S.; Koumeir, D.; Chmayssem, A. Designs and Materials of Electrodes for Electrochemical Sensors. *ChemElectroChem* **2025**, *12* (19), e202500230.

(12) N. Sandhyarani PhD. Surface Modification Methods for Electrochemical Biosensors. In *Electrochemical Biosensors*; Elsevier, 2019; pp 45–75.

(13) George, C.; Neeraj, S. N.; Kalpana, P.; Naresh, H.; Janardhan, G.; Kumar, A.; Christo, M. S. Surface-Functionalized Carbon Nanostructures for Enhanced Electrochemical Sensing of Heavy Metals and Pesticides in Contaminated Ecosystems. *Microchemical Journal* **2026**, *224*, 117451.

(14) Haroon, N.; Stine, K. J. Surface Modification of Screen-Printed Carbon Electrodes. *Coatings* **2025**, *15* (10), 1182.

(15) Divya; Singh, A.; Chandra, P. Role of Surface Engineering in Advancement of Optoelectrochemical Sensing Platforms. *Journal of Industrial and Engineering Chemistry* **2026**, *157*, 22–35.

(16) Palanisamy, S.; Lee, H. F.; Chen, S.-M.; Thirumalraj, B. An Electrochemical Facile Fabrication of Platinum Nanoparticle Decorated Reduced Graphene Oxide; Application for Enhanced Electrochemical Sensing of H_2O_2. *RSC Adv.* **2015**, *5* (128), 105567–105573.

(17) Barzegar Amiri Olia, M.; Donnelly, P. S.; Hollenberg, L. C. L.; Mulvaney, P.; Simpson, D. A. Advances in the Surface Functionalization of Nanodiamonds for Biological Applications: A Review. *ACS Appl. Nano Mater.* **2021**, *4* (10), 9985–10005.

(18) Kalita, N.; Gogoi, S.; Minteer, S. D.; Goswami, P. Advances in Bioelectrode Design for Developing Electrochemical Biosensors. *ACS Meas. Sci. Au* **2023**, *3* (6), 404–433.

(19) McCreery, R. L. Advanced Carbon Electrode Materials for Molecular Electrochemistry. *Chem. Rev.* **2008**, *108* (7), 2646–2687.

(20) Costentin, C.; Limoges, B.; Robert, M.; Tard, C. A Pioneering Career in Electrochemistry: Jean-Michel Savéant. *ACS Catal.* **2021**, *11* (6), 3224–3238.

(21) Gibi, C.; Liu, C.-H.; Barton, S. C.; Anandan, S.; Wu, J. J. Carbon Materials for Electrochemical Sensing Application – A Mini Review. *Journal of the Taiwan Institute of Chemical Engineers* **2024**, *154*, 105071.

(22) Kangmennaa, A.; Forkuo, R. B.; Agorku, E. S. Carbon-Based Electrode Materials for Sensor Application: A Review. *Sensing Technology* **2024**, *2* (1), 2350174.

(23) Khan, A.; DeVoe, E.; Andreescu, S. Carbon-Based Electrochemical Biosensors as Diagnostic Platforms for Connected Decentralized Healthcare. *Sensors & Diagnostics* **2023**, *2* (3), 529–558.

(24) Arya, S. Carbon Based Electrodes for Electrochemical Sensing and Energy Storage Applications. In *Proceedings of the Indian conference on carbon materials: book of abstracts*; 2023; pp 59–59.

(25) Uslu, B.; Ozkan, S. A. Electroanalytical Application of Carbon Based Electrodes to the Pharmaceuticals. *Analytical Letters* **2007**, *40* (5), 817–853.

(26) Švancara, I.; Vytřas, K.; Kalcher, K.; Walcarius, A.; Wang, J. Carbon Paste Electrodes in Facts, Numbers and Notes: A Review on the Occasion of the 50-Years Jubilee of Carbon Paste in Electrochemistry and Electroanalysis. *Electroanalysis* **2009**, *21* (1), 7–28.
(27) Jaiswal, N.; Khan, H.; John, S.; Singh, S.; Tricoli, A.; Liu, B.; Ramanujam, K. Advances in Boron-Doped Diamond Electrodes: Fabrication, Electrochemical Properties and Applications. *Journal of Alloys and Compounds* **2025**, *1036*, 181723.
(28) Dekanski, A.; Stevanović, J.; Stevanović, R.; Nikolić, B. Ž.; Jovanović, V. M. Glassy Carbon Electrodes: I. Characterization and Electrochemical Activation. *Carbon* **2001**, *39* (8), 1195–1205.
(29) Van der Linden, W. E.; Dieker, J. W. Glassy Carbon as Electrode Material in Electro- Analytical Chemistry. *Analytica Chimica Acta* **1980**, *119* (1), 1–24.
(30) Švancara, I.; Walcarius, A.; Kalcher, K.; Vytřas, K. Carbon Paste Electrodes in the New Millennium. *cent.eur.j.chem.* **2009**, *7* (4), 598–656.
(31) Kalcher, K. Chemically Modified Carbon Paste Electrodes in Voltammetric Analysis. *Electroanalysis* **1990**, *2* (6), 419–433.
(32) Paimard, G.; Ghasali, E.; Baeza, M. Screen-Printed Electrodes: Fabrication, Modification and Biosensing Applications. *Chemosensors* **2023**, *11* (2), 113.
(33) Bogdanowicz, R.; Ryl, J. Structural and Electrochemical Heterogeneities of Boron-Doped Diamond Surfaces. *Current Opinion in Electrochemistry* **2022**, *31*, 100876.
(34) Ryl, J.; Burczyk, L.; Zielinski, A.; Ficek, M.; Franczak, A.; Bogdanowicz, R.; Darowicki, K. Heterogeneous Oxidation of Highly Boron-Doped Diamond Electrodes and Its Influence on the Surface Distribution of Electrochemical Activity. *Electrochimica Acta* **2019**, *297*, 1018–1027.
(35) Ryl, J.; Cieslik, M.; Zielinski, A.; Ficek, M.; Dec, B.; Darowicki, K.; Bogdanowicz, R. High-Temperature Oxidation of Heavy Boron-Doped Diamond Electrodes: Microstructural and Electrochemical Performance Modification. *Materials* **2020**, *13* (4), 964.
(36) Ryl, J.; Zielinski, A.; Burczyk, L.; Bogdanowicz, R.; Ossowski, T.; Darowicki, K. Chemical-Assisted Mechanical Lapping of Thin Boron-Doped Diamond Films: A Fast Route Toward High Electrochemical Performance for Sensing Devices. *Electrochimica Acta* **2017**, *242*, 268–279.
(37) Ryl, J.; Burczyk, L.; Bogdanowicz, R.; Sobaszek, M.; Darowicki, K. Study on Surface Termination of Boron-Doped Diamond Electrodes under Anodic Polarization in H2SO4 by Means of Dynamic Impedance Technique. *Carbon* **2016**, *96*, 1093–1105.
(38) Joshi, P.; Riley, P.; Goud, K. Y.; Mishra, R. K.; Narayan, R. Recent Advances of Boron-Doped Diamond Electrochemical Sensors toward Environmental Applications. *Current Opinion in Electrochemistry* **2022**, *32*, 100920.
(39) Yang, W.; Ratinac, K. R.; Ringer, S. P.; Thordarson, P.; Gooding, J. J.; Braet, F. Carbon Nanomaterials in Biosensors: Should You Use Nanotubes or Graphene?
(40) Adhikari, B.-R.; Govindhan, M.; Chen, A. Carbon Nanomaterials Based Electrochemical Sensors/Biosensors for the Sensitive Detection of Pharmaceutical and Biological Compounds. *Sensors* **2015**, *15* (9), 22490–22508.
(41) Kalimuthu, P.; Ramachandran, R.; Anushya, G. Metal-Organic Framework for Electrochemical Biosensing Applications. In *Handbook of Nanobioelectrochemistry*; Springer, Singapore, 2023; pp 661–686.
(42) Wang, J. Carbon-Nanotube Based Electrochemical Biosensors: A Review. *Electroanalysis* **2005**, *17* (1), 7–14.
(43) Pumera, M.; Ambrosi, A.; Bonanni, A.; Chng, E. L. K.; Poh, H. L. Graphene for Electrochemical Sensing and Biosensing. *TrAC Trends in Analytical Chemistry* **2010**, *29* (9), 954–965.
(44) Li, S.; Xia, S.; Ma, X.; Du, L.; Li, Y.; Tang, Z.; Wu, Z.; Zhang, W. Graphene–Based Two-Dimensional Nanomaterials: From Scalable Synthesis, Interfacial Mechanism to Emerging Biomedical Applications. *Carbon Neutralization* **2026**, *5* (1), e70121.
(45) Ali A. Ensafi. *Electrochemical Biosensors Ali A. Ensafi Newest Ebook Edition 2025 | PDF | Biosensor | Detection Limit*. Scribd. https://www.scribd.com/document/963572928/Electrochemical-Biosensors-Ali-A-Ensafi-newest-ebook-edition-2025 (accessed 2026-02-01).
(46) Pumera, M. Graphene-Based Nanomaterials and Their Electrochemistry. *Chem. Soc. Rev.* **2010**, *39* (11), 4146–4157.
(47) Baughman, R. H.; Zakhidov, A. A.; de Heer, W. A. Carbon Nanotubes--the Route Toward Applications. *Science* **2002**, *297* (5582), 787–792.
(48) Reina, A.; Jia, X.; Ho, J.; Nezich, D.; Son, H.; Bulovic, V.; Dresselhaus, M. S.; Kong*, J. Layer Area, Few-Layer Graphene Films on Arbitrary Substrates by Chemical Vapor Deposition. *Nano Lett.* **2009**, *9* (8), 3087–3087.
(49) Chen, D.; Feng, H.; Li, J. Graphene Oxide: Preparation, Functionalization and Electrochemical Applications. *Chem. Rev.* **2012**, *112* (11), 6027–6053.

(50) Dreyer, D. R.; Park, S.; Bielawski, C. W.; Ruoff, R. S. The Chemistry of Graphene Oxide. *Chem. Soc. Rev.* **2009**, *39* (1), 228–240.
(51) Eigler, S.; Hirsch, A. Chemistry with Graphene and Graphene Oxide—Challenges for Synthetic Chemists. *Angewandte Chemie International Edition* **2014**, *53* (30), 7720–7738.
(52) Singh, R.; Gupta, R.; Bansal, D.; Bhateria, R.; Sharma, M. A Review on Recent Trends and Future Developments in Electrochemical Sensing. *ACS Omega* **2024**, *9* (7), 7336–7356.
(53) Ambrosi, A.; Chua, C. K.; Bonanni, A.; Pumera, M. Electrochemistry of Graphene and Related Materials. *Chem. Rev.* **2014**, *114* (14), 7150–7188.
(54) Ye, R.; James, D. K.; Tour, J. M. Laser-Induced Graphene. *Acc. Chem. Res.* **2018**, *51* (7), 1609–1620.
(55) Wang, H.; Zhao, Z.; Liu, P.; Guo, X. Laser-Induced Graphene Based Flexible Electronic Devices. *Biosensors* **2022**, *12* (2), 55.
(56) Li, G. Direct Laser Writing of Graphene Electrodes. *J. Appl. Phys.* **2020**, *127* (1), 010901.
(57) Pinheiro, T.; Morais, M.; Silvestre, S.; Carlos, E.; Coelho, J.; Almeida, H. V.; Barquinha, P.; Fortunato, E.; Martins, R. Direct Laser Writing: From Materials Synthesis and Conversion to Electronic Device Processing. *Advanced Materials* **2024**, *36* (26), 2402014.
(58) Gong, R.; Chen, Y.; Kim, M.; Li, M. G. Direct Laser Writing of Functional Materials for Wearable Human-Machine Interaction: Mechanisms, Materials and Applications. *Advanced Materials Technologies* **2026**, *11* (7), e01560.
(59) Zhou, Y. S.; Xiong, W.; Park, J.; Qian, M.; Mahjouri-Samani, M.; Gao, Y.; Jiang, L.; Lu, Y. Laser-Assisted Nanofabrication of Carbon Nanostructures. *J. Laser Appl.* **2012**, *24* (4), 042007.
(60) Gao, J.; He, S.; Nag, A. Electrochemical Detection of Glucose Molecules Using Laser-Induced Graphene Sensors: A Review. *Sensors* **2021**, *21* (8), 2818.
(61) Yang, D.; Kim, Y.-J. Laser-Induced Graphene Direct Writing on Textile for Smart Textile. *Journal of the Korean Society for Precision Engineering* **2025**, *42*, 543–554.
(62) Wang, F.; Wang, K.; Zheng, B.; Dong, X.; Mei, X.; Lv, J.; Duan, W. Laser-Induced Graphene: Preparation, Functionalization and Applications. *Materials Technology* **2018**, *33*, 1–17.
(63) Ameku, W. A.; Negahdary, M.; Lima, I. S.; Santos, B. G.; Oliveira, T. G.; Paixão, T. R. L. C.; Angnes, L. Laser-Scribed Graphene-Based Electrochemical Sensors: A Review. *Chemosensors* **2022**, *10* (12), 505.
(64) Wang, C.; Madou, M. From MEMS to NEMS with Carbon. *Biosensors and Bioelectronics* **2005**, *20* (10), 2181–2187.
(65) Mohammad Al Mamun; Abu Hashem; Yasmin Abdul Wahab; Ab Rahman Marlinda; M.A. Motalib Hossain; Mohd Rafie Johan. Graphene from Lab to Fab: Challenges and Opportunities. In *Graphene: Synthesis, Properties, Technology and Applications*; Woodhead Publishing, 2026; pp 343–369.
(66) Movaghgharnezhad, S.; Kang, P. Laser-Induced Graphene: Synthesis Advances, Structural Tailoring, Enhanced Properties and Sensing Applications. *J. Mater. Chem. C* **2024**, *12* (19), 6718–6742.
(67) Nghia, N. N.; Minh, D. T. C.; Hieu, N. H. Advances in Laser-Induced Graphene for Environmental and Biochemical Analysis: Synthesis, Functionalization and Applications. *Microchemical Journal* **2025**, *213*, 113713.
(68) Docherty, N.; Macdonald, D.; Gordon, A.; Dobrea, A.; Mani, V.; Fu, Y.; Pang, S.; Jimenez, M.; Corrigan, D. K. Maximising the Translation Potential of Electrochemical Biosensors. *Chem. Commun.* **2025**, *61* (71), 13359–13377.
(69) Zhou, G.; Liu, H. Commercial Translation of Electrochemical Biosensors: Supply Chain Strategy, Scale-Up Manufacturing and Regulatory–Quality Considerations. *Biosensors* **2026**, *16* (2), 112.
(70) Lin, T.; Xu, Y.; Zhao, A.; He, W.; Xiao, F. Flexible Electrochemical Sensors Integrated with Nanomaterials for *in Situ* Determination of Small Molecules in Biological Samples: A Review. *Analytica Chimica Acta* **2022**, *1207*, 339461.
(71) Xu, M.; Obodo, D.; Yadavalli, V. K. The Design, Fabrication and Applications of Flexible Biosensing Devices. *Biosensors and Bioelectronics* **2019**, *124–125*, 96–114.
(72) Theyagarajan, K.; Kim, Y.-J. Recent Developments in the Design and Fabrication of Electrochemical Biosensors Using Functional Materials and Molecules. *Biosensors* **2023**, *13* (4), 424.
(73) Renedo, O. D.; Alonso-Lomillo, M. A.; Martínez, M. J. A. Recent Developments in the Field of Screen-Printed Electrodes and Their Related Applications. *Talanta* **2007**, *73* (2), 202–219.
(74) Panáček, D.; Urban, M.; Silvestri, A.; Dědek, I.; Nalepa, M.-A.; Merkoçi, A.; Prato, M.; Otyepka, M. Nanomaterial-Based Inkjet Printing for Electrochemical Sensing. *Small* **2026**, *22* (10), e13028.
(75) Sui, Y.; Zorman, C. A. Review-Inkjet Printing of Metal Structures for Electrochemical Sensor Applications. *J. Electrochem. Soc.* **2020**, *167* (3), 037571.
(76) Mir, M.; Dondapati, S. K.; Duarte, M. V.; Chatzichristidi, M.; Misiakos, K.; Petrou, P.; Kakabakos, S. E.; Argitis, P.; Katakis, I. Electrochemical Biosensor Microarray Functionalized by Means of Biomolecule Friendly Photolithography. *Biosensors and Bioelectronics* **2010**, *25* (9), 2115–2121.

(77) Burke, M.; Larrigy, C.; Vaughan, E.; Paterakis, G.; Sygellou, L.; Quinn, A. J.; Herzog, G.; Galiotis, C.; Iacopino, D. Fabrication and Electrochemical Properties of Three-Dimensional (3D) Porous Graphitic and Graphenelike Electrodes Obtained by Low-Cost Direct Laser Writing Methods. *ACS Omega* **2020**, *5* (3), 1540–1548.
(78) Torati, S. R.; Slaughter, G. Laser-Induced Graphene for Early Disease Detection: A Review.
(79) Ye, R.; James, D. K.; Tour, J. M. Laser-Induced Graphene: From Discovery to Translation. *Advanced Materials* **2019**, *31* (1), 1803621.
(80) Ye, R.; Chyan, Y.; Zhang, J.; Li, Y.; Han, X.; Kittrell, C.; Tour, J. M. Laser-Induced Graphene Formation on Wood. *Advanced Materials* **2017**, *29* (37), 1702211.
(81) Daniels, J. S.; Pourmand, N. Label-Free Impedance Biosensors: Opportunities and Challenges. *Electroanalysis* **2007**, *19* (12), 1239–1257.
(82) Nam, V. B.; Le, P. G.; Lee, J. Laser-Induced Graphene-Based Flexible Electrodes for Advanced Electrochemical Performance. *ACS Appl. Nano Mater.* **2025**, *8* (30), 15278–15287.
(83) Nasraoui, S.; Al-Hamry, A.; Madeira, T. I.; Ameur, S.; Zahn, D. R. T.; Ben Ali, M.; Kanoun, O. Structural Characterization and Electrochemical Performance of Laser-Induced Graphene: Insights into Electron Transfer Kinetics and 4-Aminophenol Sensing. *Diamond and Related Materials* **2023**, *138*, 110207.
(84) Settu, K.; Tsai, J.-Z.; Cheng, Y.-C.; Du, Y.-M. UV Laser-Induced Graphene Electrode for Supercapacitor and Electrochemical Sensing Applications. In *Sensing Technology*; Springer, Cham, 2022; pp 327–338.
(85) Soleimani Dinani, H.; Reinbolt, T.; Zhang, B.; Zhao, G.; Gerald, R. E. I.; Yan, Z.; Huang, J. Miniaturized Wearable Biosensors for Continuous Health Monitoring Fabricated Using the Femtosecond Laser-Induced Graphene Surface and Encapsulated Traces and Electrodes. *ACS Sens.* **2025**, *10* (2), 761–772.
(86) Le, T.-S. D.; Tran, Y.-V.; Gao, Y.; Valerio, V. L.; Ge, Z.; Lim, C. T. Laser-Induced Graphene for Biomedical Applications: Innovations in Health Monitoring and Diagnostics. *Nanoscale Horiz.* **2025**, *10* (11), 2688–2721.
(87) Stanford, M. G.; Zhang, C.; Fowlkes, J. D.; Hoffman, A.; Ivanov, I. N.; Rack, P. D.; Tour, J. M. High-Resolution Laser-Induced Graphene. Flexible Electronics beyond the Visible Limit. *ACS Appl. Mater. Interfaces* **2020**, *12* (9), 10902–10907.
(88) Chyan, Y.; Ye, R.; Li, Y.; Singh, S. P.; Arnusch, C. J.; Tour, J. M. Laser-Induced Graphene by Multiple Lasing: Toward Electronics on Cloth, Paper and Food. *ACS Nano* **2018**, *12* (3), 2176–2183.
(89) Kim, H.; Kim, Y.-J. Wearable Healthcare Using Laser-Induced Graphene. *JMST Adv.* **2025**, *7* (3), 177–185.
(90) Stanford, M. G.; Yang, K.; Chyan, Y.; Kittrell, C.; Tour, J. M. Laser-Induced Graphene for Flexible and Embeddable Gas Sensors. *ACS Nano* **2019**, *13* (3), 3474–3482.
(91) Kothuru, A.; Patolsky, F. Laser-Induced Graphene as a "Materials Toolbox" for Energy Storage, Conversion and Harvesting Applications. *Journal of Energy Chemistry* **2026**, *113*, 408–443.
(92) Vorobyev, A. Y.; Guo, C. Direct Femtosecond Laser Surface Nano/Microstructuring and Its Applications. *Laser & Photonics Reviews* **2013**, *7* (3), 385–407.
(93) Choi, G.; Ko, S. H. Laser-Induced Graphene for Micro- and Nano-Manufacturing: Fundamentals, Processing Approaches and Emerging Applications. *Micro Nano Manuf.* **2026**, *2* (1), 12.
(94) Scardaci, V. Laser Synthesized Graphene and Its Applications. *Applied Sciences* **2021**, *11* (14), 6304.
(95) Lee, S. P.; Chee, P. S.; Tan, C. H.; Chong, K. F.; Lim, E. H.; Guan, C. A Review on Laser-Induced Graphene in Flexible Energy Storage: From Materials Selection to Biomedical Applications. *Chemical Engineering Journal* **2024**, *499*, 156110.
(96) Fantinelli Franco, F.; Malik, M. H.; Manjakkal, L.; Roshanghias, A.; Smith, C. J.; Gauchotte-Lindsay, C. Optimizing Carbon Structures in Laser-Induced Graphene Electrodes Using Design of Experiments for Enhanced Electrochemical Sensing Characteristics. *ACS Appl. Mater. Interfaces* **2024**, *16* (47), 65489–65502.
(97) Wang, Y.; Guo, H.; Yuan, M.; Yu, J.; Wang, Z.; Chen, X. One-Step Laser Synthesis Platinum Nanostructured 3D Porous Graphene: A Flexible Dual-Functional Electrochemical Biosensor for Glucose and pH Detection in Human Perspiration. *Talanta* **2023**, *257*, 124362.
(98) Zhang, Q.; Zhang, F.; Liu, X.; Yue, Z.; Chen, X.; Wan, Z. Doping of Laser-Induced Graphene and Its Applications. *Advanced Materials Technologies* **2023**, *8* (16), 2300244.
(99) Duy, L. X.; Peng, Z.; Li, Y.; Zhang, J.; Ji, Y.; Tour, J. M. Laser-Induced Graphene Fibers. *Carbon* **2018**, *126*, 472–479.
(100) Dallinger, A.; Steinwender, F.; Gritzner, M.; Greco, F. Different Roles of Surface Chemistry and Roughness of Laser-Induced Graphene: Implications for Tunable Wettability. *ACS Appl. Nano Mater.* **2023**, *6* (18), 16201–16211.

(101) Wan, Z.; Nguyen, N.-T.; Gao, Y.; Li, Q. Laser Induced Graphene for Biosensors. *Sustainable Materials and Technologies* **2020**, *25*, e00205.
(102) Li, Y.; Luong, D. X.; Zhang, J.; Tarkunde, Y. R.; Kittrell, C.; Sargunaraj, F.; Ji, Y.; Arnusch, C. J.; Tour, J. M. Laser-Induced Graphene in Controlled Atmospheres: From Superhydrophilic to Superhydrophobic Surfaces. *Advanced Materials* **2017**, *29* (27), 1700496.
(103) Peng, Z.; Lin, J.; Ye, R.; Samuel, E. L. G.; Tour, J. M. Flexible and Stackable Laser-Induced Graphene Supercapacitors. *ACS Appl. Mater. Interfaces* **2015**, *7* (5), 3414–3419.
(104) Zhang, Z.; Zhu, H.; Zhang, W.; Zhang, Z.; Lu, J.; Xu, K.; Liu, Y.; Saetang, V. A Review of Laser-Induced Graphene: From Experimental and Theoretical Fabrication Processes to Emerging Applications. *Carbon* **2023**, *214*, 118356.
(105) de la Roche, J.; López-Cifuentes, I.; Jaramillo-Botero, A. Influence of Lasing Parameters on the Morphology and Electrical Resistance of Polyimide-Based Laser-Induced Graphene (LIG). *Carbon Lett.* **2023**, *33* (2), 587–595.
(106) Chen, Y.; Xie, B.; Long, J.; Kuang, Y.; Chen, X.; Hou, M.; Gao, J.; Zhou, S.; Fan, B.; He, Y.; Zhang, Y.-T.; Wong, C.-P.; Wang, Z.; Zhao, N. Interfacial Laser-Induced Graphene Enabling High-Performance Liquid−Solid Triboelectric Nanogenerator. *Advanced Materials* **2021**, *33* (44), 2104290.
(107) Richard G Compton; Craig E Banks. *UNDERSTANDING VOLTAMMETRY (THIRD EDITION)*; World Scientific, 2018.
(108) Jauregui, L. A.; Cao, H.; Wu, W.; Yu, Q.; Chen, Y. P. Electronic Properties of Grains and Grain Boundaries in Graphene Grown by Chemical Vapor Deposition. *Solid State Communications* **2011**, *151* (16), 1100–1104.
(109) Pavlov, S. V. Defect Engineering in Laser-Induced Graphene (LIG) Through Temperature Control: A Reactive Molecular Dynamics Study. *Molecules* **2025**, *30* (22), 4344.
(110) Carvalho, A. F.; Fernandes, A. J. S.; Leitão, C.; Deuermeier, J.; Marques, A. C.; Martins, R.; Fortunato, E.; Costa, F. M. Laser-Induced Graphene Strain Sensors Produced by Ultraviolet Irradiation of Polyimide. *Advanced Functional Materials* **2018**, *28* (52), 1805271.
(111) Beigh, F. T.; Mallick, D. Ambient Process Controlled Laser-Induced Graphene with Tunable Wettability and Electrical Performances for Multifunctional Surfaces. *ACS Appl. Eng. Mater.* **2026**, *4* (2), 729–742.
(112) Nam, K.-H.; Abdulhafez, M.; Castagnola, E.; Tomaraei, G. N.; Cui, X. T.; Bedewy, M. Laser Direct Write of Heteroatom-Doped Graphene on Molecularly Controlled Polyimides for Electrochemical Biosensors with Nanomolar Sensitivity. *Carbon* **2022**, *188*, 209–219.
(113) Soleh, A.; Saisahas, K.; Samoson, K.; Phetrat, D.; Promsuwan, K.; Saichanapan, J.; Wangchuk, S.; Limbut, W. N-Doped Porous Laser-Induced Graphene Applied for Forensic Electrochemical Sensing of Xylazine. *Microchemical Journal* **2025**, *217*, 114935.
(114) Liu, H.; Chen, K.; Wu, R.; Pan, S.; Zhang, C. Laser-Induced Graphene-Based Flexible Substrate with Photothermal Conversion and Photoresponse Performance on Polyimide Film. *ACS Appl. Mater. Interfaces* **2023**, *15* (39), 46550–46558.
(115) Liu, M.; Wu, J.; Cheng, H. Effects of Laser Processing Parameters on Properties of Laser-Induced Graphene by Irradiating CO2 Laser on Polyimide. *Sci. China Technol. Sci.* **2022**, *65* (1), 41–52.
(116) Oh, I. J.; Kim, D.; Kim, S.-Y.; Choi, S.; Yeo, W.-H.; Lim, H.-R. Advances in Laser-Induced Graphene: Materials, Fabrication and Emerging Applications in Flexible Electronics. *Front. Nanotechnol.* **2026**, *7*.
(117) Sharma, C. P.; Zhang, K.; Sadhujan, S.; Harilal, S.; Abu Madegam, L.; Igbaria, A.; Bashouti, M. Y.; Arnusch, C. J. Defocused Laser-Induced Anisotropic Freestanding Graphene Architectures. *ACS Appl. Eng. Mater.* **2026**, *4* (3), 1269–1275.
(118) Yu, W.; Zhao, W.; Wang, S.; Chen, Q.; Liu, X. Direct Conversion of Liquid Organic Precursor into 3D Laser-Induced Graphene Materials. *Advanced Materials* **2023**, *35* (9), 2209545.
(119) Mikheev, K. G.; Zonov, R. G.; Mogileva, T. N.; Fateev, A. E.; Mikheev, G. M. Optical Anisotropy of Laser-Induced Graphene Films. *Optics & Laser Technology* **2021**, *141*, 107143.
(120) Abdou, A. M.; Mahmoud, H. A.; Alrefae, M. A.; Zhang, Y.; Rekik, H. E.; Seno, A. H.; Lubineau, G. Leveraging Processing-Induced Electromechanical Anisotropy of Laser-Induced Graphene for One-Shot Engraving of Highly Sensitive Strain Sensors. *ACS Appl. Nano Mater.* **2026**, *9* (9), 4109–4121.
(121) Murray, R.; Burke, M.; Iacopino, D.; Quinn, A. J. Design of Experiments and Optimization of Laser-Induced Graphene. *ACS Omega* **2021**, *6* (26), 16736–16743.
(122) Adiraju, A.; Al-Hamry, A.; Wang, J.; Lu, T.; Pasti, I.; Kanoun, O. Design of Experiments Based Study to Optimize Laser Induced Graphene Surfaces for Electrochemical Sensor Applications. In *2023 International Workshop on Impedance Spectroscopy (IWIS)*; 2023; pp 158–162.

(123) Yu, H.; Bian, J.; Gai, M.; Huang, X.; Liu, L.; Huang, Y. Comparative Study of Laser-Induced Graphene Fabricated in Atmospheric and Interface-Confined Environments. *Applied Surface Science* **2024**, *673*, 160889.
(124) Wu, Z.; Sahaluddin, M.; Mustafa, D. B.; Ghosh, S.; Bedewy, M. Laser-Induced Graphene: From Precursor Chemistry to Process Control and Throughput–Resolution–Performance Trade-Offs. *Nanoscale* **2026**, *18* (13), 6647–6686.
(125) Khazaee Nejad, S.; Ma, H.; Al-Shami, A.; Soleimani, A.; Mohamed, M.; Dankwah, P.; Lee, H.; Mousavi, M. Sustainable Agriculture with LEAFS: A Low-Cost Electrochemical Analyzer of Foliage Stress. *Sensors & Diagnostics* **2024**, *3*.
(126) Hoekstra, J.; Beale, A. M.; Soulimani, F.; Versluijs-Helder, M.; Geus, J. W.; Jenneskens, L. W. Base Metal Catalyzed Graphitization of Cellulose: A Combined Raman Spectroscopy, Temperature-Dependent X-Ray Diffraction and High-Resolution Transmission Electron Microscopy Study. *J. Phys. Chem. C* **2015**, *119* (19), 10653–10661.
(127) Walcarius, A. Mesoporous Materials and Electrochemistry. *Chem. Soc. Rev.* **2013**, *42* (9), 4098–4140.
(128) Wu, Z.; Sahaluddin, M.; Bani Mustafa, D.; Ghosh, S.; Bedewy, M. Laser-Induced Graphene: From Precursor Chemistry to Process Control and Throughput–Resolution–Performance Trade-Offs. *Nanoscale* **2026**, *18* (13), 6647–6686.
(129) Behrent, A.; Borggraefe, V.; Baeumner, A. J. Laser-Induced Graphene Trending in Biosensors: Understanding Electrode Shelf-Life of This Highly Porous Material. *Anal Bioanal Chem* **2024**, *416* (9), 2097–2106.
(130) Behrent, A.; Griesche, C.; Sippel, P.; Baeumner, A. J. Process-Property Correlations in Laser-Induced Graphene Electrodes for Electrochemical Sensing. *Microchim Acta* **2021**, *188* (5), 159.
(131) Ferrari, A. C.; Basko, D. M. Raman Spectroscopy as a Versatile Tool for Studying the Properties of Graphene. *Nature Nanotech* **2013**, *8* (4), 235–246.
(132) Gooding, J. J. Nanostructuring Electrodes with Carbon Nanotubes: A Review on Electrochemistry and Applications for Sensing. *Electrochimica Acta* **2005**, *50* (15), 3049–3060.
(133) Banks, C. E.; Compton, R. G. New Electrodes for Old: From Carbon Nanotubes to Edge Plane Pyrolytic Graphite. *Analyst* **2006**, *131* (1), 15–21.
(134) Cheng, L.; Yeung, C. S.; Huang, L.; Ye, G.; Yan, J.; Li, W.; Yiu, C.; Chen, F.-R.; Shen, H.; Tang, B. Z.; Ren, Y.; Yu, X.; Ye, R. Flash Healing of Laser-Induced Graphene. *Nat Commun* **2024**, *15* (1), 2925.
(135) Lin, J.; Peng, Z.; Liu, Y.; Ruiz-Zepeda, F.; Ye, R.; Samuel, E. L. G.; Yacaman, M. J.; Yakobson, B. I.; Tour, J. M. Laser-Induced Porous Graphene Films from Commercial Polymers. Nat. Commun. 2014, 5 (1), 5714.
(136) Sitsanidis, E. D.; Schirmer, J.; Lampinen, A.; Mentel, K. K.; Hiltunen, V.-M.; Ruokolainen, V.; Johansson, A.; Myllyperkiö, P.; Nissinen, M.; Pettersson, M. Tuning Protein Adsorption on Graphene Surfaces via Laser-Induced Oxidation. *Nanoscale Adv.* **2021**, *3* (7), 2065–2074.
(137) Kumar, R.; Pandey, R.; Joanni, E.; Savu, R. Laser-Induced and Catalyst-Free Formation of Graphene Materials for Energy Storage and Sensing Applications. *Chemical Engineering Journal* **2024**, *497*, 154968.
(138) Aso Navaee; Abdollah Salimi. Enzyme-Based Electrochemical Biosensors. In *Electrochemical Biosensors*; Elsevier, 2019; pp 167–211.
(139) Cui, X.; Gu, T.; Ma, K.; Zeng, J.; Xia, H. Laser-Induced Graphene Electrochemical Sensors: An Emerging Platform for Agri-Food and Environmental Detection. *Chemosensors* **2025**, *13* (12), 432.
(140) Scheidt, D. T.; Silva, L. R. G.; Rocha, D. P.; Janegitz, B. C.; Brazaca, L. C. New and Improved Strategies for Fabricating Carbon-Based Electrodes: A Critical Perspective on Additive Manufacturing, Laser-Induced Graphene and Their Combination. *MRS Commun.* **2026**.
(141) Junior, D. W.; Deroco, P. B.; Hryniewicz, B. M.; Kubota, L. T. Strategies for Electrochemical Point-of-Care Biosensors. *Annual Review of Analytical Chemistry* **2025**, *18* (Volume 18, 2025), 307–333.
(142) Pavlova, N. V.; В, П. Н.; Mardanov, R. G.; Г, М. Р.; Bubelo, O. N.; Н, Б. О. Antifouling coatings for electrochemical sensors. *Doklady Chemistry* **2024**, *515* (1), 3–17.
(143) Latour, R. A. Fundamental Principles of the Thermodynamics and Kinetics of Protein Adsorption to Material Surfaces. *Colloids and Surfaces B: Biointerfaces* **2020**, *191*, 110992.
(144) Marin, E.; Bridges, M.; Villarini, N.; Scangarello, G. J.; Henry, C. S. Laser-Induced Graphene for Electrochemical Biosensing: Advances in Functionalization and Integration into Point-of-Care Devices. *TrAC Trends in Analytical Chemistry* **2026**, *199*, 118809.
(145) Hernández-Cubas, L. L.; Sánchez-Moreno, P.; Capasso, A.; Lopez-Lopez, M. T.; Moltó-Ramírez, A.; Rodríguez, N.; Bramini, M.; Moraila-Martínez, C. L. Laser-Induced Graphene Interfaces with

Controlled Electrical Conductivity, Topography and Wettability for Biomedical Applications. *ACS Appl. Nano Mater.* **2025**, *8* (51), 24610–24622.
(146) Radha Shanmugam, N.; Rainbow, J.; Lee, J.-C.; Jolly, P.; E. Ingber, D. Label-Free Electrochemical Impedance Spectroscopy for Biosensing: Evolving Interfaces and Mechanistic Insights. *Small Science* **2025**, *5* (12), e202500380.
(147) Hu, X.; Wang, J.; Feng, C.; Yuan, J.; Wei, Q.; Wang, H. A Comprehensive Review of Laser-Induced-Graphene for Sensor Applications: Fabrication, Properties and Performance Evaluation. *J. Mater. Chem. C* **2025**, *13* (4), 1573–1591.
(148) An, J. W.; Kim, H. J.; Lee, S.-K. Review on Functionalization of Laser-Induced Graphene. *Journal of the Korean Institute of Electrical and Electronic Material Engineers* **2023**, *36* (3), 203–213.
(149) Vaddiraju, S.; Tomazos, I.; Burgess, D. J.; Jain, F. C.; Papadimitrakopoulos, F. Emerging Synergy between Nanotechnology and Implantable Biosensors: A Review. *Biosensors and Bioelectronics* **2010**, *25* (7), 1553–1565.
(150) Wisniewski, N.; Reichert, M. Methods for Reducing Biosensor Membrane Biofouling. *Colloids and Surfaces B: Biointerfaces* **2000**, *18* (3), 197–219.
(151) Peppas, N. A.; Hilt, J. Z.; Khademhosseini, A.; Langer, R. Hydrogels in Biology and Medicine: From Molecular Principles to Bionanotechnology. *Advanced Materials* **2006**, *18* (11), 1345–1360.
(152) Ullah, F.; Othman, M. B. H.; Javed, F.; Ahmad, Z.; Akil, H. Md. Classification, Processing and Application of Hydrogels: A Review. *Materials Science and Engineering: C* **2015**, *57*, 414–433.
(153) Hoffman, A. S. Hydrogels for Biomedical Applications. *Advanced Drug Delivery Reviews* **2012**, *64*, 18–23.
(154) Lee, K. Y.; Mooney, D. J. Hydrogels for Tissue Engineering. *Chem. Rev.* **2001**, *101* (7), 1869–1880.
(155) Tibbitt, M. W.; Anseth, K. S. Hydrogels as Extracellular Matrix Mimics for 3D Cell Culture. *Biotechnology and Bioengineering* **2009**, *103* (4), 655–663.
(156) Lutolf, M. P.; Hubbell, J. A. Synthetic Biomaterials as Instructive Extracellular Microenvironments for Morphogenesis in Tissue Engineering. *Nat Biotechnol* **2005**, *23* (1), 47–55.
(157) Kopeček, J. Hydrogel Biomaterials: A Smart Future? *Biomaterials* **2007**, *28* (34), 5185–5192.
(158) Castner, D. G.; Ratner, B. D. Biomedical Surface Science: Foundations to Frontiers. *Surface Science* **2002**, *500* (1), 28–60.
(159) Buddy D. Ratner. A History of Biomaterials. In *Biomaterials Science*; Academic Press, 2013; pp xli–liii.
(160) Van Vlierberghe, S.; Dubruel, P.; Schacht, E. Biopolymer-Based Hydrogels As Scaffolds for Tissue Engineering Applications: A Review. *Biomacromolecules* **2011**, *12* (5), 1387–1408.
(161) Segneanu, A.-E.; Bejenaru, L. E.; Bejenaru, C.; Blendea, A.; Mogoşanu, G. D.; Biţă, A.; Boia, E. R. Advancements in Hydrogels: A Comprehensive Review of Natural and Synthetic Innovations for Biomedical Applications. *Polymers* **2025**, *17* (15), 2026.
(162) Ullah, A.; Kim, D. Y.; Lim, S. I.; Lim, H.-R. Hydrogel-Based Biointerfaces: Recent Advances, Challenges and Future Directions in Human–Machine Integration. *Gels* **2025**, *11* (4), 232.
(163) Sun, J.; Tran, Y.; Griveau, S.; Slim, C. An Overview of Hydrogel-Modified Electrodes for Electrochemical Biosensing. *Bioelectrochemistry* **2026**, *171*, 109290.
(164) Guiseppi-Elie, A. Electroconductive Hydrogels: Synthesis, Characterization and Biomedical Applications. *Biomaterials* **2010**, *31* (10), 2701–2716.
(165) Krajewska, B. Application of Chitin- and Chitosan-Based Materials for Enzyme Immobilizations: A Review. *Enzyme and Microbial Technology* **2004**, *35* (2), 126–139.
(166) Rinaudo, M. Chitin and Chitosan: Properties and Applications. *Progress in Polymer Science* **2006**, *31* (7), 603–632.
(167) Kim, S.-K.; Rajapakse, N. Enzymatic Production and Biological Activities of Chitosan Oligosaccharides (COS): A Review. *Carbohydrate Polymers* **2005**, *62* (4), 357–368.
(168) Jayakumar, R.; Menon, D.; Manzoor, K.; Nair, S. V.; Tamura, H. Biomedical Applications of Chitin and Chitosan Based Nanomaterials-A Short Review. *Carbohydrate Polymers* **2010**, *82* (2), 227–232.
(169) Prabhakar, T.; Giaretta, J.; Zulli, R.; Rath, R. J.; Farajikhah, S.; Talebian, S.; Dehghani, F. Covalent Immobilization: A Review from an Enzyme Perspective. *Chemical Engineering Journal* **2025**, *503*, 158054.
(170) Dash, M.; Chiellini, F.; Ottenbrite, R. M.; Chiellini, E. Chitosan—A Versatile Semi-Synthetic Polymer in Biomedical Applications. *Progress in Polymer Science* **2011**, *36* (8), 981–1014.
(171) Kong, M.; Chen, X. G.; Xing, K.; Park, H. J. Antimicrobial Properties of Chitosan and Mode of Action: A State of the Art Review. *International Journal of Food Microbiology* **2010**, *144* (1), 51–63.
(172) Thévenot, D. R.; Toth, K.; Durst, R. A.; Wilson, G. S. Electrochemical Biosensors: Recommended Definitions and Classification1. *Biosensors and Bioelectronics* **2001**, *16* (1), 121–131.

(173) Sassolas, A.; Blum, L. J.; Leca-Bouvier, B. D. Immobilization Strategies to Develop Enzymatic Biosensors. *Biotechnology Advances* **2012**, *30* (3), 489–511.
(174) Alavarse, A. C.; Frachini, E. C. G.; da Silva, R. L. C. G.; Lima, V. H.; Shavandi, A.; Petri, D. F. S. Crosslinkers for Polysaccharides and Proteins: Synthesis Conditions, Mechanisms and Crosslinking Efficiency, a Review. *International Journal of Biological Macromolecules* **2022**, *202*, 558–596.
(175) Muzzarelli, R. A. A. Genipin-Crosslinked Chitosan Hydrogels as Biomedical and Pharmaceutical Aids. *Carbohydrate Polymers* **2009**, *77* (1), 1–9.
(176) Bocchetta, P.; Othman, A.; Gupta, M.; Andriani, G.; Martin, P.; Kumar, Y.; Joly, N.; Sacco, P.; Sufyan Javed, M. Chitosan in Electrochemical (Bio)Sensors: Nanostructuring and Methods of Synthesis. *European Polymer Journal* **2024**, *213*, 113092.
(177) Bai, Y.; Jing, Z.; Ma, R.; Wan, X.; Liu, J.; Huang, W. A Critical Review of Enzymes Immobilized on Chitosan Composites: Characterization and Applications. *Bioprocess Biosyst Eng* **2023**, *46* (11), 1539–1567.
(178) Kimmel, D. W.; LeBlanc, G.; Meschievitz, M. E.; Cliffel, D. E. Electrochemical Sensors and Biosensors. *Anal. Chem.* **2012**, *84* (2), 685–707.
(179) Flemming, H.-C.; Wingender, J. The Biofilm Matrix. *Nat Rev Microbiol* **2010**, *8* (9), 623–633.
(180) Lee, K. Y.; Mooney, D. J. Alginate: Properties and Biomedical Applications. *Progress in Polymer Science* **2012**, *37* (1), 106–126.
(181) Rinaudo, M. Main Properties and Current Applications of Some Polysaccharides as Biomaterials. *Polymer International* **2008**, *57* (3), 397–430.
(182) Coviello, T.; Matricardi, P.; Marianecci, C.; Alhaique, F. Polysaccharide Hydrogels for Modified Release Formulations. *Journal of Controlled Release* **2007**, *119* (1), 5–24.
(183) Zarrintaj, P.; Manouchehri, S.; Ahmadi, Z.; Saeb, M. R.; Urbanska, A. M.; Kaplan, D. L.; Mozafari, M. Agarose-Based Biomaterials for Tissue Engineering. *Carbohydrate Polymers* **2018**, *187*, 66–84.
(184) Arnott, S.; Fulmer, A.; Scott, W. E.; Dea, I. C. M.; Moorhouse, R.; Rees, D. A. The Agarose Double Helix and Its Function in Agarose Gel Structure. *Journal of Molecular Biology* **1974**, *90* (2), 269–284.
(185) Zucca, P.; Fernandez-Lafuente, R.; Sanjust, E. Agarose and Its Derivatives as Supports for Enzyme Immobilization. *Molecules* **2016**, *21* (11), 1577.
(186) Narayanan, J.; Xiong, J.-Y.; Liu, X.-Y. Determination of Agarose Gel Pore Size: Absorbance Measurements Vis a Vis Other Techniques. *J. Phys.: Conf. Ser.* **2006**, *28* (1), 83.
(187) Pernodet, N.; Maaloum, M.; Tinland, B. Pore Size of Agarose Gels by Atomic Force Microscopy. *ELECTROPHORESIS* **1997**, *18* (1), 55–58.
(188) Jiang, F.; Xu, X.-W.; Chen, F.-Q.; Weng, H.-F.; Chen, J.; Ru, Y.; Xiao, Q.; Xiao, A.-F. Extraction, Modification and Biomedical Application of Agarose Hydrogels: A Review. *Marine Drugs* **2023**, *21* (5), 299.
(189) Augst, A. D.; Kong, H. J.; Mooney, D. J. Alginate Hydrogels as Biomaterials.
(190) Grant, G. T.; Morris, E. R.; Rees, D. A.; Smith, P. J. C.; Thom, D. Biological Interactions between Polysaccharides and Divalent Cations: The Egg-Box Model. *FEBS Letters* **1973**, *32* (1), 195–198.
(191) Draget, K. I.; Skjåk-Bræk, G.; Smidsrød, O. Alginate Based New Materials. *International Journal of Biological Macromolecules* **1997**, *21* (1), 47–55.
(192) Smidsrød, O.; Skja˚k-Br̃k, G. Alginate as Immobilization Matrix for Cells. *Trends in Biotechnology* **1990**, *8*, 71–78.
(193) Roquero, D. M.; Katz, E. "Smart" Alginate Hydrogels in Biosensing, Bioactuation and Biocomputing: State-of-the-Art and Perspectives. *Sensors and Actuators Reports* **2022**, *4*, 100095.
(194) Meng, L.; Turner, A. P. F.; Mak, W. C. Conducting Polymer-Reinforced Laser-Irradiated Graphene as a Heterostructured 3D Transducer for Flexible Skin Patch Biosensors. *ACS Appl. Mater. Interfaces* **2021**, *13* (45), 54456–54465.
(195) Chen, A.; Chatterjee, S. Nanomaterials Based Electrochemical Sensors for Biomedical Applications. *Chem. Soc. Rev.* **2013**, *42* (12), 5425–5438.
(196) Maduraiveeran, G.; Sasidharan, M.; Ganesan, V. Electrochemical Sensor and Biosensor Platforms Based on Advanced Nanomaterials for Biological and Biomedical Applications. *Biosensors and Bioelectronics* **2018**, *103*, 113–129.
(197) Wang, J. Nanomaterial-Based Electrochemical Biosensors. *Analyst* **2005**, *130* (4), 421–426.
(198) Welch, C. M.; Compton, R. G. The Use of Nanoparticles in Electroanalysis: A Review. *Anal Bioanal Chem* **2006**, *384* (3), 601–619.
(199) Katz, E.; Willner, I.; Wang, J. Electroanalytical and Bioelectroanalytical Systems Based on Metal and Semiconductor Nanoparticles. *Electroanalysis* **2004**, *16* (1–2), 19–44.
(200) Pingarrón, J. M.; Yáñez-Sedeño, P.; González-Cortés, A. Gold Nanoparticle-Based Electrochemical Biosensors. *Electrochimica Acta* **2008**, *53* (19), 5848–5866.

(201) Dong, K.; Lei, Y.; Zhao, H.; Liang, J.; Ding, P.; Liu, Q.; Xu, Z.; Lu, S.; Li, Q.; Sun, X. Noble-Metal-Free Electrocatalysts toward H2O2 Production. *J. Mater. Chem. A* **2020**, *8* (44), 23123–23141.
(202) Duarte, M. M. E.; Pilla, A. S.; Sieben, J. M.; Mayer, C. E. Platinum Particles Electrodeposition on Carbon Substrates. *Electrochemistry Communications* **2006**, *8* (1), 159–164.
(203) Doria, G.; Conde, J.; Veigas, B.; Giestas, L.; Almeida, C.; Assunção, M.; Rosa, J.; Baptista, P. V. Noble Metal Nanoparticles for Biosensing Applications. *Sensors* **2012**, *12* (2), 1657–1687.
(204) Wang, J. Electrochemical Glucose Biosensors. *Chem. Rev.* **2008**, *108* (2), 814–825.
(205) Smith, B. R.; Gambhir, S. S. Nanomaterials for In Vivo Imaging. *Chem. Rev.* **2017**, *117* (3), 901–986.
(206) Daniel, M.-C.; Astruc, D. Gold Nanoparticles: Assembly, Supramolecular Chemistry, Quantum-Size-Related Properties and Applications toward Biology, Catalysis and Nanotechnology. *Chem. Rev.* **2004**, *104* (1), 293–346.
(207) Burda, C.; Chen, X.; Narayanan, R.; El-Sayed, M. A. Chemistry and Properties of Nanocrystals of Different Shapes. *Chem. Rev.* **2005**, *105* (4), 1025–1102.
(208) Guo, S.; Wang, E. Noble Metal Nanomaterials: Controllable Synthesis and Application in Fuel Cells and Analytical Sensors. *Nano Today* **2011**, *6* (3), 240–264.
(209) Quinson, J. Iridium and IrOx Nanoparticles: An Overview and Review of Syntheses and Applications. *Advances in Colloid and Interface Science* **2022**, *303*, 102643.
(210) Guo, S.; Wang, E. Synthesis and Electrochemical Applications of Gold Nanoparticles. *Analytica Chimica Acta* **2007**, *598* (2), 181–192.
(211) Rajeev, R.; Datta, R.; Varghese, A.; Sudhakar, Y. N.; George, L. Recent Advances in Bimetallic Based Nanostructures: Synthesis and Electrochemical Sensing Applications. *Microchemical Journal* **2021**, *163*, 105910.
(212) Bilge, S.; Dogan-Topal, B.; Gürbüz, M. M.; Ozkan, S. A.; Sınağ, A. Recent Trends in Core/Shell Nanoparticles: Their Enzyme-Based Electrochemical Biosensor Applications. *Microchim Acta* **2024**, *191* (5), 240.
(213) Shukla, D.; Tuteja, J. Synergistic Catalysis With Bimetallic Nanoparticles: A Pathway to Higher Efficiency Sustainability and Stability. https://doi.org/10.1002/asia.70610.
(214) Barfidokht, A.; Gooding, J. J. Approaches Toward Allowing Electroanalytical Devices to Be Used in Biological Fluids. *Electroanalysis* **2014**, *26* (6), 1182–1196. https://doi.org/10.1002/elan.201400097.
(215) Szunerits, S.; Pagneux, Q.; M'Barek, Y. B.; Vassal, S.; Boukherroub, R. Do Not Let Electrode Fouling Be the Enemy of Bioanalysis. *Bioelectrochemistry* **2023**, *153*, 108479.
(216) Dhaffouli, A. Next-Generation Antifouling Electrochemical Sensors: From Surface Design to Practical Applications. *Microchemical Journal* **2026**, *220*, 116637.
(217) Rabe, M.; Verdes, D.; Seeger, S. Understanding Protein Adsorption Phenomena at Solid Surfaces. *Advances in Colloid and Interface Science* **2011**, *162* (1), 87–106.
(218) Uzoma, P. C.; Etim, I.-I. N.; Okonkwo, B. O.; Olanrele, O. S.; Njoku, D. I.; Kolawole, S. K.; Emori, W.; Ikeuba, A. I.; Njoku, C. N.; Ekerenam, O. O.; Etim, I. P.; Daniel, E. F.; Udoh, I. I. Recent Design Approaches, Adhesion Mechanisms and Applications of Antibacterial Surfaces. *Chemical Engineering Journal Advances* **2023**, *16*, 100563.
(219) Banerjee, I.; Pangule, R. C.; Kane, R. S. Antifouling Coatings: Recent Developments in the Design of Surfaces That Prevent Fouling by Proteins, Bacteria and Marine Organisms. *Advanced Materials* **2011**, *23* (6), 690–718.
(220) Jiang, S.; Cao, Z. Ultralow-Fouling, Functionalizable and Hydrolyzable Zwitterionic Materials and Their Derivatives for Biological Applications. *Advanced Materials* **2010**, *22* (9), 920–932.
(221) Song, Z.; Han, R.; Yu, K.; Li, R.; Luo, X. Antifouling Strategies for Electrochemical Sensing in Complex Biological Media. *Microchim Acta* **2024**, *191* (3), 138.
(222) Nong, J.; Zhang, N.; Wen, A.; Hu, C. Anti-Biofouling Laser-Scribed Graphene Electrochemical Sensor for Reliable Detection of Uric Acid in Human Saliva. *Journal of Electroanalytical Chemistry* **2024**, *952*, 117982.
(223) Lowe, S.; O'Brien-Simpson, N. M.; Connal, L. A. Antibiofouling Polymer Interfaces: Poly(Ethylene Glycol) and Other Promising Candidates. *Polym. Chem.* **2014**, *6* (2), 198–212.
(224) Zhao, Y.-F.; Zhu, L.-P.; Yi, Z.; Zhu, B.-K.; Xu, Y.-Y. Zwitterionic Hydrogel Thin Films as Antifouling Surface Layers of Polyethersulfone Ultrafiltration Membranes Anchored via Reactive Copolymer Additive. *Journal of Membrane Science* **2014**, *470*, 148–158.
(225) Qu, K.; Yuan, Z.; Wang, Y.; Song, Z.; Gong, X.; Zhao, Y.; Mu, Q.; Zhan, Q.; Xu, W.; Wang, L. Structures, Properties and Applications of Zwitterionic Polymers. *ChemPhysMater* **2022**, *1* (4), 294–309.
(226) Chen, Z. Surface Hydration and Antifouling Activity of Zwitterionic Polymers. *Langmuir* **2022**, *38* (15), 4483–4489.

(227) Harris, J. M. *Poly(Ethylene Glycol) Chemistry: Biotechnical and Biomedical Applications*; Springer Science & Business Media, 1992.
(228) Szleifer, I. Protein Adsorption on Surfaces with Grafted Polymers: A Theoretical Approach. *Biophysical Journal* **1997**, *72* (2, Part 1), 595–612. https://doi.org/10.1016/S0006-3495(97)78698-3.
(229) Blaszykowski, C.; Sheikh, S.; Thompson, M. Surface Chemistry to Minimize Fouling from Blood-Based Fluids. *Chem. Soc. Rev.* **2012**, *41* (17), 5599–5612.
(230) Ostuni, E.; Chapman, R. G.; Holmlin, R. E.; Takayama, S.; Whitesides, G. M. A Survey of Structure−Property Relationships of Surfaces That Resist the Adsorption of Protein. *Langmuir* **2001**, *17* (18), 5605–5620.
(231) Moayedi, S.; Xia, W.; Lundergan, L.; Yuan, H.; Xu, J. Zwitterionic Polymers for Biomedical Applications: Antimicrobial and Antifouling Strategies toward Implantable Medical Devices and Drug Delivery. *Langmuir* **2024**, *40* (44), 23125–23145.
(232) Lowe, A. B.; McCormick, C. L. Synthesis and Solution Properties of Zwitterionic Polymers. *Chem. Rev.* **2002**, *102* (11), 4177–4190.
(233) Zhang, Z.; Zhang, M.; Chen, S.; Horbett, T. A.; Ratner, B. D.; Jiang, S. Blood Compatibility of Surfaces with Superlow Protein Adsorption. *Biomaterials* **2008**, *29* (32), 4285–4291.
(234) Zambrano, A. C.; Loiola, L. M. D.; Bukhamsin, A.; Gorecki, R.; Harrison, G.; Mani, V.; Fatayer, S.; Nunes, S. P.; Salama, K. N. Porous Laser-Scribed Graphene Electrodes Modified with Zwitterionic Moieties: A Strategy for Antibiofouling and Low-Impedance Interfaces. *ACS Appl. Mater. Interfaces* **2024**, *16* (4), 4408–4419.
(235) Jayathilake, P. G.; Jana, S.; Rushton, S.; Swailes, D.; Bridgens, B.; Curtis, T.; Chen, J. Extracellular Polymeric Substance Production and Aggregated Bacteria Colonization Influence the Competition of Microbes in Biofilms. *Front. Microbiol.* **2017**, *8*.
(236) Deka, S. R.; Sharma, A. K.; Kumar, P. Cationic Polymers and Their Self-Assembly for Antibacterial Applications. *Current Topics in Medicinal Chemistry 15* (13), 1179–1195.
(237) Lv, X.; Liu, C.; Song, S.; Qiao, Y.; Hu, Y.; Li, P.; Li, Z.; Sun, S. Construction of a Quaternary Ammonium Salt Platform with Different Alkyl Groups for Antibacterial and Biosensor Applications. *RSC Adv.* **2018**, *8* (6), 2941–2949.
(238) Zhou, P.; Li, X.; Yuan, H.; Zhou, J.; Qu, L.; Yang, Y.; He, G.; Luo, C. A Long-Acting Hygroscopic and Antibacterial Composite Filler: A New Approach to Phytoextraction Solid Residues from *Citrus Aurantium L.* *Industrial Crops and Products* **2022**, *187*, 115505. https://doi.org/10.1016/j.indcrop.2022.115505.
(239) Sarakatsanou, C.; Karastogianni, S.; Girousi, S. Promising Electrode Surfaces, Modified with Nanoparticles, in the Sensitive and Selective Electroanalytical Determination of Antibiotics: A Review. *Applied Sciences* **2023**, *13* (9), 5391.
(240) Chen, L.; Chen, D.; Lian, M. Progress in the Development of Antifouling Electrochemical Biosensors. *Current Analytical Chemistry 22* (3), 372–389.
(241) Oliveira, D. A.; Althawab, S.; McLamore, E. S.; Gomes, C. L. One-Step Fabrication of Stimuli-Responsive Chitosan-Platinum Brushes for Listeria Monocytogenes Detection. *Biosensors* **2021**, *11* (12), 511.
(242) Evdokimov, A. A.; Baldina, A. A.; Nikitina, A. A.; Aliev, T. A.; Zenkin, A. M.; Zhukov, M. V.; Pantyukhin, I. S.; Skorb, E. V.; Muravev, A. A. A Portable Electrochemical Immunosensor for Detection of *S. Aureus* Based on Polyelectrolyte-Modified Screen-Printed Carbon Electrode. *Sensing and Bio-Sensing Research* **2025**, *47*, 100744.
(243) Zhang, J.; Tang, W.; Zhang, X.; Song, Z.; Tong, T. An Overview of Stimuli-Responsive Intelligent Antibacterial Nanomaterials. *Pharmaceutics* **2023**, *15* (8), 2113. https://doi.org/10.3390/pharmaceutics15082113.
(244) Ariaeenejad, S.; Motamedi, E.; Salimi, M.; Tayi, F.; Zahouily, M. Enzyme Immobilization on Hydrogels: An Overview on Methods, Interactions and Divers Applications. *International Journal of Biological Macromolecules* **2026**, *336*, 149325.
(245) Mu, M.; Wang, X.; Taylor, M.; Castillo, A.; Cisneros-Zevallos, L.; Akbulut, M.; Min, Y. Multifunctional Coatings for Mitigating Bacterial Fouling and Contamination. *Colloid and Interface Science Communications* **2023**, *55*, 100717.
(246) Norrman, K.; Ghanbari-Siahkali, A.; Larsen, N. B. 6 Studies of Spin-Coated Polymer Films. *Annu. Rep. Prog. Chem., Sect. C: Phys. Chem.* **2005**, *101* (0), 174–201.
(247) Aslfattahi, N.; Kiai, M. S.; Baydogan, N.; Xu, C.; Samylingam, L.; Kadirgama, K. Synergistic Physical and Chemical Polysulfide Immobilization via Laser-Induced Graphene Separator in LiS Batteries. *Inorganic Chemistry Communications* **2026**, *186*, 116299.

(248) Fatkullin, M.; Petrov, I.; Dogadina, E.; Kogolev, D.; Vorobiev, A.; Postnikov, P.; Chen, J.-J.; de Oliveira, R. F.; Kanoun, O.; Rodriguez, R. D.; Sheremet, E. Electrochemical Switching of Laser-Induced Graphene/Polymer Composites for Tunable Electronics. *Polymers* **2025**, *17* (2), 192.
(249) Setiyanto, H.; Purwaningsih, D. R.; Saraswaty, V.; Mufti, N.; Zulfikar, M. A. Highly Selective Electrochemical Sensing Based on Electropolymerized Ion Imprinted Polyaniline (IIPANI) on a Bismuth Modified Carbon Paste Electrode (CPE-Bi) for Monitoring Nickel(II) in River Water. *RSC Adv.* **2022**, *12* (45), 29554–29561.
(250) Bhattacharyya, A. S. Conducting Polymers in Biosensing: A Review. *Chemical Physics Impact* **2024**, *8*, 100642.
(251) Ahuja, T.; Mir, I. A.; Kumar, D.; Rajesh. Biomolecular Immobilization on Conducting Polymers for Biosensing Applications. *Biomaterials* **2007**, *28* (5), 791–805.
(252) Barlett, P. N.; Cooper, J. M. A Review of the Immobilization of Enzymes in Electropolymerized Films. *Journal of Electroanalytical Chemistry* **1993**, *362* (1), 1–12.
(253) Domínguez-Domínguez, S.; Arias-Pardilla, J.; Berenguer-Murcia, Á.; Morallón, E.; Cazorla-Amorós, D. Electrochemical Deposition of Platinum Nanoparticles on Different Carbon Supports and Conducting Polymers. *J Appl Electrochem* **2008**, *38* (2), 259–268.
(254) Bu, F.; Shu, Q.; Zhang, Q. Effect of Pulse Electrodeposition Parameters on the Catalytic Performance of PtNi Oxygen Reduction. *Catalysts* **2026**, *16* (4), 293.
(255) D. Landolt. Fundamentals of Electrochemical Deposition, Second Ed., M. Paunovic, M. Schlesinger (Eds.), Wiley-Interscience (2006), € 87,90, 374 Pp., ISBN: 0-471-71221-3. *Electrochimica Acta* **2007**, *52* (24), 7171.
(256) Tonelli, D.; Scavetta, E.; Gualandi, I. Electrochemical Deposition of Nanomaterials for Electrochemical Sensing. *Sensors* **2019**, *19* (5), 1186.
(257) Mazzotta, E.; Di Giulio, T.; Mastronardi, V.; Pompa, P. P.; Moglianetti, M.; Malitesta, C. Bare Platinum Nanoparticles Deposited on Glassy Carbon Electrodes for Electrocatalytic Detection of Hydrogen Peroxide. *ACS Appl. Nano Mater.* **2021**, *4* (8), 7650–7662.
(258) Ahmad, R.; Wolfbeis, O. S.; Hahn, Y.-B.; Alshareef, H. N.; Torsi, L.; Salama, K. N. Deposition of Nanomaterials: A Crucial Step in Biosensor Fabrication. *Materials Today Communications* **2018**, *17*, 289–321.
(259) Datta, S.; Christena, L. R.; Rajaram, Y. R. S. Enzyme Immobilization: An Overview on Techniques and Support Materials. *3 Biotech* **2013**, *3* (1), 1–9.
(260) Wang, L.; Yamauchi, Y. Block Copolymer Mediated Synthesis of Dendritic Platinum Nanoparticles. *J. Am. Chem. Soc.* **2009**, *131* (26), 9152–9153.
(261) Białas, K.; Moschou, D.; Marken, F.; Estrela, P. Electrochemical Sensors Based on Metal Nanoparticles with Biocatalytic Activity. *Microchim Acta* **2022**, *189* (4), 172.
(262) Malekzad, H.; Zangabad, P. S.; Mirshekari, H.; Karimi, M.; Hamblin, M. R. Noble Metal Nanoparticles in Biosensors: Recent Studies and Applications. *Nanotechnol Rev* **2017**, *6* (3), 301–329.
(263) Gooding, J. J.; Mearns, F.; Yang, W.; Liu, J. Self-Assembled Monolayers into the 21st Century: Recent Advances and Applications.
(264) Liu, J.; Zhang, L.; Yang, C.; Tao, S. Preparation of Multifunctional Porous Carbon Electrodes through Direct Laser Writing on a Phenolic Resin Film. *J. Mater. Chem. A* **2019**, *7* (37), 21168–21175.
(265) Cosnier, S.; Holzinger, M. Biosensors Based on Electropolymerized Films. In *Electropolymerization*; John Wiley & Sons, Ltd, 2010; pp 189–213. https://doi.org/10.1002/9783527630592.ch10.
(266) Gerard, M.; Chaubey, A.; Malhotra, B. D. Application of Conducting Polymers to Biosensors. *Biosensors and Bioelectronics* **2002**, *17* (5), 345–359. https://doi.org/10.1016/S0956-5663(01)00312-8.
(267) Sadki, S.; Schottland, P.; Brodie, N.; Sabouraud, G. The Mechanisms of Pyrrole Electropolymerization. *Chem. Soc. Rev.* **2000**, *29* (5), 283–293. https://doi.org/10.1039/A807124A.
(268) Heinze, J.; Frontana-Uribe, B. A.; Ludwigs, S. Electrochemistry of Conducting Polymers-Persistent Models and New Concepts. *Chem. Rev.* **2010**, *110* (8), 4724–4771.
(269) Huang, J.; Virji, S.; Weiller, B. H.; Kaner, R. B. Nanostructured Polyaniline Sensors. *Chemistry – A European Journal* **2004**, *10* (6), 1314–1319.
(270) Cosnier, S. *Electrochemical Biosensors*; CRC Press, 2015.
(271) Zonov, R. G.; Mikheev, K. G.; Chulkina, A. A.; Zlobin, I. A.; Mikheev, G. M. Effect of Laser Power on the Structure and Specific Surface Area of Laser-Induced Graphene. *Diamond and Related Materials* **2024**, *148*, 111409.
(272) Thaweeskulchai, T.; Sakdaphetsiri, K.; Schulte, A. Ten Years of Laser-Induced Graphene: Impact and Future Prospect on Biomedical, Healthcare and Wearable Technology. *Microchim Acta* **2024**, *191* (5), 292.

(273) Khanmohammadi, A.; Ghazizadeh, A.; Hashemi, P.; Afkhami, A.; Arduini, F.; Bagheri, H. An Overview to Electrochemical Biosensors and Sensors for the Detection of Environmental Contaminants. *Journal of the Iranian Chemical Society* **2020**, *17*.
(274) Wanjari, V. P.; Reddy, A. S.; Duttagupta, S. P.; Singh, S. P. Laser-Induced Graphene-Based Electrochemical Biosensors for Environmental Applications: A Perspective. *Environ Sci Pollut Res* **2023**, *30* (15), 42643–42657.
(275) Chen, J.; Ding, X.; Zhang, D. Challenges and Strategies Faced in the Electrochemical Biosensing Analysis of Neurochemicals in Vivo: A Review. *Talanta* **2024**, *266*, 124933.
(276) Rivera, P.; Della Pelle, F.; Stonyte, J.; Martins Antunes de Melo, W. de C.; Abouhagger, A.; Pauliukaite, R. Overcoming Challenges in Electrochemical Sensing: Toward Continuous Monitoring. *ACS Sens.* **2025**, *10* (12), 9183–9202.
(277) Hiraka, K.; Tsugawa, W.; Asano, R.; Yokus, M. A.; Ikebukuro, K.; Daniele, M. A.; Sode, K. Rational Design of Direct Electron Transfer Type L-Lactate Dehydrogenase for the Development of Multiplexed Biosensor. *Biosensors and Bioelectronics* **2021**, *176*, 112933.
(278) Massoumi, H.; Chug, M. K.; Nguyen, G. H.; Brisbois, E. J. A Multidisciplinary Experiment to Characterize Antifouling Biocompatible Interfaces via Quantification of Surface Protein Adsorption. *J. Chem. Educ.* **2022**, *99* (7), 2667–2676.
(279) Swebocki, T.; Barras, A.; Kocot, A.; magdalena.plotka; rabah.boukherroub. Minimum Inhibitory Concentration (MIC) and Minimum Bactericidal Concentration (MBC) Assays Using Broth Micr. **2023**.
(280) Khodadadi Yazdi, M.; Manohar, A.; Olejnik, A.; Smułka, A.; Kramek, A.; Pierpaoli, M.; Saeb, M. R.; Bogdanowicz, R.; Ryl, J. Elucidating Charge Transfer Process and Enhancing Electrochemical Performance of Laser-Induced Graphene *via* Surface Engineering with Sustainable Hydrogel Membranes: An Electrochemist's Perspective. *Talanta* **2025**, *281*, 126836.
(281) Łepek, A.; Manohar, A.; Pierpaoli, M.; Bogdanowicz, R.; Gaweł, Ł.; Khodadadi Yazdi, M.; Ryl, J. Neutral-pH Electropolymerization of Aniline on Hierarchically Porous Laser-Induced Graphene Electrodes for Dual Biosensing. *Advanced Materials Technologies* **2026**, *11* (5), e01757. https://doi.org/10.1002/admt.202501757.
(282) Nicholson, R. S. Theory and Application of Cyclic Voltammetry for Measurement of Electrode Reaction Kinetics. *Anal. Chem.* **1965**, *37* (11), 1351–1355.
(283) Manohar, A.; Łepek, A.; Kocot, A. M.; Smalc-Koziorowska, J.; Swebocki, T.; Khodadadi Yazdi, M.; Ryl, J. Electrochemical Glucose Sensing at a Multifunctional Hydrogel-Modified Laser-Induced Graphene Interface. *Small Structures* **2026**, *7* (8), e70562.

List of Figures

Figure 1: Different types of carbon nanostructures for electrochemical platforms. 20
Figure 2: Evolution of carbon electrods platforms. 21
Figure 3: Representation of LIG formation on PI by laser irradiation. 24
Figure 4: Synthesis and applications of LIG. 25
Figure 5: LIG formation on different precursors 25
Figure 6: Illustration of photothermal conversion of a PI foil into a patterned LIG electrode via direct CO_2 laser irradiation 26
Figure 7: Characterization of LIG using different laser parameters 29
Figure 8: Morphological, structural and surface characteristics of LIG. 32
Figure 9: Representative TEM and HR-TEM images of LIG 33
Figure 10: Representation of multiscale formation mechanism from polyimide. 33
Figure 11: Influence of atmosphere and contact angle 36
Figure 12: Electrode designed in Lightburn. 59
Figure 13: Optimization matrix of Kapton-LIG with representative photographs for LIG fabrication on 50 µm and 100 µm Kapton substrates 72
Figure 14: SEM images for LIG formed on substrate of different thickness. 74
Figure 15: Structural and surface characterization of LIG. 76
Figure 16: Contact angle measurement. 79
Figure 17: Effect of interval spacing on a water contact angle for LIGs on 100µm Kapton-derived LIG. 80
Figure 18: Effect of interval spacing and effect of power and speed on electrical conductivity of the LIG. 82
Figure 19: Effect of laser power and laser speed of LIGs fabricated on 50µm substrate 83
Figure 20: Repeatability and CV plot showing influence of Laser fluence. 84
Figure 21: Effect of laser power and laser speed on a) max current density and b) peak separation of LIGs 85
Figure 22: EASA of P12%S160 on 50µm Kapton. 86
Figure 23: EASA of P19%S220 on 100µm Kapton.. 87
Figure 24: EIS spectra for LIG 88
Figure 25: SEM images illustrating the influence of laser focus position (Z-offset) on the morphology 90
Figure 26: Preliminary assessment of the influence of laser focus position (Z-offset) on the electrochemical behaviour of LIG electrodes. 91
Figure 27: Chemical structure of hydrogels. 92
Figure 28: SEM images at two different magnifications for comparison of CS with bare. 93
Figure 29: High-resolution XPS spectra of hydrogel-modified LIG. 94
Figure 30: Wettability of bare and hydrogel-modified LIG. 96
Figure 31: Electrochemical behaviour of bare and HM-coated LIG 97
Figure 32: Comparison of EIS spectra for bare and hydrogel modified LIGs. 101
Figure 33: Effect of crosslinking in CS 102
Figure 34: Electrodeposition of Iridium and Platinum nanostructures. 104
Figure 35: SEM images illustrating the morphological evolution of bimetallic functionalized LIG 106

Figure 36: TEM images of electrodeposited metallic nanostructures..... 107
Figure 37: HAADF-STEM for nanozyme electrode..... 107
Figure 38: XPS of nanozymes 108
Figure 39: Comparison of CV plots of bare and nanozymes modified electrodes 110
Figure 40: Estimation of EASA bare vs nanozymes..... 111
Figure 41: Bubble plot illustrating the relationship between the theoretical metal loading (calculated using Faraday's law), electroactive surface area (EASA) and heterogeneous electron-transfer rate constant (k^0) for bare and nanozyme-modified LIG electrodes. 113
Figure 42: EIS Spectra of bare LIG and Ir-Pt@LIG..... 114
Figure 43: Electrocatalytic performance of nanozyme platform 116
Figure 44: Analytical performance and operational stability..... 117
Figure 45: CV plots of electropolymerization of functional polymers. 118
Figure 46: Evolution of polymer growth. 119
Figure 47: Influence of ammonium persulfate (APS) concentration on electropolymerization of SBMA . 120
Figure 48: Proposed electropolymerization mechanisms of APTAC and SBMA. 121
Figure 49: SEM micrographs of individually electropolymerized polymer coatings on LIG 122
Figure 50: SEM micrographs of multifunctional copolymer at two different magnifications. 123
Figure 51: High-resolution XPS spectra of electropolymerized polymer-coated LIGs..... 124
Figure 52: Glucose sensing performance 127
Figure 53: Selectivity of the multifunctional copolymer electrode 128
Figure 54: Glucose sensing at lower potential. 129
Figure 55: Operational stability 130
Figure 56: Electroanalytical performance of the multifunctional Ir-Pt-CoP-GOx@LIG platform in artificial sweat..... 131
Figure 57: Time-dependent electrochemical response of the multifunctional copolymer-modified electrode in presence and absence of BSA 133
Figure 58: Semi-quantitative broth microdilution assessment of polymer suspensions derived from individually electropolymerized polymers against *E. coli* and MRSA..... 134
Figure 59: Semi-quantitative broth microdilution assessment of polymer suspensions derived from the multifunctional copolymer against *E. coli* and MRSA 135
Figure 60: Schematic illustration of the laser-processing strategy developed for cellulose-derived LIG. . 140
Figure 61: Photographs of cellulose-derived LIG fabricated..... 141
Figure 62: Photographs of cellulose substrates processed exclusively under defocused laser irradiation. . 141
Figure 63: Defocused mode only lasing with different laser parameter 142
Figure 64: Cellulose-derived LIG fabricated using the sequential defocused-focused strategy..... 142
Figure 65: Raman optical micrographs illustrating the influence of hatch interval on the continuity of cellulose-derived LIG. 143
Figure 66: Raman optical micrographs of cellulose-derived LIG fabricated at a fixed scan speed under different combinations of defocused and focused laser powers..... 143
Figure 67: Raman spectra of cellulose-derived LIG under different laser-processing condition 144

Figure 68: Representative Raman spectra of cellulose-derived LIG fabricated using the sequential defocused–focused laser-processing strategy. 145
Figure 69: Preliminary processing matrix illustrating the influence of laser power and scan speed on the laser-induced transformation of PTFE under focused irradiation. 150
Figure 70: Preliminary evaluation of PTFE processing conditions showing the influence of scribing mode and intervals 150
Figure 71: SEM and Raman microscopic images of laser-processed PTFE 152
Figure 72: PEGDA-assisted transfer of LIG. 154
Figure 73: SEM micrographs of PEGDA-assisted transferred LIG at different magnifications 155

List of Tables

Table 1. Comparison of different carbon electrode materials with respect to their electrochemical advantages and key limitations 21
Table 2. Principal laser processing parameters and their primary effects on LIG formation. 26
Table 3. Influence of laser processing parameters on LIG formation and properties. 28
Table 4. Multiscale architecture of LIG and its electrochemical function 34
Table 5. Characterization techniques commonly employed for LIG 37
Table 6. Peak deconvolution details from high-resolution XPS spectra of LIG 77
Table 7. Contact angle measurements for electrodes with different power and speed 78
Table 8. Longitudinal and transverse sheet resistance of LIG fabricated on 50μm Kapton foil 81
Table 9. Peak deconvolution details from high-resolution XPS spectra of different hydrogels. 95
Table 10. Estimated values for D for bare and HM-coated SPCE (CS, Alg, Agar). 98
Table 11. EASA of bare and HM LIG electrodes estimated from the Randles-Ševčík relationship. 99
Table 12. Heterogeneous electron-transfer rate constants of bare and HM-coated LIG electrodes. 100
Table 13. Electrodeposition parameters 105
Table 14. EASA and k^0 of the bare and nanozyme modified electrodes 112
Table 15. Sheet resistance of cellulose-derived LIG fabricated using the sequential defocused-focused laser-processing strategy at a scan speed of 150mm/s and different combinations of focused and defocused laser powers at interval spacing of 0.02mm. 146
Table 16. Sheet resistance of cellulose-derived LIG fabricated using the sequential defocused–focused laser-processing strategy at a scan speed of 150mm/s and different combinations of focused and defocused laser powers at interval spacing of 0.03mm. 147